# UNIVERSITY OF SOUTHAMPTON

Faculty of Natural and Environmental Sciences

Ocean and Earth Science


# Determining the along and across strike segmentation of the Central Sumatra Subduction Zone

by


**Thomas Richard Hall**


Thesis for the degree of Philosophy

[August 2016]

UNIVERSTIY OF SOUTHAMPTON

# ABSTRACT

**FACULTY OF NATURAL AND ENVIRONMENTAL SCIENCES**

**Ocean and Earth Science**

**Doctor of Philosophy**

**Determining the along and across strike segmentation of the Central Sumatra Subduction Zone**

**By Thomas Richard Hall**

The Sumatra subduction zone is one of the most seismically active subduction zones on the planet. In the last decade it has produced one of the largest events in recorded history, the $M_W$ 9.2 northern Sumatra earthquake, as well as a subsequent event in 2005 at $M_w$ 8.7. Rupture propagation along subduction zones is fundamentally linked to the structure of the subduction zone. Understanding the structure within the Sumatran subduction zone is paramount to not only being able to identify fundamental processes that occur within the subduction zone but also the effects structures can have on rupture propagation.

In this thesis I present a new method to jointly invert for body wave arrival times for teleseismic and local events at a local scale to further image the finer scale structures of the shallow part of the central Sumatran subduction zone as well as image some of the deeper structures to a higher resolution than conducted before. I present Vp and Vp/Vs ratios for the central part of the Sumatran subduction zone spanning from the trench to the volcanic front down to depths of 450 km using the new method. The model shows a clear vertical velocity boundary between the accretionary domain of Sumatra and its inner forearc, where below the inner forearc the Moho is 10 km shallower then below the continental arc inferring that the inner forearc is of different composition to the mainland.

I improve the Vp models for the shallow part of the Sumatran forearc (<50 km) by inverting the body wave arrival times of local and active shot data. From these models I discuss the general structure of the Sumatran forearc and identify common links with other subduction zones around the world. From the improved resolution we can further quantify the structure and composition of the inner forearc crust. Velocities of 7.0 km $s^{-1}$ are observed as shallow as 10 km depth, compared to 4.0 km $s^{-1}$ for the accretionary domain to the east and 5.5 km $s^{-1}$ for the continental arc to the west at 10 km depth. The continental Moho beneath the inner forearc is observed at 30 km, approximately 10 km shallower than beneath the continental arc. Moho variations and the observed velocity profiles across strike lead us to suggest that the inner Sumatran forearc is composed of an uplifted ophiolitic complex which acts as a backstop for the accretionary domain.

Finally, I examine spatial patterns in seismicity to better quantify the rupture potential of the Sumatran subduction zone. To do this we apply *K*-means algorithm to partition seismicity into clusters and use the cluster model as a base to generate a segmentation model for the Sumatran seismogenic interface. From the models I show that segmentation boundaries coincide with termination points of known ruptures as well as suggest potential rupture scenarios for the Mentawai segment, a region that is overdue for a >$M_w$ 8.0 rupture. A potential future rupture of the Mentawai islands could be as large as $M_w$ 9.0-9.2.

# Contents

**ABSTRACT** ..... **i**

**List of Tables** ..... **vi**

**List of Figures** ..... **vii**

**Declaration of Authorship** ..... **xiii**

**Acknowledgements** ..... **xv**

**1 Chapter 1: Introduction** ..... **1**

1.1 Overview ..... 1

1.2 Key elements in Subduction Zones ..... 4

1.2.1 Subducting Slab ..... 4

1.2.2 Forearc ..... 5

1.2.3 Mantle Wedge ..... 6

1.2.4 Sub-slab Mantle ..... 7

1.3 Interface Seismicity and Along-strike Segmentation of Subduction Zones ..... 7

**2 Chapter 2: The Sumatra Subduction Zone** ..... **10**

2.1 Formation ..... 11

2.2 Forearc Structure ..... 12

2.3 Plate Boundary Earthquakes ..... 15

2.4 Relative Plate Motions ..... 16

2.5 Plate Coupling ..... 17

2.6 Subducting Slab ..... 19

**3 Chapter 3: Brief overview of seismic tomography methods** ..... **20**

3.1 Introduction ..... 20

3.2 Basic Theoretical Framework ..... 21

3.3 Model Parameterisation ..... 21

3.4 Forward Problem ..... 21

3.5 Inversion ..... 22

3.6 Resolution and Error Analysis ..... 23

3.7 Joint Inversion ..... 23

3.8 Aims and Objectives ..... 24

**4 Chapter 4: Evidence for a shallow Forearc Moho in central Sumatra from joint inversion of local and teleseismic data** ..... **26**

4.1 Introduction ..... 26
4.1.1 Subduction Zones ..... 26
4.1.2 Sumatra ..... 27
4.1.3 Outer Forearc (Trench-Landward Edge of the Islands) ..... 29
4.1.4 Inner Forearc ..... 29
4.1.5 Subducting Plate ..... 30
4.1.6 Past Seismicity ..... 30
4.1.7 Mainland and Mantle Wedge ..... 31
4.1.8 Current Tomography Studies ..... 31
4.2 Data ..... 31
4.2.1 Local Events ..... 33
4.2.2 Teleseismic Events ..... 34
4.3 Method ..... 35
4.3.1 Forward Problem: Local Earthquake, Shot or Blast. ..... 35
4.3.2 Forward Problem: Teleseismic Event ..... 35
4.3.3 Inverse Problem ..... 37
4.4 Modelling process ..... 38
4.4.1 Model Setup ..... 39
4.4.2 Model Parameters ..... 40
4.4.3 Smoothing Process ..... 44
4.4.4 Squeezing Tests ..... 44
4.4.5 Checkerboard and Synthetic Tests ..... 44
4.4.6 Model Error ..... 46
4.4.7 Comparison between independently and jointly inverting local and teleseismic data. 47
4.5 Results ..... 48
4.5.1 Incoming Oceanic Plate ..... 49
4.5.2 Active Domain (10-75 km across strike) ..... 50
4.5.3 Forearc High (75-130 km across strike) ..... 52
4.5.4 Inner Forearc Crust (130-220 km across strike) ..... 52
4.5.5 Sumatran Mainland: Volcanic Arc and the Great Sumatran Fault (220-390 km across strike) 53
4.5.6 Continental Mantle Wedge (150-350 km across strike) ..... 55
4.5.7 Oceanic Asthenosphere Mantle ..... 55
4.6 Discussion ..... 55
4.6.1 Inner Forearc Moho and Basins Boundary. ..... 55

4.6.2 Presence/Absence of the Forearc islands and Basins Along-Strike ..... 57
4.6.3 Mantle Wedge ..... 57
4.6.4 Sub-Slab Mantle ..... 58
4.6.5 Slab Structure ..... 58
4.7 Conclusions ..... 59
**5 Chapter 5: Evidence for an ophiolitic complex acting as a backstop within Sumatra's forearc ..... 61**
5.1 Introduction ..... 61
5.2 Method ..... 63
5.2.1 Forward Problem: Local Earthquake, Shot or Blast. ..... 64
5.2.2 Inverse Problem ..... 65
5.3 Data ..... 65
5.3.1 Earthquake Sources ..... 65
5.3.2 Active Source ..... 66
5.4 Model Parameterisation ..... 68
5.4.1 Model Set Up ..... 69
5.4.2 Checkerboard Tests ..... 72
5.5 Results ..... 73
5.5.1 Outer Forearc. ..... 73
5.5.2 Inner Forearc ..... 75
5.5.3 Subducting Oceanic Crust ..... 75
5.5.4 Deep Hypocenters ..... 75
5.6 Discussion ..... 76
5.6.1 Inclusion of Active source data ..... 76
5.6.2 Accretionary Wedge ..... 76
5.6.3 Location of the Forearc Islands and Forearc Basins ..... 76
5.6.4 Earthquake Hypocenter Distribution within the Oceanic Plate ..... 77
5.6.5 Comparison of Velocity Structure between Local and Active Source Models ..... 77
5.6.6 Inner Forearc Block ..... 79
5.7 Conclusions ..... 80
**6 Chapter 6: Segmentation of the Sumatra Subduction Zone ..... 82**
6.1 Introduction ..... 82
6.2 Method ..... 84
6.3 Data ..... 88
6.4 Results ..... 90

6.4.1 Chosen Model ..... 91
6.4.2 Common K Ranges ..... 91
6.4.3 Optimum K Range ..... 92
6.4.4 NEIC Data Sets ..... 93
6.4.5 GCMT Data Sets ..... 94
6.4.6 Trends within Model Results ..... 94
6.4.7 Tessellation into segment zones ..... 96
6.5 Discussion ..... 96
6.5.1 Segment Boundary Locations and Relationships to Historic/Recent Ruptures. ..... 96
6.5.1.1 2004 Rupture Zone –Light Green, Dark Blue, Green ..... 96
6.5.1.2 2005 Rupture Zone – Yellow ..... 97
6.5.1.3 1799/1833 Rupture Zones – Purple and Green ..... 98
6.5.1.4 Southern Sumatra Clusters and Boundaries – Red, Light Blue and Blue ..... 98
6.5.2 Potential Earthquake Magnitude of Segment Ruptures ..... 98
6.5.3 The 1797 and 1833 Events and Central Sumatra Hazard Potential ..... 100
6.5.4 Orientation of Cluster Boundaries ..... 102
6.6 Conclusions ..... 102
**7 Chapter 7: Conclusions ..... 103**
7.1 Overview ..... 103
7.2 Model Development and Improvements ..... 103
7.3 Structure and Properties of the Central Sumatran subduction zone as revealed from joint tomography ..... 104
7.4 Composition of the Central Sumatran Inner Forearc ..... 105
7.5 Segmentation of the seismogenic interface ..... 106
7.6 Future work ..... 107
7.6.1 Sumatra ..... 107
7.6.2 Tomography ..... 107
7.6.3 K-means clustering ..... 107
**8 Chapter 8: Appendix ..... 124**

# List of Tables

Table 6.1. Summary of the catalogues used in the analysis. All subsets had the initial magnitude limitations for the spatial and temporal dimensions stated in section 6.3. For each of the subsets (1-7), the data source, number of events within the subset and the filters applied are shown, a black box indicates an applied filter to the subset. There were three possible filters, filtering the subset for thrust events (GMCT only), for events seaward of the trench, and for events pre-2004. The mean KL value for the 2: K clusters achieved standard deviation (SD) in the KL index across the 2: K clusters. The KL cut-off value is the value of which the cluster models achieving less than that score can be ignored. ..... 90

Table 6.2 Summary of cluster parameters: southern termination, number of events within each cluster, length of each segment. 6$^{th}$ column shows notable ruptures that have occurred within the segment. Calculated magnitudes derived from Eq. 6.7 (RA) and 6.9 ($M_o$). Magnitude M is based on a rupture area of S*200 km where S is segment length. $M_w$ is based on Area of S*200 km and a slip of 10 meters with a rock rigidity of $3x10^{10}$ $Nm^{-2}$ ..... 100

# List of Figures

Figure 1.1 Basic schematic of a subduction zone. Showing the subducting slab (Oceanic crust +lithospheric mantle) the asthenospheric mantle, mantle wedge, mantle wedge corner and overriding island arc crust and trench with their approximate relation to the surface expression of Sumatra. (source:www.earthobservatory.sg) ..... 1

Figure 1.2 An example of the current state of the art using joint tomography taken from Zhao et al., (1992). Local region and teleseismic data are used in inversion to model the deep structure of the Japan subduction zone. Blue and red denote high and low velocity perturbations. White dots represent earthquake and solid black triangles represent volcanoes. ..... 2

Figure 1.3 An example of the current state of the art for local scale (<1000km) teleseismic inversion. VP/VS heterogeneity beneath the Mantle Electromagnetic and Tomography Experiment (MELT) region of the East Pacific Rise from analysis of Pand S body waves (Hammond and Toomey (2003). .. 3

Figure 2.1: General tectonic setting of Sumatra. Earthquake rupture areas from: 1797 and 1833 (Natawidjaja et al., 2006), 1861 (Newcomb and McCann 1987), 2007a and 2007b (Konca et al., 2008), 2004 (Lay et al., 2005) and 2005 (Briggs et al., 2006). The trace of the Mentawai Fault is taken from Diament et al., (1992), the Great Sumatran Fault is taken from Burton and Hall (2014) with different colours along the fault showing segmentation as defined by seismicity (colours have no relation to the rupture zones). GSF=Great Sumatran Fault, MF=Mentawai Fault, IFZ=Investigator Fracture Zone, WF=Wharton Fossil Ridge, WAF = Western Andaman fault zone. The Investigator Fracture Zone is mapped from local topography. Convergence rates for the subducting plate are taken from McNeill and Henstock (2014). Black arrow indicates total convergence and red arrow indicates convergence between the subducting plate and the forearc sliver. Slip rates for the GSF are taken from Bellier and Sebrier (1995) and correspond to the same segment colour. Studies across the Sumatra margin are shown by parallel dashed lines and referred to in the text. Focal mechanisms for the 2012, 2004 and 2005 events are shown in relevant rupture areas and are taken from the CMT global catalogue. Parallel dashed lines correspond to previous studies in the area. SUME15, SUMD07 are reflection profiles taken from McNeill and Henstock (2014), Line A is local tomography study taken from Collings et al. (2012). The corresponding profiles are shown in figures 2.3-2.5 ..... 10

Figure 2.2: The evolution of the Sumatran subduction zone taken from Hall (2012). The figure insets show the position of southeast Asia and Australia at 80,50,30 and 5 million years ago. At 80 Ma, subduction along Sumatra was perpendicular to the margin. Due to the collision of India with Eurasia at 30 Ma subduction became highly oblique resulting in the present day scenario. ..... 11

Figure 2.3 Seismic profile SUME15 across prism toe offshore North Sumatra (McNeill and Henstock 2014). ..... 12

Figure 2.4 Seismic profile SUMD07 across the outer accretionary prism offshore Batu Islands at ~1°S, Central Sumatra (McNeill and Henstock, 2014) ..... 13

Figure 2.5 The 2D velocity model for the forearc around the Mentawai islands derived by Collings et al., 2012. Location shown in Figure 2.1. ..... 14

Figure 2.6 A seismic reflection profile taken across the Sumatran margin (Schlüter et al., 2002). Top is the reflection profile. Bottom image is the interpretation of the main structural bodies present in southern Sumatra as defined by Schlüter et al. (2002) ..... 16

Figure 2.7: Coupling across the Sumatran megathrust as reported by Chlieh et al., (2008) for 1999-2007. Data from GPS surveys from 1991 to 2001 provided vertical uplift measurements while data from 2002 onwards provided additional horizontal estimates. Fully coupled areas are shown in red, areas that having no coupling are shown in white ..... 17

Figure 2.8 Cross-sections showing the contrasting dips of the slab in different regions. Perturbations relative to ak135 (Kennett et al., 1995) are shown from −1.5% to 1.5%. Earthquake relocations (Engdahl et al., 2007) (circles) and volcano positions (triangles) are also shown. Profiles A-D represent the slab perpendicular to the trench at 22°N, 10°N, 2°N and 6°S respectively. Image taken from Pesicek et al. (2008). ..... 18

Figure 4.1: General tectonic setting of Sumatra. Earthquake rupture areas from: 1797 and 1833 (Natawidjaja et al., 2006), 1861 (Newcomb and McCann 1987), 2007a and 2007b (Konca et al., 2008), 2004 (Lay et al., 2005) and 2005 (Briggs et al., 2006). The 2012 intraplate plate event is marked by the yellow star. The trace of the MF is taken from Diament et al. (1992) the Great Sumatran Fault is taken from Burton and Hall (2014) with different colours along the fault showing segmentation as defined by seismicity (colours have no relation to the rupture zones). The Investigator Fracture Zone is mapped from local topography. The dashed black box represents the study area. GSF=Great Sumatran fault, MF=Mentawai Fault, IFZ=Investigator fracture zone. Convergence rates for the subducting plate are taken from McNeill and Henstock et al. (2014). Black arrow indicates absolute convergence and red arrow indicates amount of convergence taken up by the plate interface. Slip rates for the GSF are taken from Bellier (1995) and correspond to the same segment colour. Inset A shows a breakdown of key terms used in this paper. ..... 28

Figure 4.2. Shows the location of the local (circle) and teleseismic (stars) events used in this study. Events in red represent the events used within the joint inversion code and events in yellow represent events relocated within the final velocity model. The top left and right figures are a plan and along strike slice taken from the data set, respectively. The bottom right and left are a across strike slice and global view of the local and teleseismic data, respectively. The initial event catalogue came from Lange et al. (2010). The bottom right figure shows the location of the 88 teleseismic events used in this study. Triangles represent the stations used in this study. ..... 32

Figure 4.3. Top: An example of P wave arrival picks from a local source in the data set. Bottom: An example of the weighting window associated with each pick. Weights were manually assigned after automated picking. P0, P1, P2 and P3 labels represent the corresponding weighting associated with its error. The boxes are a visual representation of the pick error with boundaries marked correlating to pick error. ..... 34

Figure 4.4. 2D starting model derived from interpolation of 1D models. Nodes are orange circles. Setup for the 2D model and the 3D model in the X plane. ..... 39

Figure 4.5 Rays paths for the local (right), teleseismic (middle) and joint (left). Orange triangles are volcanoes. Red triangles are stations in this study. Blue lines are predicted ray paths. ..... 40

Figure 4.6 The hit counts for 3D model. Top slice shows a depth slice taken at 50 km and bottom shows an X slice taken at 0 km along strike. ..... 41

Figure 4.7: Input (left) and recovered (right) checkerboard tests from the 3D Vp models. The depth slice (top) is taken at 37 km the X transects are taken at 365, 310, 210 , 150 and 100 km across strike. ..... 42

Figure 4.8: Input (left) and recovered (right) checkerboard tests from the 3D Vs models. The depth slice (top) is taken at 37 km the X transects are taken at 365, 310, 210 , 150 and 100 km across strike. ..... 43

Figure 4.9 A synthetic test of an approximate slab model for the region, based on hypocenter locations (top), and the recovered model (bottom). The slice is taken from the 3D model at 225km along strike (perpendicular to Batu islands). ..... 45

Figure 4.10 The station correction for P wave arrivals used in the joint inversion for local and teleseismic data. Red circles indicate a positive adjustment. Blue circles indicate a negative adjustment. The black circle in the bottom left shows the scale of the circles. Inverted triangles represent stations and colours represent the station network as seen in Figure 4.2 ..... 46

Figure 4.11 The station correction for S wave arrivals used in the joint inversion for local and teleseismic data. Red circles indicate a positive adjustment blue circles indicate a negative adjustment. The black circle in the bottom left shows the scale of the circles. Inverted triangles represent stations and colours represent the station network as seen in Figure 4.2. ..... 47

Figure 4.12 Histogram plot of the P and S wave residual before the inversion process and the final 3D models ..... 48

Figure 4.13. Results from the 2D model for Vp (right) and Vp/Vs (left). The white (Vp) and black (Vp/Vs) dots represent the relocated hypocenters from the 3D model. The thicker white (Vp) and black (Vp/Vs) lines represent the plate interface based on a profile taken from the SLAB 2.0 model. The 3 thinner lines beneath are 10, 20 and 30km below the plate interface. PIS and PIP are labels discussed in the text. ..... 49

Figure 4.14. Results from the 3D Vp models. Lower panels show transects taken at 50, 200, 300, 350 and 400 km along strike. Upper panels show a depth slice taken at 24km (left) and an along strike slice taken at Y=100 km (right). Relocated Hypocenters are shown as circles, hypocenters within +/- 20km of the transect are shown. MF=Mentawai Fault, RA=label discussed in text, BS is the location of the proposed accretionary domain backstop. BF=possible inner forearc faults. The curved black line is the plate interface. ..... 51

Figure 4.15. Residual of incoming teleseismic ray. Blue is arriving too fast red is arriving too slow ... 54

Figure 5.1 Tectonic setting of Sumatra. The 1797 and 1833 rupture areas come from Natawidjaja et al. (2006). The 2004 (Lay et al., 2005) and 2005 (Ishii et al., 2005). IFZ=Investigator fracture zone, WF=Wharton Fossil ridge, GSF= Great Sumatran Fault, BF=Batee fault, FB= Forearc Basin, MF=Mentawai Fault zone. ..... 62

Figure 5.2: Stations (triangles), events (circles) and active shots (black line) used in this study. ..... 67

Figure 5.3: The starting model and X transect node set up for the 2D and 3D models. Black circles are nodes. The initial model came from the final model for the 2D inversion in Chapter 4. Df, deformation front, FB across-strike location of the forearc basins. FI is the forearc high and CL is the Sumatra coast line. The Black line represents the Moho (7.5 km s-1 contour) ..... 68

Figure 5.4: Results from the 2D checkerboard tests. Input (top) and output models (bottom) using blocks of 20x10 km in X-Z. ..... 69

Figure 5.5: Input and output results from the 3D checkerboard tests. Anomaly block size is 20x30x10 km for XYZ. Taken at 100, 175, 250, 325 and 350 km along strike. The black line indicates the area that we believe is resolved. ..... 70

Figure 5.6: Final velocity model from the 2D inversion. MF is the approximate location of the Mentawai Fault. FMW is the forearc mantle wedge, IA is the island arc crust and FB are the forearc basins. Black squares are hypocenters relocated within the 3D model. The dashed line is the plate interface estimated from SLAB 2.0. ..... 71

Figure 5.7 The station correction for P wave arrivals used in the active source study. Red circles indicate a positive adjustment Blue Circles indicate a negative adjustment. The Black circle in the bottom left shows the scale of the circles. Inverted triangles represent stations and colours represent the station network as seen in Figure 5.2 ..... 72

Figure 5.8: Slices through the final 3D velocity model taken at 100, 175, 200, 325 and 350 km along strike (bottom to top). Slices shown correspond to red lines in inset. Hypocenters (white stars) are taken +/- 20 km around each slice. Faded area represents unresolved area. ..... 74

Figure 5.9: Difference in the shallow forearc velocity of Sumatra between models derived from local/teleseismic joint inversion against local/active inversion. Negative infers that the active model is predicting slower velocities than the local/teleseismic model. ..... 78

Figure 5.10: Interpretation of velocity model obtained for the Sumatran forearc. ..... 80

Figure 6.1 Earthquake clusters along the Sumatran seismogenic interface. Each cluster is coloured differently. Cluster distribution identified using a K-means algorithm. The is the global optimum solution, with 9 clusters best representing seismogenic interface seismicity. Ruptures for the 1797 (white dashed box) and 1833 (black dashed box) (Natawidjaja et al., 2006), 1861 (black dashed box) (Newcomb and McCann 1987), 2007a and 2007b (Konca et al., 2008), 2004 (Lay et al., 2005) and 2005 (Briggs et al., 2006) earthquakes are shown. The black arrow indicates convergence direction. Inset (top right) shows the KL index results from the chosen model (yellow) and 3 other models based on different catalogues, black arrows indicate chosen models for each subset (Figure 6.2). ... 83

Figure 6.2 Optimum cluster models for subsets 6 (top right), 7 (top left), 4 (bottom right) and 2 (bottom left) from table 6.1. Individual clusters have different colors. ..... 89

Figure 6.3 Probability Density Function centroid method. Green dots represent location of the 9 centroids in the chosen cluster model. PDF functions for the 9000 possible centroids from the chosen K=9 model. White means no clusters out of the 1000 models were located there, black means 1000 centroids were located there. Black crosses represent the 9000 centroid locations. ..... 91

Figure 6.4 Segmentation model of the Sumatra seismogenic interface based on the cluster model for K=9 for the filtered GCMT catalogue. Hypocenter colour is based on cluster number. Segment length and estimated magnitude is labelled next to each segment. Segment length (in km) is calculated from the deformation front proximal to the cluster centroid. Black dashed boxes represent a rupture width of 200 km (purple cluster) and 50 km (red cluster). ..... 97

Figure 6.5 Coral record data from Natawidjaja et al. (2006). Black line is the raw data for the 1797 event and red line is the 1833 event. Uplift was used to calculate the rupture areas for the 1833 and 1797 ruptures..... 101

Figure S 8.1 Schematic explain the teleseismic methodology. Were $T^{cal}$=Calculated travel time, $T^{mod}$=Travel time within the model space, $T^{p}$=plane wave correction, $BA^{avg}$ is the bulk average correction for the teleseismic event, VS(s) and station(j) are the virtual source (s) and station(j) for the in coming observation k. ..... 124

Figure S 8.2 Full 2D node setup for the 2D and 3D X planes. ..... 124

Figure S 8.3 Squeezing tests for when the virtual source is at 200,300,400,450 and 500km depth.. 125

Figure S 8.4 The resulting 2D Vp models based on different starting models. A and B are the shallow and deep oceanic 1D starting models with C and D the resulting shallow and deep Vp velocity model. E and F and G and H are the same but using a continental starting model. White dots are hypocenters. ..... 126

Figure S 8.5 Checkerboard test for the 2D model based on 2 different input models..... 127

Figure S 8.6 A slice taken from the 3D model showing errors in the Vp and Vp/Vs models. The slice was taken at 200km across strike, Perpendicular to the Batu islands. ..... 128

Figure S 8.7 Bootstrapping tests conducted to test the robustness of the features in the model. Shown here are the 2D Vp and Vp/Vs results from 5 models each randomly removing 10% of the input data. All features discussed in the text are seen to be present in all the models. ..... 129

Figure S 8.8 Comparison results for the 2D Vp Model showing the joint 2D Vp model (bottom), local data only 2D Vp model (middle) and difference between the joint and local inversions (top). ..... 130

Figure S 8.9 Comparison results for the 2D Vp/Vs model showing the joint 2D Vp/Vs model (bottom), local data only 2D Vp/Vs model (middle) and difference between the joint and local inversions (top). ..... 131

Figure S 8.10 Errors in origin time (o.t), X,Y and Z for the relocated hypocenters from the local/active source 3D model. ..... 132

Figure S 8.11 K-means Schematic depicting how the algorithm chooses optimum cluster location for 5 clusters ..... 133

Figure S 8.12 Explanations of how the KL index is calculated based on a K cluster model ..... 134

# Declaration of Authorship

I, .....

declare that this thesis and the work presented in it are my own and has been generated by me as the result of my own original research.

.....

.....

I confirm that:

This work was done wholly or mainly while in candidature for a research degree at this University;
Where any part of this thesis has previously been submitted for a degree or any other qualification at this University or any other institution, this has been clearly stated;
Where I have consulted the published work of others, this is always clearly attributed;
Where I have quoted from the work of others, the source is always given. With the exception of such quotations, this thesis is entirely my own work;
I have acknowledged all main sources of help;
Where the thesis is based on work done by myself jointly with others, I have made clear exactly what was done by others and what I have contributed myself;
None of this work has been published before submission

Signed: .....

Date: .....

# Acknowledgements

The project is funded by NERC (NE/D004381/1). Land seismic data come from instruments provided by the UK Geophysical Equipment Facility – Leicester to University of Liverpool and the GIPP to GFZ. We acknowledge the support of colleagues at BPPT and Geotek-LIPI, Indonesia for this project. We thank EOS (Earth Observatory of Singapore, Nanyang Technological University) for supporting logistical costs of deployment on the Mentawai and Batu islands. LIPI and EOS provided data from some sites of the SuGAr GPS network. We also thank the Indonesian BMG and German GEOFON for station data from their permanent networks. Ocean Bottom Seismometers (OBS) were provided by the UK Ocean Bottom Instrument Facility. We thank the master and crew of the R/V SONNE for support during research cruises SO-198 and SO-200 for the deployment and recovery of the OBS.

I would like to thank the Steven Hicks and Dietrich Lange for their help in the beginning of this project for training in relevant software. Penny Barton and Marianne Karplus provided the active source picks, and Dietrich Lange provided the initial local event locations and picks.

I would also like to thank my 3 supervisors, Tim Henstock, Lisa McNeill and Nick Harmon for their continued support and guidance throughout this thesis. Without them this work would not have been completed.

# 1 Chapter 1: Introduction

## 1.1 Overview

Subduction zones occur when two tectonic plates collide resulting in one of the plates subducting underneath the other. Either a denser, thinner oceanic plate subducts underneath a continental plate, or two oceanic plates are involved. Subduction zones can be broadly split into 5 constituent parts, which are the subducting slab (consisting of the oceanic crust and oceanic mantle lithosphere), the forearc, the arc, the mantle wedge and the sub-slab asthenospheric mantle ( 1.1). The interaction of these regions with each other, as well as the internal structure of the regions has been seen to vary at global and local scales. Subduction zone processes are important for understanding fundamental processes in the Earth. They are the location where oceanic lithosphere is recycled back into the mantle and key to the understanding of the mass balance of the earth. Subduction zones are the location of the formation of basaltic, intermediate and felsic crust in the arc and so are important for our understanding of the formation of continental crust and cratons. In addition, subduction zones are the centres for the nucleation of mega earthquakes and tsunamis and explosive volcanic eruption, so understanding the underlying phenomenon is key to understanding major geohazards.

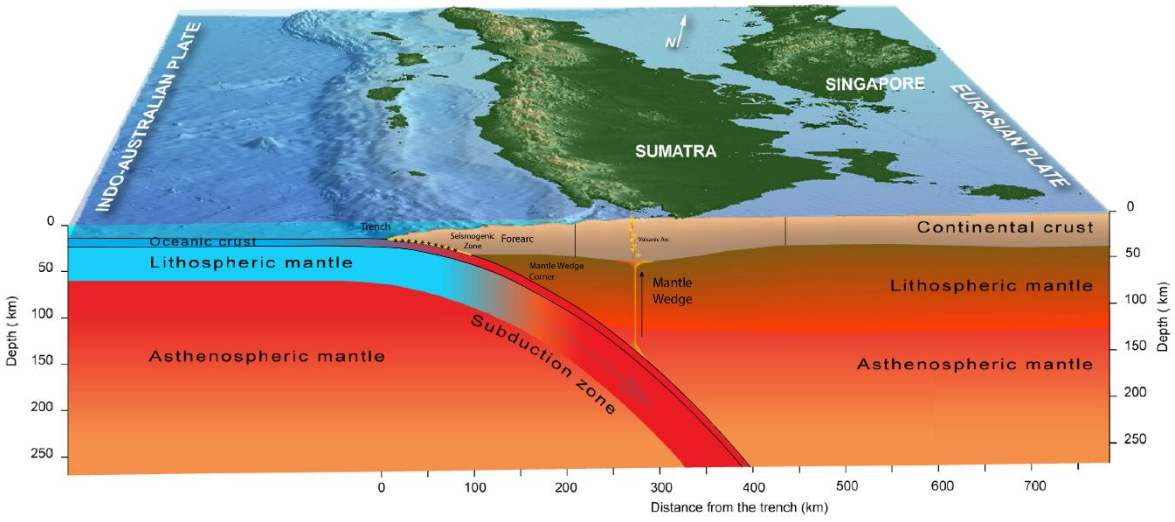


*1.1 Basic schematic of a subduction zone. Showing the subducting slab (Oceanic crust +lithospheric mantle) the asthenospheric mantle, mantle wedge, mantle wedge corner and overriding island arc crust and trench with their approximate relation to the surface expression of Sumatra. (source:www.earthobservatory.sg)*

The Sumatra subduction zone, which is the focus of this dissertation, is an important region as it has produced mega earthquakes in its recent and geologic history as well as some of the most spectacular and disruptive volcanic eruptions in recorded history. Understanding the structure and seismic behaviour of this subduction zone sheds light on the conditions that give rise to these major

geohazards and also informs our understanding of these processes in general when compared to our global understanding of subduction processes.

Seismology is one of the major tools used to interrogate the structure of the earth, both through structural imaging of the earth and also detection and quantification of seismic phenomenon. Observations of seismic phases allow us to estimate the seismic velocity and attenuation structure within the earth. The seismic waves radiate out from a seismic source, pass through the Earth and get recorded at a seismic station. Seismic tomography, used extensively in this dissertation, uses the arrival times and/or the amplitude of seismic phases to invert for the seismic velocity or attenuation. Earthquakes recorded locally, regionally or globally can all be used to improve resolution of the models. The array aperture and the type of event recorded dictates the resolvable scale for each study and allows us to image from the meter to hundreds of km scale. Figure 1.2 and Figure 1.3 show examples of two tomographic studies, one using teleseismic data only (Figure 1.3) and the other a joint inversion of teleseismic regional and local events (Figure 1.2). One of the aims of this thesis is to improve the resolution of the images obtained from the joint inversion process. Often with current joint inversions, a slab has to be added a priori (e.g., Zhao et al., 1994, 1992) and this addition has significant implications for the final model.

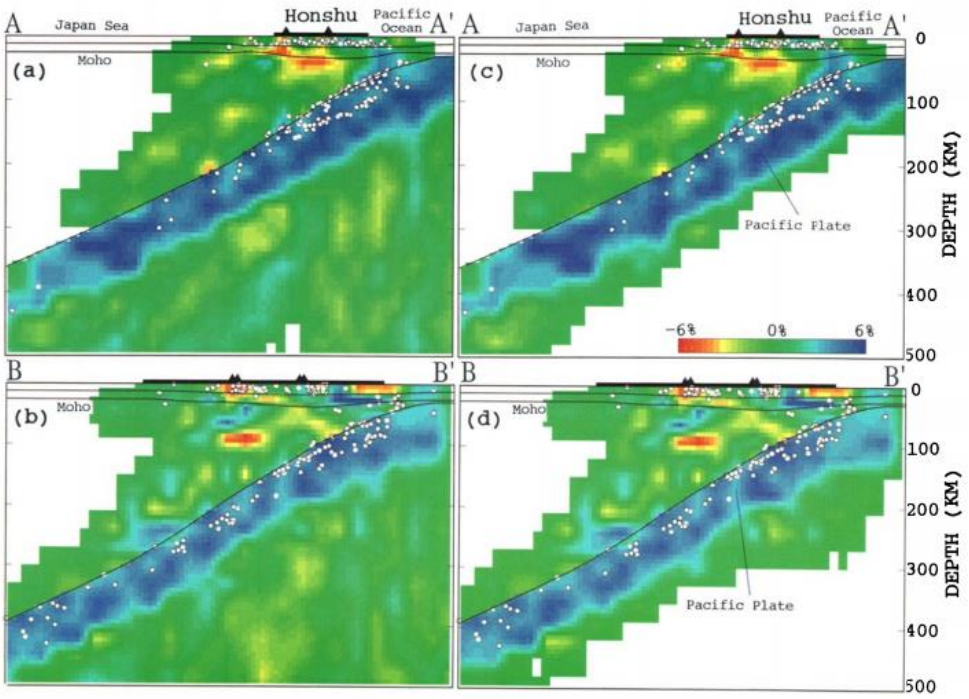


*Figure 1.2 An example of the current state of the art using joint tomography taken from Zhao et al., (1992). Local region and teleseismic data are used in inversion to model the deep structure of the Japan subduction zone. Blue and red denote high and low velocity perturbations. White dots represent earthquake and solid black triangles represent volcanoes.*

Improved models of seismic structure can be used to improve the locations of local seismicity, which provides information about the patterns and characteristics of fault slip and rupture, which are important for hazard assessment for a given region. The location of seismicity is also important for mapping faults at depth. In addition, the patterns of seismicity can be used to estimate

segmentation on a fault system, which can then be used to improve hazard assessment by evaluating the maximum credible magnitude that could take place.

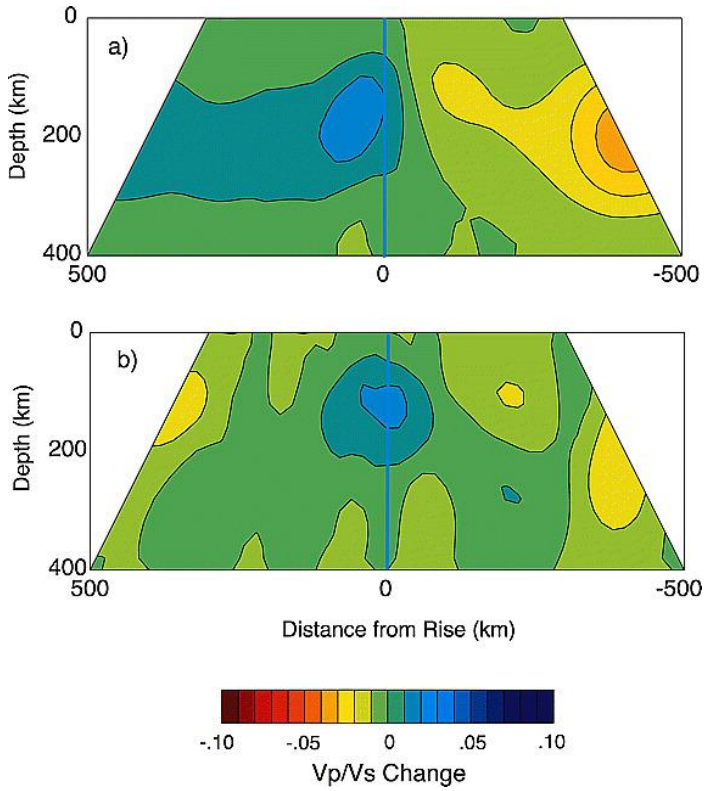


*Figure 1.3 An example of the current state of the art for local scale (<1000km) teleseismic inversion. VP/VS heterogeneity beneath the Mantle Electromagnetic and Tomography Experiment (MELT) region of the East Pacific Rise from analysis of Pand S body waves (Hammond and Toomey (2003).*

There are three overall aims for the research conducted in this thesis. The first aim is to image the central Sumatra subduction system down to depths of 450 km at a finer scale than conducted previously on this part of the Sunda margin. To do this I modified an existing local tomography inversion code to jointly invert for local and teleseismic events. This allowed me to derive P-wave velocity and Vp/Vs ratio for the central Sumatran subduction system from just seaward of the trench to landward of the volcanic arc down to depths of 450 km. To enable an enhanced imaging process I develop and modify an existing code to invert local and teleseismic source data at a finer scale than previously attempted; the new code does not require a slab to be added a priori. Secondly, I imaged the central Sumatran subduction zone forearc (i.e. shallower structure) at high resolution by including active source data in the model. The third aim of this thesis was to develop a segmentation model for the Sumatra subduction zone plate interface based on the statistical relationships between clusters of seismicity. I demonstrate the utility of this new method for subduction interfaces. The method highlights the critical boundaries within the subduction zone which apparently impede earthquake rupture. From these models, likely rupture magnitudes and potential rupture scenarios were determined and discussed and potential for global application to other subduction zones evaluated.

Within this introduction I will give a brief overview of the subduction zone system, highlighting some of the global trends seen from subduction zones around the world and introduce the

Sunda/Sumatran subduction zone. In the second part I will discuss the need for understanding the rupture potential of subduction zones and a new method to identify spatial trends in seismicity and from that produce likely rupture scenarios and hence segmentation along the subduction zone.

## 1.2 Key elements in Subduction Zones

### 1.2.1 Subducting Slab

The structure of subducting slabs has been observed in many places using tomography studies, which show high velocities or a strong positive velocity anomaly (depending on the type of study and location) associated with the old, colder, subducting plate compared with the surrounding mantle (e.g. Amato et al., 1993; Gorbatov et al., 2000; Hall and Spakman, 2002; Martin and Ritter, 2005; Wen and Anderson, 1995; Widiyantoro et al., 1999; Zhang et al., 2004). Many properties of subducting slabs appear to vary between subduction zones.

Local tomography studies from Java (Koulakov et al., 2007), Chile (Hicks et al., 2012), New Zealand (Eberhart-Phillips and Bannister, 2015), Pacific islands arcs (Woodhouse and Dziewonski, 1984), Central Sumatra (Collings et al., 2012) and Costa Rica (Dinc et al., 2010) have imaged the shallow structure of the slab (<100 km) and show velocity variation within the slab on scales of roughly 20 km. Often local tomography studies can differentiate between the upper plate? crust and subducting lithosphere and identify the potential metamorphism the slab goes through as the basaltic oceanic crust subducts and reacts to changing pressure and temperature conditions with depth (e.g. Gubbins et al., 1994; Ito and Kennedy, 1971). This is often imaged as a low velocity anomaly associated with the subducting oceanic crust becoming a high velocity anomaly that is indistinguishable from the rest of the slab, imaging the basalt to eclogite process (Fukao et al., 1983). The Vp/Vs structure of the slab is variable with the crust often displaying Vp/Vs ratios >1.8, suggesting that the oceanic crust is heavily hydrated (e.g., Collings et al., 2012; Matsubara et al., 2005; Tsuji et al., 2008; Xia et al., 2008). The subducting oceanic lithosphere displays Vp/Vs ratios of 1.6-1.7, thought to be indicating?? the forsterite-enstatite-water system (Eberhart-Phillips et al., 2015; Ji and Wang, 1999; Reyners et al., 2006a). The exact depth and termination of these processes varies between subduction zones and needs further fine scale imaging of subducting slabs to greater depths to identify key controls in the processes.

The deeper structure of subducting slabs is revealed by either global seismicity studies (e.g. Pesicek et al., 2010) or from global teleseismic tomography (e.g. Grand and Hilst, 1997; Zhao, 2004). Seismicity and global tomography studies fail to image the finer scale structure of the slab but allow the slab to be imaged down to depths of 660 km. Observations from the deeper parts of subducting slabs (125 to 660 km) show significant variation in the slab dip between and along subduction zones. For example the Sumatran slab appears to bend and contort as it subducts (Pesicek et al., 2010) being 60°-90° in the south? compared to 40°-60° in the north. Slabs have been observed subducting at a range of geometries: In Peru the slab subducts horizontally for hundreds of kilometres (e.g. Engdahl and Hilst, 1995); in Cascadia the slab is subducting at <30° (e.g. Rasmussen and Humphreys, 1988); below Rykuku there is intermediate angle subduction with the slab dipping between 30° and 60° (e.g., Ando et al., 2009); and in the Marianas there is high angle subduction with slab dips steeper than 60° (e.g. Zhao and Hasegawa, 1994a). The causes of slab dip variability are not always

clear and where possible further information about the finer scale structure of slab orientation within individual subduction zones would be a benefit.

### 1.2.2 Forearc

The forearc region of the subduction zone includes the accretionary prism, if present, and the part of the upper plate up to the volcanic arc (  1.1). The frontal part of the forearc can further be distinguished as erosional or accretionary zones (e.g. Clift and Vannucchi, 2004). Within accretionary zones, sediment on the incoming plate is either underplated to the bottom of the overriding plate or accreted directly to the front of the overriding plate. Within subduction zones where accretionary wedges form, the wedge is often composed of many imbricate thrust faults. Subduction is often oblique and it is common to see strike-slip faults form to accommodate the non-normal strain in the system. The Great Sumatra fault (GSF) (Burton and Hall, 2014), the Median Tectonic Line (MTL) in Japan (Wibberley and Shimamoto, 2002) are both examples of major faults that have developed as a result of oblique subduction.

Information about the early formation of a subduction zone can also be preserved within the forearc domain (e.g. Whattam and Stern, 2011). Often the structure of a forearc is a complicated with several phases of formation and prism development and several backstops (e.g. Byrne et al., 1993). Subduction zones may also alternate between accretionary and erosionary behaviour over geological time or along a single margin (e.g. Clift and Vannucchi, 2004). Evidence for such changing behaviour can be preserved within the forearc (e.g. Dumitru et al., 2010; Parkinson et al., 1998). Studying and understanding the structure of a subduction zone forearc can therefore help to understand the history of its development, including phases of accretion and erosion, and accretion of distinctive plate fragments or terranes.

As the oceanic crust subducts beneath the forearc dehydration of minerals within sediments in the shallow crust are released into the overriding plate (e.g. Saffer and Tobin, 2011). Fluids may travel up through faults within the forearc region as well as along the plate interface (e.g. Saffer and Tobin, 2011; Zhao et al., 1996). Vp/Vs ratios of the subducting oceanic crust and forearc region commonly have values of >1.8 usually indicating oversaturated fluid-bearing sediments (e.g., Collings et al., 2012; Eberhart-Phillips et al., 2015; Husen et al., 2000; Reyners, 2006). The fluids will often travel along faults within the forearc region, including prism faults or other forearc faults. Fluids can affect faults in what seems contradicting ways. The Kobe earthquake (e.g. Zhao, 1996) was seen to be triggered by fluid processes along the fault caused from the expulsion of fluid by sediments and an underlying subducting slab. However, observations from other faults, including the San Andreas fault, have suggested that where fluids are present along the fault it is weakened and is less seismically active (e.g. Chester et al., 1993). Identifying key forearc faults and their seismogenic potential is an imperative, as even though the magnitude of events generated is likely to be less than that of the seismogenic interface the ground motion hazard associated with these ruptures can be far greater given the closer proximity to population centres.

The depth of the Moho typically varies between 30 and 50 km for continental crust?? with crust imaged as a block having velocities of approximately 5 km $s^{-1}$ and a continuous increase to 7.5 km $s^{-1}$ at the Moho for island arc systems (e.g. Bostock et al., 2002; Collings et al., 2012; Hicks et al., 2012; Lange et al., 2010; Salmon et al., 2013; Shiomi et al., 2006; Yuan et al., 2002). The composition of the

overriding plate is often difficult to determine from velocity modelling but from geological studies and the presence of an active volcanic arc it is often composed of igneous material (e.g., Debari and Sleep, 1991; Holbrook et al., 1999; Pearce and Peate, 1995; Taylor, 1977). At crustal depths volcanic arcs are often imaged with low velocity anomalies caused by active magma chambers (e.g. Collings et al., 2012; Koulakov et al., 2007; Koulakov et al., 2009; Zhao and Hasegawa, 1994).

### 1.2.3 Mantle Wedge

The mantle wedge is the part of the mantle between the subducting plate and the overriding plate Moho. The mantle wedge can be split into two parts: the mantle wedge corner seaward of the arc and the mantle wedge beneath the arc and in the back arc region. Initially observations suggested that the forearc mantle wedge was predominantly aseismic and could possibly control the downdip limit of ruptures on the seismogenic interface (Peacock and Hyndman, 1999). At shallow depths (20-50 km) fluid from the subducting slab is released into the overriding mantle potentially causing it to become partly serpentinised leading to aseismic behaviour. Geological observations from forearcs have included exhumed and exposed ultra-mafic rocks that are extensively serpentinised and thought to derive from the mantle wedge (Hyndman and Peacock, 2003). Tomography studies show that often the forearc mantle wedge exhibits anomalies with low Vp and high Vp/Vs. Such observations have been made at the Cascadia margin (Brocher et al., 2003), Costa Rica (DeShon and Schwartz, 2004) and Nankai, Japan (Hyndman and Peacock, 2003), all compatible with serpentinisation. However recent ruptures, such as the 2004 Sumatra-Andaman event, showed that nucleation and rupture is possible into the mantle wedge (Dessa et al., 2009). Subduction zones that experience ruptures within the mantle wedge are often characterised by minimal anomalies within the forearc mantle wedge e.g., Central Sumatra (Collings et al., 2012) and the central Andes. In these cases the mantle wedges are likely not heavily serpentinised. Seno (2005) suggested that a possible reason for why we see serpentinisation in some forearc mantle wedges but not in others is that fluid pathways in the slab or at the interface can allow for fluids to escape up the slab and into the overriding forearc at shallower depths rather than escaping directly into the forearc mantle.

The landward part of the mantle wedge beneath the volcanic arc often shows low Vp anomalies and high Vp/Vs ratios. As the slab subducts, pressure and temperature increase with depth. As pressure and temperature increase phase changes occur within the slab, releasing fluid into the overriding mantle wedge causing melting and the formation of volcanic fronts and the arc (Anderson et al., 1978). Tomography studies have extensively imaged this process at most of the major subduction zones around the world (e.g., Collings et al., 2012; Dinc et al, 2010; Eberhart-Phillips et al., 2015; Hicks et al., 2012; Hyndman and Peacock, 2003; Reyners and Eberhart-Phillips, 2006; Xia, 2008; Zhao et al., 2011)). Often low velocity and high Vp/Vs anomalies are observed around the plate interface beginning at depths greater than 90 km and extending to the overriding plate Moho. For example, this phenomenon has been observed beneath the Toba caldera in Sumatra (Koulakov et al., 2009), in north-east Japan (Zhao et al., 2009) and Chile (Hicks et al., 2012). Studies from Japan, where the seismic network is incredibly dense, show that tomography studies have the ability to distinguish between areas of volcanic activity and areas with none along the volcanic front (e.g. Zhao, 2009).

Observations from seismic anisotropy characterises flow within the mantle wedge. Flow patterns in the mantle wedge have been observed to be predominantly either trench- or convergence-parallel. Observations from Northern Chile (Polet et al., 2000), New Zealand (Marson-Pidgeon et al., 2001)

and Western Honshu (Fouch and Fischer, 1996) all display trench-parallel flow. Trench-parallel observations within the mantle wedge have been proposed to be caused by melt filled cracks generated by compressional strain forces caused by the direction of convergence (Fischer et al., 2000). Convergence-parallel observations have been made at Izu-Bonin (Fouch and Fischer, 1998), northern Japan (Sandvol and Ni, 1997) and the Marianas (Nakajima and Hasegawa, 2004). Convergence-parallel observations are attributed to flow patterns caused by a strong coupling between the subducting slab and overriding mantle wedge.

### 1.2.4 Sub-slab Mantle

Direct observations of the sub-slab mantle are rare. The majority of information mostly comes from anisotropy measurements (e.g. Fischer et al., 1994; Hicks et al., 2012b; Katayama et al., 2009; Long and Silver, 2008). The mantle has been shown to be highly anisotropic with the predominant cause hypothesised as flow patterns within the mantle (Long and Silver, 2008; Song and Kawakatsu, 2012). Mantle anisotropy is predominately caused by Lattice Preferred Orientation (LPO) of olivine crystals in response to a flow direction (Ribe, 1989; Tommasi, 1998). Typically anisotropy within the sub-slab mantle beneath subduction zones can be split into the fast direction being either trench parallel or convergence parallel (Long and Silver, 2008). Convergence-parallel observations like those seen in Izu-Bonin (Anglin and Fouch, 2005) and Sumatra (Collings et al., 2013) suggest that there is a large amount of mantle asthenosphere being subducted with the slab. A trench-parallel fast direction is often associated with mantle flow induced by trench migration. Trench-parallel fast directions have been observed beneath the Nazca plate (Russo and Silver, 1994), South Ryuku (Lin and Kuo, 2013), Mariana and Andes subduction zones (Kneller and Keken, 2007).

## 1.3 Interface Seismicity and Along-strike Segmentation of Subduction Zones

Subduction earthquakes reflect the rapid release of strain associated with prior locking of the shallow plate interface and strain accumulation during interseismic periods typically lasting hundreds of years. However, we do not fully understand why some subduction earthquakes are relatively small in size ($<M_w7.5$), rupturing relatively small areas with limited along strike rupture length (<100 km), while others such as the M >9 1960 Chile, 1964 Alaska and 2004 Sumatra-Andaman events rupture extensive lengths of the plate boundary, e.g. 1200 km or more along strike (Briggs et al., 2006; Lay et al., 2005).

There has been significant work done on what controls the along-strike propagation or arrest of these great earthquakes along the subduction interface (e.g. Henstock et al., 2016; Sparkes et al., 2010; Hicks et al., 2012; Tang et al., 2013; Wang and Bilek, 2011; Das and Watts, 2009). Subducting topographic features appear to have a strong correlation with the termination point of several large events (e.g. Henstock et al., 2016; Sparkes, 2010). However, counter to this there are several examples that either ignore incoming topographic features or in fact initiate rupture at these features (e.g. Contreras-Reyes and Carrizo, 2011; Hicks et al., 2012). Topographic highs can present regions of asperity on the plate interface, strongly affecting the seismogenic zone. The two hypotheses are that ruptures beginning away from topographic highs end when they meet a high

due to not having enough energy to trigger rupture across them or due to contrasting properties at the interface of the topographic high (e.g. Das and Watts, 2009; Henstock et al., 2016; Sparkes et al., 2010b; Wang and Bilek, 2009). Counter to this, topographic highs have been seen to act as asperities on the incoming plate (e.g. Bilek et al., 2003; Cloos, 1992; Husen et al., 2002), i.e., places where the plates are highly coupled. The 1990 $M_w$ 7.0 Costa Rica earthquake occurred on the projected path of a subducted seamount (Husen, 2002). A similar situation was seen in Java, where the 1994 $M_w$ 7.8 event ruptured on the path of a subducting topographic high (Abercrombie et al., 2001). Analysing patterns of rupture from recent large earthquakes and comparing them with forearc and subducting plate structure is important for predicting behaviour on margins with limited earthquake history.

A new method, proving successful at spatially clustering seismicity into zones, is the *K* means algorithm (Burton and Hall, 2014; Weatherill and Burton, 2009). The algorithm determines how many clusters of seismicity are within a dataset given the current spatial distribution of events. From the cluster model, segmentation models can be developed to show the segmentation of seismic structures such as faults (Burton and Hall, 2014). Applying the *K*-means algorithm to the subduction interface needs to be tested to assess its effectiveness.

# 2 Chapter 2: The Sumatra Subduction Zone

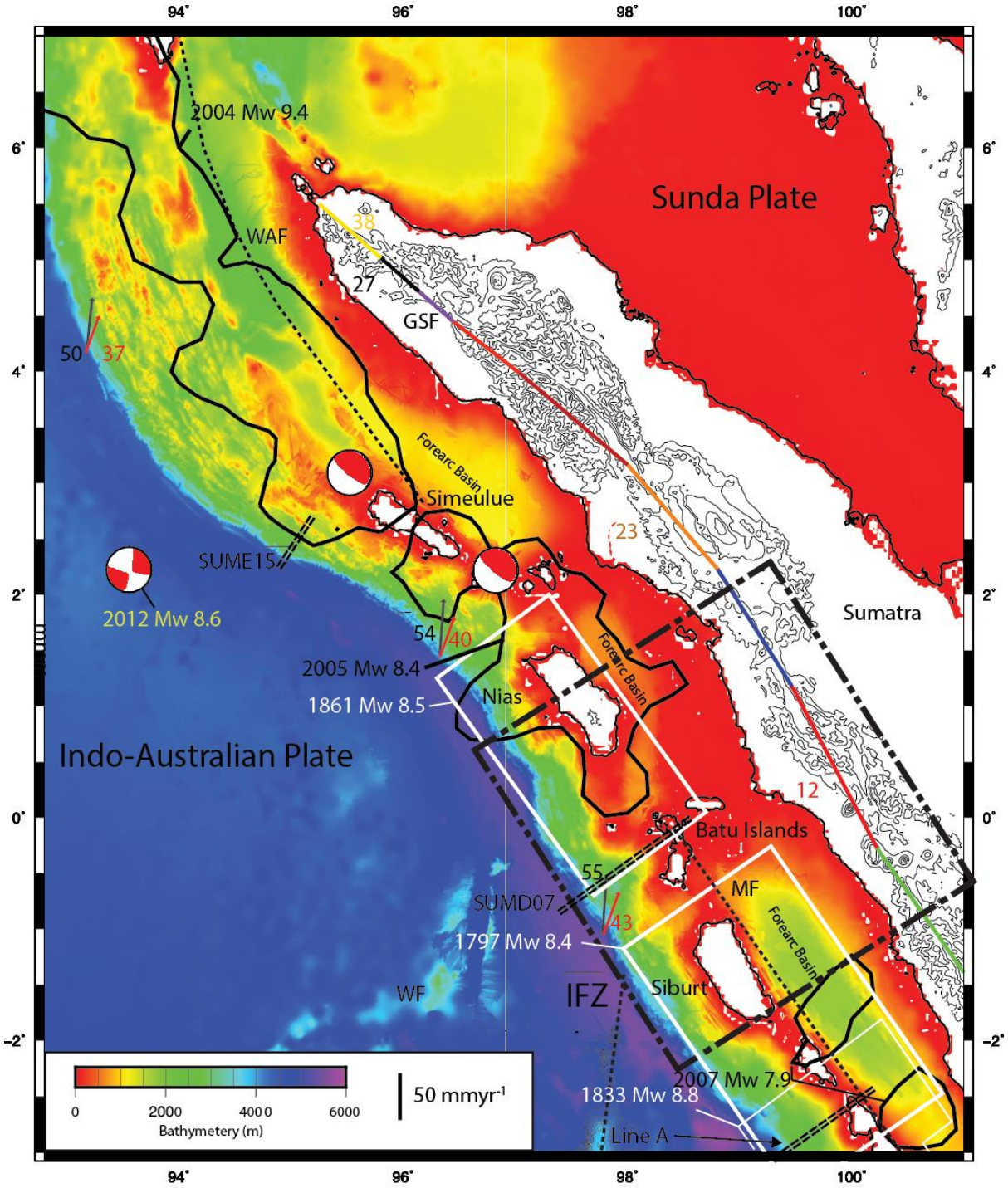


*Figure 2.1: General tectonic setting of Sumatra. Earthquake rupture areas from: 1797 and 1833 (Natawidjaja et al., 2006), 1861 (Newcomb and McCann 1987), 2007a and 2007b (Konca et al., 2008), 2004 (Lay et al., 2005) and 2005 (Briggs et al., 2006). The trace of the Mentawai Fault is taken from Diament et al., (1992), the Great Sumatran Fault is taken from Burton and Hall (2014) with different colours along the fault showing segmentation as defined by seismicity (colours have no relation to the rupture zones). GSF=Great Sumatran Fault, MF=Mentawai Fault, IFZ=Investigator Fracture Zone, WF=Wharton Fossil Ridge, WAF = Western Andaman fault zone. The Investigator Fracture Zone is mapped from local topography. Convergence rates for the subducting plate are taken from McNeill and Henstock (2014). Black arrow indicates total convergence and*

*red arrow indicates convergence between the subducting plate and the forearc sliver. Slip rates for the GSF are taken from Bellier and Sebrier (1995) and correspond to the same segment colour. Studies across the Sumatra margin are shown by parallel dashed lines and referred to in the text. Focal mechanisms for the 2012, 2004 and 2005 events are shown in relevant rupture areas and are taken from the CMT global catalogue. Parallel dashed lines correspond to previous studies in the area. SUME15, SUMD07 are reflection profiles taken from McNeill and Henstock (2014), Line A is local tomography study taken from Collings et al. (2012). The corresponding profiles are shown in figures 2.3-2.5*

Within this PhD I have focused on improving estimates of the properties of the central Sumatran subduction zone. In this brief introductory chapter, I will discuss some of the background on the Sumatran subduction zone that is not covered in chapters 4-6. Figure 2.1 gives a basic overview of the structure of the zone.

## 2.1 Formation

The Sunda Arc is a 5600 km long tectonic feature that is the result of the subduction of the Indian and Australian plates under the Sundaland plate (Hall, 1997). Figure 2.2 shows reconstructions by

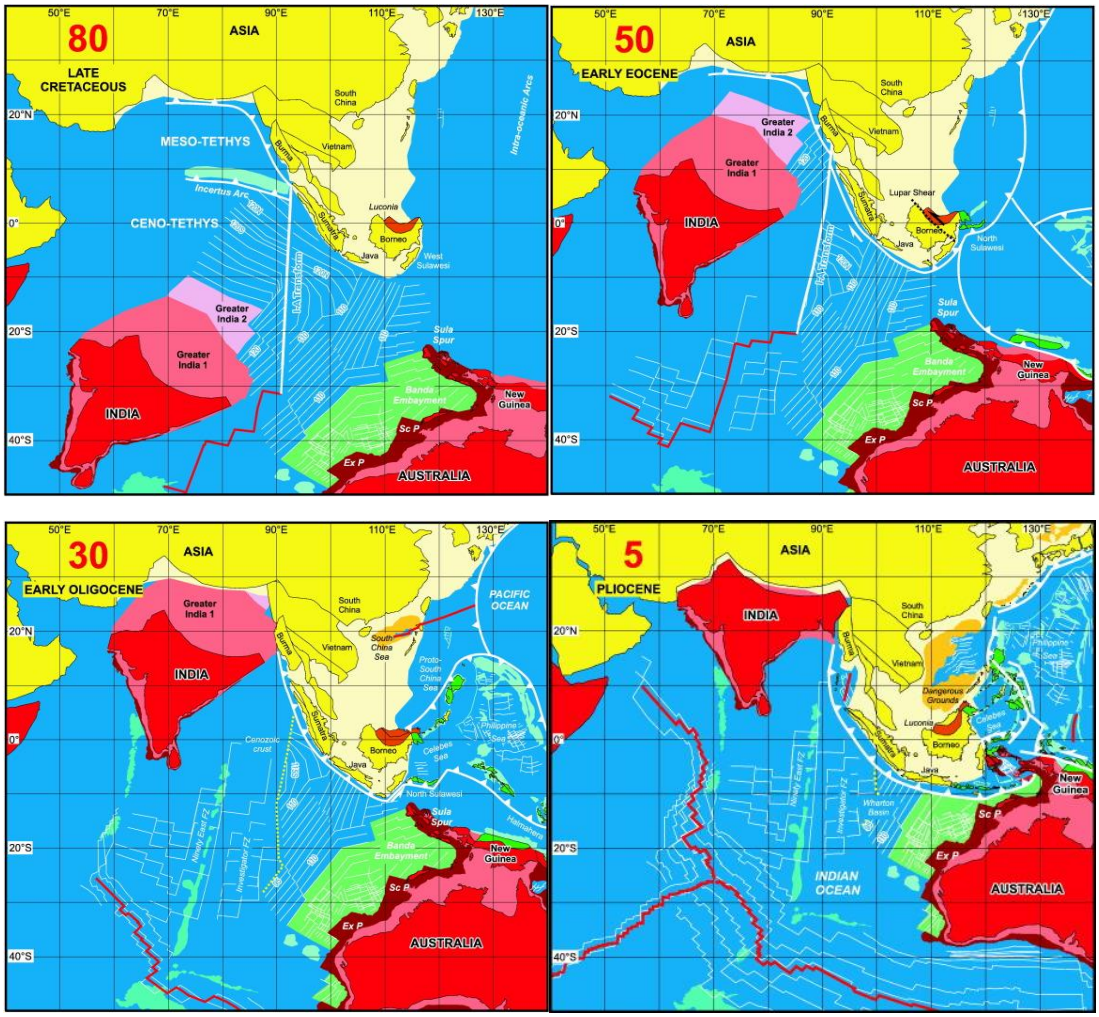


*Figure 2.2: The evolution of the Sumatran subduction zone taken from Hall (2012). The figure insets show the position of southeast Asia and Australia at 80,50,30 and 5 million years ago. At 80 Ma, subduction along Sumatra was perpendicular to the margin. Due to the collision of India with Eurasia at 30 Ma subduction became highly oblique resulting in the present day scenario.*

Hall (2012) of the formation of the region since 80 Myr. The zone has been active since the early Eocene (Karig et al., 1980a) with evidence showing that convergence rate has varied over time (Izart et al., 1994; Karig et al, 1980; Moore et al., 1982). Subduction has been both normal and highly oblique along the coast of Sumatra (Hall, 2012). During the early Cenozoic the Indian and Australian plate became one and the onset of Indo-Australian subduction beneath Sundaland plate began (Hall, 1997; Hamilton, 1979). Hall (2012) used paleomagnetic data and plate motions to model the tectonic evolution of southeast Asia. In the early Paleogene Sumatra and Java formed a linear structure and trench-normal subduction occurred along the entire margin, forming the first accretionary prism and forearc basins of the area (Karig et al, 1980; Moore et al., 1982; Moore et al., 1980). The collision of India with Eurasia in the early Oligocene led to a slowdown of subduction along Sumatra (Karig et al, 1980; Moore et al., 1982). This slow down allowed for the consolidation and subsidence of tectonic features within the margin. With the activation of a rifting event in the Indian ocean (the IFZ is a remnant of this) (Müller et al., 1997) in the mid Miocene subduction renewed/increased (Hall, 1997; Hamilton, 1979; Müller, 1997). The renewed plate motion caused the rotation of Sumatra against Java leading to subduction that was highly oblique along the coast of Sumatra and trench normal off the coast of Java (Hall, 1997). With the renewed motion and change in obliquity along Sumatra this led to the formation of the Great Sumatra Fault (GSF).

## 2.2 Forearc Structure

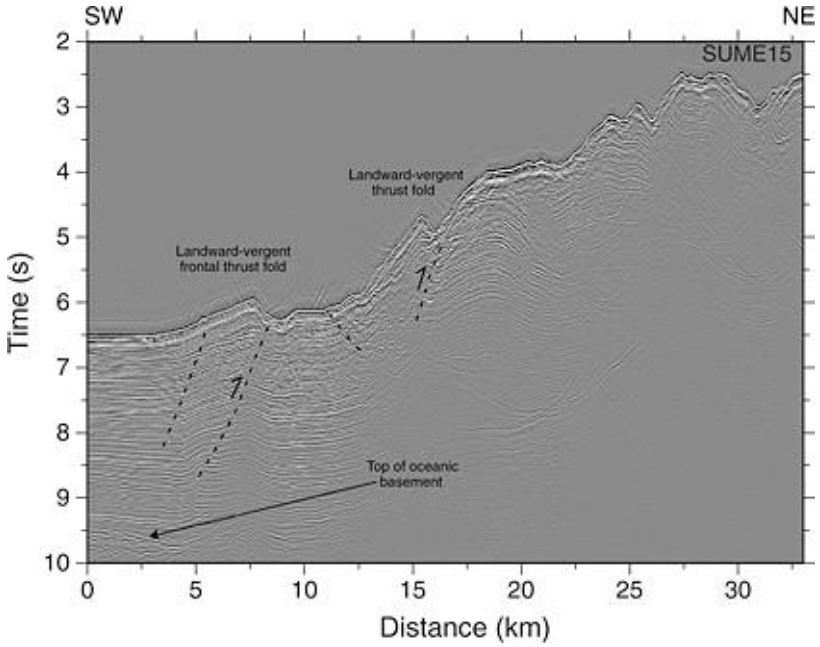


*Figure 2.3 Seismic profile SUME15 across prism toe offshore North Sumatra (McNeill and Henstock 2014).*

From seismic reflection studies (e.g., McNeill and Henstock, 2014; Schlüter et al., 2002) two distinct accretionary bodies in the outer forearc domain, seaward of the forearc islands, are present (Figure 2.6). The more seaward wedge shows a coherent structure of imbricate thrust faults while the second more landward wedge has a more complex nature of tectonic deformation (Schlüter et

al., 2002). Schlüter et al., (2002) proposed that the two structural bodies are the accretionary complexes from the two stages of subduction, one being the old fossil prism from the Eocene and the second being the prism which developed from the mid Miocene to the present day. Geological fieldwork carried out on and around the forearc islands may support this interpretation (Moore et al., 1982; Samuel et al., 1997).

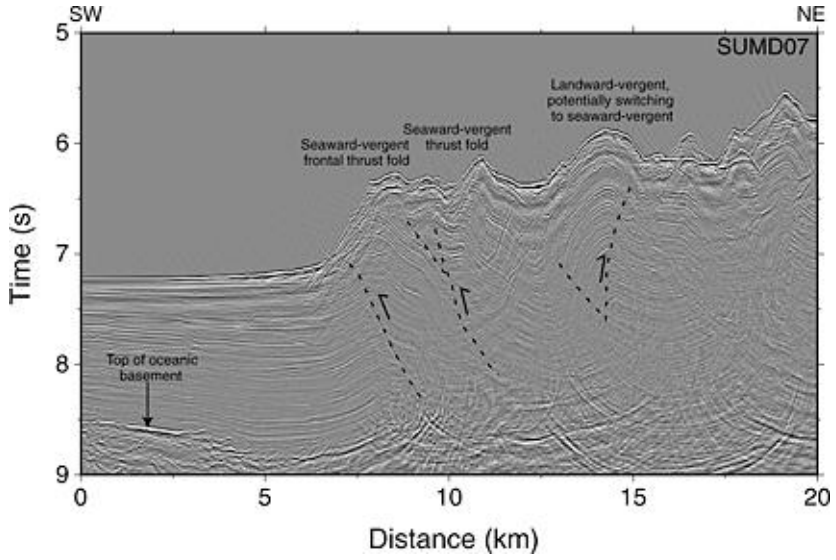


*Figure 2.4 Seismic profile SUMD07 across the outer accretionary prism offshore Batu Islands at ~1°S, Central Sumatra (McNeill and Henstock, 2014)*

With the onset of oblique subduction in the mid Miocene strain partitioning of the convergence into strike-slip and thrust motion occurred. The highly segmented Great Sumatra strike slip fault (GSF) parallel to the trench accommodates a large component of the strike slip motion (Burton and Hall, 2014; Sieh and Natawidjaja, 2000). In the Mentawai region GPS data shows that the Sumatran Fault only accommodates 1/3 of the strike-slip motion, with ~2/3 taken up by the subduction interface and/or on strike-slip faults within the forearc (Sieh and Natawidjaja, 2000). Diament et al., (1992) proposed that the majority of the arc parallel shear is taken up by the 600 km long Mentawai fault zone (MFZ) located between the forearc islands and the forearc basin, parallel to the trench. The nature of this fault is debated. Based on the linearity and the positive flower structures along the fault (Diament et al., 1992) suggest it is a strike-slip fault. Recent studies looking at focal mechanisms of hypocenters along the MF (Collings et al., 2012) show the MF as a series of active southwest dipping back-thrusts. Yet, from bathymetry, the classic features of a strike-slip system are observed suggesting that the MF has exhibited both strike-slip and thrust behaviour. With similar characteristics to the MF the West Andaman fault (WAF) is observed in northern Sumatra along the edge, of the forearc islands. Both the MF and WAF faults are thought to accommodate non-normal strain of oblique subduction, however the relationship between the 2 faults is not properly understood, are they two separate fault systems or continuations of each other (Curray, 2005; Diament et al., 1992; Raju et al., 2004). Similarly the relationship between the main forearc faults and the GSF is not well understood with branches coming off the GSF, such as the Batee fault (BF), possibly connecting with the MF and WAF (Genrich et al., 2000).

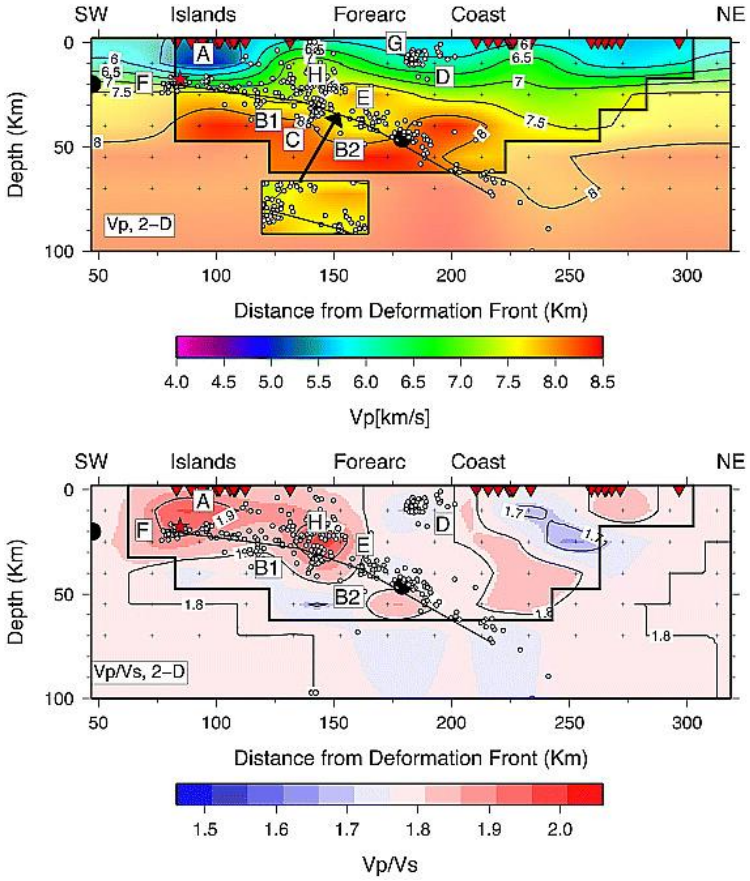


*Figure 2.5 The 2D velocity model for the forearc around the Mentawai islands derived by Collings et al., 2012. Location shown in Figure 2.1.*

Variations in the Sumatran accretionary prism occur along strike. Sumatra shows variations in thrust vergence and prism width along strike (e.g., McNeill and Henstock, 2014; Figure 2.3; Figure 2.4). In the South of the zone the prism has a moderate width and slope with mixed vergent thrust folds (Kopp et al., 2002; Kopp and Kukowski, 2003; Schlüter et al., 2002). In central Sumatra the prism narrows and becomes steeper with many-mixed vergent folds (Cook et al., 2014; McNeill and Henstock, 2014; Moeremans et al., 2014). In the northern domain the accretionary prism becomes much wider and landward vergent thrust folds dominate the structure (Henstock et al., 2006; McNeill and Henstock, 2014; Moeremans, 2014; Mosher et al., 2008; Singh et al., 2012). Variations in sedimentary thickness and sediment properties on the incoming plate are thought to control the prism morphology (Geersen et al., 2013; McNeill and Henstock, 2014). Sediment thickness varies along strike from up to 5 km offshore North Sumatra reducing to <1 km in the south. The variation in overlying plate sediment thickness along strike is not linear. Variations in oceanic basement topography create local highs and lows in sediment thickness, prime examples of this are the central regions where oceanic basement highs such as the investigator fracture zone (IFZ) and Wharton fossil ridge (WF) cause relatively low sediment thickness of 0.8 km (Figure 2.1). McNeill and Henstock (2014) conclude, after examining the whole margin, the prism can be divided into regions of distinct morphology and structure, with some links between changes in forearc structure and segmentation of megathrust earthquake rupture zones, noting this is especially apparent at the segment boundary between the 2004 and 2005 earthquakes (Dean et al., 2010).

## 2.3 Plate Boundary Earthquakes

Newcomb and McCann, (1987), using records of historic shaking intensity, published initial estimates for two great historic earthquakes on the central Sumatran margin, in 1833 and 1861. Later Natawidjaja et al., (2006), using coral microatolls, revised the area of the 1833 event and also showed that a similar event occurred in 1861 (Figure 2.1). The 1797 event occurred beneath the Mentawai islands with an estimated uplift of 0.8 meters implying a $M_w$ 8.5-8.7 (Natawidjaja et al., 2006). The 1833 event had an estimated $M_w$ 8.6-8.9. These two rupture areas have some overlap with each other and some coincidence with more recent earthquake ruptures, e.g., 2007, However, much of the 1797 rupture area remains unruptured in spite of significant strain accumulation (Chlieh et al., 2008).

In the past decade some of the largest earthquake ruptures in recorded history have occurred along the Sumatran megathrust. The sequence started in 2004 with the great Andaman-Sumatran $M_w$ 9.2 (Lay et al., 2005) earthquake followed by the 2005 Nias 8.7 $M_w$ (Briggs et al., 2006) earthquake and the twin $M_w$ 8.6 event of 2007 (Konca et al., 2008); the zone is highly active and produces many devastating tsunamis. The 2004 event ruptured northward from the north coast of Sumatra to the Nicobar and Andaman Islands spanning a rupture length of ~1300 km (e.g., Chlieh et al., 2007; Lay et al., 2005). Parts of the rupture were unusual in extending far beneath the accretionary prism and probably close to the trench. As discussed above, the north Sumatra forearc has a very large, wide prism with many landward vergent thrusts present. Dean et al., (2010) imaged a strong reflector, probably characterised by overpressure, outboard of the prism, and interpreted this as the horizon where the décollement will form. This pre-décollment reflector is found on the 2004 side of the segment boundary but is absent in the 2005 segment. Lithological and rheological properties of the lowermost sediments, shown by the pre-décollement, likely differ on either side of the 2004–2005 rupture boundary implying the importance of sediment properties for behaviour of the megathrust (Dean et al., 2010; Geersen et al., 2013). The near trench rupture, wide rupture area, and the extremely long rupture, is also linked to the amplification of the devastating tsunami seen in the 2004 event. From convergence rates along the zone the event takes between 140-220 years to accumulate enough energy to produce an $M_w$ 9.0 event (Chlieh et al., 2007; Natawidjaja et al., 2006). Tsunami deposit on the mainland and forearc islands show that tsunamis of a similar size to the one generated by the 2004 event occur every 700 years suggesting that great $M_w$ >9.0 events have a longer seismic cycle then events around $M_w$ 9.0 or less (Sieh et al., 2008).

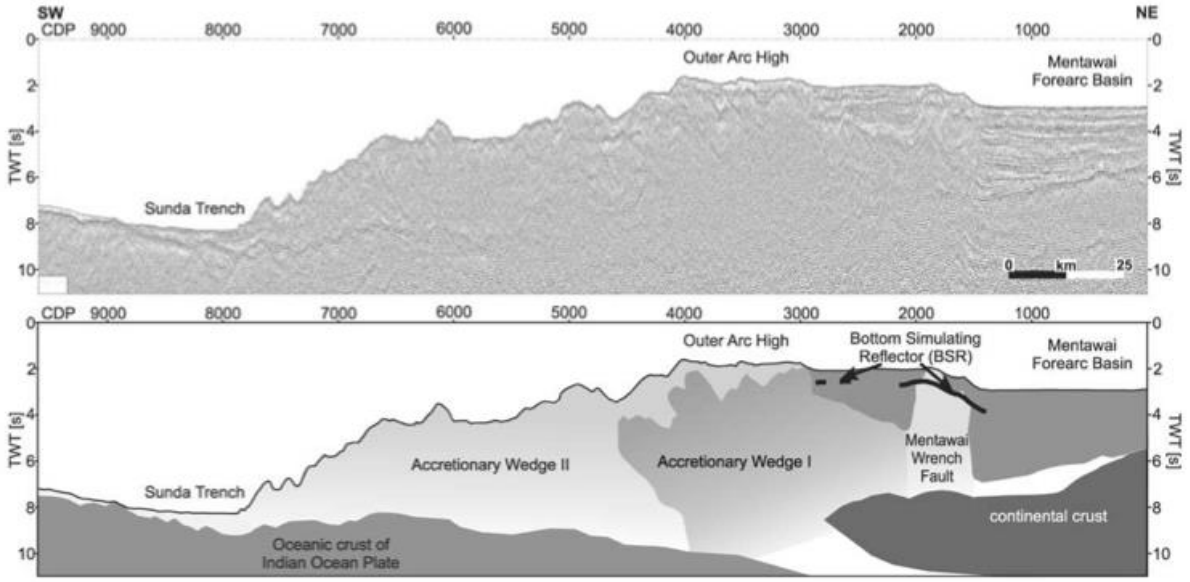


*Figure 2.6 A seismic reflection profile taken across the Sumatran margin (Schlüter et al., 2002). Top is the reflection profile. Bottom image is the interpretation of the main structural bodies present in southern Sumatra as defined by Schlüter et al. (2002)*

Occurring 3 months later to the south was the $M_w$ 8.7 Nias earthquake. The event ruptured a much shorter section of the margin, and did not extend as far seaward as the 2004 rupture. The rupture shows distinct areas of maximum slip. Briggs et al., (2006), attribute the varying areas of maximum slip to semi-permanent rupture barriers on the megathrust interface. Briggs et al., (2006) showed contours of uplift and subsidence for the forearc islands. Much of the aftershock seismicity of the 2004 event occurred on prism thrusts and/or on the plate boundary interface (Pesicek et al., 2010)

A pair of events occurred in 2007, a $M_w$ 8.4 earthquake beneath Pagai island and a second event to the north (Figure 2.1). The delayed second event is attributed to semi-permanent rupture barriers (Konca et al., 2008), similar to the suggestions of Briggs et al., (2006) for the Nias earthquake. The twin events of 2007 ruptured the Mentawai segment of the Sumatran zone. Konca et al., (2008) and Chlieh et al., (2007) conclude that the energy released from the 2007 events only accounts for ~ 33% of the energy that has accumulated since the previous event in 1833. Thus a large event in this segment is likely given the apparent ~200 year seismic cycle in the area (Sieh et al., 2008).

## 2.4 Relative Plate Motions

The convergence along the margin has been characterised from both GPS and large-scale plate motion studies. The incoming plate subducts beneath Sumatra at a rate of ~60 mmyr$^{-1}$ relative to the Sunda plate (McNeill and Henstock, 2014). Small variations in the motion are observed along strike. At 4°N the convergence rate is 50 mm yr$^{-1}$ increasing to 55 mm yr$^{-1}$ at the equator and further increasing to 60 mm yr$^{-1}$ at 6°S. Subduction velocity relative to the forearc sliver, the part of the convergence accommodated at the megathrust interface, mirrors the trend in convergence estimated at 37 mm yr$^{-1}$, 40 mm yr$^{-1}$, and 47mm yr$^{-1}$ in the northern, central and southern domains respectively (McNeill and Henstock, 2014). The GSF is highly active with slip rates of ~20 mm yr$^{-1}$ and

~25 mm yr$^{-1}$ occurring in the northern and central area, respectively, reducing to 6 mm yr$^{-1}$ in the southern domain (Bellier and Sebrier, 1995; Bellier and Sébrier, 1994; Ito et al., 2012; Prawirodirdjo et al., 1997; Sieh and Natawidjaja, 2000), implying that a large portion of the obliquity, particularly in the south, is accommodated within the forearc of the zone by faults such as the MF.

## 2.5 Plate Coupling

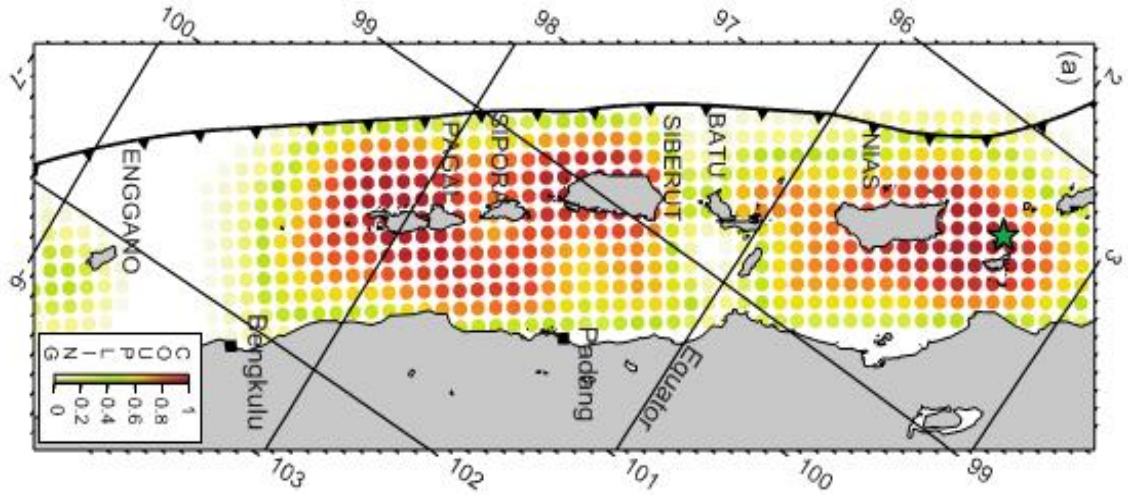


*Figure 2.7: Coupling across the Sumatran megathrust as reported by Chlieh et al., (2008) for 1999-2007. Data from GPS surveys from 1991 to 2001 provided vertical uplift measurements while data from 2002 onwards provided additional horizontal estimates. Fully coupled areas are shown in red, areas that having no coupling are shown in white*

Chlieh et al. (2007), derived the short-term seismic coupling across the seismogenic interface of the Sumatran megathrust using geodetic data (Figure 2.7). From the data the authors calculated the amount of uplift and horizontal motion the zone should experience using a back slip modelling approach (Savage, 1983) and theory of dislocations in an elastic half-space (Okada et al., 1992). They compared the present-day motions and computed interseismic strain and hence coupling along the megathrust. They estimated the convergence taken up at the interface by removing motion of the Sumatran fault and the forearc. Areas of significant megathrust events, such as, the 2004 Boxing Day event, have a high degree of coupling. This suggests that rupture areas are long-lived features, consistent with the similarity to paleogeodetic data based on vertical uplift inferred from coral growth rings. Areas of low coupling coincide with subducting basement topography highs some of which coincide with earthquake segments boundaries (e.g., Henstock et al., 2016; Meltzner et al., 2012; Natawidjaja et al., 2006; Tang et al., 2013), reinforcing the idea of features on the downgoing plate affecting rupture along strike.

The 2007 earthquake released ~25-33% of the accumulated strain energy on the Mentawai segment since the last event in 1833, showing that the northern part of the Mentawai segment may produce another large event in the near future (Chlieh et al., 2008; Konca et al., 2008).

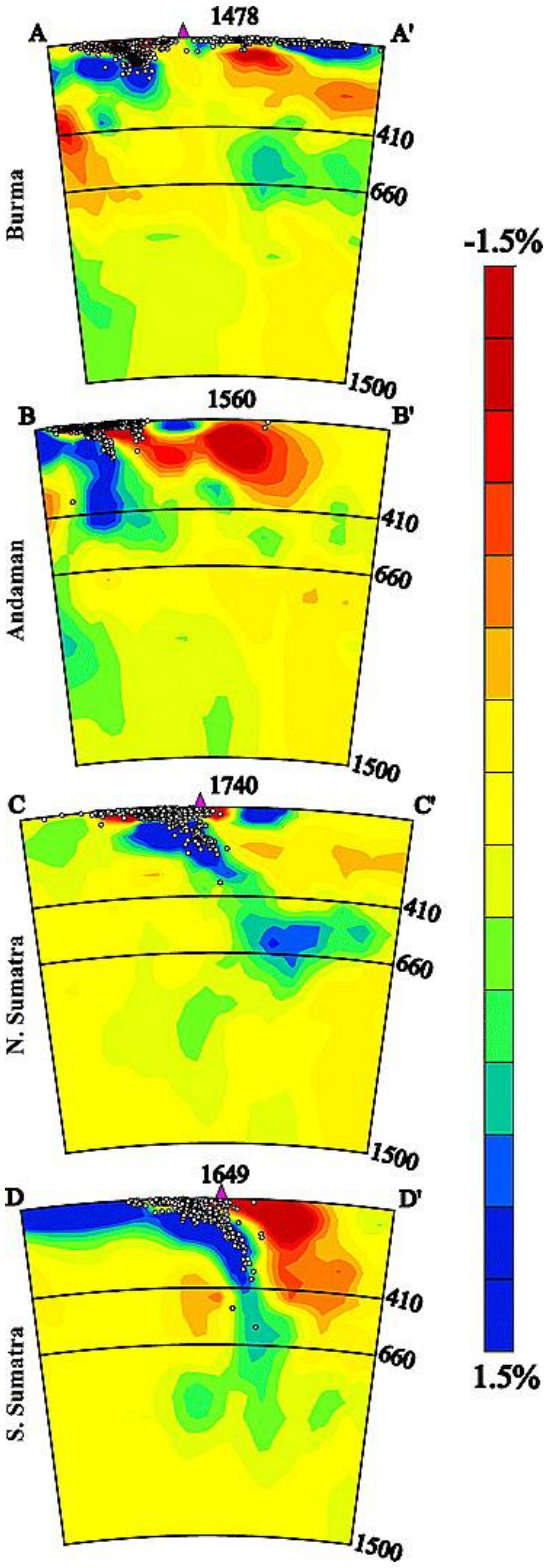


*Figure 2.8 Cross-sections showing the contrasting dips of the slab in different regions. Perturbations relative to ak135 (Kennett et al., 1995) are shown from −1.5% to 1.5%. Earthquake relocations (Engdahl et al., 2007) (circles) and volcano positions (triangles) are also shown. Profiles A-D represent the slab perpendicular to the trench at 22°N, 10°N, 2°N and 6°S respectively. Image taken from Pesicek et al. (2008).*

## 2.6 Subducting Slab

The subducting slab may influence where the volcanic arc forms as ,well as and controls where the intermediate depth seismicity occurs. The Sumatran slab, revealed in part from active source, local seismicity and tomography studies (Chauhan et al., 2009; Collings et al., 2012; Klingelhoefer et al., 2010; Kopp et al., 2003; Lange et al., 2007; Lange et al., 2010; Moeremans et al., 2014b; Newcomb and McCann, 1987; Schlüter et al., 2002; Singh et al., 2012) dips at ~5° at 30 km from the deformation front in the south (4°S) being slightly steeper in the north (4°N) at 5-8° 30 km from the deformation front. These dips increase to 35° at distances greater then 150 km. At depth, the dip of the slab varies to a much greater extent. For depths greater then 400 km the slab is estimated to dip at 25-50° in the north (4°N), compared to 60-90° in the south (4°S) (Pesicek et al., 2008) (Figure 2.8). The location of the volcanic front mirrors the trend seen in the dip in the down going plate.

# 3 Chapter 3: Brief overview of seismic tomography methods

## 3.1 Introduction

In seismology seismic waves are generated by passive (earthquakes or tides) or active sources (explosions, airgun shots). Seismic waves are recorded on a seismometer which records the motion of the ground in response to seismic waves passing through it. Fundamentally seismic waves can be split into body waves and surface waves. Tomography makes use of the information within seismic waves to derive models about the earths subsurface. This thesis is focused on body wave tomography and now the overview of the current state-of-the-art for body wave tomography will be discussed. Body wave tomography is performed at local, regional and global scales. Each scale has its advantages and disadvantages and will be discussed loosely in the text below.

Global tomography uses relative travel time residuals from earthquakes outside of the region of investigation to determine relative velocity structure of the earth. Global studies often achieve a fine scale resolution of 100-1000's of kilometres and can image down to the core (e.g. Grand and Hilst 1997; Zhao et al., 1992). Teleseismic/regional studies benefit from increasing the resolved area due to vertical ray geometry but the trade-off is a reduction in the resolution achievable. Due to vertical ray geometry and model parameterisation, the crustal structure at scales less than 50 km is often unresolved. Regional studies are parameterised in the same way global studies are but often focus on a specific region. Regional studies often employ a denser station network allowing for higher resolution then their global counter-parts but still are effected by all the problems associated with global tomography.

Local tomography which uses arrival times from earthquakes within the region of investigation, typically <500 km wide and ~100 km deep, and report absolute velocity, resolves velocity structure on the order of 30 km (Amato et al., 1993; Gorbatov et al., 2000; Hall and Spakman, 2002; Martin and Ritter, 2005; Wen and Anderson, 1995; Widiyantoro et al., 1999; Zhang et al., 2004). Local studies often use dense arrays (<30 km station spacing) and record a higher frequency of earthquakes which result in a higher resolution then at a global scale. Resulting ray paths are mainly limited to the region above the plate interface. This provides excellent resolution above the subducting plate but no information below the plate.

Local tomography studies are further split into two groups based on the sources of seismic energy: Passive (earthquake) sources, or active sources (Zelt el al., 2006; Korenaga et al., 2012) using shots from an airgun or explosions. Active studies often generate many hundreds of thousands of observations with known shot location and origin time but the ray coverage is typically limited to 15-25 km depth (e.g. Rawlinson and Urvoy, 2006; Stefano and Chiarabba, 2002; Tang et al., 2013). Active source tomography offers the highest resolution currently possible for shallow surface structures within an area with studies reporting a resolution of <1 km (e.g. Achauer et al., 1988). While local earthquake studies often have less than 10,000 observations whose location and origin time is initially unknown they occur at depths up to 150km. This provides reasonable imaging of structures at depths <150 km but limited resolution in the very shallow portions (<10 km) of the

models, with studies often employing techniques, such as station corrections, to make sure errors in the shallow surface do not get mapped into the deeper structures.

An ideal solution would be to combine both local and teleseismic/regional methods to counter the weakness of each one.

## 3.2 Basic Theoretical Framework

Within seismic tomography the modelling process can be split into 3 distinct parts: model parametrization, the forward problem and the inversion problem. The forward problem primarily contains the ray tracer or forward wave simulation, which is used to calculate a theoretical ray path/ waveform through an assumed model which is then compared to the observed travel time/waveform (Epanomeritakis et al., 2008; Komatitsch and Tromp, 1999; Tromp et al., 2004). Based on the residual between the calculated and observed travel times/waveform the inversion problem solves a set of linear equations relating the residuals to the model parameters, and allowing the assumed model to be updated.

## 3.3 Model Parameterisation

The model parametrisation dictates many aspects of the tomography problem such as what approaches can be taken in the forward and inverse model, and ultimately controls the minimum scale at which features can be resolved. Two basic approaches can represent the earth structure. They are either a large block or a dense grid node approach. The large block approach is often seen in teleseismic and regional studies (e.g., Fichtner et al., 2009; Huang and Zhao, 2006; Magistrale et al., 2000) as it allows for a reduced number of parameters and less computationally intensive than the dense grid approach. However, due to the reduced parameters the large block approach cannot model fine scale structures, and can introduce artefacts into the model space along the bounding edges of the model blocks.

Local studies often adopt a grid node approach which allows for a continuous velocity structure but cannot define discontinuities within the model, such as the 440km boundary layer. When using a set of grid nodes, a regular (Thurber, 1983) or irregular grid (Thurber and Eberhart-Phillips, 1999) can be adopted. For instance Thurber and Eberhart-Phillips, (1999) introduced a non-uniform grid spacing allowing for better resolution where observations permitted whereas uniform spacing does not. However, with an irregular grid care must be taken to not allow overfitting of parameters within a small area of dense nodes, which can lead to local minima or maxima within a model space (Thurber and Eberhart-Phillips, 1999).

## 3.4 Forward Problem

The forward problem is the method used to predict the times of seismic waves through a known model. Within body wave tomography this is usually done with ray theoretical approach (e.g. Um and Thurber, 1987), as is used in this dissertation. I focus my discussion on these methods although other methods can be used such as simulation of the full seismic waveform (e.g. Komatitsch, 1999). Rays are traced through the velocity model and the integrated travel time of the ray path is

calculated. There are several methods for calculating the ray path, broadly they can be split into one of three groups: First, the shooting method starts with a straight line travel path between the source and receiver, then a large number of circular arcs based on the straight line are constructed and the arc with the shortest travel time chosen as the optimum ray (Thurber and Aki, 1987; Thurber and Ellsworth, 1980; Um and Thurber, 1987). Second, exact two-point 3-D Ray tracing algorithms (Jacob, 1970) whereby the ray is calculated using Snell's law which are time-consuming even with today's computing standards. Third, is wavefront propagation using the eikonal equation (Vidale et al., 1990) which initially calculates the arrival times of the wavefront throughout the model space and then determines the ray path used as perpendicular to the surfaces of equal travel time (e.g. FMTOMO (Rawlinson, 2006)).

## 3.5 Inversion

All tomographic problems use the observations to determine parameters of the medium through which the waves propagate and solve a linear set of equations given compactly by:

$$d = Gm + e \qquad \textit{Eq. 3.1}$$

Here d, m, e are vectors for data, unknown models parameters and errors respectively (e.g. Aki and Lee, 1976; Spencer and Gubbins, 1980). G is the matrix of partial derivatives which allows observations to be predicted from the model. There are several ways to solve the initial equation, early studies (Aki and Christoffersson, 1977; Aki, 1976) adopted a damped least squares approach that constructed normal equations such that:

$$|d - Gm + m^T \square m|^2 = 0 \qquad \textit{Eq. 3.2}$$

And by minimising equation Eq. 3.2:

$$(G^T G + \square)m = G^T d \qquad \textit{Eq. 3.3}$$

where $\square$ is a damping factor. This initial approach was improved using parameter separation techniques (Pavlis and Booker, 1980; Spencer and Gubbins, 1980; Thurber, 1983) which helps to reduce the size of the $G^T G$ matrix making it more computationally viable. The inversion process is iterative and will take many cycles for forward problem – inversion problem before it stops; this is because the problem is strongly non-linear as the model controls where the rays sample, as well as the determined earthquake locations depending on the model. Current methods in determining when a model has reached a stable state are F-tests (Thurber, 1983) and chi squared. Both these techniques look at the variances in the modelled and observed data and derive cut off to prevent random error being mapped into the model.

## 3.6 Resolution and Error Analysis

Inversion results require the model to be evaluated properly. Typically, tomography studies use a chequerboard test combined with standard errors of the model parameters. The chequerboard test is calculated by slightly perturbing the final velocity model with positive and negative blocks and calculating synthetic travel times based on the perturbed model; the perturbations must be small to avoid modifying the ray paths. Synthetic travel times are determined through the perturbed model, and then inverted using the same parameters as used for the main inversion, with the recovered model compared against the known chequerboard (e.g. Zhao, 1992, 1994). From this you can find out the limits and resolution within your model and identify first-order artefacts such as ray path smearing that may be present.

Secondly formal errors of the final velocity model can be calculated by evaluating the $G^T G$ matrix. These formal errors show the error associated with each inverted parameter which can infer accuracy within certain parts of the model; however, this essentially is a linear analysis of a non-linear problem. Another common tool used in assessing the error in tomography problems is a technique called Monte Carlo error analysis, where random sampling of the model space is used to explore the acceptable range of models that still satisfy the data (e.g. Mosegaard and Sambridge 2002).

## 3.7 Joint Inversion

By jointly inverting local and teleseismic data, the shallow scale structure is better resolved by the addition of vertical rays from the teleseismic data; similarly, the deeper structure can be better resolved as the shallow structure is better controlled by the local inversion. Current joint inversion studies have focused on including local travel time observations into a teleseismic/regional model (e.g. Zhao, 1994a). In the current approaches the local data is used to better constrain the shallow subsurface of the models to more accurately predict deeper structure and improve earthquake locations within the model. The scale of current joint inversions between local and teleseismic sources is often at a minimum of 100's km. In this thesis, I present a method to jointly invert local and teleseismic data at a local scale.

Little work has been done on quantifying the effects of joint inversions through comparing the models from independent methods to quantify what the absolute errors within the model may be. This can be achieved through comparing methods using the same data set and methods but at varying scales.

## 3.8 Aims and Objectives

The broad research aims of this PhD are to image the structure of the Central Sumatran subduction zone and to analyse how subduction zone structure impacts earthquake potential and rupture processes. The primary objectives are:

- To develop a new method to jointly invert the teleseismic and local earthquake observations for an area of the subduction zone to increase the resolution of the method.
- To apply this new joint inversion method to the Central Sumatra subduction zone to increase the resolution of the structure, properties and composition of this part of the subduction zone. To use these results to determine how properties and composition vary across the subduction forearc and with depth and to assess the relationship between subduction zone domains and seismicity.
- To examine the difference between active and local source inversions compared to local source and teleseismic inversions to assess the potential for and to generate a combined active, local and teleseismic inversion model. The aim is to maximise the resolution of the resulting seismic tomographic models at a range of different scales and depths.
- To examine the spatial distribution of earthquakes along the Sumatran subduction zone to assess the effectiveness of 3-D clustering algorithms to segment the seismogenic interface.
- To use the resulting earthquake cluster model to identify predominant segment boundaries along the entire Sumatran subduction zone and to predict the likely future rupture scenarios along the margin.

# 4 Chapter 4: Evidence for a shallow Forearc Moho in central Sumatra from joint inversion of local and teleseismic data


## ABSTRACT

We determine 2D and 3D velocity models for the subduction zone around the Batu Islands, central Sumatra from the inversion of first arrivals from local and teleseismic data. We use a new approach to jointly invert for local and teleseismic first arrivals by modifying the Simul2000 package. We image the subducting slab down to depths of 200 km, shown to be a dipping region of high Vp (8.2-8.5 km $s^{-1}$). The oceanic crust has Vp values of 7.5-8.0 km $s^{-1}$ down to depths of 70km. The shallow forearc has velocities ranging from 1.5 km $s^{-1}$ to 6.5 km $s^{-1}$ at depth with elevated Vp/Vs ratios of 1.9 suggesting they consist of fluid-saturated sediments. Seismicity shows that there are many active faults within the incoming plate, which reach depths of 40 km. The continental Moho beneath the forearc is at 30 km, compared to mainland Sumatra where the Moho is at 40 km. The shallow forearc Moho suggests that rather than being composed of continental crust, it is more likely an uplifted ophiolitic structure which may act as a backstop to the accretionary domain of the forearc. The forearc mantle wedge corner does not show evidence for widespread serpentinisation, with compressional velocities being 8.0-8.2 km $s^{-1}$ and Vp/Vs ratios of approximately 1.77, suggesting unaltered mantle peridotite.


## 4.1 Introduction

### 4.1.1 Subduction Zones

Subduction zones are the major sites of important physical and chemical processes including high seismic activity, magmatism, volcanism, and serpentinization of the forearc mantle. Many subduction zone forearcs exhibit accretionary behaviour (e.g. Clift and Vannucchi, 2004). Within an accretionary forearc, sediment from the incoming plate is accreted onto the front of the overriding plate or fixed to the bottom of the overriding plate through underplating. In many subduction zones accreted material often form accretionary wedges which is built up against a more tectonically strong material such as the overriding plate, this formation is known as a backstop (e.g. Byrne, 1993; Clift and Vannucchi, 2004). Sediments are accreted over geological time, meaning that within a forearc information about the history and early formation of the zone can be preserved (e.g. Godfrey et al., 1997). The evolution of subduction zones forearc has implications for rupture propagation of the seismogenic interface and the development of faults within the forearc. By understanding the structure of subduction zone forearcs we can better predict the processes and associated and gain insight into the early formation of the zone.

Often within accretionary domains not all the sediment on the incoming plate is accreted onto the overriding plate. During subduction, oceanic lithosphere, capped by variably hydrated uppermost

mantle, oceanic crust, and sediments, undergoes progressive metamorphism and devolatilization. The fate of sediments being subducted with the slab influences chemical properties within the mantle wedge affecting factors such as degree of melting and p migration. Often subducting sediments carry with them a large amount of water (Hyndman and Peacock, 2003). The mantle wedge corner, which are heavily hydrated from subducting sediments, often promotes aseismic behaviour suggesting that the contact of the overriding plate Moho with the subducting plate signifies the downdip limit of the seismogenic zone. The 2004 Sumatra event was seen to begin within the mantle wedge corner, suggesting that the mantle wedge corner in Sumatra promotes brittle failure rather than stable sliding (Dessa et al., 2009). Examining the fate of subducting sediments and the properties of the mantle wedge corner are imperative to further our understanding about hazard within the subduction system.

Most subducting oceanic crust passes through the basalt to eclogite transition where large amounts of $H_20$ are released by the breakdown of minerals present in the slab. The large amounts of $H_20$ released by continuous basalt-eclogite reactions can cause large-scale hydration of the overriding lithosphere and can trigger partial melting of the mantle wedge. Body wave tomography has imaged many of these phase changes within the upper 100km of subduction systems. Within the mantle wedge corner, a low velocity zone is often seen suggesting that there is a high percentage of serpentinization caused by the release of water. More recent studies have been able to image the velocity structure within the slab and show that the lower part of the slab has reduced Vp/Vs possible from release of water into the overhead oceanic crust, forearc and mantle wedge. Low Vp/Vs slabs have been observed in Japan (Nakajima et al., 2001) and New Zealand (Eberhart-Phillips et al., 2015).

Most well-resolved subduction systems with island arc volcanism show an inclined low-velocity, high-attenuation region above the subducting slab extending from the Moho beneath the arc to depths of ~150 km. This region is caused by the releasing of fluids from the slab into the overlying mantle wedge, which promotes partial melting of the mantle causing the volcanic chain (Anderson, 1978).

The sub-slab mantle is often neglected within tomography studies but information about flow patterns within the sub-slab mantle can be extracted from anisotropy studies. The anisotropy of the sub-slab mantle at subduction zones has been studied greatly in recent years. Long and Silver, (2008) found either a strong sense of trench parallel or perpendicular anisotropy beneath subducting slabs. The two dominant observations are thought to be caused by lattice preferred orientation (LPO) from either a strong sense of mantle entrainment along with the subducting slab or trench parallel flow underneath the subducting slab caused by trench retreat. They conclude by suggesting that mantle entrainment is more common in older subduction zones such as Japan compared to trench parallel flow in younger subduction zones such as Sumatra.

### 4.1.2 Sumatra

The Sumatra Subduction zone is located on the boundary of the Indo-Australian plate and the Sunda plate (**Error! Reference source not found.**). The plate subducts at a rate of ~55 mm $yr^{-1}$. Due to the highly oblique subduction only ~40 mm $yr^{-1}$ is accommodated at the plate interface (McNeill and Henstock, 2014) and the remaining 15 mm $yr^{-1}$ is accommodated through forearc faults such as the Mentawai Fault (MF) and the onshore Great Sumatran fault (GSF), a trench-parallel strike-slip fault. Within Sumatra many

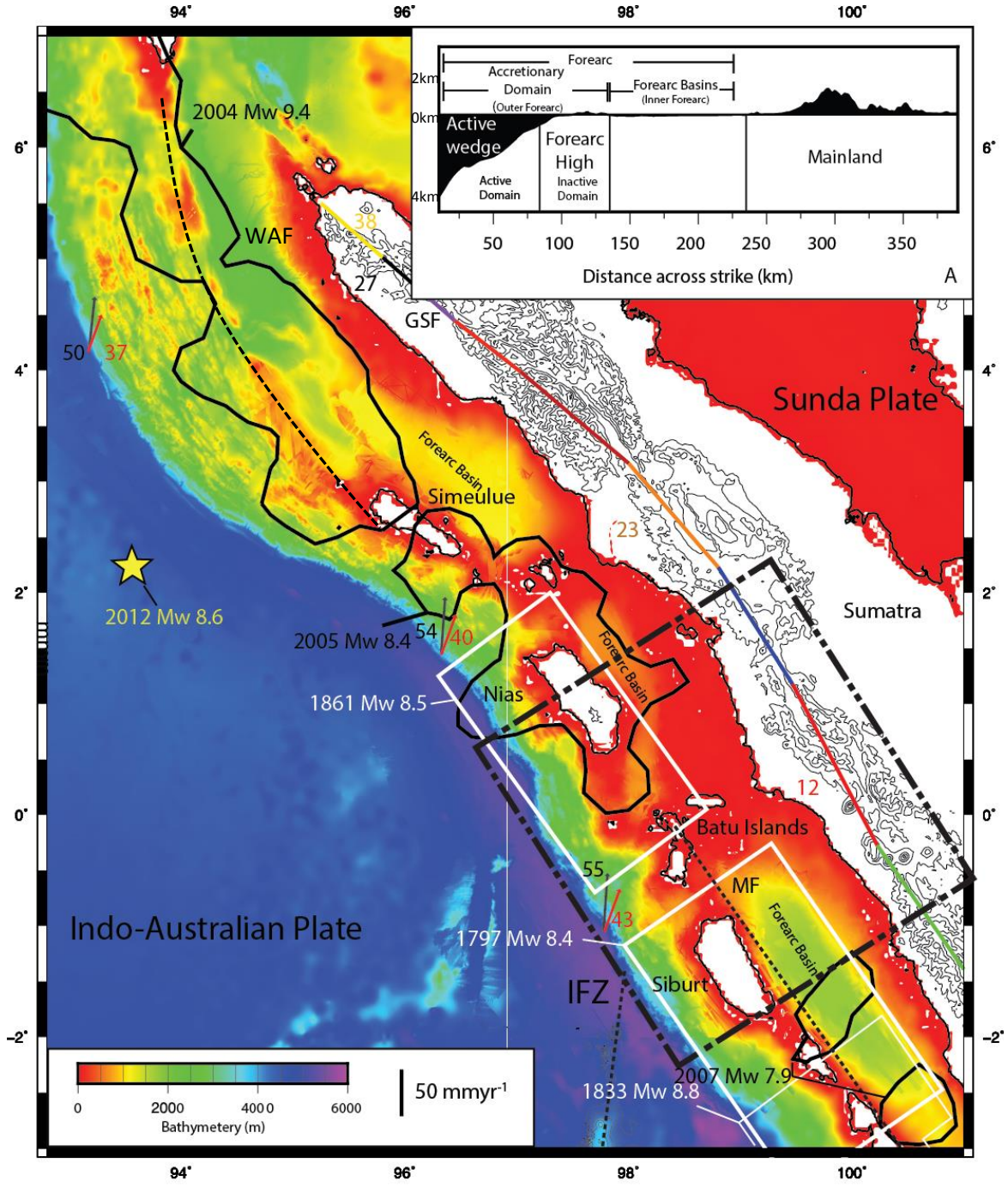


*Figure 4.1: General tectonic setting of Sumatra. Earthquake rupture areas from: 1797 and 1833 (Natawidjaja et al., 2006), 1861 (Newcomb and McCann 1987), 2007a and 2007b (Konca et al., 2008), 2004 (Lay et al., 2005) and 2005 (Briggs et al., 2006). The 2012 intraplate plate event is marked by the yellow star. The trace of the MF is taken from Diament et al. (1992) the Great Sumatran Fault is taken from Burton and Hall (2014) with different colours along the fault showing segmentation as defined by seismicity (colours have no relation to the rupture zones). The Investigator Fracture Zone is mapped from local topography. The dashed black box represents the study area. GSF=Great Sumatran fault, MF=Mentawai Fault, IFZ=Investigator fracture zone. Convergence rates for the subducting plate are taken from McNeill and Henstock et al. (2014). Black arrow indicates absolute convergence and red arrow indicates amount of convergence taken up by the plate interface. Slip rates for the GSF are taken from Bellier (1995) and correspond to the same segment colour. Inset A shows a breakdown of key terms used in this paper.*

studies have looked at varying scales of deformation from regional (e.g., Pesicek et al., 2008) to very fine scale process such as results obtained from a single fault within an accretionary domain (e.g. Cook et al., 2014). The subduction zone offshore Sumatra is a prime example of an accretionary margin which can be split into an outer forearc of the active prism, an inner forearc including the forearc basins, the mantle wedge and the volcanic arc. Although many parts of the system have been studied independently there is little work looking at the whole system from seaward of the trench to east of the volcanic arc. By looking at all these systems together we can further understand their interactions within the subduction system.

### 4.1.3 Outer Forearc (Trench-Landward Edge of the Islands)

The Sumatra forearc can generally be split into two major units, (1) extending from the trench to the landward edge of the forearc islands containing the accretionary domain (outer forearc); and (2) from the landward edge of the forearc islands to the mainland containing the forearc basins (inner forearc). **Error! Reference source not found.** inset A shows summary of the key terms and their meaning used in this chapter. Sumatra's accretionary domain is composed of two prominent domains the active and the inactive domain (Schlüter et al., 2002). The internal structure of the two accretionary domains is significantly different with the older more landward section being highly folded and faulted due to a complicated tectonic history (Schlüter et al., 2002).The seaward active wedge contains many imbricated thrust faults (Chauhan et al., 2009; Cook et al., 2014; Fisher et al., 2007; Henstock et al., 2006; McNeill and Henstock, 2014) with both landward- and seaward-dipping thrust faults observed varying in dominance along strike (McNeill and Henstock, 2014). These faults are active including seismological evidence of recent activity (Lange et al., 2010; Tilmann et al., 2010).

Within the accretionary domain there are several structures that could act as backstops for the build-up of the accretionary wedge. The boundary between the inner and outer forearc, further landward, however is more apparent with many studies showing a clear velocity boundary (Chauhan et al., 2009; Schlüter et al., 2002; Singh et al., 2011). In the southern part of the domain the MF is thought to be the surface expression of this boundary. The MF traces from the south to just north of the Batu islands where its surface expression disappears. Geological evidence suggests that it reaches Nias, although whether this is the MF fault or a separate fault is questionable. Immediately north of Nias island the MF disappears completely reappearing further north at 3°N and is known as the West Andaman fault (Diament et al., 1992). The relationship between the MF and WAF is unclear as to whether they are one fault or two separate faults. The nature of this boundary, and what combination of strike-slip and thrust faulting is occurring and how these components might vary along strike is still debated (e.g. Chauhan et al., 2009; Diament et al., 1992; Schlüter et al., 2002; Tang et al., 2013).

### 4.1.4 Inner Forearc

The inner forearc offshore Sumatra has a shallow basement (Kopp et al., 2003) and Moho of 20-30 km depth (Dessa et al., 2009; Kieckhefer et al., 1980; Klingelhoefer et al., 2010; Simoes et al., 2004). Throughout the region forearc basins are present although the reason for their location is unknown with there being no direct correlation with other observed features within the zone such as incoming topographic highs. The structure of the forearc basins is mainly stratified sediments (Beaudry and Moore, 1985; Berglar et al., 2008; Moore and Karig et al., 1980) which have originated from the volcanic complex on the mainland (Moore, 1980).

### 4.1.5 Subducting Plate

The slab, revealed in part from active source, local seismicity and tomography studies (Newcomb and McCann 1987; Schlüter et al., 2002; Kopp and Kukowski 2003; Singh et al., 2008; Singh et al., 2009; Lange et al., 2010; Collings et al., 2012; Singh et al., 2012) is seen to be dipping at ~5° at 30 km from the deformation front in the south (4°S) being slightly steeper in the north (4°N) at 5-8° 30 km from the deformation front increasing to 35° at distances greater than 150 km. At depth the dipping of the slab varies to a much greater extent. For slab depths greater than 400 km the slab is estimated to dip at 25-50° in the north (4°N), compared to 60-90° in the south (4°S) (Pesicek et al., 2008).

The upper plate structure is relatively well known for the shallow subducting oceanic crust (Cook et al., 2014; McNeill and Henstock, 2014; Singh et al., 2012). Sedimentary cover on the plate varies along strike from a maximum of 4 km at 4° N reducing to 1-2 km by the 5-7°S, with local minima of 1km over the top of basement topography features such as fracture zones and fossil spreading ridges (**Error! Reference source not found.**) (McNeill and Henstock, 2014). Basement topographic highs are well-documented on the plate interface with several prominent fracture zones in the area (**Error! Reference source not found.**). These fracture zones have been shown to influence the spatial distribution and segmentation of large $M_w$>8.0 earthquakes (e.g., Henstock et al., 2016) and also may be linked with additional seismicity as they subduct deeper into the zone (Lange et al., 2010).

### 4.1.6 Past Seismicity

Seismicity within the Sumatra subduction zone comes from 4 primary areas: within the accretionary domain including major faults such as the MF; from the plate interface; within the subducting slab; and from the GSF (Collings et al., 2012; Lange et al., 2010; Tilmann et al., 2010). The subduction zone has been host to many large earthquakes such as the 2004 $M_w$ 9.1 (Lay et al., 2005) and 2005 $M_w$ 8.7 (Briggs et al., 2006) events. The most recent events are thought to be repeats of previous historic events, the 2005-1861 and 1833-2007 event pairs being examples (**Error! Reference source not found.**). Significant oceanic intraplate events have also occurred, the most dominant being the pair of 2012 earthquakes in the oceanic plate offshore Sumatra, $M_w$ 8.6 and $M_w$ 8.2 events (Decluse et al., 2012) (Figure 4.1).

### 4.1.7 Mainland and Mantle Wedge

Knowledge of the internal structure of the Sumatran mainland is limited. Geological studies (e.g., Barber and Crow, 2009) show that the mainland is composed of volcanic provinces overlain by basinal deposits. The shallow (<10km) velocity structure along the Great Sumatran fault has been shown to be controlled by geothermal fluid flow within the area linked to active volcanism (Muksin et al., 2013). Moho depths vary from 20 km at the coast to 40 km beneath the volcanic arc (Collings et al., 2012; Macpherson et al., 2012). Low-velocity anomalies have been observed beneath the volcanic arc and extending from the surface down to the plate interface at 110 km depth (Koulakov et al., 2009).

Mantle wedge observations in Sumatra are scarce with only a few studies looking at the velocity structure of the mantle wedge beneath the Sumatran mainland (Collings et al., 2012). The downdip limit of the seismogenic zone of subduction zones is often taken as where the continental Moho meets the subducting plate (Hyndman et al., 1997; Ruff and Tichelaar, 1996). In Sumatra's case there is significant evidence to suggest that large ruptures are able to nucleate in the forearc mantle, such as the 2004 event, (Collings et al., 2012; Klingelhoefer et al., 2010; Dessa et al., 2009) suggesting that the limit of the seismogenic zone is not the contact between the continent and oceanic crust.

Our objective in this paper is to develop a new method to combine the high resolution imaging possible in the shallow part of the system from local seismicity with lower resolution imaging showing the geometry and properties of the slab, the sub-slab mantle, and the arc-forearc mantle to greater depths. The study zone for this research is shown in **Error! Reference source not found.** and encompasses the area of Siberut, Nias and the Batu Islands offshore Central Sumatra and extends from seaward of the trench to ~450 km landward of the trench.

### 4.1.8 Current Tomography Studies

Current studies, using local networks, are generally limited to imaging the fine structure of the subducting plate down to depths of 50 km (e.g., Collings et al., 2012; Eberhart-Phillips et al., 2015; Hicks et al., 2012) and the surface of the plate down to 100km due to the geometry of rays from events largely on the plate boundary to a surface array. From teleseismic events recorded on a global network subducting slabs are imaged extending down into the lower mantle (e.g., Pesicek et al., 2010; Wang, Z. and Zhao, 2006; Zhao et al., 1992), but due to having to conduct full earth inversions these only resolve broad scale variations in slab geometry, such as the folding of the Sumatran slab at depth (Pesicek et al., 2008), rather than the fine structure of the subducting slab. Equally, teleseismic events recorded on a local array have shown the ability to image features within the upper mantle to depths similar to the array aperture (e.g. Baba et al., 2006; Martin and Ritter., 2005). It has been shown that simultaneous inversion of datasets produces much more stable results rather than conducting them independently. Thurber, (1992) showed that joint inversion of hypocenter and velocity structure produces far superior results then inverting for them independently. Previous studies such as Zhao et al. (1996) have used joint inversions including both teleseismic and local events; the main problem faced by these approaches is how to incorporate teleseismic body travel times into the inversion problem.

## 4.2 Data

Data from a dense seismic network deployed from 2007-2009 were used in this study (ZB (2007-2009), Sumatra Segmentation and Aftershocks Deployment). The deployment consisted of 42 broadband land seismometers (Guralp 6TD (.03-100 Hz) and Guralp 3ESP (.06-100 Hz)) and 10 ocean bottom seismometers (Mark Products Geophone 4-100 Hz) (Figure 4.2). Relevant data from adjacent deployments were also used in this study, including GFZ networks to the north covering the Toba caldera complex, the UK Mentawai network to the south extending from the trench to the coastline (Guralp 6TD)(Collings et al., 2012), a 14-day deployment of 46 OBS from 25/05/08-10/06/08 covering the forearc region of central Sumatra, and permanent stations from both the GEOFON (STS-2) and Indonesian national networks spread across the mainland (Figure 4.2). Not all stations deployed had usable observations on them, Figure 4.2 shows all stations used in this study and not the complete deployed station network. All events used in this study were recorded at a sample rate of 100 Hz.

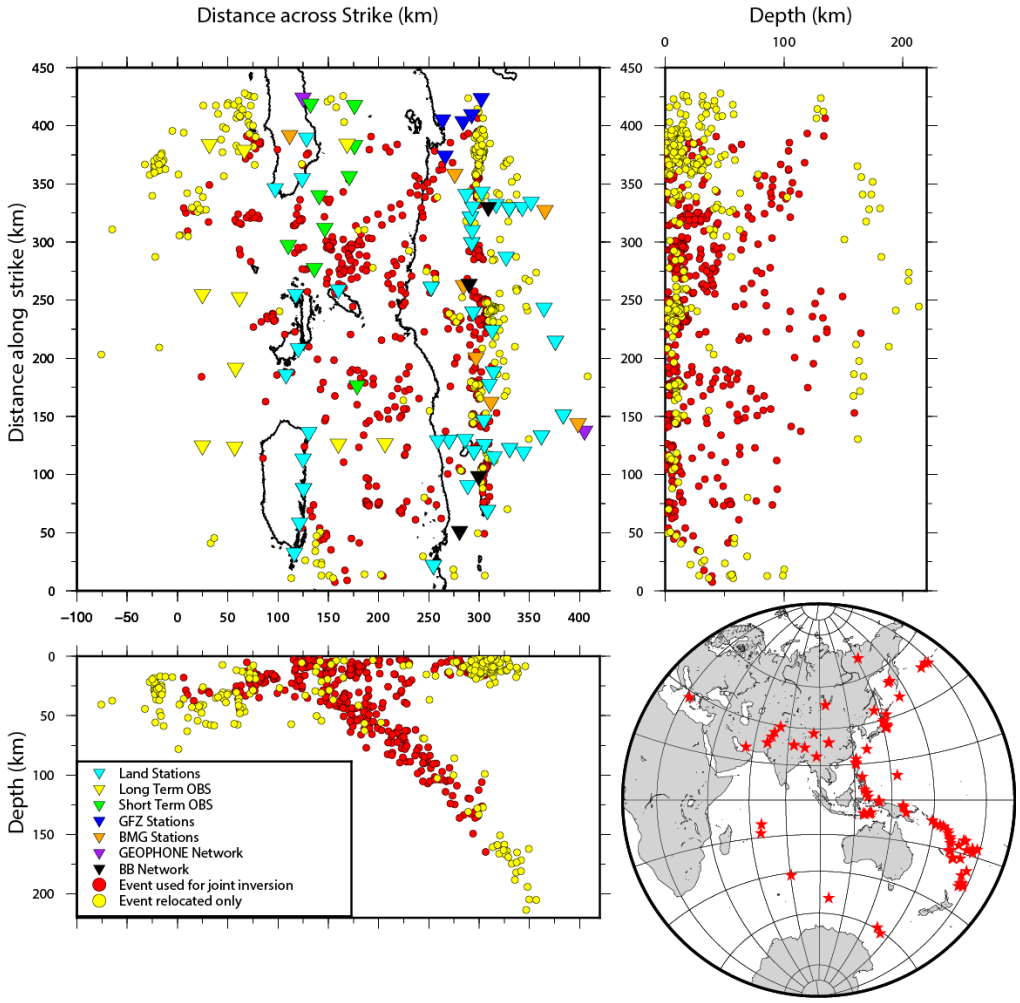


*Figure 4.2. Shows the location of the local (circle) and teleseismic (stars) events used in this study. Events in red represent the events used within the joint inversion code and events in yellow represent events relocated within the final velocity model. The top left and right figures are a plan and along strike slice taken from the data set, respectively. The bottom right and left are a across strike slice and global view of the local and teleseismic data, respectively. The initial event catalogue came from Lange et al. (2010). The bottom right figure shows the location of the 88 teleseismic events used in this study. Triangles represent the stations used in this study.*

### 4.2.1 Local Events

From the primary deployment Lange et al., (2010) initially identified and picked 1271 local events using an MPX automated picking algorithm. The events were inspected manually and of the 1271 events, 1051 were of high enough quality to be used in the Simul2000 program. Of the 1051 events 651 events had greater than 10 P and 5 S picks and were used in the joint inversion of velocity and hypocenter parameters, giving 9928 P picks and 3322 S picks. The remaining 391 events had between 4-10P picks and 1-5 S picks and were relocated in the final velocity model using the Simul2000 program. Figure 4.3 shows an example of a P wave pick on an event and the relevant weighting windows used to classify the pick. Weighting windows directly correlated to pick error. For example within the inversion, a weighting of P0 would mean that we are confident that the arrival falls into +/- 0.1s of the pick giving the pick an error of +/- 1s. Figure 4.3 visual represents the pick window, weighting and the associated error used throughout the inversion. Both local and teleseismic and P and S waves adopted this format.

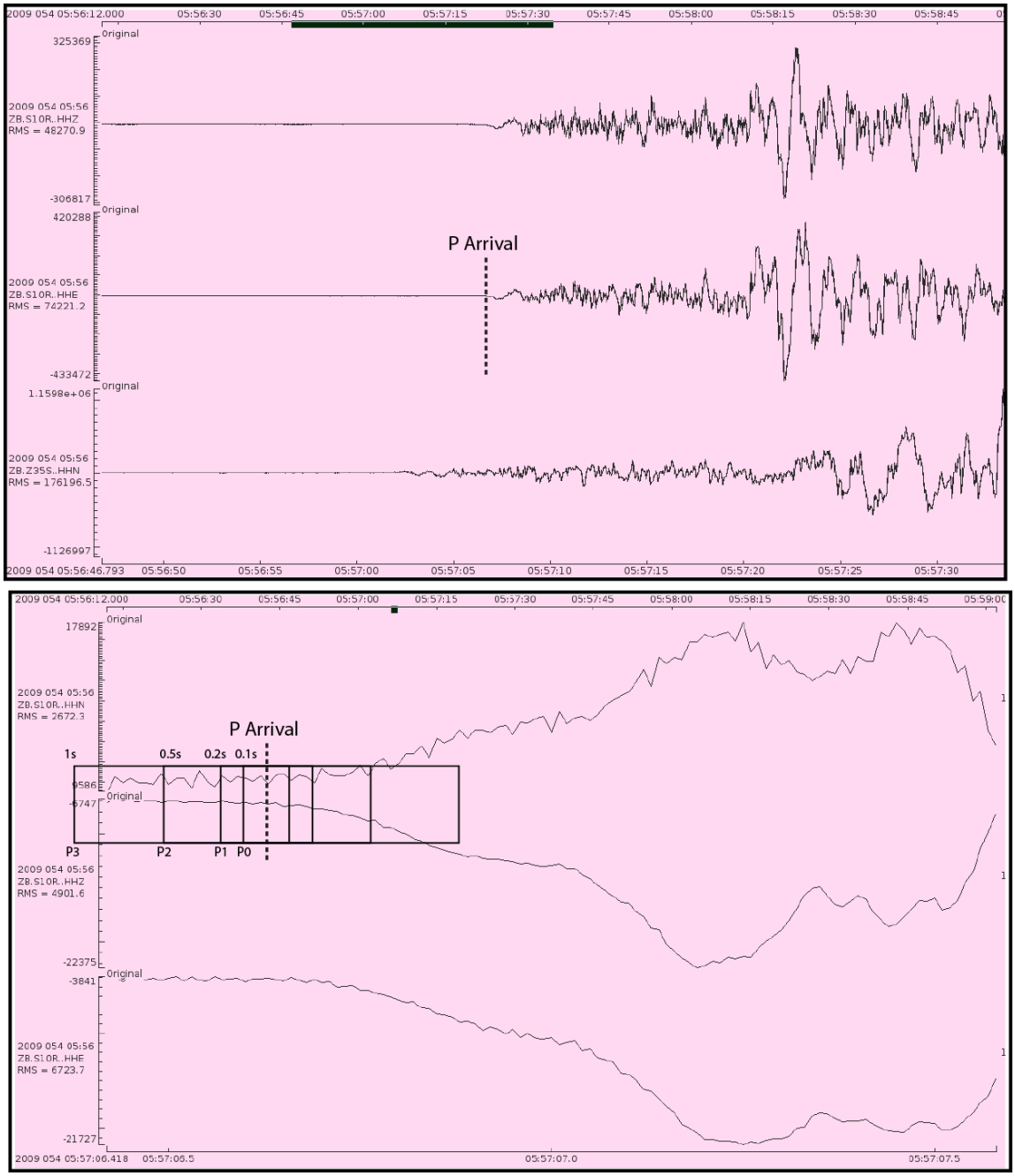


*Figure 4.3. Top: An example of P wave arrival picks from a local source in the data set. Bottom: An example of the weighting window associated with each pick. Weights were manually assigned after automated picking. P0, P1, P2 and P3 labels represent the corresponding weighting associated with its error. The boxes are a visual representation of the pick error with boundaries marked correlating to pick error.*

### 4.2.2 Teleseismic Events

Data recorded from the initial 52 stations in the study and the 2-week active source experiment were screened for teleseismic events with a moment magnitude greater than 6 based on the NEIC catalogue. A total of 164 events were identified in the catalogue, of which 120 had clear enough first arrivals to pick their P and S waves. To ensure the teleseismic events were of high quality, only events that satisfied 2 criteria were selected. Firstly, that the event had 15 clear P wave arrivals and

8 clear S arrivals. The increase in arrival number when compared to local events was to minimise artefacts that may get introduced into the model during the averaging process the method uses. The 2nd criteria was that events were between 30-90 degrees distance. After data control 88 high quality events remained. Figure 4.2 shows the teleseismic event locations. The 88 events provided 3525 P and 3200 S additional picks, giving a total of 19,453 picks.

## 4.3 Method

### 4.3.1 Forward Problem: Local Earthquake, Shot or Blast.

In this study we modify the program Simul2000 (Thurber, 1983b) to jointly invert for local and teleseismic body wave arrivals. For each event *I,* there are two sets of forward problems: if the event is a local earthquake, blast or shot then the forward equations denoted by 4.1-4.3 are used; if event *i* is a teleseismic event equations 4.4-4.11 describe the forward problem. A more in depth description of the setup of the velocity grid (Thurber, 1999b) and ray path algorithm (Um and Thurber, 1987b) can be found in these papers.

The body wave travel time of a local event, $T_{ij}^{cal}$, is calculated using ray theory with a path integral and the event origin time:

$$T_{ik}^{cal} = \tau_i + \int_{Station(j)}^{Event(i)} U * ds \qquad \textit{Eq. 4.1}$$

where $T_{ik}$, $\tau_i$ and $U * ds$ are calculated travel time for event *i* , observation *k*, station *j*, origin time for event *i*, slowness field and an element of the path integral, respectively. This gives the residuals for a single local event:

$$r_{ik} = T_{ik}^{obs} - T_{ik}^{cal} \qquad \textit{Eq. 4.2}$$

where $T_{ik}^{obs}$ is the observed travel time for event *i* observation *K* and $r_{ik}$ is the residual for the event observation pair. The residuals are related to the unknown model parameters by adopting a discrete velocity structure of N velocity nodes, and the 4 unknown hypocenter parameters. Meaning:

$$r_{ik} = T_{ik}^{obs} - \sum_{h=1}^{3} \frac{\partial T_{ik}}{\partial x_h} \Delta x_h + \Delta\tau_i + \sum_{n=1}^{N} \frac{\partial T_{ik}}{\partial m_n} \Delta m_n \qquad \textit{Eq. 4.3}$$

Where $m_n$ is the $n^{th}$ parameter out of the N parameters of the model. If event *i* is a teleseismic earthquake, then the algorithm follows equations 4.4-4.11.

### 4.3.2 Forward Problem: Teleseismic Event

Figure S 8.1 outlines the key parts of the teleseismic forward problem. The residual for teleseismic event *i* observation *k* is:

$$r_{ik} = T_{ik}^{obs} - T_{ik}^{cal} \qquad \textit{Eq. 4.4}$$

Where $r_{ik}$ , $T_{ik}^{obs}$ and $T_{ik}^{cal}$ are the residual, observed and calculated travel time for event *i,* observation *k,* respectively. The calculated travel time can be split into two parts:

$$T_{ik}^{cal} = T_{ik}^{mod} + BA_{i}^{avg} \qquad \textit{Eq. 4.5}$$

Were $T_{ik}^{cal}$ is the calculated travel time for event *i* observation *k*, $T_{ik}^{mod}$ is the travel time taken within the model space and $BA_{i}^{avg}$ is the travel time outside the model space. Using ray path theory, the travel time from a virtual source to the relevant station can be related to the unknown model parameters by adopting a discrete velocity structure of N velocity nodes. Meaning:

$$T_{ik}^{mod} = \int_{Station(j)}^{VS(s)} U * ds = \sum_{n=1}^{N} \frac{\partial T_{ik}}{\partial m_n} \Delta m_n \sum_{n=1}^{N} \frac{\partial T_{ik}}{\partial m_n} \Delta m_n \qquad \textit{Eq. 4.6}$$

Where $VS(s)$ is the Virtual source *s* for Station *j* corresponding, to event *i*, observation *k*. The virtual source is assumed to occur somewhere along the incoming ray. To calculate the location of the virtual source we use the incidence angle of the ray:

$$\theta_{ik} = \sin^{-1}\left(\frac{P_{ik} * V}{R}\right) \qquad \textit{Eq. 4.7}$$

Were $\theta_{ik}, P_{ik}$ are the incidence angle and ray parameter for event *i* observation *k,* and V and R are the velocity below the station and the radius of the earth respectively. Using the incidence angle, a point at depth is calculated:

$$O_{ik} = \tan(\theta_{is}) * D$$

Where the distance between the station *j* and VS *s* will be $O_{ik}$ at depth of *D* beneath station *j* in the direction of the azimuth of the incoming ray. As the velocity model updates, the virtual source is recalculated.

To convert from spherical to Cartesian coordinates a plane wave correction is applied:

$$T_{ik}^{p} = P_{ik} * d_{ik} \qquad \textit{Eq. 4.8}$$

Where $P_{ik}$ is the ray parameter, $T_{ik}^{p}$ is the plane wave correction and $d_{ik}$ is the distance between the VS and the center of the model space for event *i* observation *k*.

$$g_{ik} = T_{ik}^{obs} - T_{ik}^{cal} + T_{ik}^{p}$$

$g_{ik}$ is the initial residual for event *i* observation *k*. Using $g_{ik}$ the weighted mean residual of the event *i* is calculated:

$$BA_i^{avg} = \frac{\sum_{i=1}^{k} w_{ik}\, g_{ik}}{\sum_{i=1}^{k} w_{ik}} \qquad \textit{Eq. 4.9}$$

Were $w_{ik}$ is the weighting for event *i* observation *k*. The weighting is calculated from the pick error and the distance from the station at which this event was recorded. The weighting is 1 for a pick error of <0.01 s, 0.75 for <0.05 s, 0.5 < 0.1 s, 0.25 < 0.2 s - 0.5 s and 0 for >0.5 s. The distance weighting has a factor of 1 for 0-150km, 0.5 for 150km-250km and 0 for distances greater then 250 km. Weighting is applied to residuals such that residuals with more certainty i.e. small pick error and small distance are favoured in the inversion. After every iteration, $BA_i^{avg}$ is recalculated for each event. Combining Eq. 4.6,Eq. 4.8 and Eq. 4.9 the calculated travel time of a teleseismic ray is:

$$T_{ik}^{cal} = \sum_{n=1}^{N} \frac{\partial T_{ik}}{\partial m_n} \Delta m_n + BA_i^{avg} \sum_{n=1}^{N} \frac{\partial T_{ik}}{\partial m_n} \Delta m_n + BA_i^{avg} + T_{ik}^{p} \qquad \textit{Eq. 4.10}$$

Therefore, the residuals of a teleseismic observation are:

$$r_{ik} = T_{ik}^{obs} - \sum_{n=1}^{N} \frac{\partial T_{ik}}{\partial m_n} \Delta m_n + BA_i^{avg} \sum_{n=1}^{N} \frac{\partial T_{ik}}{\partial m_n} \Delta m_n + BA_i^{avg} + T_{ik}^{p} \qquad \textit{Eq. 4.11}$$

### 4.3.3 Inverse Problem

Each event *i* yields L equations representing each event observation pair. This can be written in matrix notation as:

$$R_i = H_i \Delta h_i + M_i \Delta m_n \qquad \textit{Eq. 4.12}$$

Where $R_i$ has the dimensions Lx1 containing the L residuals, H and h have the dimensions Lx4 and 4x1 and represent the hypocenter partial derivatives and the four unknown hypocenter parameter adjustments. *M* and m have dimensions LxN and Nx1 representing the velocity partial derivatives and the velocity adjustments. For a teleseismic event $H_i \Delta h_i = 0$. Thurber (1983) employs parameter separation to reduce the size of the inversion matrix making it more computationally efficient and enabling sequential addition of events row by row.

Writing Eq. 4.12.

$$R_i^{'} = M_i^{'} \Delta m \qquad \textit{Eq. 4.13}$$

As each event's hypocenter parameters are decoupled, a new set of L rows representing the linear equations of the new event is added to the matrix equations. Further manipulation of is conducted before the inversion. Eq. 4.13 is transformed such that:

$$M_i^{'T} R_i^{'} = M_i^{'T} M_i^{'} \Delta m \qquad \textit{Eq. 4.14}$$

Once all events are processed the set of linear equations is solved using a damped least squares solution such that (Eberhart-Phillips, 1986):

$$\Delta m = \left\{ M^{'T} M' + \varphi^2 I \right\}^{-1} M^{'T} R' \qquad \textit{Eq. 4.15}$$

Where $\varphi$ is the damping parameter. Where in this instance the damping parameter is chosen to satisfy:

$$\varphi^2 = Cd/Cm \qquad \textit{Eq. 4.16}$$

Where Cd is the data variance ($s^2$) and Cm is the model variance ($kms^2/s^2$ ). The units of the damping parameter are $s^2\ km^{-1}$.

## 4.4 Modelling process

We developed models using an iterative process from simple to complex. We started with 2D inversions for both velocity and hypocenters. We then used the final 2D velocity models, relocated hypocenters and station corrections as the starting model for a 3D inversion.

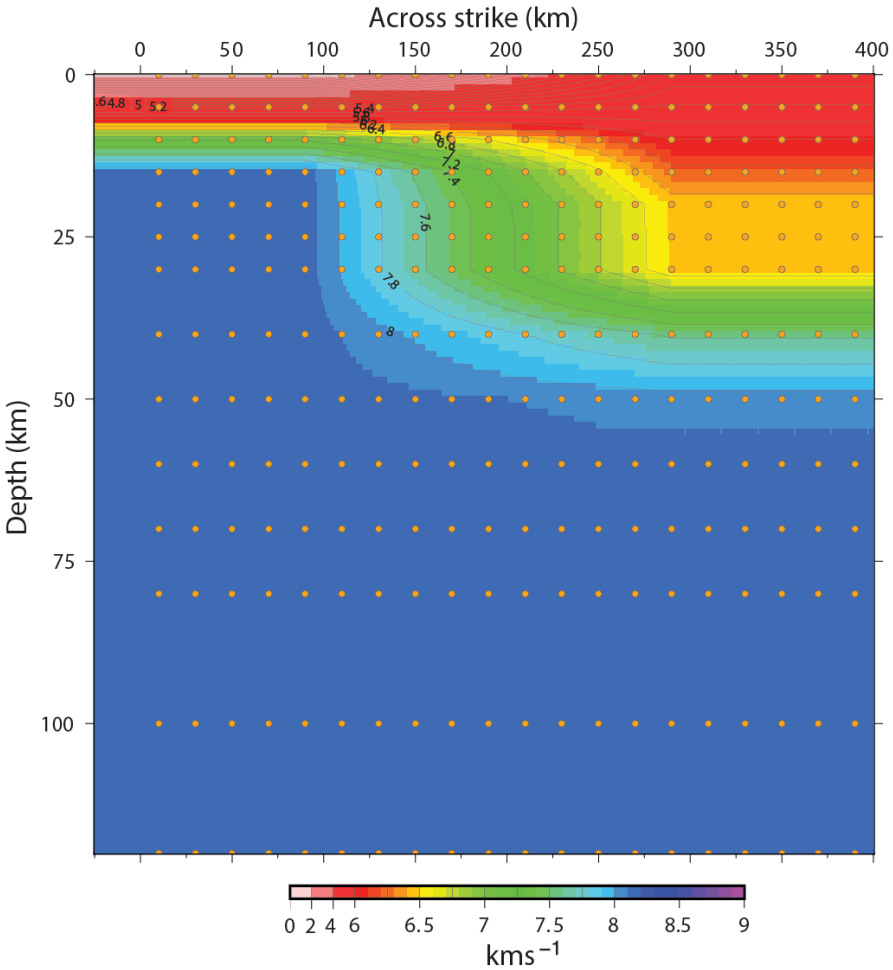


*Figure 4.4. 2D starting model derived from interpolation of 1D models. Nodes are orange circles. Setup for the 2D model and the 3D model in the X plane.*

### 4.4.1 Model Setup

Node spacing was chosen based on two criteria: (1) to allow residuals to reduce without causing instability within the model; and (2) to allow the same across-strike spacing for both the 2D and 3D models. From running a suite of models, the 2D model had a node spacing of 20km in X and a variable spacing in depth being 5, 10, 20 and 50km for depth ranges 0-40, 40-100, 100-300, and 300-450 km, respectively (Figure 4.4 and **Error! Reference source not found.**). Sets of bounding nodes were at X=-999,999 and Z=-100,500 (**Error! Reference source not found.**). For the 3D model the node spacing remained the same in the X and Z but was repeated 17 times in the Y with a spacing of 30km between each X-Z plane beginning at 0km along strike.

Initial testing found that using a single 1D-starting model caused severe instability (**Error! Reference source not found.**). Therefore, for the starting model we combine the 1D land model of Lange et al. (2010) for 290-390 km across strike with the oceanic model of CRUST 2.0 for 0-90km across strike and interpolate between 90-290 km across strike (Figure 4.4). Figure 4.5 shows the predicted ray paths for the local and teleseismic events.

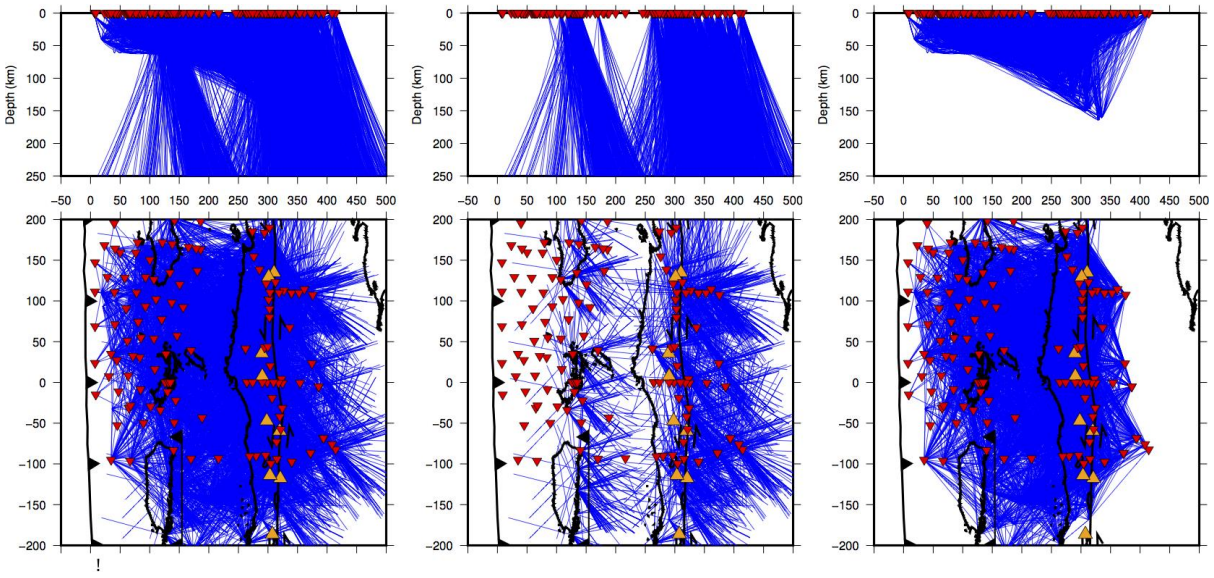


*Figure 4.5 Rays paths for the local (right), teleseismic (middle) and joint (left). Orange triangles are volcanoes. Red triangles are stations in this study. Blue lines are predicted ray paths.*

### 4.4.2 Model Parameters

The maximum iterations the model was allowed were 100 unless certain criteria were met. Using a weighted F-Test the program calculates variance within the model and compares it to the critical value. The critical value is at which the residuals within the model can be explained by random fluctuations within data. Dropping below this value infers that you are now modelling random fluctuations in data rather than actual structure. When the model variance drops below the critical value the model stops iterating and is assumed converged. For all iterations the model inverted for both teleseismic and local data. In the 2D model, for the first five iterations the local hypocenters were kept fixed only inverting for velocity structure. The 2D models took 12 iterations to converge, reducing rms residuals from 0.89 s to 0.51 s. For the 3D model hypocenters were free to relocate from the start. The 3D model took 23 iterations to converge and reduced the average residual from 0.51 s-0.40 s.

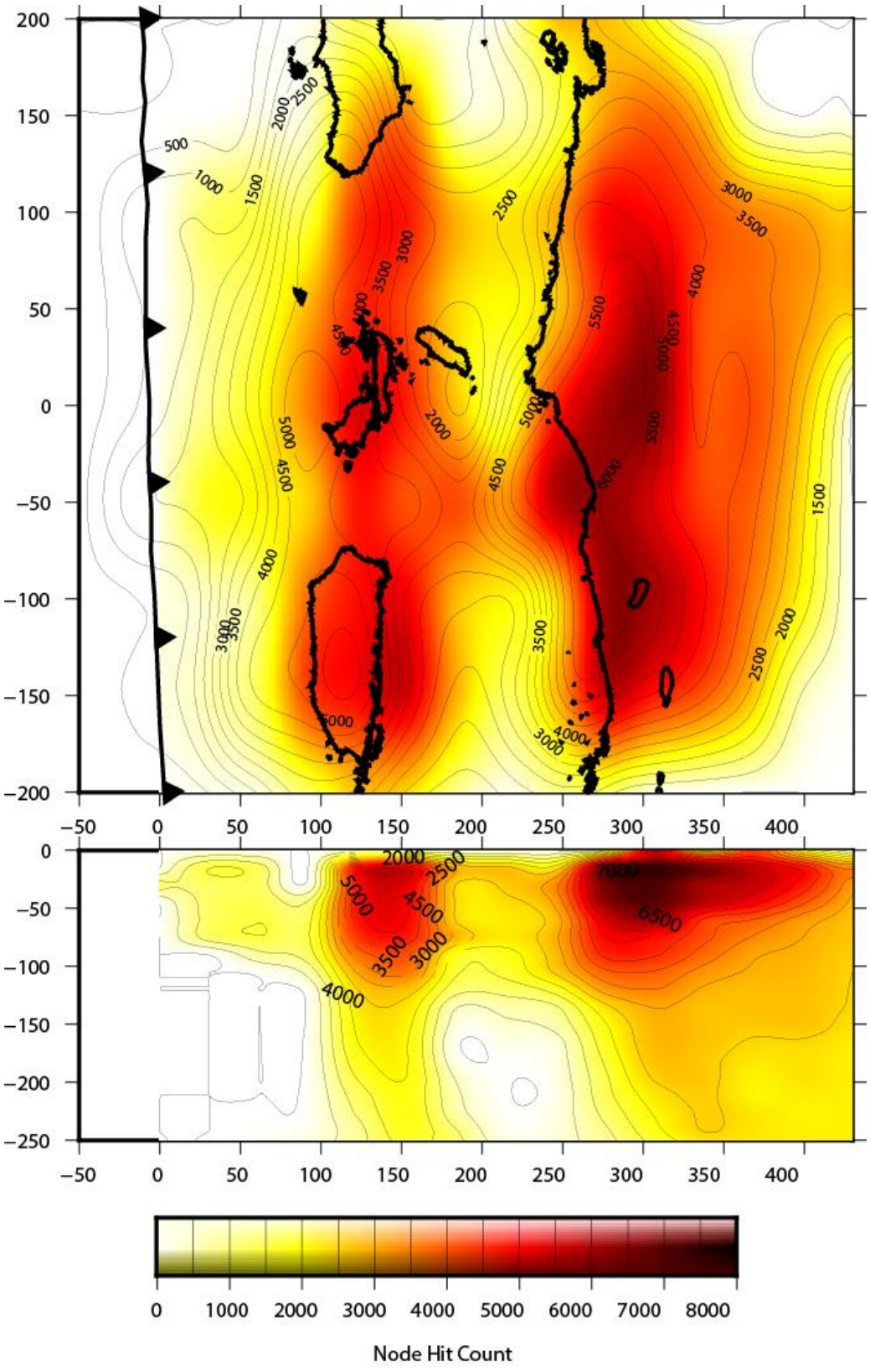


*Figure 4.6 The hit counts for 3D model. Top slice shows a depth slice taken at 50 km and bottom shows an X slice taken at 0 km along strike.*

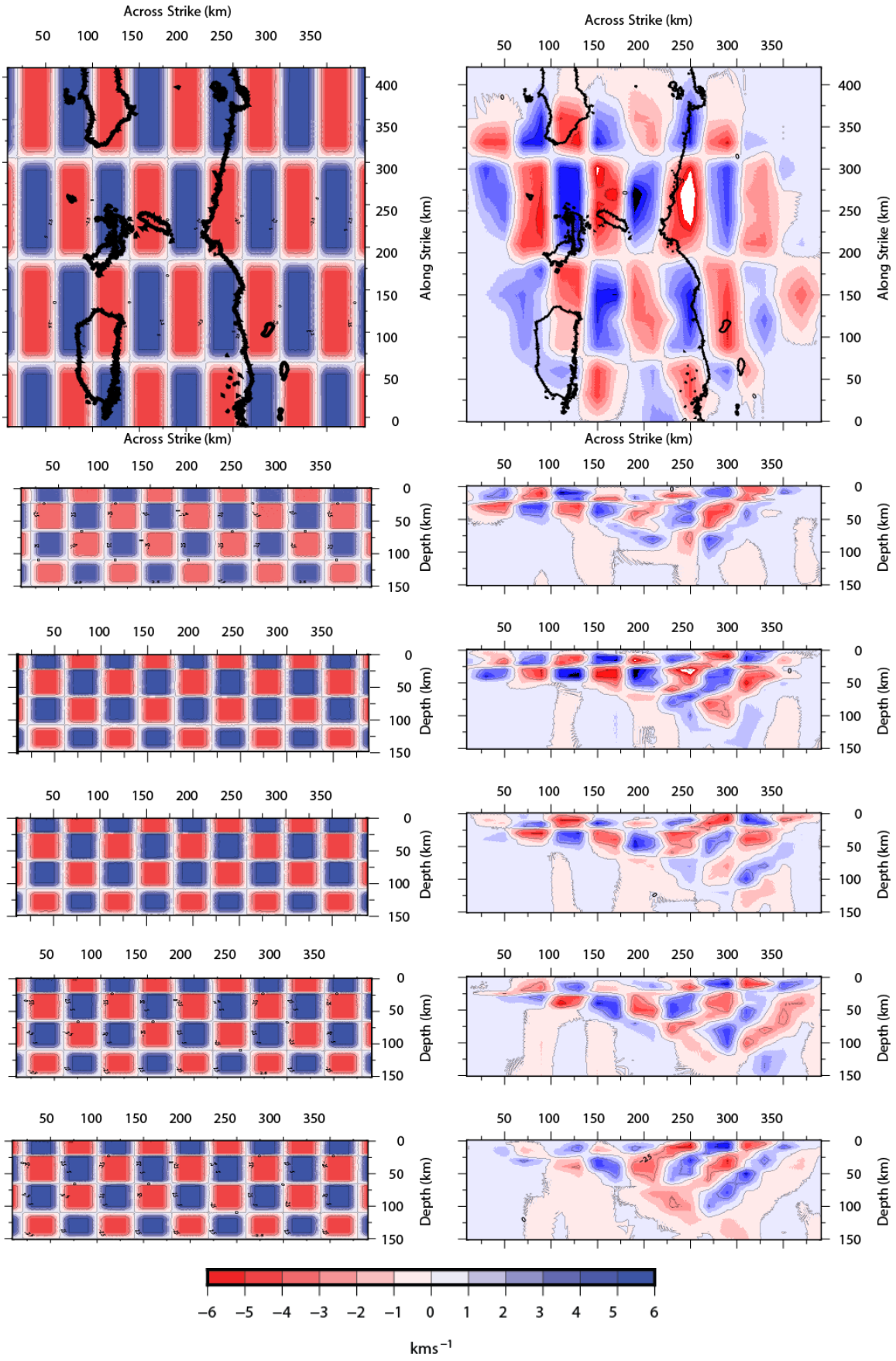


*Figure 4.7: Input (left) and recovered (right) checkerboard tests from the 3D Vp models. The depth slice (top) is taken at 37 km the X transects are taken at 365, 310, 210 , 150 and 100 km across strike.*

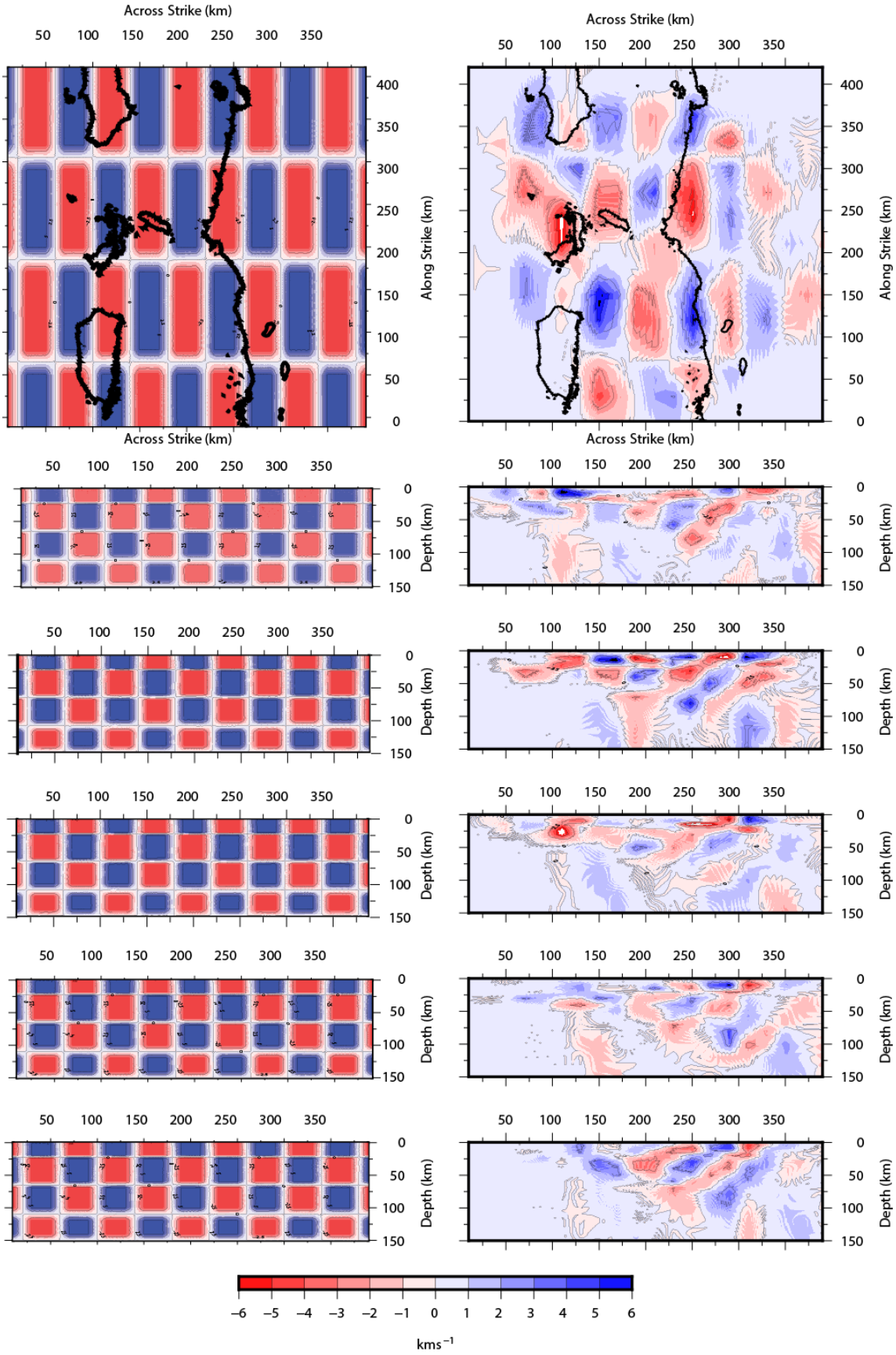


*Figure 4.8: Input (left) and recovered (right) checkerboard tests from the 3D Vs models. The depth slice (top) is taken at 37 km the X transects are taken at 365, 310, 210 , 150 and 100 km across strike.*

models, however the trade-off curves were unable to identify an optimum value through conventional means. Instead we chose to run a suite of models and varying the damping parameter to see how it affected the outcome. Models with damping values below 1000 produced unstable model results and over 1000 produced highly similar results. The only aspect of the modelling process the damping values affected was the number of iterations the model required. Damping values were set to 6000, 6000 and 1000 for Vp, Vp/Vs and station correction, respectively. Raw hit counts for the model are shown in Figure 4.6. Station correction terms shown in Figure 4.10 and Figure 4.11.

The maximum change to Vp and Vp/Vs ratios per iteration was 0.5 km $s^{-1}$ and 0.05, respectively. The models largest change for any one iteration was 0.2 km $s^{-1}$ and 0.03 for Vp and Vp/Vs, respectively. Hypocenters were allowed to move a maximum of 5 km in the X,Y and Z per iteration.

### 4.4.3 Smoothing Process

The algorithm does not inherently allow for a smoothing parameter within the inversion. To replicate velocity smoothing parameters often seen in other tomography codes we took a base grid then 2 sub grids +/- a half grid spacing in the X of the base grid. We ran the inversion for the 3 grids and took an average and projected it onto the base grid. This process was done for the 2D and 3D models.

### 4.4.4 Squeezing Tests

We have conducted a set of squeezing tests to determine the effect of changing the depth of the piercing points of the teleseismic events over the depth range 200-550 km (**Error! Reference source not found.**). This is important to avoid artefacts due to vertically compressing velocity anomalies and hence increasing their amplitude (piercing point depth too shallow) or from reduced resolution (piercing point too deep). For depths less than 400 km, there are consistent sets of artefacts in the nodes around X=110 km and X=170 km, even though checkerboard tests would suggest that these parts of the model are well resolved. From these tests a piercing point depth of 450 km was chosen as this model showed features that were present in all depth test models and also well recovered in the checkerboard tests.

### 4.4.5 Checkerboard and Synthetic Tests

To test the resolution of the model we ran two checkerboard tests using anomalies in both Vp and Vp/Vs of +/-5% relative to the final model for both 2D (**Error! Reference source not found.**) and 3D inversions (Figure 4.7 and Figure 4.8).

Checkerboard dimensions were chosen by conducting a suite of tests. Block size was initially set at the node spacing in x,y and z and we generated checkerboard models for every increment of 10km until the blocks were 100km in x,y and z. From this suite of models, we were able to access the minimum resolution achievable in each part of the model and develop checkerboard tests to show the highest achievable resolution within different parts of the model. For the 2D, first a combined checkerboard using a 20x20 km grid for the top 200km of the model with a coarse 20x100 km grid below 200 km and then a model of purely a coarse 20x100 km grid were used. Features down to the scale of 20x20 km are well-resolved in both the Vp and Vp/Vs inversions where there are constraints from the local earthquakes, giving confidence in the features we discuss in sections 4.5 and 4.6. The

parts of the model constrained only by teleseismic arrivals have good lateral but poor vertical resolution, showing features 20x100 km. We have good resolution to depths of 40-50 km beneath the incoming plate and the accretionary prism, but up to 120 km underneath the Sumatra mainland. We repeated the process for the 3D models and ran tests with block size increased to 40x90x40 km in X, Y and Z respectively for the upper 200 km and 40x90x100 km for below 200 km (Figure 4.7).

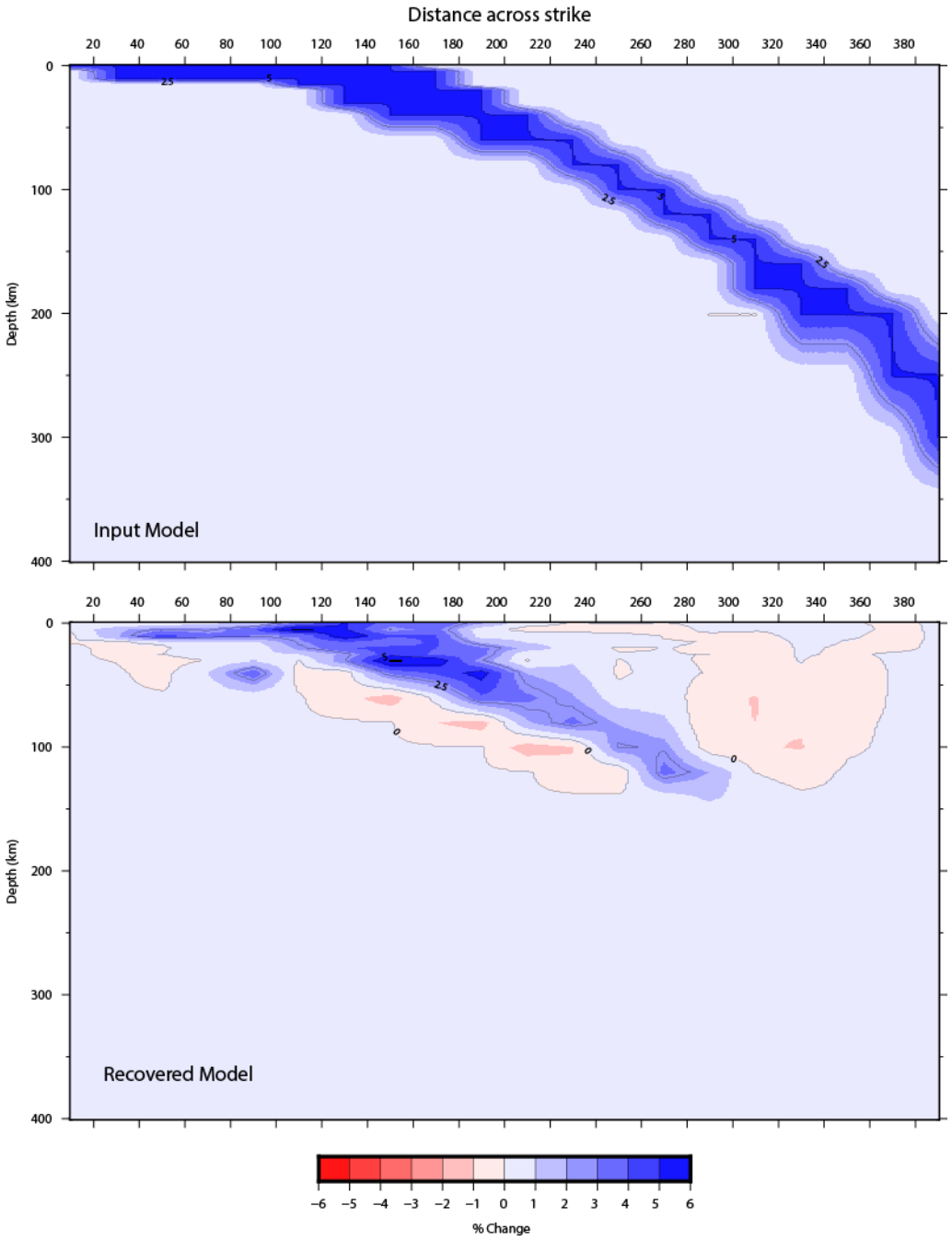


*Figure 4.9 A synthetic test of an approximate slab model for the region, based on hypocenter locations (top), and the recovered model (bottom). The slice is taken from the 3D model at 225km along strike (perpendicular to Batu islands).*

Once again the checkerboards mirror the limits and trends of the 2D models across strike and depth but with reduced resolution.

We generate a synthetic test representing the subducting slab in the region. The slab is estimated from the location of the hypocenters used in this study and given a presented as a +5% velocity anomaly. Figure 4.9 shows a slice of taken from the 3D synthetic model at 225km across strike (perpendicular to Batu islands). The synthetic tests show similar results to the checkerboard models showing we have good resolution and recovery down to 150km depth for anomalies >30km. However, dropping below 150km depth we are no longer able to recover the slab. The checkerboards in this region show they are only able to recover anomalies of 100km or greater.

### 4.4.6 Model Error

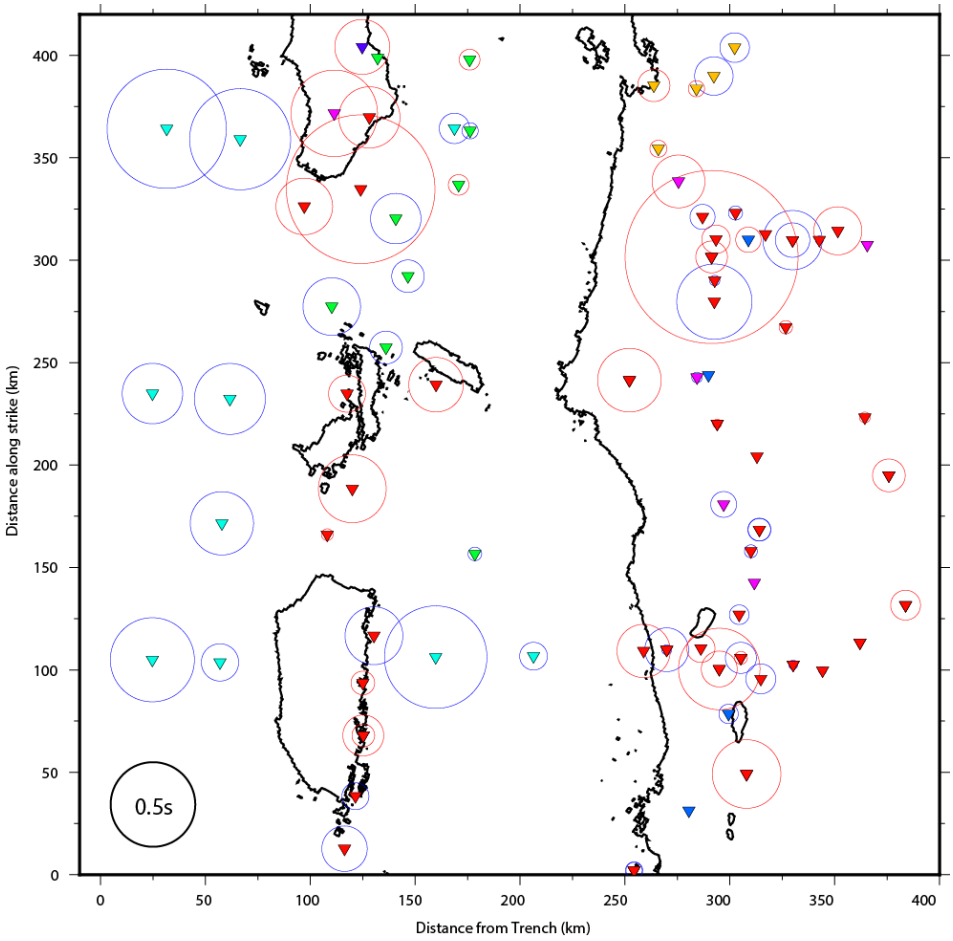


*Figure 4.10 The station correction for P wave arrivals used in the joint inversion for local and teleseismic data. Red circles indicate a positive adjustment. Blue circles indicate a negative adjustment. The black circle in the bottom left shows the scale of the circles. Inverted triangles represent stations and colours represent the station network as seen in Figure 4.2*

Error is calculated for the 2D model (**Error! Reference source not found.**) and 3D model. The model error is the standard error of each velocity node coefficient estimate. The model error shown here is the formal error calculated from the inversion matrix. The error in the Vp model is +/-0.2 km $s^{-1}$ with local maxima of 0.5 km $s^{-1}$ beneath the GSF and the shallow inner forearc. The average error in modelled Vp/Vs is 0.03 with local maxima occurring beneath the GSF of 0.1. Below the subducting slab Vp errors of +/- 0.4 km $s^{-1}$ are estimated, this is down to the loss of local event ray paths. Figure S 8.7 shows the errors in XYZ and origin time for the hypocenters within the final model. Errors are approximately 0.5 km in the X and Y and 1 km in Z and 0.5 seconds origin time. Station

corrections are calculated from the mean residuals at that station. The calculation is conducted alongside the inversion for velocity and hypocenter parameters and acts as another variable allowed in the inversion (Figure 4.10, Figure 4.11).

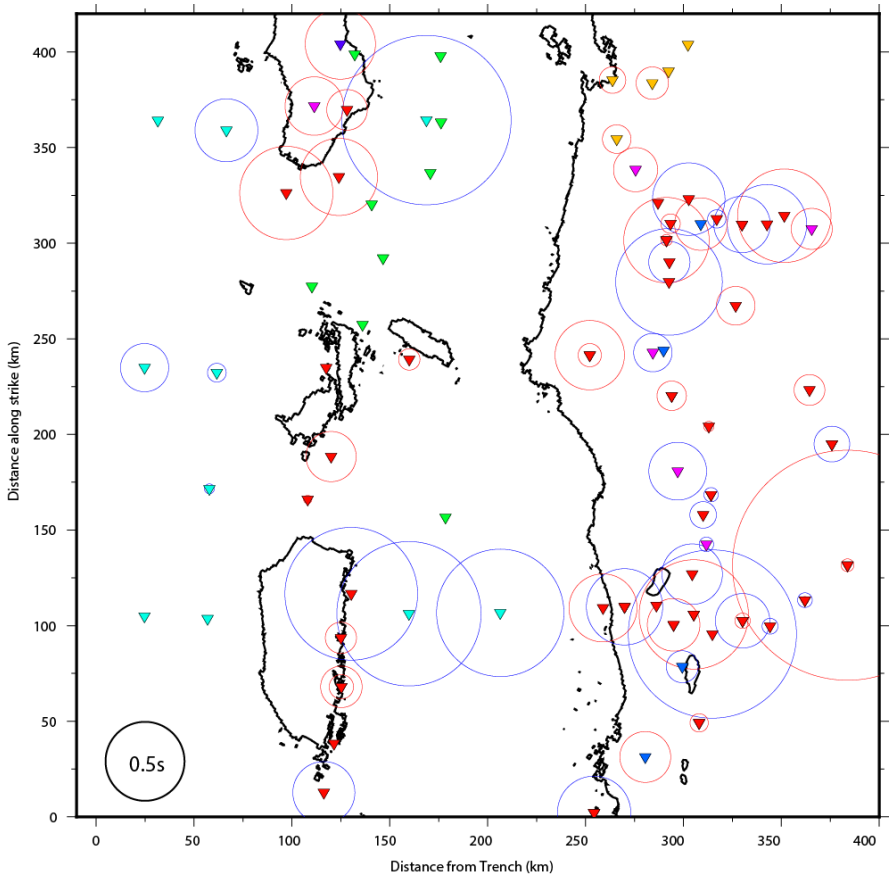


*Figure 4.11 The station correction for S wave arrivals used in the joint inversion for local and teleseismic data. Red circles indicate a positive adjustment blue circles indicate a negative adjustment. The black circle in the bottom left shows the scale of the circles. Inverted triangles represent stations and colours represent the station network as seen in Figure 4.2.*

We conducted bootstrapping tests by randomly removing 10% of the data and comparing the final results from several runs. **Error! Reference source not found.** shows the results from 5 test runs each having removed 10% of the input data randomly. This was to assess the robustness of are model and allowed us to talk about several features within the model that we are confident are actually geological features instead of artefacts.

### 4.4.7 Comparison between independently and jointly inverting local and teleseismic data.

**Error! Reference source not found.** and 8.9 show the results of inverting the data local data independently compared to the joint inversion of the teleseismic and local data. Features below 200 km depth are only seen in the joint inversion. This is to be expected as there are no local rays penetrating that deep. When looking at the structure above 200 km we see that the local inversion

captures all the dominant features that are seen in the joint inversion. However there is evidence that the local data set captures more variability for depths less then 50km.

## 4.5 Results

From our modelling process we produce 2D and 3D models based on the travel times of 651 local events and 88 teleseismic events. The tomography reduces the travel time residuals from 0.88 seconds to 0.41 seconds, representing a reduction of ~50%. For teleseismic and local results, residuals reduce from 0.9 and 0.55 down to 0.62 and 0.23, respectively. Figure 4.12 shows a histogram of the residuals before and after the inversion process. The plate interface, indicated on all plots, is estimated from the SLAB 2.0 model. Figure 4.13 shows the Vp and Vp/Vs results of the 2D model to depths of 450 km and relocated hypocenters. **Error! Reference source not found.** shows the shallow results from the 3D models and hypocenters within +/-20 km of each slice. Below, the results of the 2D and 3D models for velocity and Vp/Vs and comparison with hypocenter locations are described by region of the subduction zone system from the incoming plate to the volcanic arc and from crustal levels into the mantle at depth. The Moho on all figures is marked as the 7.5 km $s^{-1}$ contour as this represents the velocity change from crustal material to mantle material.

Within the modelling process local topography is accounted for by a station correction, with all stations corrected to Z=0 km in the model. The upper 5-10 km of the model are not well resolved due to the dominance of vertical rays, the lack of crossing rays and the change in topography in the model region in the order of 5-10 km.

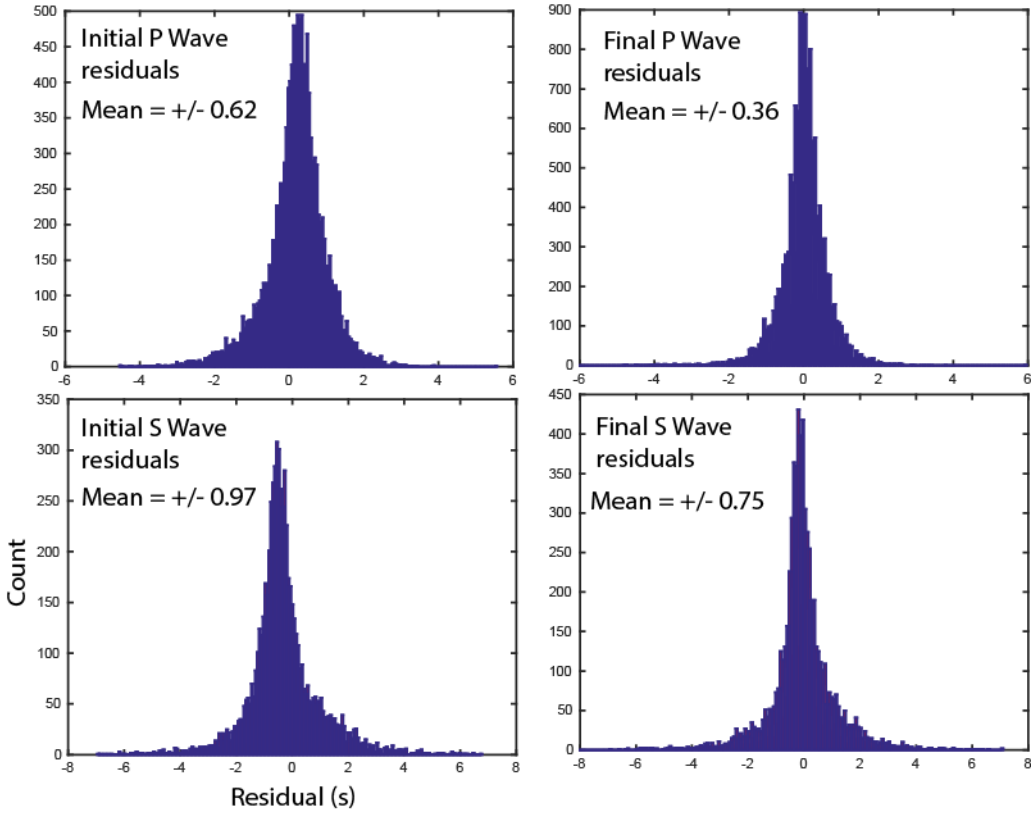


*Figure 4.12 Histogram plot of the P and S wave residual before the inversion process and the final 3D models.*

### 4.5.1 Incoming Oceanic Plate

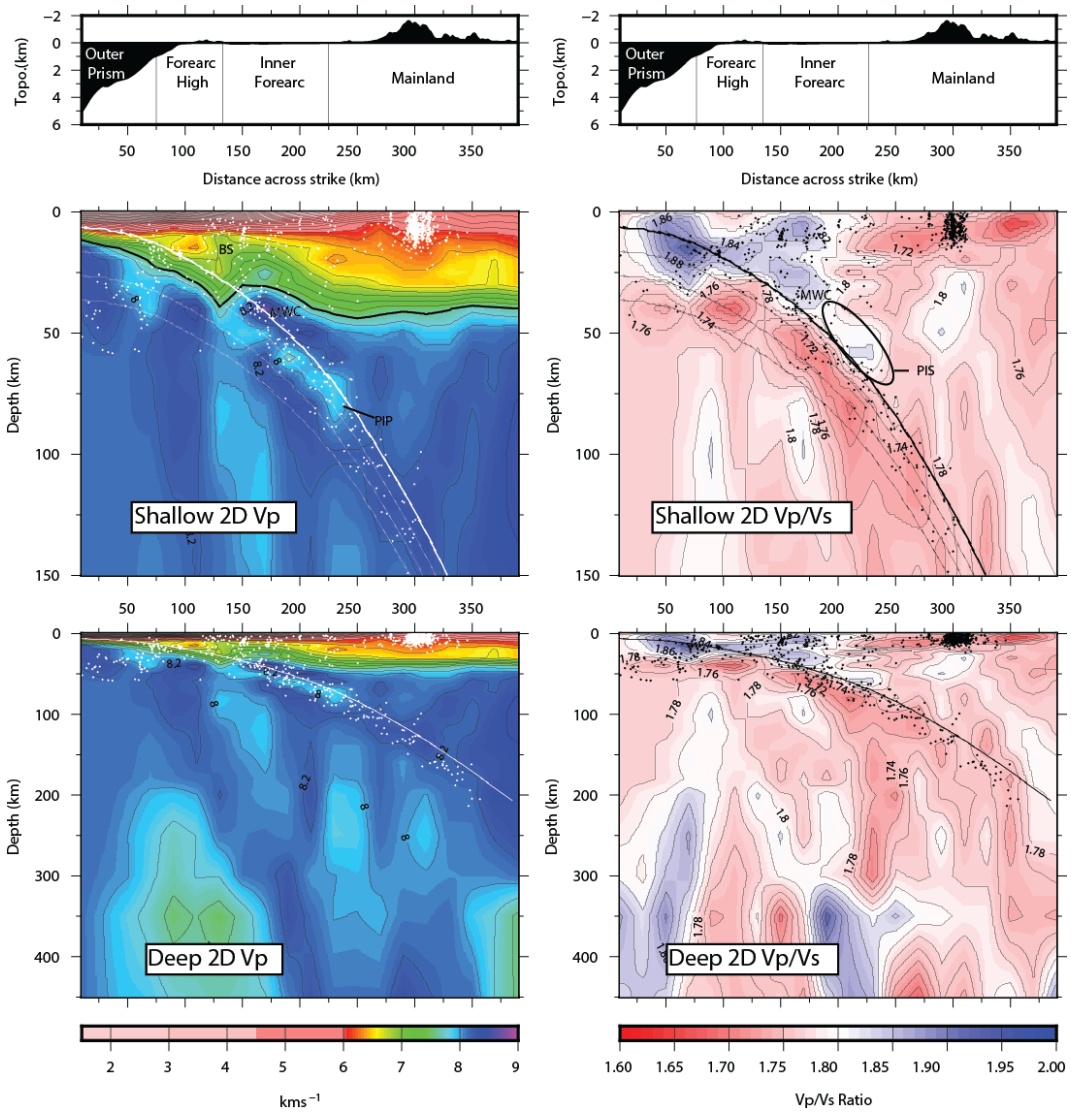


*Figure 4.13. Results from the 2D model for Vp (right) and Vp/Vs (left). The white (Vp) and black (Vp/Vs) dots represent the relocated hypocenters from the 3D model. The thicker white (Vp) and black (Vp/Vs) lines represent the plate interface based on a profile taken from the SLAB 2.0 model. The 3 thinner lines beneath are 10, 20 and 30km below the plate interface. PIS and PIP are labels discussed in the text.*

The properties of the incoming oceanic plate are well documented by several previous studies (e.g. Cook et al., 2014; Henstock et al., 2006; Henstock et al., 2016; Kopp et al., 2001; McNeill and Henstock, 2014; Schlüter et al., 2002). Within the model space, sediment thickness is 2-4 km north of the IFZ (McNeill and Henstock, 2014) and 1-2 km in the south. Basement topographic variations reach a maximum of ~3 km. However, due to the resolution of the model, any features that are caused by these variations in sediment thickness or basement topography will be unresolvable given the maximum resolution we can achieve is 20x20 km.

Clusters of hypocenters occur within the incoming oceanic crust (at X = 300 km) extending from 10 to 40 km depth with a particularly dense cluster located at X=370, Y=-10 (**Error! Reference source not found.** X=370 Label RA), this set of hypocenters sits beneath an unnamed fracture zone within the incoming oceanic plate. The thickness of the incoming plate offshore Central Sumatra is shown to be 5-8 km (Cook et al., 2014). The depth range of these events suggests faults extend deep into the oceanic lithospheric mantle and possibly the sub-plate asthenosphere. Active reflection studies of the oceanic plate offshore Simeulue island show faults extending up to 45 km deep into the ocean lithospheric mantle (Qin and Singh., 2015). Large events occurring on the incoming Indian oceanic plate are predominantly strike-slip (Delescluse et al., 2012) occurring in the depth range of 0-50 km depth, with the April 2012 $M_w$=8.6 event, occurring at a depth of 27 km, being the largest (Satriano et al., 2012). Within the region of the model space the IFZ approaches and enters the subduction system. The projected area of the IFZ beneath the forearc has many events located in it from our data set, but within the incoming plate itself we see no events in close proximity to the IFZ zone.

### 4.5.2 Active Domain (10-75 km across strike)

The Vp velocities within the outer prism are 1.5 km $s^{-1}$ at Z = 0 km increasing to 4 km $s^{-1}$ at the plate interface (Z = 10 km) of the landward edge of the outer prism. Vp/Vs values in the outer prism are high, at ~1.9 and show no along- or across-strike variability. High Vp/Vs ratios and low Vp velocities are common for accretionary prisms, which tend to incorporate rapidly deposited sediment sections of relatively undercompacted and unlithified, fluid-saturated, and potentially overpressured sediments. Similar values have been observed in the outer prism of the Mentawai islands (Collings et al., 2012), Southern Sumatra (~4°S) (Kopp et al., 2001) and north of Simeulue island (Klingelhoefer et al., 2010).

The oceanic crust is approximately 5-10 km thick and has velocities of 7.0-7.5 km $s^{-1}$ (Klingelhoefer et al., 2010; Singh et al., 2012). The plate dip from the trench to just seaward of the forearc high increases from ~0° to 3°. The oceanic lithospheric mantle has velocities of 7.5 km $s^{-1}$ – 8.5 km $s^{-1}$. The oceanic crust and the first 10 km of the oceanic mantle lithosphere have Vp/Vs values of 1.88 reducing to 1.74 for the rest of the oceanic lithosphere. Vp and Vp/Vs values for the oceanic crust at this depth have been reported from a local tomography study encompassing the trench and the Mentawai islands (Collings et al., 2012). The asthenospheric mantle has values of 1.77; such localised mantle Vp/Vs estimations are rare but from global studies the Vp/Vs of oceanic mantle is 1.77 (e.g. Kennett and Engdahl, 1995) Based on the Vp/Vs and hypocenter distribution we estimate the subducting plate thickness (oceanic crust and lithospheric mantle) to be 30 km. Pesicek et al. (2010) estimate the plate thickness to be 50 km but this was based off a global tomography study which reach depths of 700 km and spanned the entire margin.

Seismicity in the outer forearc area occurs in 2 main domains, within the outer prism and within the subducting plate. We believe the depth uncertainty of our hypocenter locations permits distinction between the upper/continental plate, interface and lower/subducting oceanic plate. Hypocenters

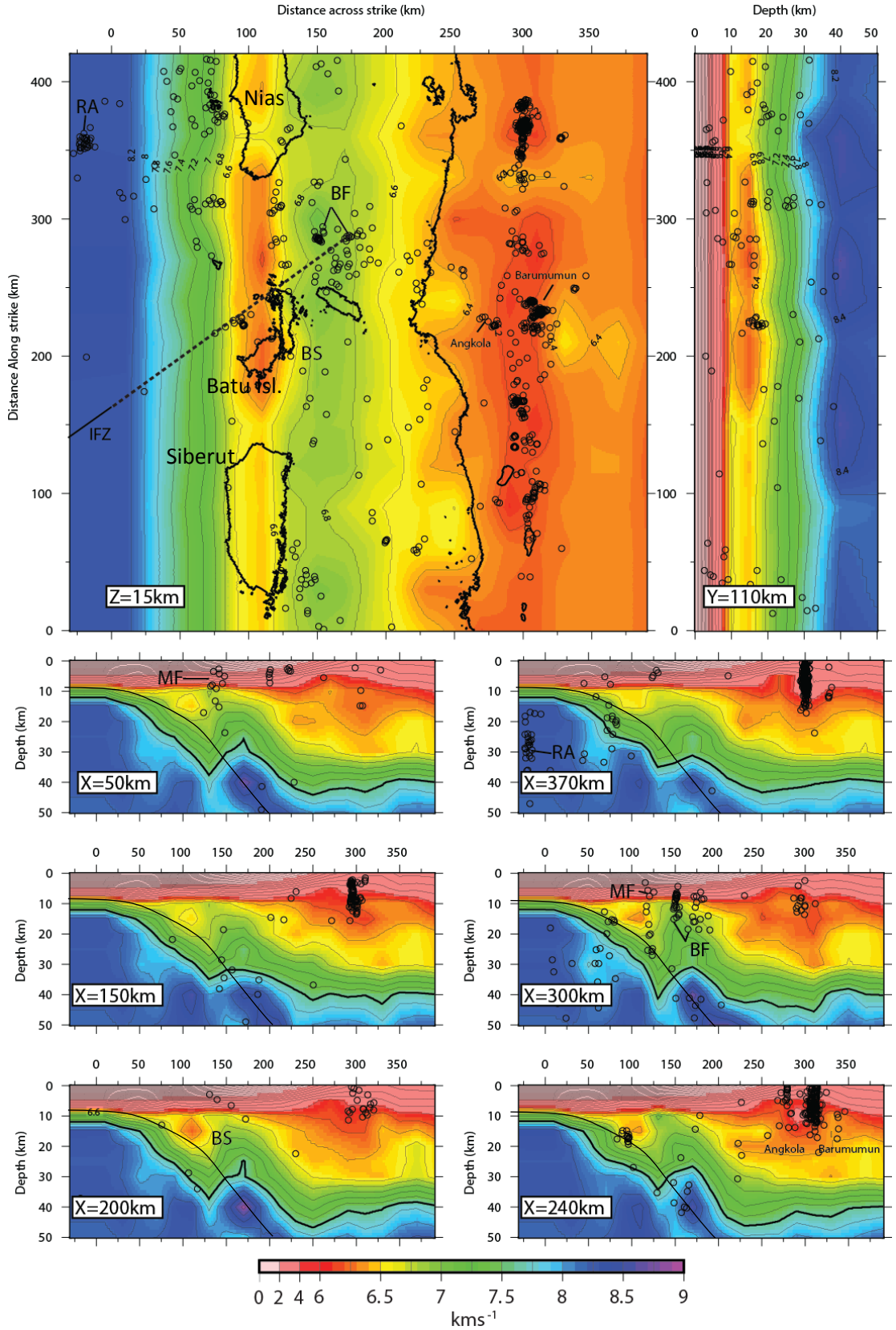


*Figure 4.14. Results from the 3D Vp models. Lower panels show transects taken at 50, 200, 300, 350 and 400 km along strike. Upper panels show a depth slice taken at 24km (left) and an along strike slice taken at Y=100 km (right). Relocated Hypocenters are shown as circles, hypocenters within +/- 20km of the transect are shown. MF=Mentawai Fault, RA=label discussed in text, BS is the location of the proposed accretionary domain backstop. BF=possible inner forearc faults. The curved black line is the plate interface.*

locating within the prism itself relate to the many imbricated thrusts with the outer prism (Cook et al., 2014). Events belonging to the plate mainly come from within the plate with very few events occurring on the plate interface itself. Other hypocenter studies from the region also show similar trends in hypocenter distribution in the outer prism (Collings et al., 2012; Tilmann et al., 2010). Seismicity within the oceanic crust has been interpreted as reactivation of pre-existing fractures such as the IFZ (Lange et al., 2010). However, from our hypocenter dataset, at this location in the subduction system, the projected location of the IFZ has little or no events associated with it.

### 4.5.3 Forearc High (75-130 km across strike)

The Sumatran forearc high has been studied extensively (Karig et al, 1980; Kieckhefer et al., 1981; Klingelhoefer et al., 2010; Kopp et al., 2001; Schlüter et al., 2002). At and beneath the forearc high, velocities increase from 1.5 km $s^{-1}$ at Z=0 km to 6.5 km $s^{-1}$ at 20 km depth, and Vp/Vs values are ~1.9 throughout this region, apart from directly underneath the forearc high where reduced VP/VS values of <1.77 are observed for depths <10 km. High Vp/Vs ratios are potentially over pressured, fluid-bearing sediments. Similar Vp,Vp/Vs and depth ranges have been reported by several other studies of the Sumatran forearc high region (Collings et al., 2012; Kopp et al., 2003; Tang et al., 2013). The oceanic plate maintains its Vp velocity profile and thickness beneath the outer prism to the forearc high region, but steepens from 3° to 13° degrees directly beneath the forearc high. The Vp/Vs of the lower plate significantly changes from beneath the forearc high, with the high Vp/Vs of the crust and upper lithospheric mantle reducing to ratios of 1.72, similar to the values observed in the lower plate beneath the outer prism. Vp/Vs ratios increase to 1.77 at 30 km depth indicating the presence of asthenospheric mantle and the base of the subducting slab.

Seismicity in the forearc high region can be divided into two areas; the accretionary wedge and the subducting plate. Within the Sumatran forearc, many imbricated thrust faults form (e.g., Cook et al., 2014; McNeill and Henstock, 2014). Within the 2004 rupture area thrust faults appear to be seismically active and produce many events (Collings et al., 2012; Lange et al., 2010; Tilmann et al., 2010). There are more significant forearc faults that exist at the outer-inner forearc (forearc high-forearc basin) boundary, for example the Mentawai Fault (Diament et al., 1992), with higher levels of seismicity associated with them. Several clusters of seismicity are associated with the trace of the Mentawai Fault. One cluster occurs landward of Siberut (X=50) and a second landward of the region the Batu islands and Siberut (X=300) (**Error! Reference source not found.** Label BF). Seismicity of the plate is also still present. Seismicity in close proximity to the plate interface is much more frequent beneath the forearc high relative to the outer prism region. Within the subducting plate, events within the oceanic crust are common. The boundary at X=130 marks a natural termination point of the forearc high and accretionary domain. The nature of this boundary will be discussed later (**Error! Reference source not found.** Label BS).

### 4.5.4 Inner Forearc Crust (130-220 km across strike)

The velocity structure beneath the inner forearc (between the forearc islands and the Sumatran coastline) is significantly different to the velocity structure of the outer forearc. Vp velocities vary from 1.5 km $s^{-1}$ to 6.5 km $s^{-1}$ from Z=0 km to 10 km, respectively. Beyond 10 km depth, we see

velocities increase gradually from 6.5 km $s^{-1}$ to 7.5 km $s^{-1}$ at 30 km depth. Vp/Vs in the inner forearc maintains elevated values of ~1.9 and shows no significant variation along- or across-strike. Vp/Vs abruptly reduces at the coastline, which we interpret as the boundary between the forearc basin/inner wedge and the volcanic arc. Within the model area, 2 distinct forearc basins are present landward of the islands of Nias and Siberut (**Error! Reference source not found.**). We observe no significant Vp or Vp/Vs variations along strike at depth ranges of Z=0 km to the plate interface (~Z=40 km) beneath the inner forearc correlating with the positions of the forearc basins. The continental Moho beneath the inner forearc region is at ~30 km. Similar depths for the forearc Moho have been observed just north of Simeulue Island, close to the boundary between the 2004-2005 earthquakes (Klingelhoefer et al., 2010)

The subducting plate continues to increase in dip from 13° at X=130 beneath the Inner forearc to 35° at X=200 beneath the volcanic arc, the dips are estimated from the Slab 2.0 model. The depth to the interface at the western edge of the forearc basin is ~30 km with no resolvable variability in position along the strike of the modelled area. The oceanic crust in this region has Vp of 7.8 - 8.0 km $s^{-1}$ and the oceanic lithospheric mantle has velocities of 8.2-8.4 km $s^{-1}$. Vp/Vs ratios maintain a value of ~1.72 throughout the subducting slab beneath the inner forearc.

Hypocenters within this region predominantly occur within the forearc crust and the subducting oceanic plate (interface and intra-slab). Within the forearc, hypocenters are concentrated just north of Pulau Pini (part of the Batu islands). Events occur over a range in depth of 5-20 km. The profile of both sets of events has a similar orientation to the events occurring on the MF and GSF, suggesting a fault of strike-slip or thrust nature. A sparse amount of events also occurs across the forearc above the Moho following no clear pattern. Events on the interface and within the slab continue to occur within the plate beneath the forearc. Within this region, events begin to appear on the projected trace of the IFZ.

### 4.5.5 Sumatran Mainland: Volcanic Arc and the Great Sumatran Fault (220-390 km across strike)

Beneath Sumatra, the continental crust has velocities increasing from 4 km $s^{-1}$ at Z=0 km to 7.5 km $s^{-1}$ at 40 km. Vp/Vs in this region does no vary significantly at 1.76-1.77 for 0-40 km depths. The continental Moho is observed at 40 km depth beneath Sumatra with little to no spatial variation observed in the modelled space. There is significant internal variation in velocity structure between 5 km $s^{-1}$ and 6.5 km $s^{-1}$, but no clear pattern is evident. The composition of the Sumatran crust is complicated by multiple volcanic provinces overlain with sedimentary basins (Barber, 2009) that may be linked with the observed variations in velocity and Vp/Vs ratios (Koulakov et al., 2009; McCaffrey et al., 2001). Unfortunately, the resolution of our models prevents derivation of the specifics of internal structure.

Hypocenters (depths of 0 – 15 km) are predominantly associated with the margin-parallel dextral Great Sumatran Fault (**Error! Reference source not found.**). At 200 km along strike, at the same latitude as the central Batu Island, a second set of vertical hypocenters parallel to and ~20 km west of the main GSF fault is present. These 2 parallel clusters of hypocenters show where the GSF bifurcates into two parallel faults, the Barumumun and Angkola segments of the GSF (Sieh and Natawidjaja, 2000), **Error! Reference source not found.** X=240). The GSF returns to one fault trace at X=300 km and this is confirmed by the absence of bifurcation in the hypocenter distribution.

The subducting plate beneath Sumatra maintains the velocity structure observed beneath the forearc. The plate dip increases to ~40° and the interface is at a depth of ~110 km beneath the volcanic arc. Once the plate reaches 80 km depth, the low velocities of the oceanic crust (~8.0 km $s^{-1}$) abruptly increase to velocities of 8.5 km $s^{-1}$ and become indistinguishable from the velocities associated with the oceanic lithospheric mantle (**Error! Reference source not found.** Label PIP).

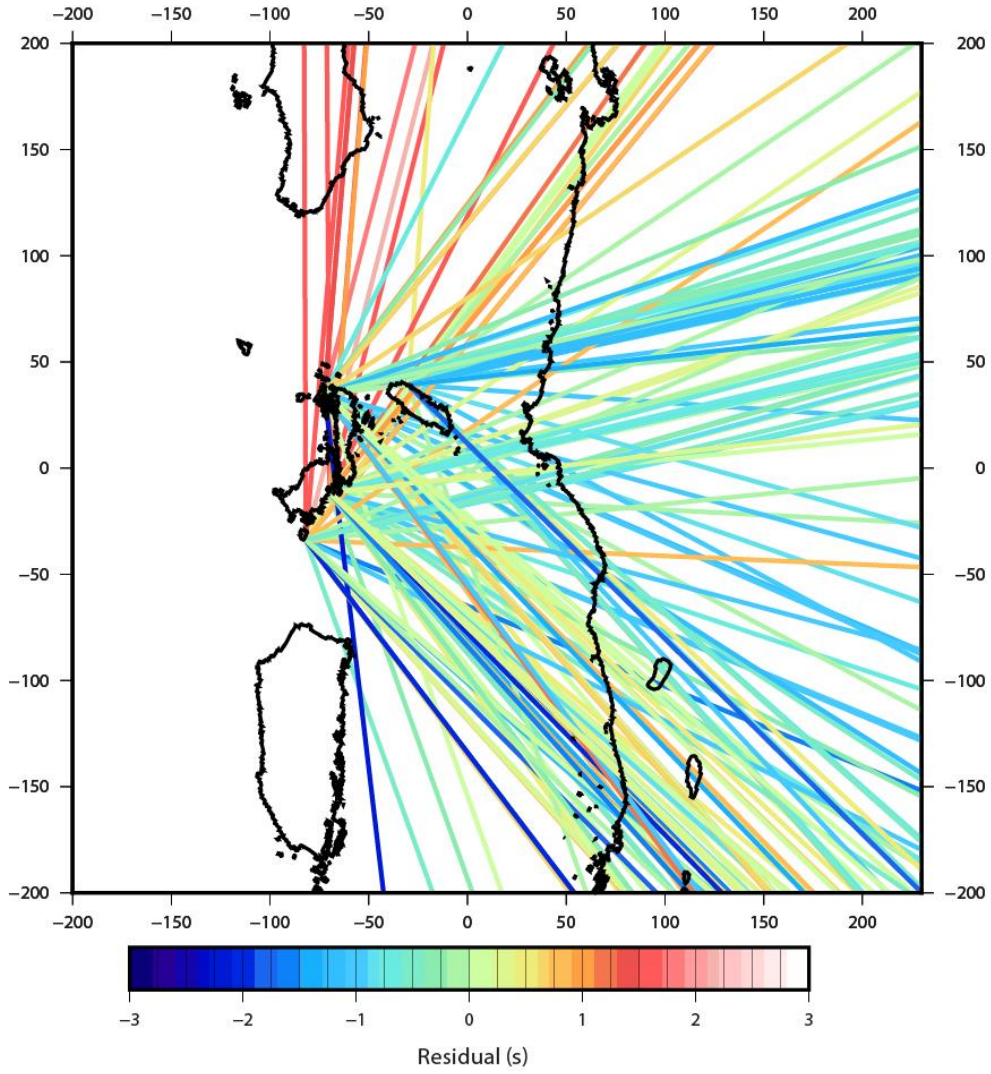


*Figure 4.15. Residual of incoming teleseismic ray. Blue is arriving too fast red is arriving too slow*

Hypocentres are all close to or below the Slab 2.0 plate interface, with none present in the overlying mantle wedge, unlike in the shallower/more seaward regions of the system where hypocenters appeared +/- ~10 km above and below the interface. However the significance of this is unclear as the Slab 2.0 plate interface is based on global hypocentre locations and will inherently contain errors. A linear profile of events continues on the projected path of the IFZ if it was subducted straight, but given the angle of convergence and dip of the plate, the IFZ on the subducting plate is expected to bend to the south with depth. Events within the plate itself reach a maximum measurable depth of 220 km for this dataset, but events in the Sumatran region have been recorded to depths of 600 km (Masturyono et al., 2001).

### 4.5.6 Continental Mantle Wedge (150-350 km across strike)

The mantle wedge occupies the area between the subducting plate interface and the continental Moho, and the seaward corner of the mantle wedge appears at X=150 km at a depth of 30 km. P-wave velocities are 8-8.2 km $s^{-1}$ with no significant variations throughout the model space (either with depth and along and across the strike of the margin and model space). Similar values of mantle wedge velocity have been reported from the Mentawai islands (Collings et al., 2012) and around Nias (Kieling et al., 2011). We see no resolvable Vp velocity anomalies associated with the volcanic arc within the mantle wedge.

Vp/Vs for the majority of the mantle wedge is 1.77, although there are elevated values of 1.82 at depths of 25-60 km beneath the volcanic arc indicative of melting caused by fluid release of the subducting slab (Anderson, 1978).A small portion of the mantle wedge corner has elevated Vp/Vs values of 1.8. Elevated Vp/Vs ratios in the mantle wedge corner may suggest a very small part of the corner wedge is serpentinisation caused by fluid release from the subducting slab, although the size of the anomaly is just below the resolution of our study.

Between 30-70 km depth we see elevated values of >1.8 on the plate interface, changing to 1.77 at 70 km depth (Figure 4.13 label PIS). This layer of high Vp/Vs infers that active fluid processes are occurring at the interface where fluids are released from the slab of the downgoing slab. There are no hypocenters within the mantle wedge beneath the continental crust.

### 4.5.7 Oceanic Asthenosphere Mantle

The oceanic asthenospheric mantle has velocities of 8.1-8.6 km $s^{-1}$. At depths of 300-400 km there is a pronounced area of low mantle velocity occurring 50-150 km across strike below the forearc islands, with the centre of this anomaly having velocities of 7.5 km $s^{-1}$. Velocities of 7.5 km $s^{-1}$ for a depth of 300-400 km are unlikely within the Earth; therefore, this is interpreted as an artefact. From analysis of the azimuthal spread of residuals, we find that this area has a strong azimuthal component. Figure 4.15 shows the breakdown of the arrival times for the teleseismic events arriving at the stations above the anomaly. Rays arriving trench parallel have a -2 to -3 second residual whereas rays arriving trench perpendicular have a +/- 1 second residual suggesting the nature of this anomaly is anisotropic. The significance of this observation will be discussed further below.

## 4.6 Discussion

### 4.6.1 Inner Forearc Moho and Basins Boundary.

Previous gravity surveys and wide-angle refraction surveys, within the rupture area of the 2004 and 2005 earthquakes, have suggested that the continental Moho intersects the subducting slab at shallow depths of less than 30 km (Dessa et al., 2009; Kieckhefer et al., 1980; Klingelhoefer et al.,

2010; Simoes et al., 2004). This, as well as the preliminary results of receiver function studies on mainland Sumatra, suggest that the Moho lies at a depth of ~30 km, increasing to 40 km depth below the active volcanic arc (Collings et al., 2012; Macpherson et al., 2012). Our results give a similar geometry of the Moho/plate-interface intersection and depth of the Moho under the volcanic arc for Central Sumatra.

The shallow Moho beneath the Sumatran forearc combined with the contrasting velocity profile between the inner and outer forearc suggests that the block below the forearc basin (inner forearc) has a different composition than the accretionary domain of the outer forearc. Geological results from Nias island (Moore and Karig., 1980; Samuel et al., 1997) show that ophiolitic complexes are exposed on the landward edge of the islands, incorporated into the older wedge through tectonic processes. Barber, (2009) argues that mainland Sumatra is composed of volcanic provinces overlain by sedimentary basin deposits. Combining these results suggests that the crust beneath the forearc basins is of a different origin to both the accretionary domain and the continental arc. Our models show that the bulk velocity beneath the inner forearc is approximately 7 km $s^{-1}$ with a Vp/Vs ratio of about 1.8. Many studies have looked at the Vp and Vs values of ophiolitic complexes taken from various locations (Christensen, 1978; Salisbury and Christensen, 1978). The velocity structure of the Troodos ophiolite (Mackenzie et al., 2006) show similar high velocities of 7 km $s^{-1}$ being observed at 10 km below the surface, similar to what is observed within our models. Overall, the mean Vp of an ophiolitic complex is 7 km $s^{-1}$ with a Vp/Vs of approximately 1.85. These values mirror the velocities we observe underneath the inner forearc. Most likely what we observe underneath the inner forearc of Sumatra is an ophiolitic complex. Ophiolitic complexes are present within numerous other forearcs, such as Japan (Ogawa and Naka, 1984),New Zealand (Nicholson et al., 2000) and Southern Alaska (Lytwyn et al., 1997). Other possibilities for high Vp at shallow depth are possible upwelling mantle caused by a spreading episode in Sumatra's past although there is no topographic evidence for this and we observe no crustal thinning in the inner forearc.

If the forearc is indeed an uplifted ophiolitic complex it has probably acted as a contrasting-strength backstop to the accretionary domain. However, given the very definitive vertical velocity boundary observed (Figure 4.6, Label BS) it is highly likely that there is a forearc fault within the domain that potentially assisted in placing the ophiolite to where it is or helped shape the boundary the ophiolite makes with the accretionary domain. The MF is shown to run along this velocity boundary where its surface expression is available and is believed to have a strong normal fault element to it (Diament et al., 1992; Mukti et al., 2012). It is believed that there is a similar fault to the north, the WAF, which is observed North of Simeulue although whether this is a continuation of the MF or a new fault is still under debate. Regardless of whether the 2 faults are the same or separate, there is evidence for a dominant thrust fault running along the landward edge of the forearc high in many places along strike. The fault or faults running along the landward edge of the forearc high likely played a role in the shaping of this boundary and potentially were the cause or influenced the emplacement of the ophiolitic complex before sediments began to be accreted within the margin.

We suggest that an ophiolitic complex was formed, uplifted and emplaced between the continental basement and the accretionary complex of the Sumatra forearc. Deducing the time of emplacement is difficult, however it is highly probable that the ophiolitic complex was emplaced in the Palaeocene or earlier as the oldest accreted sediments within the wedge are built up against it (Moore et al., 1982).

### 4.6.2 Presence/Absence of the Forearc islands and Basins Along-Strike

The formation of the forearc islands offshore Sumatra is not well understood. Schlüter et al., (2002) suggests that the forearc high, of which the islands are part of, are formed from an old accretionary wedge, which has been uplifted further. The generation of islands in certain areas but not others suggests that there is variability in uplift across the forearc high. The subduction of topographic features has been shown to affect uplift within the forearc of the New Hebrides (Taylor et al., 2005), Costa Rica (Corrigan et al., 1990) and New Zealand (Scherwath et al., 2005). Offshore Sumatra, while some islands are in line with incoming topographic highs, such as the IFZ/Wharton spreading ridge and the Batu islands, and the 96E Fracture Zone and Simeulue, many of the islands are not in line with any incoming topographic structure, for example Nias, and the Engano Islands. In addition, although other fracture zones interact with the margin from 3°N-10°N, there are no equivalent forearc islands. Processes such as underplating of the forearc by sediments or slices of oceanic crust or tectonic erosion (e.g. Clift and Vannucchi, 2004; Scherwath et al., 2010) also result in vertical displacement and tectonic evolution of a forearc on a million-year timescale. Our results show no obvious variations in velocity profiles beneath and between the islands. If processes such as underplating or tectonic erosion were taking place we would expect to see some notable change in the velocity structure along strike. Hence, either differences in the subsurface are on a finer scale than our models can resolve or the formation of islands is due to several interacting factors not generating a significant velocity structure change.

### 4.6.3 Mantle Wedge

Below the inferred continental Moho, an area with *Vp* velocities typical of unaltered mantle (8.0–8.2 km $s^{-1}$) is found. High *Vp*/*Vs* > 1.85 at the toe of the mantle wedge implies that a very localised part of the mantle wedge, adjacent to the subducting slab, may be hydrated (Hyndman and Peacock, 2003). This implies most of the mantle is normal with only a very small area in the toe region hydrated. Collings et al, (2012) found similar Vp and Vp/Vs results from the Mentawai islands to the south. A *Vp*/*Vs* < 1.85 in these regions beneath the Moho suggests that widespread serpentinization of the continental mantle, which has been postulated at several subduction zones around the world including central Cascadia (Nakajima et al., 2001), Costa Rica (DeShon and Schwartz, 2004) and Japan (Seno et al., 2001), does not occur here. Other studies from Chile (Haberland et al., 2009) also indicate that widespread serpentinization of the mantle forearc is not ubiquitous.

The oceanic crust has Vp/Vs ratios of >1.8 suggesting the crust is heavily hydrated. High Vp/Vs at shallow depth is often indicative of trapped over pressured fluids suggesting that the lack of a serpentinized mantle wedge is not because there is not enough water entering the system. The presence of a Vp/Vs layer of 1.8 on the plate interface (Figure 4.5 label PIS) suggest that fluids are only active in close proximity to the plate interface. Seno, (2005) have suggested that fluid escaping from the slab instead of entering the mantle wedge, percolates back up through fractures and faults present in the subducting crust. As fluids escape back up the slab they are then released into the overriding accretionary domain instead of entering the mantle wedge corner. Although this theory is hard to believe as this suggests that the forces stopping the fluids escaping into the overriding mantle wedge corner are stronger then the forces stopping the fluid escaping back up the slab. More

work is needed in this area to better identify where fluid can go if it does not escape back into the overriding mantle wedge. This likely to be happening in the Sumatran forearc mantle wedge

. We know the Indo-Australian plate is heavily fractured (Quin et al., 2015), suggesting that fluids are possibly escaping back through fractures within the crust.

### 4.6.4 Sub-Slab Mantle

At depths of 300-400 km below the forearc Vp velocities of 7.2-8.0 km $s^{-1}$ are observed. This is anomalously low for oceanic mantle velocities at these depths and is almost certainly a model artefact. From analysing the data we found that within the teleseismic data there is a strong azimuthal-residual component for arrivals beneath the forearc high region (Figure 4.15). Trench-parallel arrivals have an ~-2 second delay and reduce as you move from trench parallel to trench perpendicular where they assume a more normal residual pattern. Given the magnitude of the residual, structures in the crust are unlikely to be causing the observed results.

Collings et al., (2013) find that anisotropy within the shallow zone (<50 km) is dominated by structures parallel to the trench and conclude that mainly SPO anisotropy is occurring caused by tectonic deformation structures such as prism faults and the MFZ. They note that structures, such as fracture zones, within the incoming plate do not seem to affect anisotropy at both shallow (<50 km) and deeper (<400 km) depths. The anisotropy observed by Collings et al., 2013 in the shallow portion of the model is directly opposite to what we infer from the velocity in the deep portions of our model. This makes it unlikely that anisotropy within the shallow portions of the model is getting mapped into deeper structure. Most likely the anisotropy is caused by properties of the sub-slab mantle.

The majority of subduction zones around the world exhibit trench-parallel fast directions, suggesting flow induced by trench migration and decoupling between the slab and asthenosphere (Long and Silver, 2008). Long and Silver (2008) hypothesise for Cascadia, where the teleseismic SWS observations exhibit trench-perpendicular splitting, that there is a strong sense of mantle entrainment. We suggest that the observed residuals in Sumatra are caused by lattice preferred orientation (LPO) sub-slab anisotropy that has developed due to a thick layer of asthenosphere being entrained by the subducting slab. SKS studies from Sumatra (Collings et al., 2013), Cascadia (Currie et al., 2004) and Chile (Hicks et al., 2012) show similar findings and conclusions.

### 4.6.5 Slab Structure

The lower part of the subducting slab has low Vp/Vs values of <1.72, also observed in other subduction zones, such as New Zealand (Edheart-Phillips et al., 2015) and Japan (Zang et al., 2004). The lowered Vp/Vs is suggested to be caused by dehydration of the lower slab. Laboratory studies show that a forsterite–enstatite composite with a forsterite volume fraction of 0.6 has Vp $\sim$ 8.5 km s−1 and Vp/Vs $\sim$ 1.71 (Ji and Wang 1999). These Vp and Vp/Vs values are similar to our observations in the Sumatran lower slab, suggesting that serpentine within the lower part of the slab has largely dehydrated and we are imaging a forsterite–enstatite–water system. Fluid pathways in the lower slab are likely to be faults and fractures running throughout the subducting plate. (Qin and Singh,

2015) suggest that the fractures and faults within the subducting Sumatran slab extend deep into the mantle and reach depths of at least 40 km meaning there could be suitable fluid pathways.

Reinforcing this idea of faults extending deep into the mantle below the incoming plate, the $M_w$ 8.8 2012 event occurred offshore northern Sumatra below the incoming plate at a depth of 24 km (Delescluse et al., 2012). From our models we see that the depth to the base of the subducting crust is approximately 18 to 20 km (Figure 4.13). This supports the idea of events occurring below the crust and is what most likely causes the cluster events we observe below the incoming plate in our models. Deep offshore faults extending into the upper mantle are not uncommon having been observed at Cascadia (Han et al., 2016), Nicaragua and Chile (Grevemeyer et al., 2005).

## 4.7 Conclusions

We modify the Simul2000 program to jointly invert for local and teleseismic body. The modified code allows for joint inversion of local hypocenter and velocity parameters with teleseismic velocity parameters. Using a modified code we derive Vp and Vp/Vs ratio is for the Sumatran subduction beginning at the trench and extending to just east of the volcanic arc. We relocate 651 local events within the new model, providing improved accuracy in the locations. The accretionary domain of Sumatra has Vp of <6.5 km $s^{-1}$ and Vp/Vs ratios of 1.9 reaching a maximum depth of 25 km below the forearc high. There is a clear vertical velocity boundary between the accretionary domain of Sumatra and its inner forearc where below the inner forearc we see Vp values of 7 km $s^{-1}$ as shallow as 10 km depth. Vp/Vs values remain elevated within the inner forearc and end at the coastline of Sumatra. The Moho beneath the inner forearc is observed at depths of 25-30 km approximately 10 km shallower than the Moho observed underneath the mainland. We suggest that the high velocities at shallow depths and the shallow Moho beneath the inner forearc is caused by an ophiolitic complex which acts as a backstop to the accretionary domain of Sumatra.

Within the Sumatran forearc islands and basins are present along strike however we observe no velocity anomalies along strike correlating with the location of the basins. This is most likely down to our model being unable to resolve the velocity variation, if there is any at all.

The Sumatra mantle wedge does not show evidence for widespread serpentinisation with the bulk velocities of the wedge being 8.0-8.2 km $s^{-1}$ and VP/VS ratios of approximately 1.77. Only in a very localised part of the mantle wedge corner do we observe increased Vp/Vs ratios of 1.85 suggesting that widespread serpentinisation of the mantle wedge is not present here. We suggest the lack of a serpentinised forearc mantle is caused by fluids percolating back up through fractures and faults present in the subducting crust.

Hypocenters within Sumatra's forearc are mainly located around the plate interface and dominant faults such as the MFZ. We observe a cluster of seismicity seaward of the trench below the incoming plate at a depth range of 30-50 km. The seismicity is most likely caused by faults within the incoming plate extending into the mantle. Deep offshore faults extending into the upper mantle are not

uncommon having been observed at Casciacda (Han, 2016), Nicaragua and Chile (Grevemeyer, 2005).

Within the sub-slab mantle we see indirect evidence for a strong sense of trench perpendicular anisotropy. From our observations, as well as other studies, we suggest there is a high degree of mantle entrainment along with the Sumatran slab being subducted underneath Sumatra.

# 5 Chapter 5: Evidence for an ophiolitic complex acting as a backstop within Sumatra's forearc

**Abstract**

In this study we jointly invert travel times from local earthquakes and active shots to derive the fine scale P wave velocity structure of the Sumatran forearc. First arrivals from 218 local events and 9153 shots were jointly inverted to derive velocity and hypocenter parameters. Approximately 74,000 P wave arrivals were used in this study, 4500 from passive sources and 69,000 from active sources. The velocity structure directly beneath the inner forearc is significantly different from the accretionary domain to the west and the island arc to the east: Velocities of 7.5 km $s^{-1}$ are observed at depths as shallow as 9 km compared to 5 km $s^{-1}$ and 6.5 km $s^{-1}$ at the same depth for the accretionary domain and island arc, respectively. We hypothesise that the inner forearc is composed of an ophiolitic complex possibly emplaced during the start of subduction in Sumatra. The increased density and strength of the ophiolitic complex likely acts as a backstop for the accretionary domain to build against in this part of the margin.

## 5.1 Introduction

The structure of subduction zone forearcs is key to understanding seismicity in the seismogenic zone and tectonic evolution of the subduction through their preservation of sedimentation and tectonic structures. Depending on the nature of subduction, forearcs tend to be either erosionary or accretionary (Clift and Vannucchi, 2004) although this is likely to change on both short and long timescales. Within an accretionary margin an accretionary wedge, composed of accreted sediments, builds up against a backstop (Byrne, 1993). Imbricated thrust faults and fold ridges within the wedge form to accommodate compressional deformation (e.g. Cook et. al 2014).

Often the continental arc basement acts as a backstop for accretionary zones (e.g. Byrne et al., 1993). However Godfrey et al, (1997) find that the inner forearc basement of the Great Valley, California, is likely composed of an ophiolite and they argue that this acts as the backstop for the accretionary complex. Ophiolitic complexes have also been theorised to be present at several other subduction zones ( Ishiwatari, 1991; Kusky and Young, 1999; Samuel, 1997; Whattam, 2011), but in each case their origin and role in the subduction zone system is under debate.

Perhaps one of the most important impacts of forearc regions is the properties of the seismogenic interface. The seismogenic zone of the subduction zone generates earthquakes over a limited depth range. The updip and downdip limits of subduction zones control the extent of across strike ruptures. The updip limit is often assumed to be at approx. 5-15 km depth where the temperature

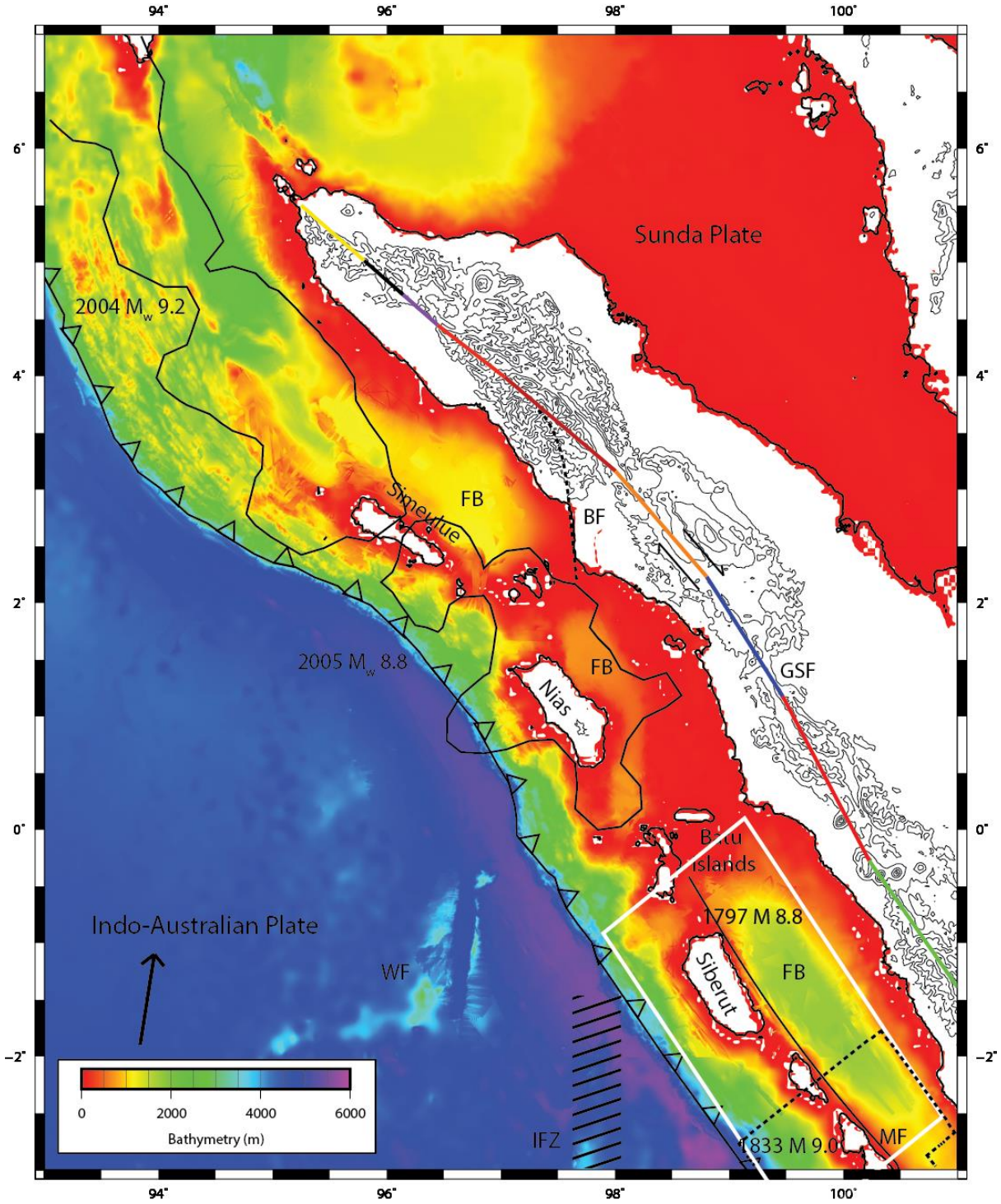


*Figure 5.1 Tectonic setting of Sumatra. The 1797 and 1833 rupture areas come from Natawidjaja et al. (2006). The 2004 (Lay et al., 2005) and 2005 (Ishii et al., 2005). IFZ=Investigator fracture zone, WF=Wharton Fossil ridge, GSF= Great Sumatran Fault, BF=Batee fault, FB= Forearc Basin, MF=Mentawai Fault zone.*

reaches 100-150° C and the accreted sediments of the accretionary toe dehydrate sufficiently to allow brittle failure (e.g. Saffer and Marone, 2003). However this point was called into question when the 2004 Sumatra event was seen to rupture all the way to the trench (Rajendran et al., 2005) promoting the need for further studies to look at the finer controls of this updip limit. Recent work

from Sumatra (Geersen et al., 2013) and Makran (Smith et al., 2013) suggest that the updip temperature limit may be reached close to the trench when sediments are thick. This may explain the apparently shallow updip limit for the $M_w$ 9.2 2004 Sumatran event. The down dip limit of the subduction zone has been argued to be either controlled by highly serpentinisied forearc mantle (Hyndman and Peacock, 2003) or in hotter subduction zones a temperature-controlled limit of 350°C (Hyndman and Wang, 1993; Oleskevich and Hyndman, 1999). The controls on the seismogenic interface need to be better understood in order to be able to better quantify the hazard associated with them.

In this study we focus on the Central Sumatran forearc. The Sumatran subduction zone is a result of the Indo-Australian plate subducting beneath the Sunda plate obliquely at a rate of about 60 $mmyr^{-1}$ (McNeill and Henstock, 2014)(**Error! Reference source not found.**). The Sunda margin is a classic example of an accretionary subduction zone, with a well-developed accretionary complex spanning from the trench to the landward edge of the forearc islands (e.g. Cook et al., 2014; Kieckhefer et al., 1981; Kopp et al.,2008; McNeill and Henstock, 2014; Schlüter et al., 2002). Numerous studies have investigated the forearc of the Sumatran part of this subduction zone looking at aspects ranging from incoming plate topography (Schlüter et al., 2002; Klingelhoefer et al., 2010; Kopp et al., 2003) to the nature of the forearc basins (Misawa et al., 2014; Moore et al., 1982). The presence of an old inactive accretionary wedge which forms the forearc Islands (Schlüter et al., 2002) has been hypothesised to be part of the Sumatran forearc. The difference between two Sumatran wedges has been observed in reflection studies, with the more seaward younger wedge characterised by a clear imbricated fold-thrust belt compared to the older more landward "inner" wedge which has a heavily deformed, typically higher velocity internal structure often poorly imaged in reflection data (Chauhan et al., 2009; Kieckhefer, 1981; Kieckhefer et al., 1980; Schlüter et al., 2002). The along strike placement of the forearc islands and basins is not well understood. For example, islands are only present on part of the margin, and even there do not correlate with any observable properties such as incoming topographic features.

A boundary between the landward edge of the forearc high and the inner forearc has been commented on by other studies including tomography studies and active reflection and refraction studies (Chauhan et al., Shannon et al., 2009, Singh et al., 2008). The boundary is fault-controlled (e.g., the West Andaman Fault, Mentawai Fault) but there is debate and potential variability along strike of the style of faulting. Where the Mentawai fault (Diament et al., 1992) is exposed at the surface it is believed that this surface expression marks the location of this major crustal boundary. The nature of the Mentawai fault is debated. Based on the linearity and the positive flower structures along the fault (Diament et al., 1992) suggest it is a strike-slip fault. Recent studies looking at focal mechanisms of hypocenters along the MFZ (Collings et al., 2012) show the MFZ as having thrust events occurring on it, suggesting that the MFZ has exhibited both strike-slip and thrust behaviour.

In this paper we jointly invert first arrivals from active and passive source data to determine a high-resolution velocity structure of the forearc offshore central Sumatra. From the structure we will pose new hypotheses about the contact between the overriding plate and subducting crust.

## 5.2 Method

### 5.2.1 Forward Problem: Local Earthquake, Shot or Blast.

In this study we use the program Simul2000 (Thurber, 1983) to jointly invert for local and active source body wave arrival. We *a priori* relocate the shots to the seabed as the water column is not included in the model. To do this we apply two corrections. First the observed travel time has the estimated water column component removed:

$$T_i^{obs} = T_i^{obs} - Wd_i/Ws \qquad \textit{Eq. 5.1}$$

Where $T_i^{obs}$ is the observed travel time for event i, and $Wd_i$ is the water depth for event i and Ws is the P wave speed in water, 1.5 km $s^{-1}$. Second the shot hypocenter is moved from the ocean surface to the sea floor.

$$Sdi = Wd_i$$

Were $Sdi$ is shot depth for shot i. Water depths were obtained from swath bathymetry data that was taken alongside the shots (e.g., Cook et al., 2014; Henstock et al., 2016).

The body wave travel time of a local event, $T_{ij}^{cal}$, is calculated using ray theory with a path integral and the event origin time:

$$T_{ik}^{cal} = \tau_i + \int_{Station(j)}^{Event(i)} U * ds \qquad \textit{Eq. 5.2}$$

Were $T_{ik}$, $\tau_i$ and $U * ds$ are calculated travel time for event *i* , observation *k*, station *j*, origin time for event *i*, slowness field and an element of the path integral respectively. Thus giving the residuals for a single local event:

$$r_{ik} = T_{ik}^{obs} - T_{ik}^{cal} \qquad \textit{Eq. 5.3}$$

Were $T_{ik}^{obs}$ is the observed travel time for event *i* observation *k* and $r_{ik}$ is the residual for the event observation pair . The residuals are related to the unknown model parameters by adopting a discrete velocity structure of N velocity nodes, and the 4 unknown hypocenter parameters. Meaning:

$$r_{ik} = T_{ik}^{obs} - \sum_{h=1}^{3} \frac{\partial T_{ik}}{\partial x_h} \Delta x_h + \Delta\tau_i + \sum_{n=1}^{N} \frac{\partial T_{ik}}{\partial m_n} \Delta m_n \qquad \textit{Eq. 5.4}$$

Where $m_n$ is the nth parameter out of the N parameters of the model

### 5.2.2 Inverse Problem

Each event *i* yields L equations representing each event observation pair. This can be written in matrix notation as:

$$R_i = H_i \Delta h_i + M_i \Delta m_n \qquad \textit{Eq. 5.5}$$

Where $R_i$ has the dimensions Lx1 containing the L residuals, H and h have the dimensions Lx4 and 4x1 and represent the hypocenter partial derivatives and the four unknown hypocenter parameter adjustments. *M* and m have dimensions LxN and Nx1 representing the velocity partial derivatives and the velocity adjustments. For shots $H_i \Delta h_i = 0$ as hypocenter parameters are known.

Once all events are processed the set of linear equations is solved using a damped least squares solution such that (Eberhart-Phillips, 1986):

$$\Delta m = \left\{ M'^T M' + \varphi^2 I \right\}^{-1} M'^T R' \qquad \textit{Eq. 5.6}$$

Where $\varphi$ is the damping parameter.

## 5.3 Data

We use data from temporary deployments carried out during 2008-2009. Active source data were collected with a deployment of 50 ocean-bottom seismometers (OBS) during cruise SO198-1 [Dean et al., 2008a]. We also use data from airgun shots between 20/06/08 -28/07/08 collected during SO198-2 (Dean et al., 2008b), and earthquakes between June 2008 and February 2009 recorded on a temporary local array of 10 OBS and 50 land stations spanning from the trench to the volcanic front on central Sumatra (Lange et al., 2010) (**Error! Reference source not found.**).

The combination of shots and earthquakes gives a broad distribution of sources from the trench to the Sumatra mainland (**Error! Reference source not found.**) ranging in depth from the surface to 50km. Additional data from neighbouring deployments (Toba, (Koulakov et al., 2009); offshore Islands, Collings et al., 2012) and the GEOFON and BMG permanent networks were also incorporated (**Error! Reference source not found.**).

### 5.3.1 Earthquake Sources

The original source of the hypocenter dataset used in this study is Lange et al., (2010) which provided 651 relocated events in a 1D model. In the Chapter 2 tomography study, these 651 events were relocated within a 3-D velocity model improving their locational accuracy. From the improved locations we took a subset of the 651 events. The subset included events that were seaward of the coastline and shallower than 50 km depth. This left us with 218 events providing 4268 P wave observations.

### 5.3.2 Active Source

The active dataset used in this study came from the offshore experiment collected during SO198-2 (Dean et al., 2008b). Within this deployment period 47,368 shots were fired providing a total of 101,268 observations. Only shots that were recorded on three or more stations were used, generating 9138 shots and 67,268 observations. Picks were assigned and quality controlled by hand by P. Vermeesch and M. Karplus, with pick uncertainties of 50-100 ms assigned to each pick. Ocean bottom data were corrected for a linear clock drift upon recovery. The land station data have had a bandpass filter between 5-30 Hz depending on instrument type, as well as a predictive deconvolution with an operator length of 300 ms and a lag of 300 ms (**Error! Reference source not found.** Red triangles). The picks from the long deployment OBS (**Error! Reference source not found.** light blue triangles) are made on data with a bandpass of 5-30 Hz with predictive deconvolution with a length of 260 ms and a lag of 160 ms. The picks from the main refraction experiment use a bandpass of 5-30 Hz (**Error! Reference source not found.** Green triangles); for some instruments a deconvolution of 200 ms length and 150 ms lag has been used. Mostly the data are similar to the hydrophone data although for some instruments the vertical component gives better arrivals and these have been used.

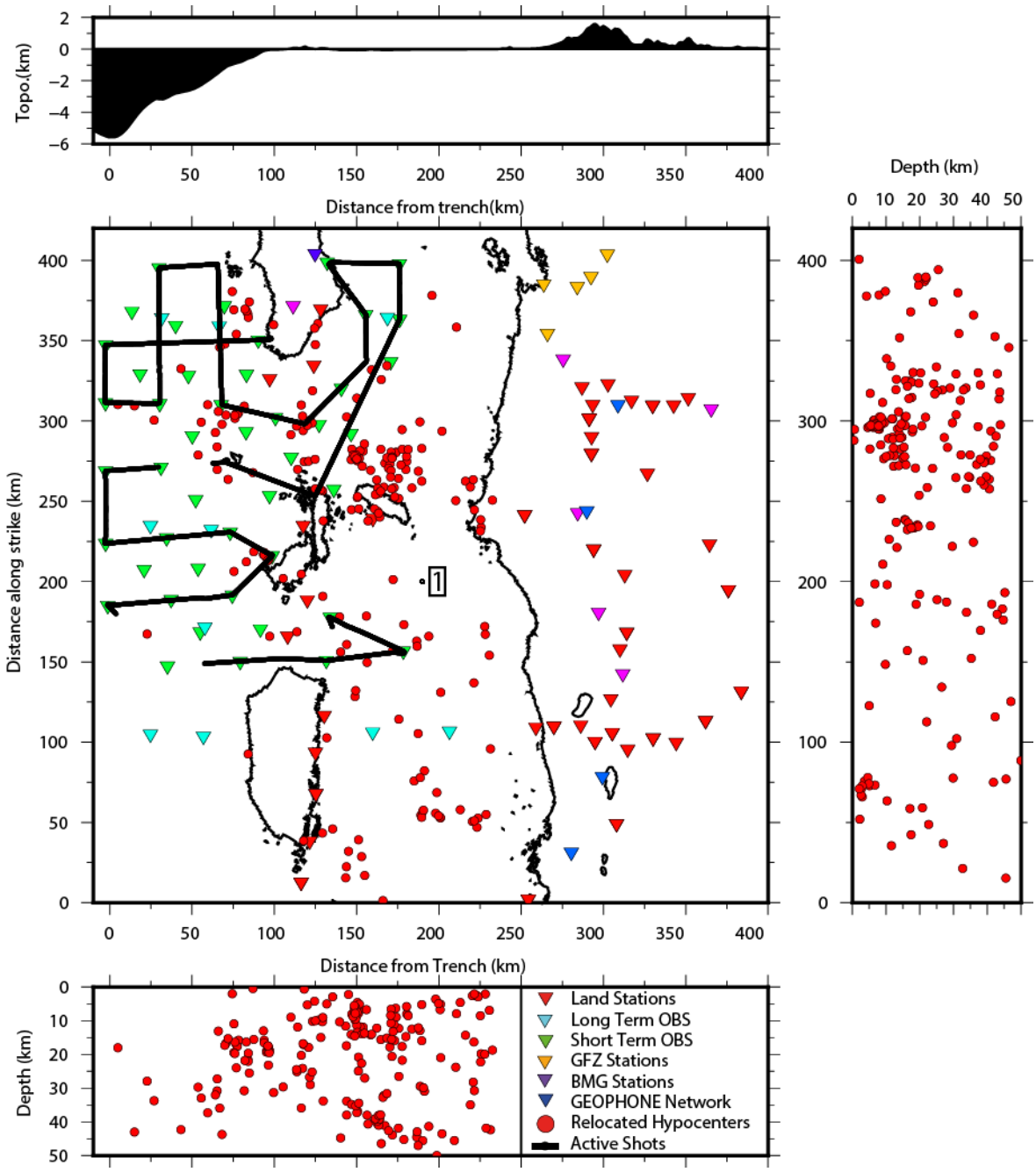


*Figure 5.2: Stations (triangles), events (circles) and active shots (black line) used in this study.*

## 5.4 Model Parameterisation

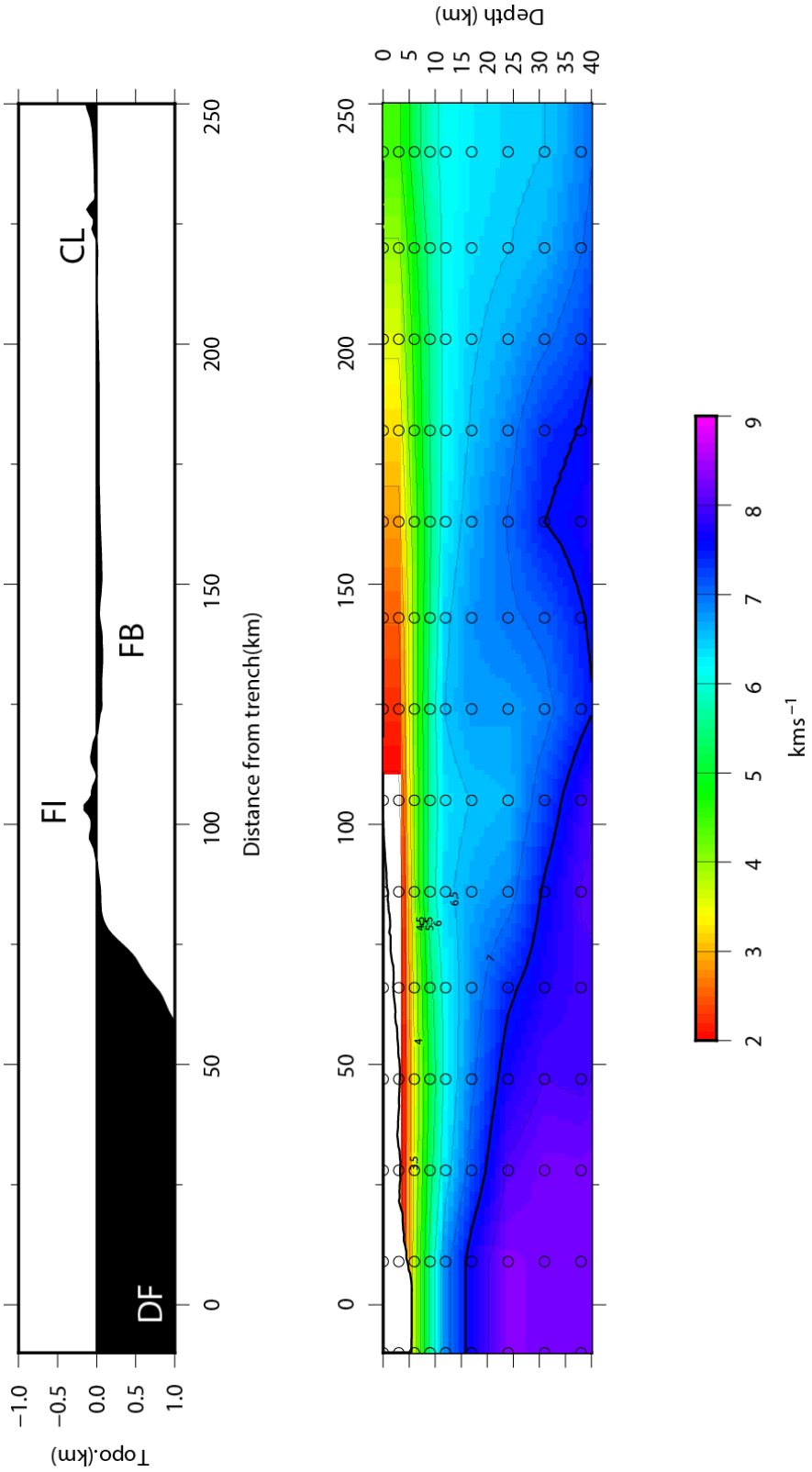


*Figure 5.3: The starting model and X transect node set up for the 2D and 3D models. Black circles are nodes. The initial model came from the final model for the 2D inversion in Chapter 4. Df, deformation front, FB across-strike location of the forearc basins. FI is the forearc high and CL is the Sumatra coast line. The Black line represents the Moho (7.5 km s-1 contour)*

### 5.4.1 Model Set Up

Initial tests found that using a generic 1D model or hybrid 1D model produced anomalous results as the accretionary domain of Sumatra was not accurately represented. This led to active source rays being incorrectly predicted, especially those sampling shallower than 10 km depth. Using 1D average Earth models such as the oceanic model from ak135 (Kennett and Engdahl, 1995) pushed rays much deeper than they would likely go. This was to compensate for the fast predicted travel times due to not incorporating the effect of the accretionary prism into the starting model. To overcome this, we tested starting models that better represented the velocities of the accretionary prism. After running several models to better represent the accretionary domain we found that the predictions of active rays started producing residuals of <2 seconds, compared to residuals of >10 seconds when trying a 1D starting model. The optimum starting model was the final 2D P wave velocity model presented in chapter 4. We ran a suite of models with varying node spacing and found that the optimum node spacing in X was 17 km. Smaller node spacings introduced artefacts into the model, such as spurious spikes in velocity located on single nodes. Z node spacing was 3 km for 0-12 km, 5 km for 12-52 km, and 25 km for 52-152 km. Node spacing less than 5 km deeper than 12 km depth introduced anomalies similar to those when X-Y was < 17 km. **Error! Reference source not found.** shows the initial starting model overlaid with the final node set up for X transects. To calculate the velocity on a grid we use an averaging method whereby the initial grid was shifted +/- a half a node spacing in X. From the 3 grids an average was taken and this was the final velocity model. This process was repeated for both 2D and 3D models. In the model we weighted the data such at a ratio of 1:0.2 for local to active observations.

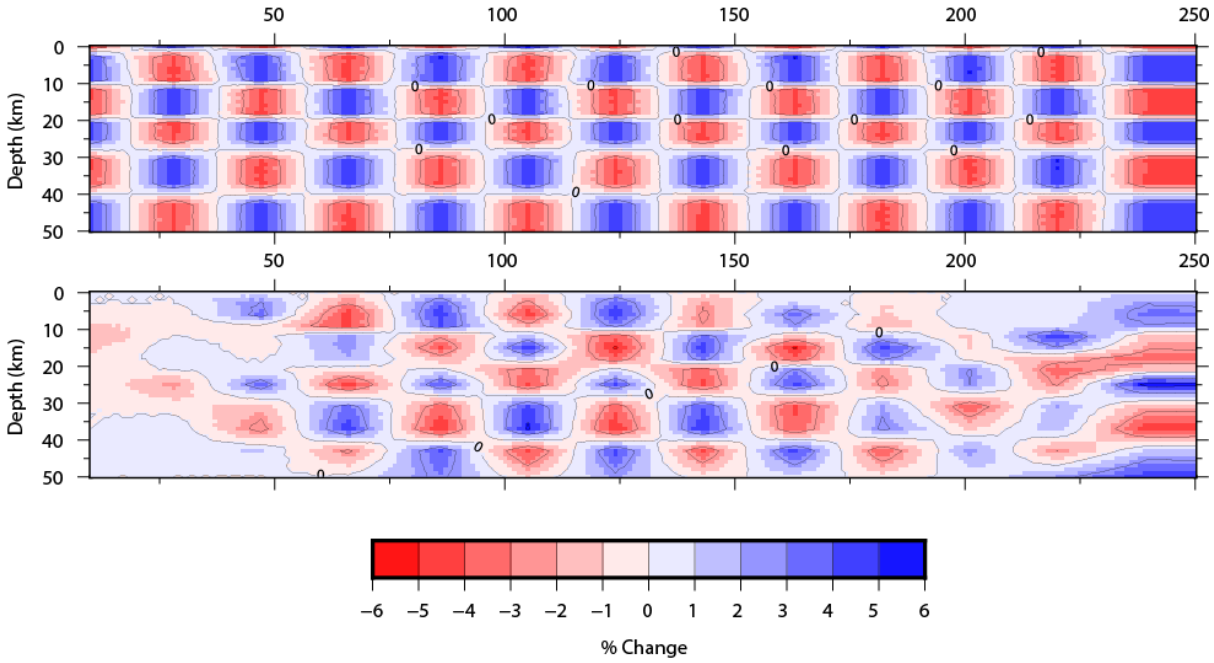


*Figure 5.4: Results from the 2D checkerboard tests. Input (top) and output models (bottom) using blocks of 20x10 km in X-Z.*

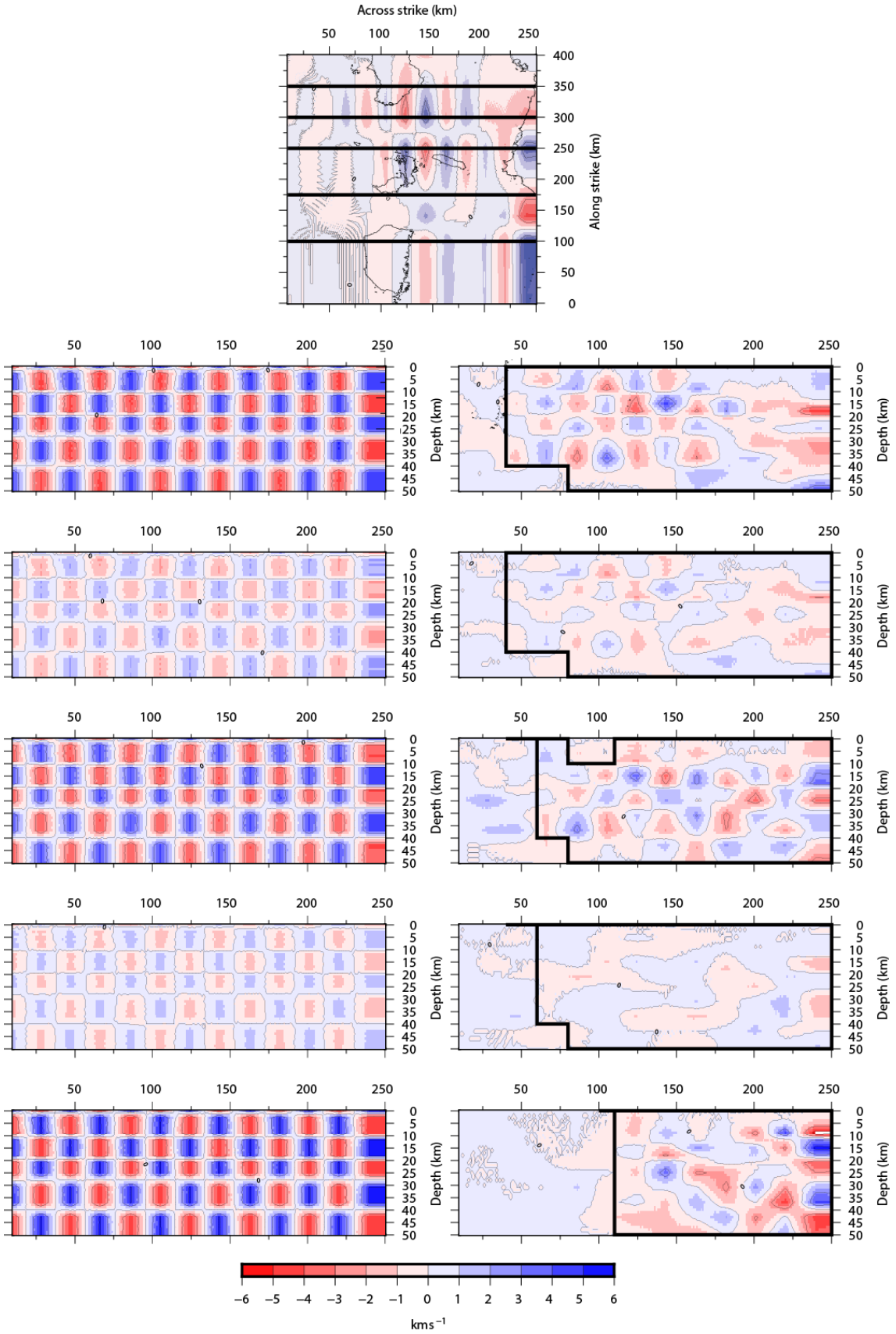


*Figure 5.5: Input and output results from the 3D checkerboard tests. Anomaly block size is 20x30x10 km for XYZ. Taken at 100, 175, 250, 325 and 350 km along strike. The black line indicates the area that we believe is resolved.*

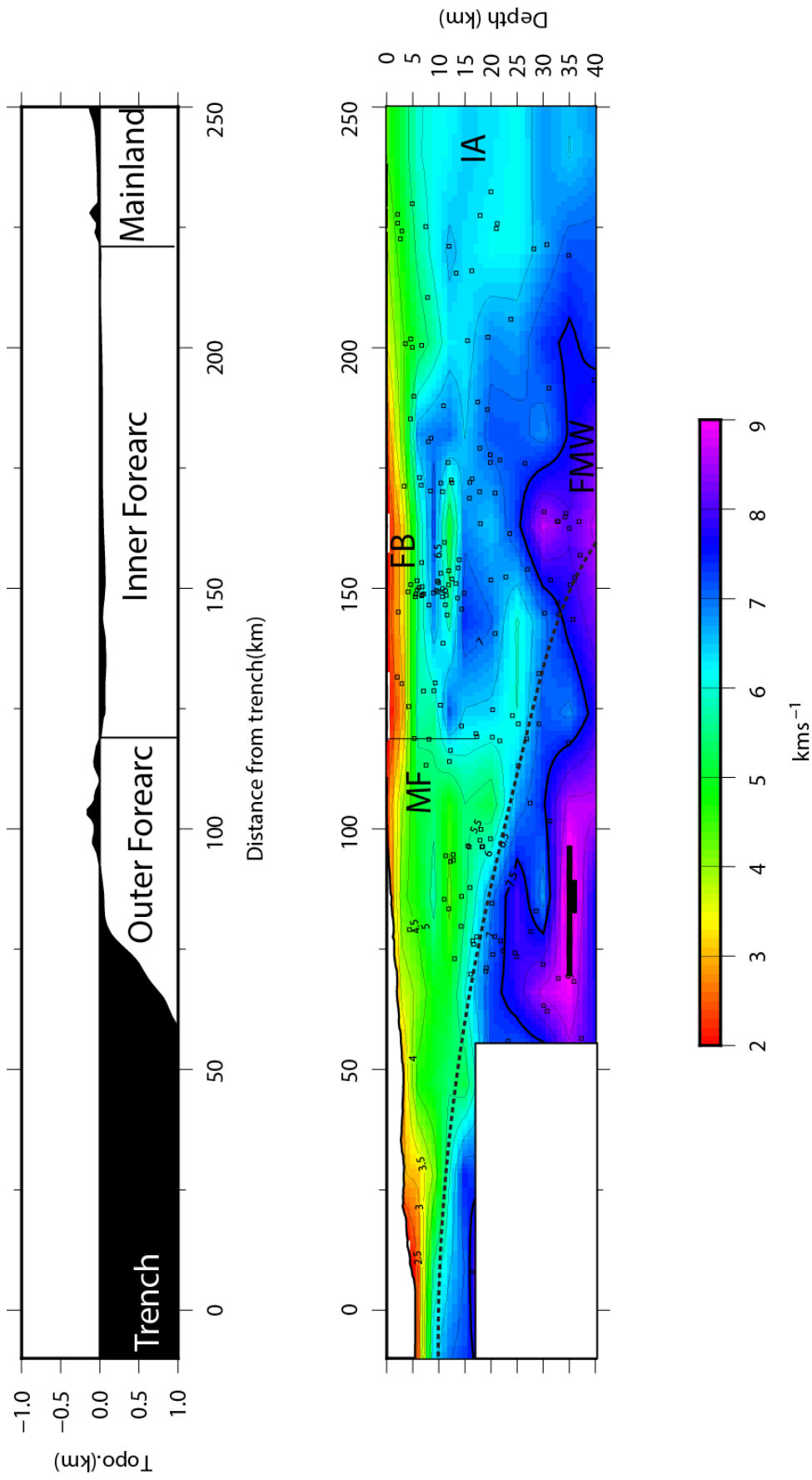


*Figure 5.6: Final velocity model from the 2D inversion. MF is the approximate location of the Mentawai Fault. FMW is the forearc mantle wedge, IA is the island arc crust and FB are the forearc basins. Black squares are hypocenters relocated within the 3D model. The dashed line is the plate interface estimated from SLAB 2.0.*

The final 2-D model was used as a base for the 3-D model. The 3-D model comprised 12 planes of the same node set up as the 2-D model with planes spaced 30 km starting from central Nias Island (350 km along strike) and ending at central Siberut Island (50 km along strike). Spatial parameters were kept fixed for the first iteration with only the origin time being inverted. After that, hypocenter parameters were jointly inverted for velocity parameters.

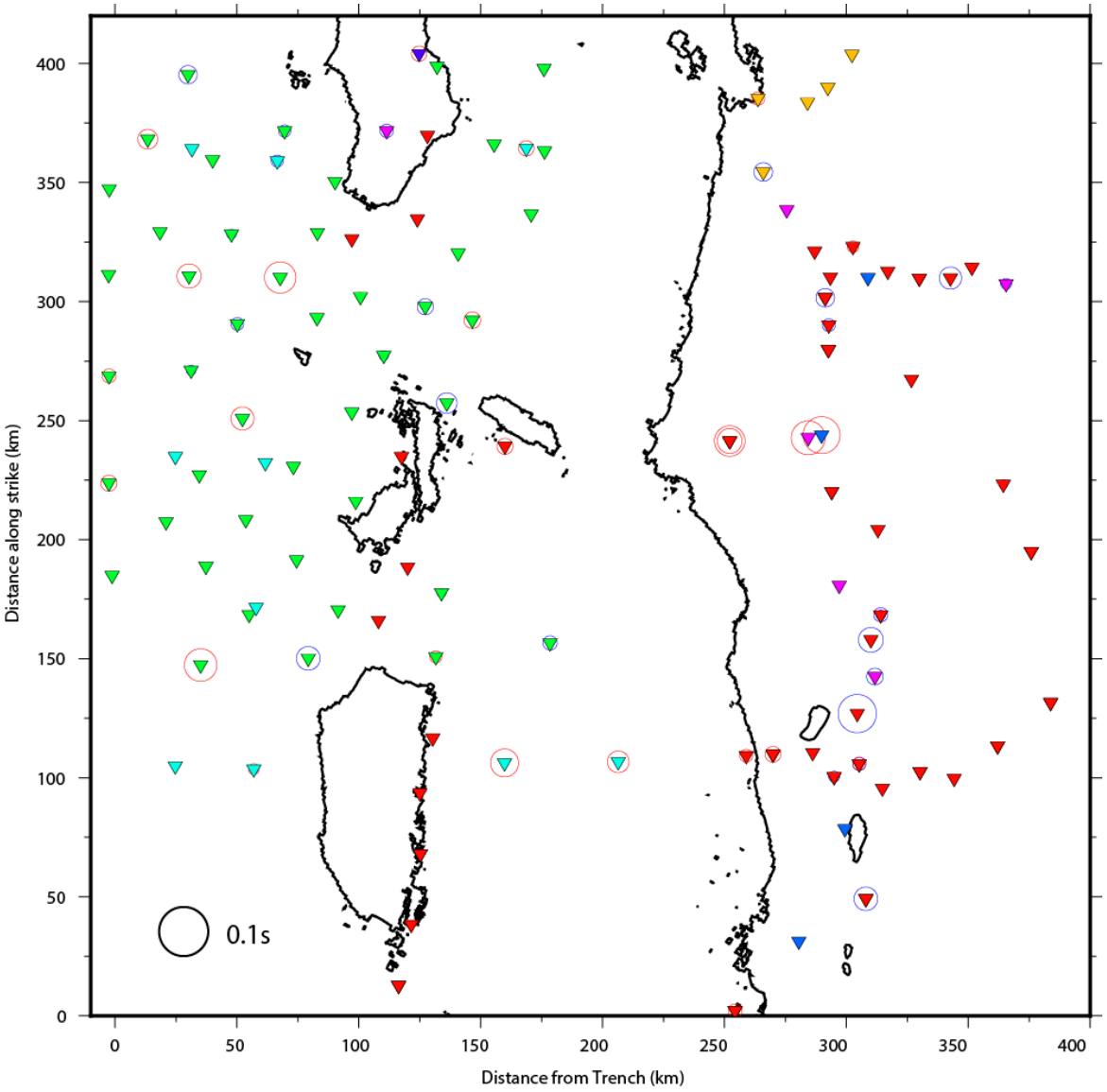


*Figure 5.7 The station correction for P wave arrivals used in the active source study. Red circles indicate a positive adjustment Blue Circles indicate a negative adjustment. The Black circle in the bottom left shows the scale of the circles. Inverted triangles represent stations and colours represent the station network as seen in Figure 5.2*

### 5.4.2 Checkerboard Tests

For the 2-D and 3-D final models standard checkerboard tests were conducted with a range of block sizes **Error! Reference source not found.** and **Error! Reference source not found.**. The finest resolvable scale within the models is shown in the checkerboard figures with block size set at

15x10X30 km in XYZ. The 2D model shows excellent resolution throughout the model space from the surface down to 50 km. The 3D tests show we have good resolution >175 km along strike for 50-230 km across strike. Areas <175 km along strike show no resolution within the accretionary domain due to the lack of shots present in the south of the model space (**Error! Reference source not found.**). We used the results obtained from the checkerboard to shade out parts of the final velocity model with low resolution. The water column is shaded out on all transects.

## 5.5 Results

**Error! Reference source not found.** shows the final results from the 2D model. The 2D inversion reduces the residuals from 1.2 s through the original model to 0.38 s. **Error! Reference source not found.** shows the 3D results, which reduce the residuals from 0.38 to 0.24 seconds. Final hypocenter errors were less than +/- 0.2 km for XYZ and 0.05 s for origin time (**Error! Reference source not found.**). Considering the inclusion of active source data we would have expected the final rms error to be lower as 0.24 s is poor for tomography studies containing active source. When looking at station correction terms (**Error! Reference source not found.**) we see that no station as significantly anomalous correction applied to it. When breaking down the rms of the local and active sources we see a clearer picture. The rms for the active sources shots was 0.11 seconds compared to the local source events that was 0.28 seconds. The weighting scheme used in the inversion has a local earthquake to active source ratio of 1:0.2. This means the final rms figure is heavily weighted to the local event residual, which has produced the observed large residual of 0.24 s. In addition, the coarseness of our model with respect to the sensitivity of the active source data may have limited our error reduction in the active source data set.

In our results we refer to the domain that encompasses the active accretionary wedge as the outer forearc and the domain between the landward edge of the forearc islands and the islands arc as the inner forearc. We define the Moho as the 7.5 km $s^{-1}$ contour. The plate interface is estimated from the SLAB 2.0 model.

### 5.5.1 Outer Forearc.

The region of velocities that encompasses the accretionary domain span from the trench to the landward edge of the forearc islands (175km). The new velocity models show that the accretionary wedge of central Sumatra has a velocity of ~2 km $s^{-1}$ at the surface increasing to a maximum of 6 km $s^{-1}$ at 20 km depth beneath the forearc Islands. The wedge thickens from 5 km at the trench to 20km beneath the forearc high where it abruptly stops and the velocity profile changes significantly underneath the inner forearc.

Hypocenters within the wedge are mainly located at the boundary between the wedge and the inner forearc. Looking at the wedge velocity profile beneath the forearc Islands compared to between the forearc Islands we see no significant difference in velocity structure along strike. Almost no events occur within the accretionary domain despite the large number of imbricated thrust faults within the

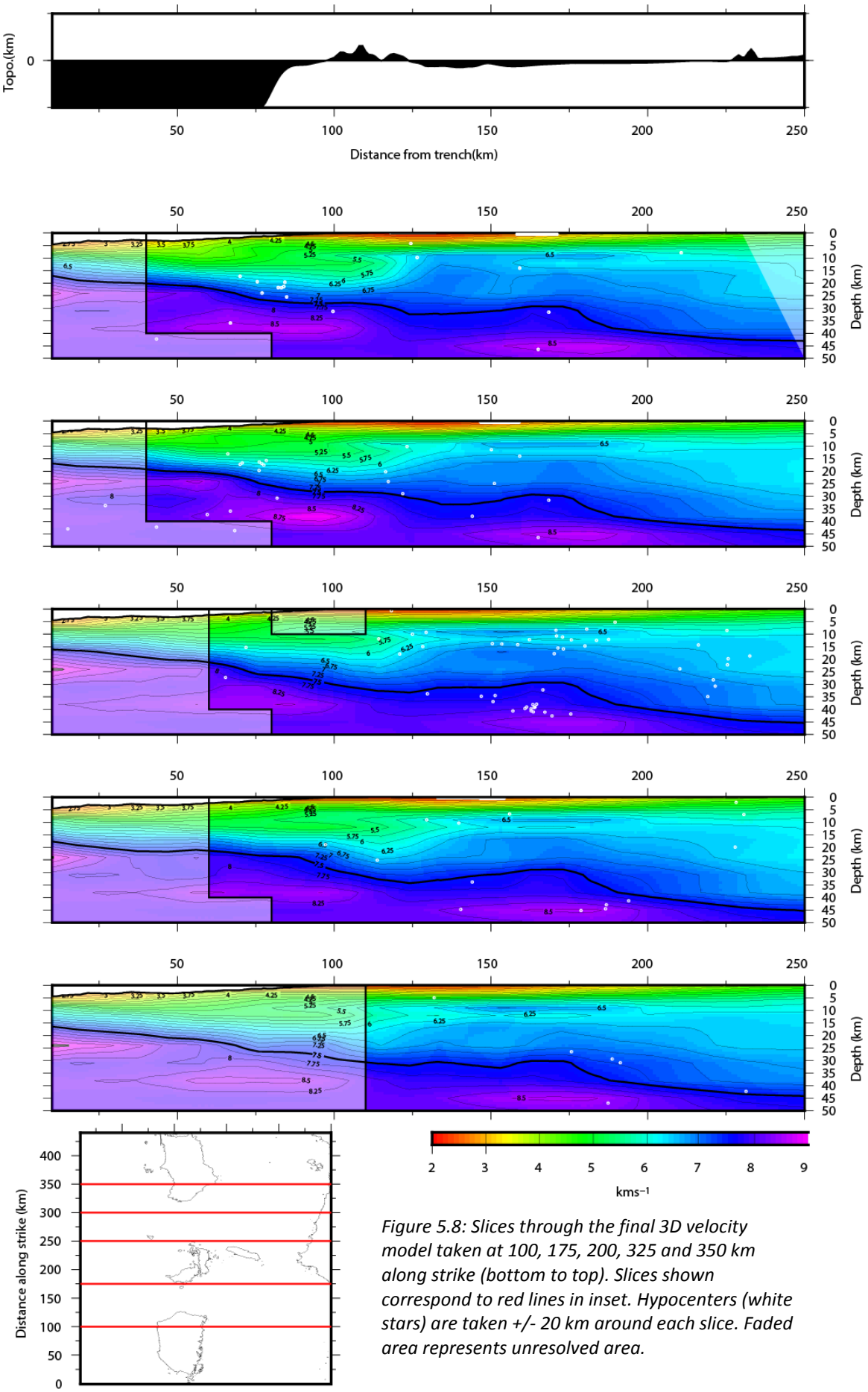


*Figure 5.8: Slices through the final 3D velocity model taken at 100, 175, 200, 325 and 350 km along strike (bottom to top). Slices shown correspond to red lines in inset. Hypocenters (white stars) are taken +/- 20 km around each slice. Faded area represents unresolved area.*

active prism in central Sumatra, some of which show morphological evidence of recent motion (Cook et al., 2014).

### 5.5.2 Inner Forearc

Velocities of 2 km $s^{-1}$ are observed in the shallow subsurface of the inner forearc (< 5 km) but end at the Sumatran coastline where shallow velocities increase to 5 km $s^{-1}$. Seismic reflection studies and industry borehole data show that the shallow subsurface of basins in the inner forearc is composed mainly of recent sediments (Moore et al., 1982; Karig et al., 1980).

At the boundary between the landward edge of the forearc islands and the inner forearc a clear change in velocity structure (>5 km) is observed. Higher velocities of >7 km $s^{-1}$ are observed at depths as shallow as 9 km. These shallow high velocities form a block that extends down to the oceanic Moho throughout the inner forearc. The high velocities of the inner forearc end at the coastline of Sumatra where the velocities at a similar depth decrease to ~6.5 km $s^{-1}$, typical of island arc crust. This suggests that the inner forearc has different composition from both the accretionary domain and the continental arc crust. Hypocenters are scattered within the inner forearc with events occurring on the boundary between the inner and outer forearc as well as within the inner forearc block. Within the forearc mantle wedge events are present on the plate interface as well as within the mantle wedge itself.

### 5.5.3 Subducting Oceanic Crust

We use the plate interface estimated from hypocenter distribution from chapter 2. We see that the shallow subducting slab has velocities of 6.5-7.5 km $s^{-1}$. We estimate the crust to be 5 km thick. We cannot distinguish between different sections of the subducting slab such as the crust and subducting lithosphere. We see events located around the plate interface. We see no along-strike variations in the magnitude or structure of the shallow down going oceanic crust. The smaller scale plate topography identified by Henstock et al. (2016) from seismic reflection data around the IFZ is below the lateral resolution of our 3D models.

### 5.5.4 Deep Hypocenters

Below the accretionary domain we observe the oceanic Moho (the 7.5 km $s^{-1}$ contour) at 15 km depth at the trench increasing to 30 km depth below the forearc Islands. Velocities below the oceanic Moho are 8-9 km $s^{-1}$. There are a significant number of hypocenters below the oceanic Moho at depths of 25-35 km. These events were initially at depths of 30-50 km, surprisingly deep, but have shallowed with the improved resolution velocity model of this study.

## 5.6 Discussion

### 5.6.1 Inclusion of Active source data

Including the active source data greatly increased the resolution of shallow structure (<20 km), as seen when comparing Figures 4.6 and 5.6. This has improved the model in several ways: 1) The inclusion of the active source data has decreased the size of the resolvable anomaly from 20 km down to 10 km. 2) The improved shallow structure resulted in more reasonable locations for several of the hypocenters beneath the incoming plate which I focus on later. 3) The station correction terms within the inversion are also reduced compared to the passive source inversion (**Error! Reference source not found.** and Figure 4.10), which is results from less trade-off with shallow structure underneath the stations.

### 5.6.2 Accretionary Wedge

A wedge of velocities observed at 2 km $s^{-1}$ at the surface increasing to 6 km $s^{-1}$ at 5 km depth at the trench thickening to a maximum depth of 20 km beneath the forearc high. This wedge shape is indicative of unconsolidated sediments at the surface becoming compacted and lithified at depth. Similar P velocity structure has been observed from other accretionary prisms elsewhere in Sumatra (Klingelhoefer et al., 2010; Shulgin et al., 2013; Tang et al., 2013) and around the world, such as Japan (Kita et al., 2012), Barbados (Bangs et al., 1990) and Makran (Kopp et al., 2000). We see no variation in the wedge velocity or structure along strike. Although seismic reflection studies (Cook et al., 2014; Moore et al., 1982, Karig et al., 1980; McNeill and Henstock, 2014; Schlüter et al., 2002; Singh et al., 2012) distinguish active and ancient accretionary wedges across strike, we see no resolvable difference in the seismic velocities.

We observe few to no earthquakes within the accretionary prism of Sumatra. A possible explanation is that events generated by faults within the prism are smaller than the lower magnitude limit of the dataset ~$M_w$ 3.0; (Lange et al., 2010). (Tilmann et al., 2010) looked at the aftershock seismicity of the 2004/2005 events to the north of the margin, and from the few events located within the prism itself they calculate that they have magnitudes <$M_w$ 3.0. Considering the location of the stations used in this study, focusing mostly on the forearc high region and the inner forearc, lower magnitude events within the accretionary toe are unlikely to be of high enough quality to be used within this study and discarded in the quality control stages.

### 5.6.3 Location of the Forearc Islands and Forearc Basins

Shallow low velocities in other forearc basins are similar to those we see here (e.g., Bangs et al., 1990; Zhao et al., 2007) and active source tomography studies from North Sumatra also report similar shallow low velocities (Singh et al., 2011; Tang et al., 2013). No along strike variation in shallow velocity structure of the inner forearc is observed. This was unexpected, as we would have expected the up to 5-10 km thick, rapidly deposited sediments of the forearc basins to have lower velocities extending to greater depths than the intervening shallow water (Moore et al., 1982). This may indicate that the velocities of the material within and between the basins is similar, or

alternatively that either our model does not have the resolution to distinguish between the materials of these regions, or perhaps because shots and stations are preferentially in the deeper water.

The lack of difference in velocity structure between where islands are present versus not suggests that the islands are not formed by material differences along strike. From checkerboard test we can resolve differences of up to 5% down to a scale of 20 km. This equates to a velocity difference of <0.25km $s^{-1}$ which is on the order of error of the models. This leaves several possibilities for the cause of the location of the islands. The orientation and structure of the backstop on which the accretionary domain builds up against can cause variations in uplift and subsidence along a subduction zone (Yamazaki and Okamura, 1989). Subducting topographic features can also play a role in the development of the accretionary domain (Yamazaki, 1989). But in Sumatra, forearc islands do not directly correlate with incoming topographic highs. Given the small elevation differences between islands and areas between islands, it is very likely that the processes behind this are undetectable by current tomography models. The presence of the islands is likely a combination of factors such as slightly varying composition, structure and uplift of the accretionary prism, incoming topographic features and geometry of the subducting plate interface, and across margin structures. Similar arguments can be made for the locations of the forearc basins but it is important to note the lack of difference in deeper velocity structure of the inner forearc where basins are present versus not.

### 5.6.4 Earthquake Hypocenter Distribution within the Oceanic Plate

We observe events 10 to 20 km beneath the oceanic Moho on the incoming plate. The formal errors on the hypocenters are <1km which is small, but even if the errors were similar to the hypocenter errors of 5-10 km observed in similar studies (e.g. Collings et al., 2012; Hicks et al., 2012) this still means they are deeper than the oceanic Moho. Qin and Singh, (2015) showed that reflections from faults within the incoming oceanic plate extend to depths of up to 50 km. Events seaward of the trench further to the north along the Sumatra margin have been observed with the largest being $M_w$ 8.6 occurring at a depth of 23 km, well below the oceanic Moho (Meng et al., 2012). This event was shown to be associated with an existing fracture zone, however the rupture pattern was complex. The authors inferred that the fracture zones at the surface must extend deep into the oceanic mantle. The events are most likely caused by these deep cutting faults extending into the mantle. The events observed in this study beneath the forearc suggest that the fracture zones remain active as they enter the subduction zone.

### 5.6.5 Comparison of Velocity Structure between Local and Active Source Models

**Error! Reference source not found.** shows the percentage change in velocity between the 2-D velocity models derived from the local and teleseismic inversion (Chapter 4) compared to the local and active source inversion (this Chapter). A large proportion of the difference between the two models comes from the shallow subsurface (less than 5 km) where we observe a 100% increase in velocity above Sumatra's accretionary domain. This increase means that the local/teleseismic inversion was predicting velocities that were 100% faster than derived from the active/local

inversion. Given the limited earthquake hypocenters within this shallow zone here the difference in shallow velocity structure is not unexpected. However, the velocities up to 30% slower in the accretionary domain are surprising as the majority of the wedge is located below 10 km depth where the passive source inversion should have good coverage to  determine velocity. The spatial extent of velocities anomalies associated with each structure, for example the wedge of low velocity material representing the accretionary wedge, have a similar spatial extent but considerable difference in velocity magnitude also resulting in falsely deep hypocenters from the passive source model. In the future the development of tomography models, using active source data to constrain the shallow subsurface, is imperative as the effect of not constraining the shallow sub-surface may be greater than previously assumed.

Comparing figure 5.7, 5.9 and **Error! Reference source not found.** we can assess the first order errors in the model. The station correction terms in figure 5.7 and 4.10 show that the change in shallow velocity structure has resulted in much smaller station corrections suggesting that the velocity model is better capturing the shallow velocity structure due to the inclusion of active source data. Errors on the hypocenters also mirror the trend showing that the inclusion of active source data has reduced the errors. Within the active source model the location error in X, Y and Z is 0.2km which suggests a pick error of 0.05 second within a velocity structure of 4km $s^{-1}$ (average of the top 20km of the model). The vast majority of the local P wave arrivals had a pick error of 0.01-0.05 second. Now the errors on the hypocenters are approaching the pick error. Changes in shallow velocity structure produce smaller error on the locations compared to the hypocenter centre errors detailed in section 4.4.6. The reduction in both hypocenter errors and station correction terms suggests that the inclusion of active source data is improving the model by better capturing the shallow surface structure.

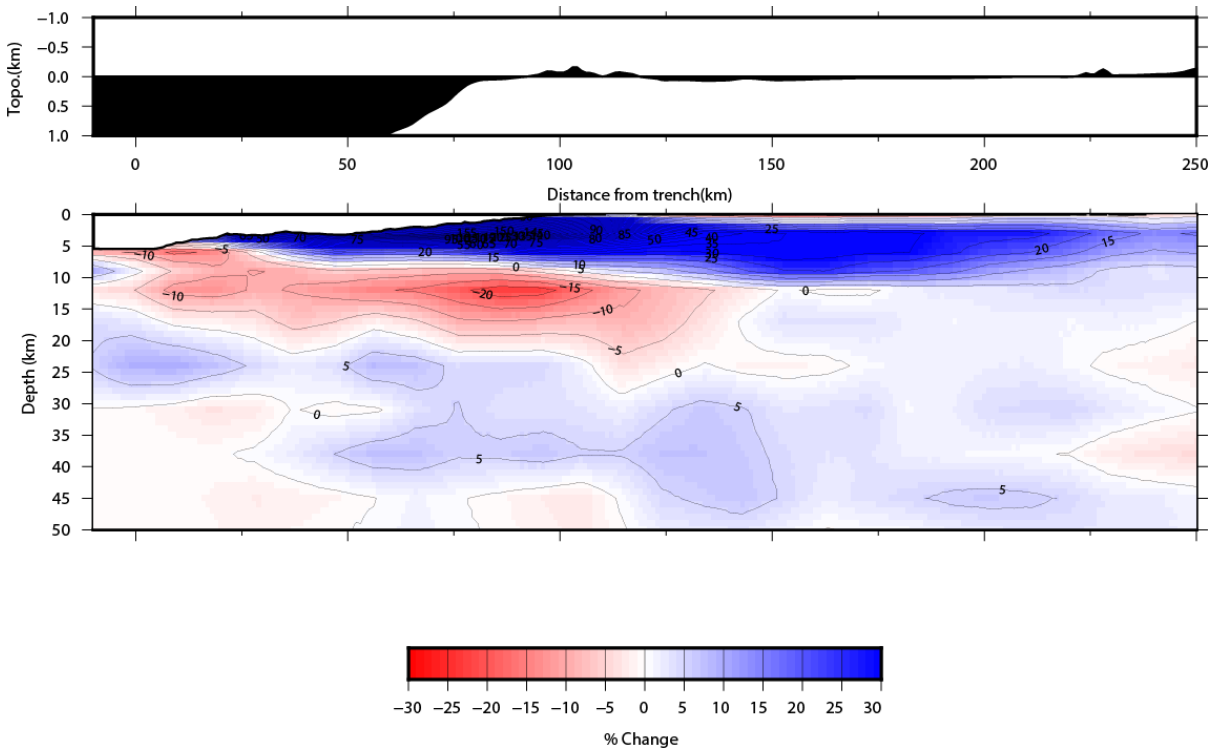


*Figure 5.9: Difference in the shallow forearc velocity of Sumatra between models derived from local/teleseismic joint inversion against local/active inversion. Negative infers that the active model is predicting slower velocities than the local/teleseismic model.*

### 5.6.6 Inner Forearc Block

The Moho beneath the inner forearc is at a depth of 25-30 km. Other studies, including Chapter 4, found similar depths for the inner forearc Moho. The Moho beneath the island of Sumatra is estimated to be between 35 and 40 km depth (Collings et al., 2012). The models presented in this chapter do not extend landward sufficiently to capture the full extent of the continental Moho, but the trend observed beneath the coastline suggests that the Moho increases from a depth of 25-30 km beneath the inner forearc to at least 40 km at the Sumatran coastline, compatible with the results of Collings et al. (2012) and Chapter 4.

The vertical boundary between the landward edge of the forearc Islands and the inner forearc has been noted by other studies along the margin (Diament et al., 1992; Karig et al, 1980; Kopp et al., 2001; Singh et al., 2011; Tang et al., 2013). Active reflection surveys spanning the forearc (Diament et al., 1992; Kieckhefer et al., 1980; Kopp et al., 2008; Schlüter et al., 2002), suggest that they are possibly two different geological units. This major intra-forearc fault, the Mentawai fault offshore central Sumatra and the West Andaman Fault offshore north Sumatra, is likely a transpressional structure potentially with varying lateral versus thrust components thought to accommodate a large amount of the oblique strain energy caused by the oblique subduction. It appears to mark the boundary between the accretionary domain and the inner forearc, thus a major structural boundary. Our models also show marked velocity structure change across this boundary as well as showing that the high velocity material beneath the inner forearc extends to the coastline of Sumatra where it ends. The across-strike velocity profile shows the inner forearc block is compositionally distinct from the accretionary domain and the Sumatran arc block. The inner forearc block likely acts as a backstop to the modern accretionary domain allowing the accretionary wedge to build up against it.

The composition of the inner forearc block has not previously been explained. Geological field studies from Nias Island show that there are ophiolitic materials within the inner forearc (Karig et al, 1980; Moore, 1980). The velocity structure of the bay of islands Ophiolite, Newfoundland, ranges from 5.7 km $s^{-1}$ at the top to 7.4 km $s^{-1}$ at the base (Salisbury and Christensen, 1978); similar velocity profiles have been reported from ophiolite complexes in Japan (Ogawa and Naka, 1984), the Great Valley (Godfrey et al., 1997), and Nicaragua (Walther et al., 2000). Based on velocity information alone the high velocity material could be mantle wedge material that has been intruded due to some spreading event in Sumatra's past. Spreading events are accompanied by faulting events within the newly developing crust. Refraction studies spanning the inner forearc (Kopp et al., 2001, 2003; Schlüter et al., 2002) show no evidence for any significant faulting activity within the inner forearc only at the landward edge of the forearc high. Based on these exhumed materials and our velocity models, we propose that the main geological unit between the accretionary domain and the mainland is an ophiolitic complex. Ophiolitic complexes within subduction zone forearcs have been observed in Japan (Hayman et al., 2012; Takashima et al., 2004), Alaska (Kusky and Young, 1999) and Barbados (Lepez et al., 2006), although in each case the emplacement and timing of emplacement is unique and/or difficult to discern. Many studies have suggested that ophiolites are emplaced during subduction zone initiation or the very early stages of subduction (Kusky and Young,

1999; Whattam, 2011). Ages estimated from the deepest deposited sediments are around the mid Eocene (Karig et al, 1980; Moore, 1980). Subduction has been known have been occurring as early as the Palaeocene/Early Eocene (Schlüter et al., 2002; Yu et al., 2013). The vertical boundary between the forearc islands and the inner forearc has been observed from velocity (Singh et al., 2011) and reflection (Singh et al., 2011) studies in the north of the margin and refraction studies (Kopp et al., 2001, 2003; Schlüter et al., 2002) in the south of the margin. From these studies it appears the anomaly is present along strike. Given this, we suggest that the ophiolitic complex may have been emplaced when subduction began in Sumatra or in its very early stages. **Error! Reference source not found.** shows our interpretation of the Sumatran forearc.

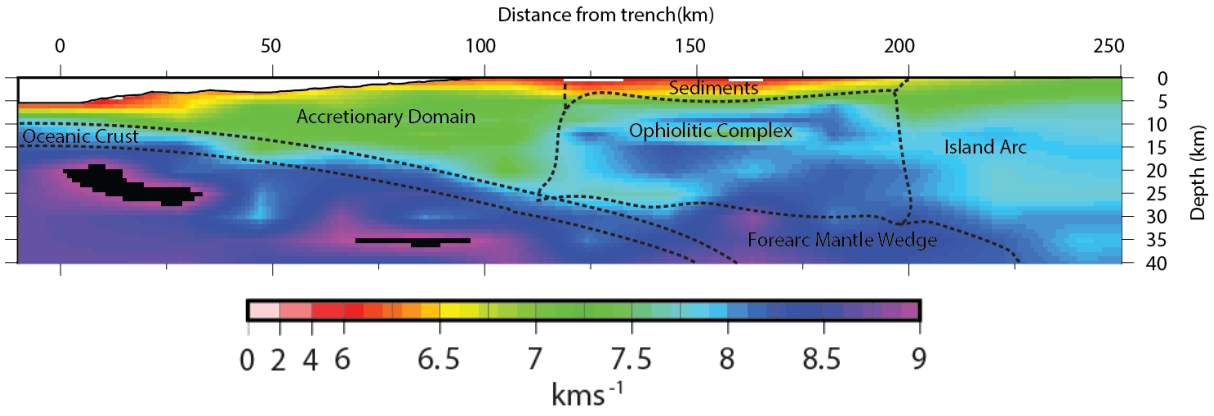


*Figure 5.10: Interpretation of velocity model obtained for the Sumatran forearc.*

## 5.7 Conclusions

From our modelling we have 3 main findings of the chapter:

1. Hypocenters observed beneath the oceanic Moho suggest that fractures and faults within the incoming plate extend down into the mantle and remain seismically active as they enter the subduction zone.
2. From comparison with velocities models from chapter 2 we find that local/teleseismic inversion overestimate the velocities of the accretionary wedge of Sumatra. A result of this is that events observed under the subducting plate within the oceanic mantle and located deeper in local/teleseismic models compared to local/active models.
3. The inner forearc offshore central Sumatra has significantly different composition from the accretionary domain to the west and the continental block to the east. There are high velocities of >7 km $s^{-1}$ at depths as shallow as 9 km within this block compared with 6 km $s^{-1}$ at each side, and the high velocities extend down to Moho. Given geological evidence from other studies we hypothesise that the material beneath the inner forearc of Sumatra is an ophiolitic complex. The seismic structure does not constrain when or how this ophiolitic complex was emplaced but suggest it was emplaced during the initiation of subduction within Sumatra.

# 6 Chapter 6: Segmentation of the Sumatra Subduction Zone

**Abstract**

Subduction zones are host to the largest earthquakes on the planet. Understanding the structure of subduction zones is key in being able to quantify likely rupture scenarios. In this work we propose a segmentation model for the Sumatran subduction zone using a *K*-means algorithm to analyse spatial patterns in seismicity between the major events. The Sumatra subduction zone is composed of 9 distinct seismological segments; segments range from 220 km to 1370 km long. The potential magnitude of the zone ranges from $M_w$ 9.4 in the north to $M_w$ 8.6 at the Sunda Strait, with potential magnitudes in central Sumatra of $M_w$ 8.7. Segment boundaries do not show a 1:1 correlation with incoming topographic highs and other structural variations, although structures such as the IFZ and Wharton fossil ridge both have strong segment boundaries associated with them. The segment model we present here suggests two likely rupture patterns for the Mentawai islands, either a single segment rupture or a multi-segment rupture with each able to produce a $M_w$ ~9.0 event. This has large implications for hazard potential of the Mentawai segment of the Sumatra subduction zone.

## 6.1 Introduction

Subduction zone plate boundaries and other long/large fault systems are known to be segmented, that is large earthquakes break only a part of the fault boundary along-strike in a way that is repeatable between different events. The Sunda margin, primarily offshore Sumatra (**Error! Reference source not found.**), exhibits a repeating nature in some parts of the margin, with $M_w$ >8.0 earthquakes rupturing the same region every ~200 years (Sieh et al., 2008), such as the 2005 $M_w$ 8.7 and 1861 $M_w$ 8.5 event offshore Central Sumatra (**Error! Reference source not found.**). Seismic cycles simulating this behaviour have been proposed at other subduction zones, e.g., on the southern Kuril trench the 1843 and 1894 $M_w$>8.0 resembled those of 1952 and 1973 (Atwater et al., 2004). The Maule 2010 $M_w$ 8.8 is thought to mirror the 1835 $M_w$ ~8.5 offshore central Chile (Vigny et al., 2011). Given the probable repeating nature of large events and longevity of some rupture boundaries, this implies that features within the subduction zone (upper or lower plate) control rupture propagation.

Controls on individual earthquakes have been examined for many of the great subduction events. Subducting topographic features are often proposed to control great rupture patterns (Wang and Bilek., 2011). Results from Ecuador show that the subducting Carnegie ridge was the cause of the southern termination point of the 1979 Ms 7.7 event (Kanamori and McNally, 1982). Recent/historic events in Sumatra also suggest that topographic highs limit rupture potential. The 2005 Nias $M_w$ 8.7 southern termination point was caused by the subduction of topography formed from the Wharton Spreading Ridge and Investigator fracture zone (IFZ) (Henstock et al.,, 2016; **Error! Reference source not found.**). The estimated rupture extent of the 1861 (Newcomb and McCann, 1987) and 1797 (Natawidjaja et al., 2006) events also terminate in close proximity to the Wharton Ridge/IFZ. The

Chilean Maule $M_w$ 8.8 2010 event was shown to ignore certain incoming topographic features and instead was proposed to be controlled by a

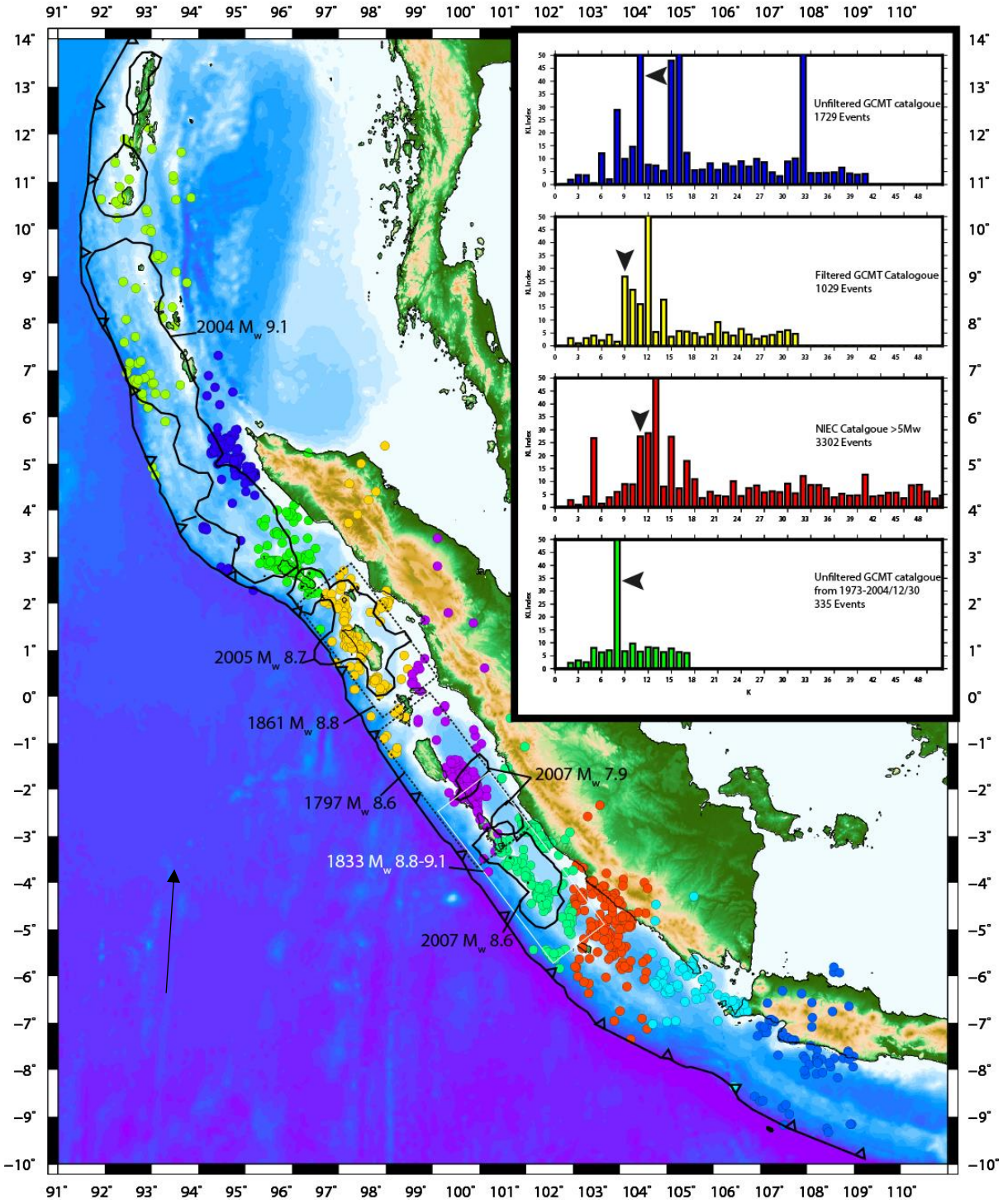


*Figure 6.1 Earthquake clusters along the Sumatran seismogenic interface. Each cluster is coloured differently. Cluster distribution identified using a* K-*means algorithm. The is the global optimum solution, with 9 clusters best representing seismogenic interface seismicity. Ruptures for the 1797 (white dashed box) and 1833 (black dashed box) (Natawidjaja et al., 2006), 1861 (black dashed box) (Newcomb and McCann 1987), 2007a and 2007b (Konca et al., 2008), 2004 (Lay et al., 2005) and 2005 (Briggs et al., 2006) earthquakes are shown. The black arrow indicates convergence direction. Inset (top right) shows the KL index results from the chosen model*

*(yellow) and 3 other models based on different catalogues, black arrows indicate chosen models for each subset (Figure 6.2).*

combination of the down-going plate geometry and strain energy accumulated over multiple seismic cycles (Moreno et al., 2012), yet the northern termination of the rupture was likely controlled by the Juan Fernandez ridge (Sparkes et al., 2010). The geometry of the subducting plate elsewhere has been proposed as the reason for the limits of ruptures in Japan (Ito et al., 2005), Cascadia (Hyndman et al., 1995; Crosson et al., 1987) and Chile (Moreno et al., 2011).

Currently the controls on what influences subduction zone events are not fully understood, with large ruptures showing conflicting reports of being controlled by certain topographic highs while ignoring others (Sparkes et al., 2010; Wang and Bilek, 2011). Without the presence of large ruptures identifying barriers and controls on rupture patterns, determining the extent of future great events is almost impossible. This situation has significant implications for seismic risk posed by a subduction zone.

A technique that has proved effective at identifying clustering of earthquakes in a dataset is a *K*-means algorithm (Burton and Hall, 2014; Weatherill and Burton, 2009). Burton and Hall, (2014) use this method to identify segments of the strike-slip Great Sumatran Fault (GSF) and from that infer segment boundaries  and maximum credible magnitudes . Burton and Hall, (2014) found good agreement between their cluster boundaries and the segment boundaries identified through geological field studies (Sieh and Natawidjaja, 2000) and with historic and recent ruptures, showing that the boundaries identified are long-term controls on rupture propagation.

Seismicity along major, strike-slip onshore faults such as the GSF, San Andreas fault (SAF) and North Anatolian fault (NAF) exhibits strong clustering behaviour both generally and also within aftershock sequences. Segments of the GSF identified from geological fieldwork are primarily controlled by geological stepovers (Sieh and Natawidjaja, 2000), but Burton and Hall (2014) showed that not all of these segments correlate with seismicity clustering along the fault. In general where they had a seismicity cluster boundary there was a correlating geological boundary, however, some geological boundaries (<20%) did not seem influential in the cluster model. These geological boundaries also had earthquakes rupturing across them whereas no previous ruptures have broken the boundaries from the Burton and Hall, (2014) cluster model. Work done on the rupture styles of subduction zones shows that the seismogenic interface is often segmented and will rupture in discreet repeatable patches. Less work has been conducted on seismicity clustering and its relation to overall rupture controls within a zone. In this work we apply a *K*-means algorithm to identify clusters on the interface of the Sumatran/Sunda subduction zone. We explore the implications for potential boundaries of major ruptures and the associated maximum credible magnitudes.

## 6.2 Method

We use a *K*-means algorithm (Burton and Hall, 2014; Hartigan and Wong, 1979; Weatherill and Burton, 2009) to identify clusters in seismicity along the Sumatran subduction zone. The *K*-means algorithm (Hartigan, 1979) has 5 major steps.

- *K* random centroids are seeded throughout the region.
- Each earthquake is assigned to their nearest centroid making an initial cluster.
- The centroids are moved to the centre of the new cluster.
- Steps 2-3 are repeated until no elements change cluster or a maximum number of times the centroid is allowed to move is reached, in this case 100 movements.
- Once no elements are reassigned or the centroid has moved 100 times it is assumed that the optimum for the *K* clusters is reached.

Figure S 8.11 outlines steps 1-5

The *K*-means algorithm finds the optimum arrangement for *K* clusters by minimising the sum of squared distances between events within a cluster and the centroid for that cluster, measured by the Total within cluster sum of the squares (**Error! Reference source not found.**).

$$TWCSS = \sum_{i=1}^{N} \sum_{K=1}^{K} I\left(x_i \in C_k\right) \parallel x_i - m_k \parallel^2 \qquad \textit{Eq. 6.1}$$

Where N is the total number of earthquake locations, *K* the cluster number, xi the location of earthquake i, $m_k$ is the mean position of Cluster Ck and I(X) is 1 if statement X is true, otherwise 0. When clustering in Euclidean space, and using Euclidean square distance as the metric, the mean of the data points (xi) in cluster Ck is calculated by:

$$\overline{x} = \frac{\sum_{i=1}^{T} x_i}{T} \qquad \textit{Eq. 6.2}$$

Where *T* is the number of events within the cluster. This would be the new centroid location, $m_k$, of cluster $C_k$. However, if each point is associated with a weighting ($W_i$), the centroid becomes:

$$\overline{x} = \frac{\sum_{i=1}^{T} w_i \, x_i}{\sum_{i=1}^{T} w_i} \qquad \textit{Eq. 6.3}$$

The weighting is a linear scale based on the moment magnitude of an event. This modification will pull the cluster centroid towards the location of the largest magnitude events in the catalogue.

Given the random nature of seeding the centroids, it has proved crucial for multiple runs to be conducted to produce a true global optimum for the dataset (Burton and Hall, 2014). In this case we chose to conduct 1000 repeats for each value of *K* investigated. Certain datasets cause the algorithm to enter an infinite loop whereby 1 or 2 elements on the boundaries between two clusters will

change between the two clusters indefinitely. It is assumed that by 100 iterations for cluster model K the algorithm has found the optimum arrangement. We place an upper limit on the number of centroids to investigate ($K_{max}$) as the square root of the number of data, *N*, within the dataset. In previous research this has proved to be a useful guideline as well as being adopted by other studies (Burton and Hall, 2014; Ansari et al., 2015). This process is repeated for all 2:$K_{max}$ clusters.

To determine *K*'s that produce a good fit for the data and warrant closer inspection we use a Krzanowski and Lai (1988) (KL) index to identify optimal *K*. The *KL* index assesses the successive variances (Figure S 8.12 Explanations of how the KL index is calculated based on a K cluster modelFigure S 8.12) of the clusters as *K* increases from 2: *K*=N where N is the number of data in the dataset. Explicitly the KL index for a given *K* is:

$$\mathrm{KL} = \frac{(K-1)^{\frac{2}{d}} WK_{k-1} K^{2/d} WK_K}{K^{\frac{2}{d}} WK_k (K+1)^{2/d} WK_{(K+1)}} \qquad \textit{Eq. 6.4}$$

Where d refers to the dimensions of the data, $WK_K$ are the pooled within-cluster sum of the squares or *K, K*-1 and *K*+1 respectively. For purely random data, every additional *K* decreases the standard deviation and variance of the data by a factor of *g* and *g^2* respectively. For purely random data this is a linear relationship as *K* increases, the model variance decreases by a factor of g^2 (Krawiski and Lai, 1988). For data that has an optimum number of groups the relationship is exponential and the factor g^2 does not decrease at a linear rate, instead decreasing at an exponential rate. The bend in the exponential curve is taken as optimum *K* (Krzanowski and Lai, 1988) ; Figure S 8.12). A given dataset may have several *K* values that are linked with significantly reduced variances (Figure S 8.12). Any *KL* value that is more than 2 standard deviations away from the mean KL should be inspected.

Burton and Hall (2014) chose the optimum model for *K* centroids as the model that produced the highest *KL* index out of the *X* repeats. Although this criterion produces stable results it gives no information about the uncertainty of the solution. In this study we improve the robustness and demonstrate the uncertainty in the optimum cluster arrangement using a probability density function approach. From the 1000 realisations of the model with *K* clusters, we generate a probability density (PD) of the *K*x1000 centroids and take the highest *K* peaks in the region as the preferred optimum centroid location for the dataset for *K* clusters (**Error! Reference source not found.**). Since it is unlikely that a model will produce a centroid arrangement that is in the exact same place as the preferred *K* peaks in the PD plot, we use the *K* peaks in the PD and find the model that has the *K* centroid positions closest to the preferred *K* peaks and chose that as our optimum model for *K* clusters. In practice, the average distance between the *K* preferred peaks and the optimum *K* centroid model was <5 km. This method proved most stable producing models for *K* clusters that are identical between separate model runs.

Different catalogues will be located through different methods such as a local tomography study that derives velocity and locations for a region such as shown in Chapter 4 and compared with a teleseismic study which locates events based on a teleseismic network (e.g., Tillman et al., 2010). To

combat this difference in location methodology between and within certain datasets, we run serval different datasets and only take features that are present in all of them for the optimum model.

## 6.3 Data

We start with the National Earthquake Information Center (NEIC; http://earthquake.usgs.gov/contactus/golden/neic.php) catalogue and limit it to 12°N-12°S and 92°E-103°E for 1973-01-01 to 2016-01-25. Events from the pre-instrumental record were not included as they can bias the algorithm with high magnitudes and poor locations. The data were homogenised to the moment magnitude ($M_w$) scale using equations 6.5-6.7 (Scordilis, 2006).

$$M_w = 0.67M_s + 2.07 \quad 3 \leq M_s \leq 6.1 \qquad \textit{Eq. 6.5}$$

$$M_w = 0.99M_s + 0.08 \quad 6.2 \leq M_s \leq 8.2 \qquad \textit{Eq. 6.6}$$

$$M_w = 0.85M_b + 1.03 \qquad \textit{Eq. 6.7}$$

The original unfiltered NEIC catalogue had ~15000 events. The algorithm struggled to converge to a true global optimum producing KL indices <20 for the investigated K range 1<K<122 because the dataset contains a mix of earthquake types. Burton and Hall (2014) commented on this apparent complexity when studying the Sumatran fault and concluded that careful filtering of data is paramount. It is possible that a dataset containing a complete seismic cycle could be stably analysed. However even then it is possible to have multiple source structures at different depths for any surface location. Currently, given the amount of data available for the Sumatra subduction zone, there are not enough events to distinguish between sources at different depths. An example of this is that, in preliminary models, clusters were being identified as including events from both the subducting interface and the overlying Great Sumatran fault. From this it became clear that we needed to focus the aims of this study as it was not yet possible to distinguish between first-order sources at varying depths most likely due to a lack of data.

We focused our approach on clustering events on the seismogenic interface of the Sumatra subduction zone. Previous studies (Burton and Hall, 2014) have noted that the earthquake catalogue used in *K*-means studies must be filtered to eliminate any bias that can be caused by artificially lowering the Total within cluster sum of the squares (TWCSS). The three main sources of bias that affect the *K*-means algorithm are spatial and temporal windows for the dataset and source type. Fundamental factors that cause the dataset to have a varying magnitude of completeness, include

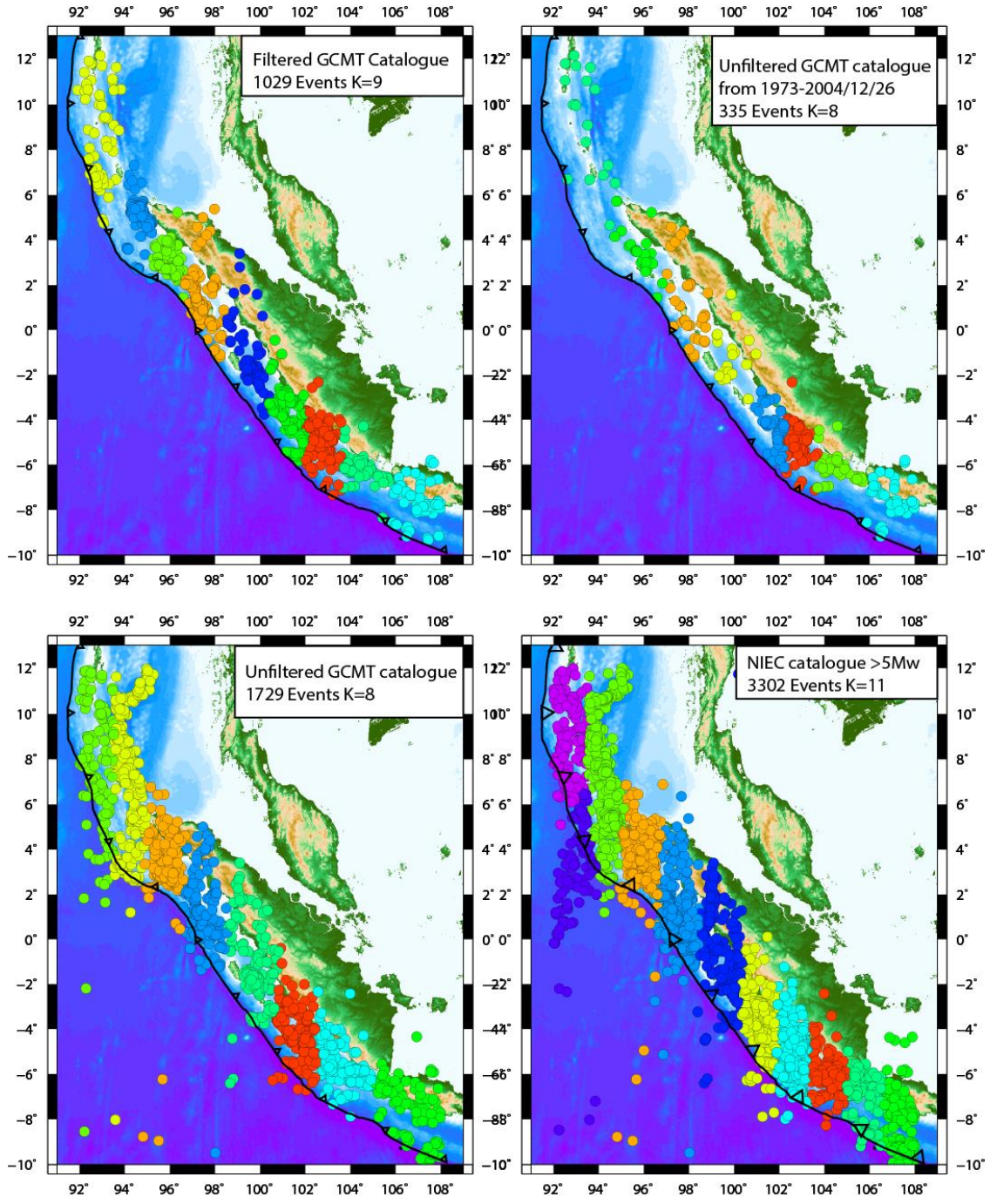


*Figure 6.2 Optimum cluster models for subsets 6 (top right), 7 (top left), 4 (bottom right) and 2 (bottom left) from table 6.1. Individual clusters have different colors.*

data from the aftershocks of a large event or data from our local temporary network. The difference in magnitude of completeness across an area causes over fitting of parameters and generates a false global optimum (Burton and Hall, 2014). We set a lower magnitude limit on all datasets to $M_w$ 5. The magnitude threshold was to make sure we had no over-fitting of clusters due to a varying magnitude of completeness, as we believe all events greater than magnitude 5 that have occurred along the Sumatra subduction zone have been recorded since the start date of the catalogue.

We constructed a second catalogue based on the Global centroid moment tensor (GCMT; http://www.globalcmt.org/CMTsearch.html) catalogue using the same spatial, temporal and magnitude limitations as the NEIC catalogue. Using the GCMT catalogue we limit our catalogue to thrust events only and, given the magnitude limitations already in place, we were confident that a high proportion of these events within the GCMT catalogue occurred on the subduction interface.

We also generated a sub-catalogue from each dataset for events prior to 2004/12/25 to test bias due to aftershock seismicity from recent large events. From the two base catalogues (NEIC and GCMT, with spatial, temporal and magnitude limitations applied), we analysed 7 sub-catalogues (Table 6.1) with 335-5432 events. All sub-catalogues identified optimum cluster models in the *K* range of 9-11 and had comparable cluster geometries. Table 6.1 shows the breakdown of the 7 sub-catalogues used in this study which all converge to similar optimum *K* ranges.

## 6.4 Results

| **Subset** | **Data Source** | **Number of Events** | **Filters** | | | **Mean KL** | **SD KL** | **Optimum K** | **KL cutoff** |
|---|---|---|---|---|---|---|---|---|---|
| | | | Thrust Event | Seaward of the trench | Pre-2004 | | | | |
| 1 | NEIC(ALL) | 5432 | | | | 8.25 | 8.42 | 5,11,12,13 | 24 |
| 2 | NEIC | 3315 | | ■ | | 8.17 | 8.25 | 5,9,15 | 25 |
| 3 | NEIC | 2021 | | ■ | ■ | 7.97 | 8.25 | 3,8,9,24 | 25 |
| 4 | GCMT(ALL) | 1748 | | | | 8.21 | 14.37 | 9,11,31 | 38 |
| 5 | GCMT | 1342 | ■ | | | 8.19 | 10.16 | 8,9,15 | 29 |
| 6 | GCMT | 1079 | ■ | ■ | | 4.3 | 9.20 | 9,10,11,12 | 22 |
| 7 | GCMT | 335 | ■ | ■ | ■ | 2.55 | 7.29 | 8 | 17 |
| **Average** | | | | | | 5.83 | 9.8 | 9-11 | >30 |

*Table 6.1. Summary of the catalogues used in the analysis. All subsets had the initial magnitude limitations for the spatial and temporal dimensions stated in section 6.3. For each of the subsets (1-7), the data source, number of events within the subset and the filters applied are shown, a black box indicates an applied filter to the subset. There were three possible filters, filtering the subset for thrust events (GMCT only), for events seaward of the trench, and for events pre-2004. The mean KL value for the 2: K clusters achieved standard deviation (SD) in the KL index across the 2: K clusters. The KL cut-off value is the value of which the cluster models achieving less than that score can be ignored.*

### 6.4.1 Chosen Model

We chose the model from the GCMT dataset filtered for thrust events landward of the trench (Table 6.1**Error! Reference source not found.** subset 6) as our final model for the Sumatra subduction zone. We chose the optimum clusters for the zone as K = 9. We will now discuss similarities and differences between the results as well as

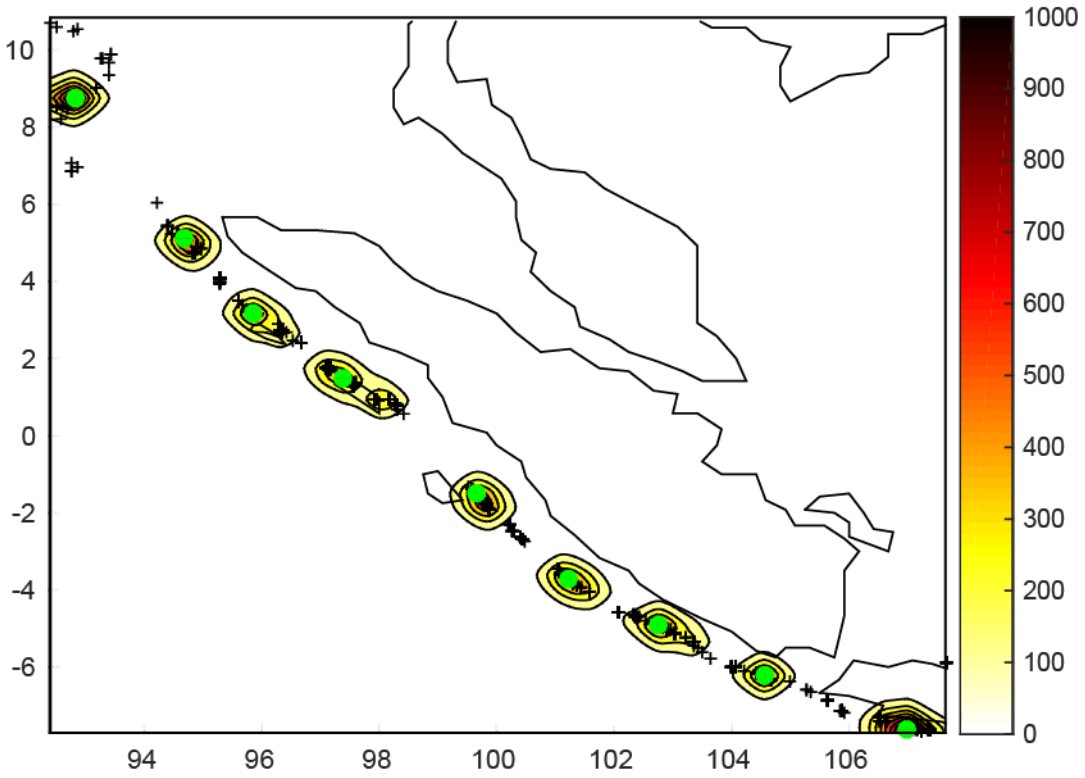


*Figure 6.3 Probability Density Function centroid method. Green dots represent location of the 9 centroids in the chosen cluster model. PDF functions for the 9000 possible centroids from the chosen K=9 model. White means no clusters out of the 1000 models were located there, black means 1000 centroids were located there. Black crosses represent the 9000 centroid locations.*

how we arrived at the conclusion that the GCMT dataset provided the best model for representation of the subduction interface.

### 6.4.2 Common K Ranges

A common K range is a range of K where optimum K values are identified in all sub-catalogues. *K* values exceeding the cutoff (Table 6.1) were found in the range of K=8-13 across all sub-catalogues. The cutoff value is the value at which a KL index is assumed to have not been achieved by chance, in this case the cutoff value is ~30. Only K values that are identified within this range warranted closer inspection as values outside this range were not present in a majority of the datasets.

### 6.4.3 Optimum K Range

**Error! Reference source not found.** shows the KL indices from the 4 datasets (see also **Error! Reference source not found.** for the optimum arrangement of the 4 datasets). The mean KL achieved across 4000 runs (4x1000 repeats) is 8.47 with a standard deviation of 9.8. Any KL value below ~30 does not warrant closer inspection as a value that low can be attributed to random noise. There is a common *K* range amongst all models for a global optimum of *K* between 8-13. The varying number of events between the datasets causes minor differences between the models for optimum *K*. For example, in the complete GCMT catalogue events seaward of the trench are included and identified as an independent cluster. Similarly, when including events with depths greater than 50 km some are identified as a separate cluster. From our results a common pattern is seismicity in the region of the subduction interface split into 8-9 clusters.

### 6.4.4 NEIC Data Sets

Sub-catalogues created from the NEIC dataset identify 4 possible *K* numbers as a global optimum model: *K*=5, 11, 12, 13. We can exclude *K*=5 as it does not fall within the *K* range of 8-13. **Error! Reference source not found.** shows the optimum arrangement for the *K*=11 cluster model based on the PD (Probability Density **Error! Reference source not found.**) method, the sub-catalogue used to generate this model is NEIC 2. The mean KL achieved for ensemble analysis of 2:58 cluster models is 8.25 with a standard deviation of 8.42. Other variations of the NEIC dataset not shown here also produced optimum values in the identified *K* range. Although the NEIC dataset contains seismicity from a wide range of faults, it still produced cluster models of the subduction zone similar to the GCMT dataset.

### 6.4.5 GCMT Data Sets

For the GCMT datasets, optimum *K* for the seismogenic zone (subduction interface) corresponds to 9-11 clusters, and was much more precise than for the NEIC datasets (K range of 8-13). The reason the GCMT had a smaller optimum K range is because the two GCMT datasets are more heavily biased towards interface events as it allows for filtering of not only magnitude but also event type. Whether the optimum is 9, 10 or 11 comes from variability in the 2004 rupture region. Cluster fitting in the 2004 rupture area mainly generates either 2 or 3 clusters. We believe 3 clusters best represents the seismogenic interface of this region. Previous studies conducted on the 2004 rupture show that the rupture process broadly split into three different sections (Ammon et al., 2005; Lay et al., 2005) also supported by results from analysing the aftershock seismicity which identified three separate clusters within the 2004 rupture zone.

### 6.4.6 Trends within Model Results

From all models the orientation of boundaries between clusters appears to be sub-parallel to the direction of convergence and not perpendicular the margin strike. This is particularly apparent in the larger datasets, e.g., the NEIC catalogue (**Error! Reference source not found.**), and remains in models with events seaward of the trench. The trend only disappeared with inclusion of earthquakes deeper than 60 km.

The along-strike location of many cluster boundaries was also similar between models. Boundaries south of the 2004/2005 rupture boundary at Simeulue are almost identical between all models. The 2004 rupture domain contained the most variability in the location of boundaries. Although the southernmost cluster within the 2004 rupture domain (green cluster) routinely placed the cluster boundary off the southeast coast of Simeulue, this contradicts what is currently believed about the southern termination point of the 2004 rupture domain, with the 2004 (and 2005) rupture ending at the much studied Simeulue saddle (Meltzner et al., 2010, 2012, 2015). In general, the 2004 clustering agrees well with what is known about the 2004 event in terms of rupture propagation (Ammon et al., 2005; Ishii et al., 2005) and aftershock seismicity (Lay et al., 2005).

For <20% of the models, there was variability in cluster numbers (1 versus 2) around Enggano island (**Error! Reference source not found.**, 5°S-7°S, teal cluster). This variability is caused by a slight smearing of the density function generating one very dominant peak and then a smaller secondary peak (Figure 6.3**Error! Reference source not found.**). Given the weakness of the secondary peak, our preferred model is 1 cluster in this region.

### 6.4.7 Tessellation into segment zones

Having established optimum cluster centroids, a Voronoi tessellation (VT) algorithm develops the clusters into a geometrical zonation and segmentation model. VT decomposes a metric space determined by distances to a specified discrete set of objects in the space; in our case, the points are cluster centroids. Tessellation constructs a polygon around each cluster, and VT interpolates between centroids so that adjacent clusters share one side. Segment length is assumed to be the part of the trench that is within each tessellated zone. Segment length is taken as synonymous with potential rupture length.

## 6.5 Discussion

### 6.5.1 Segment Boundary Locations and Relationships to Historic/Recent Ruptures.

#### 6.5.1.1 2004 Rupture Zone –Light Green, Dark Blue, Green

Two boundaries are identified within the 2004 rupture zone at 3.5N and 2N. The 2004 rupture propagation (Lay et al., 2005) and aftershock seismicity also suggest a multi-segment rupture. The 2004 earthquake ruptured in 3 distinct phases/sections with minimum slip and a slow rupture at 2 boundaries within the 2004 domain (Lay et al., 2005), 1) just South of the Nicobar Islands and 2)

between the Andaman Islands and the Nicobar Islands. The boundary just South of the Nicobar Islands agrees well with our cluster model (boundary between light green/dark blue cluster). Our model does not identify a cluster boundary between the Andaman and Nicobar islands and instead places 1 cluster for the whole region compared to 2 segments proposed by Lay et al. (2005). Our model instead places a further boundary between the Nicobar Islands and northern Sumatra which is not documented in the rupture process (dark blue/green cluster). Still, both datasets and methods agree on a three cluster arrangement for the region.

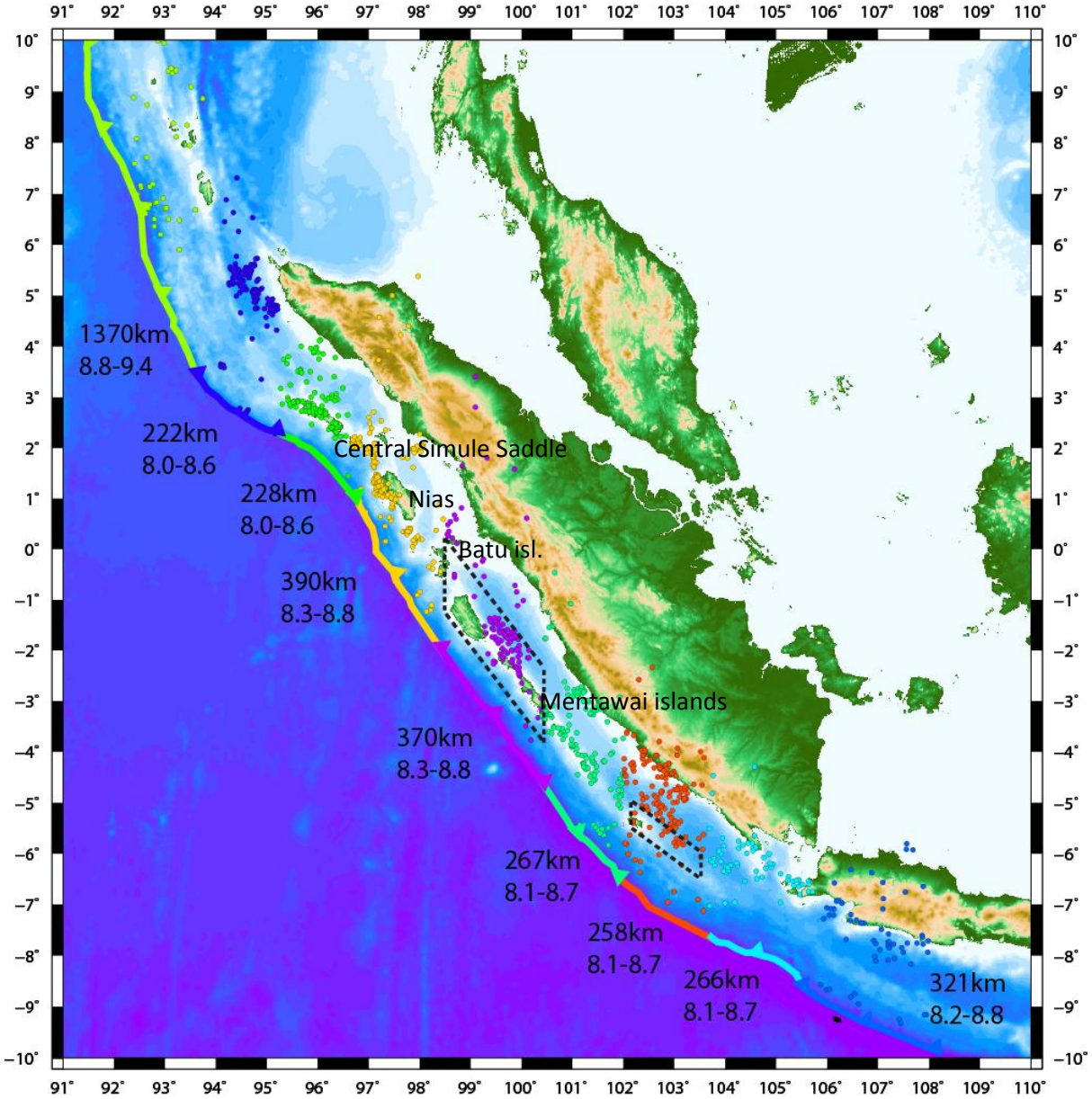


*Figure 6.4 Segmentation model of the Sumatra seismogenic interface based on the cluster model for K=9 for the filtered GCMT catalogue. Hypocenter colour is based on cluster number. Segment length and estimated magnitude is labelled next to each segment. Segment length (in km) is calculated from the deformation front proximal to the cluster centroid. Black dashed boxes represent a rupture width of 200 km (purple cluster) and 50 km (red cluster).*

#### 6.5.1.2 2005 Rupture Zone – Yellow

Two segment boundaries mark the northern and southern termination of the 2005 and the 1861 events. The northern boundary at 2°N is located where the 97°E fracture zone subducts and the boundary at 0°N is located where the Wharton ridge/IFZ subducts. Walker et al. (2005) suggested that the 2005 event had two distinct phases of rupture, the first from 0-50 seconds ruptured to the north (green cluster at 2.5 °N), while the second 50-120 s of the rupture propagated to the south rupturing the entirety of the yellow cluster. We propose there may be a segment boundary here that was ruptured during both 1861 and 2005. In contrast, the boundary between the yellow and purple clusters (at the Batu Islands, southern termination of the 2005 and 1861 events) appears to more strongly affect rupture and is proposed to be caused by the subducting Wharton ridge (Henstock et al., 2016).

The only point of contention within the model is the boundary close to Simeulue Island and the 2004/2005 earthquake rupture boundary (observed seismologically and from recorded coseismic uplift/subsidence patterns of corals). The Central Simeulue saddle has been shown to be a persistent barrier to rupture through time (Meltzner et al., 2010, 2012, 2015). Our model however places a boundary ~50km southeast of Simeulue and not on the island itself. One possible explanation is that the 3 seismic cycles from coral vertical motion data may not be representative of longer term patterns (Meltzner et al., 2010). Alternatively, a complex zone may exist around Simeulue, for example smaller ruptures (2002, 2008, 2010), $M_w$ 7's) have occurred at Simeulue itself crossing the saddle boundary (DeShon et al., 2005).

#### 6.5.1.3 1799/1833 Rupture Zones – Purple and Green

The boundaries at 5.5°S and 7°S (southern ends of the purple and green clusters) separate two clusters at the Mentawai and Siberut islands and northern Enggano island. Two notable ruptures have occurred here since 1973, both in 2007, the $M_w$ 7.9 and 8.6 events (Konca et al., 2008). The 2007 $M_w$ 8.6 event completely ruptured the northern Enggano island cluster (green) and the $M_w$ 7.9 involved partial rupture of both clusters (purple and green). There are no notable subducting topographic features to explain the inferred segment boundaries here. The historic 1797 and 1833 earthquakes in this area will be discussed separately (Section 6.5.3).

#### 6.5.1.4 Southern Sumatra Clusters and Boundaries – Red, Light Blue and Blue

South of the 2007 $M_w$ 8.6 rupture region, two proposed segment boundaries are identified at 6°S and 7°S separating clusters. Due to the lack of tectonic features in the area it is hard to identify geological control of these boundaries. There has only been one minor rupture in this location in 2000 (Abercrombie et al., 2003) and it appeared to partially rupture the red cluster only.

### 6.5.2 Potential Earthquake Magnitude of Segment Ruptures

From the chosen cluster model (**Error! Reference source not found.**) we calculate the length of each segment (**Error! Reference source not found.**) and calculate potential magnitude using two methods. First using Wells and Coppersmith (1994) we compute Maximum credible magnitude ($M_{cred}$) by using Eq. 6.8 (Kanamori, 1983).

$$\mathrm{M} = 4.07 + 0.98 * \log(\text{Rupture Area}) \qquad \textit{Eq. 6.8}$$

Secondly we calculate moment magnitude from the seismic moment based on Eq 6.9 and 6.10 (Kanamori, 1983). We use values of $3x10^{10}$ $Nm^{-2}$ for the rigidity and calculate the area using a rupture width of 50 or 200 km (to simulate the varying rupture patterns observed along strike). Slip used is 10 meters (~200 years of convergence at 50 $mmyr^{-1}$). It has been shown that, at least for Central Sumatra, interface earthquakes have a return period for >Mw 8 events of ~200 years (Sieh et al., 2008). **Error! Reference source not found.** shows a summary of the input parameters and calculated magnitudes for each segment.

$$\mathrm{M_o} = \text{Rigidity} * \text{Fault Area} * \text{Slip} \qquad \textit{Eq. 6 9}$$

$$\mathrm{M_w} = \frac{2}{3} * [\log 10(\mathrm{M_o}) - 16.1] \qquad \textit{Eq. 6.10}$$

The calculated $M_{cred}$ agree well with observed magnitudes where available with no observed magnitudes exceeding calculated magnitudes. Areas in the south of the subduction zone have smaller magnitude events (by 0.1-0.2). The difference between the two methods of calculating magnitude is 0.1 for all segments < 400 km length. Only the northern segment (Simeulue segment/light green) has a magnitude difference of 0.2, with magnitudes based on Wells and Coppersmith (1994) being higher. We expect the magnitudes from seismic moment to be more accurate, as the Wells and Coppersmith equations are based from fault observations, meaning they lose accuracy at the higher magnitudes as there are fewer observations to constrain their model.

The seismic hazard posed by earthquakes and tsunami around the Mentawai and Siberut islands region is high given the lack of a large event since 1797 and the roughly 200 year seismic cycle of central Sumatra (Sieh et al., 2008). From historical events and current slip rates is has been suggested that, at least for Central Sumatra, interface earthquakes have a return period for >Mw 8 events of ~200 years (Sieh et al., 2008).

| Segment/cluster color | Southern boundary (lat°) | N° of events | Length (km) | Observed Event | Calculated magnitude | |
|---|---|---|---|---|---|---|
| | | | | | RA (M) | $M_o$ ($M_w$) |
| Andman and Nicobar Islands*/light green | 6.3 | 68 | 1370 | $M_w$ 9.2, 2004 | 8.8-9.4 | 9.2 |
| Banda Aceh Segment/dark blue | 3.4 | 141 | 222 | $M_w$ 9.2, 2004 | 8.2-8.8 | 8.7 |
| Simeulue Segment/green | 1.6 | 99 | 228 | $M_w$ 9.2, 2004<br>$M_w$ 7.3, 2002 | 8.1-8.7 | 8.7 |
| Nias Segment/yellow | -0.7 | 185 | 390 | $M_w$ 8.7$M_w$ 2005 | 8.3-8.8 | 8.8 |
| Batu-Siberut-Mentawai Islands/purple | -3.4 | 119 | 370 | M 8.8, 1797<br>M 8.8, 1833<br>$M_w$ 7.9, 2007 | 8.3-8.8 | 8.8 |
| Northern Enggano Segment/teal | -5.5 | 138 | 267 | $M_w$ 8.4, 2007 | 8.1-8.6 | 8.7 |
| Southern Enggano Segment/red | -7.1 | 149 | 258 | $M_w$ 7.9, 2000 | 8.0-8.6 | 8.7 |
| Sunda Strait/light blue | -8.2 | 66 | 266 | | 8.1-8.6 | 8.7 |
| Western Java*/blue | -10.4 | 64 | 321 | | 8.2-8.8 | 8.8 |

*Table 6.2 Summary of cluster parameters: southern termination, number of events within each cluster, length of each segment. 6th column shows notable ruptures that have occurred within the segment. Calculated magnitudes derived from Eq. 6.7 (RA) and 6.9 ($M_o$). Magnitude M is based on a rupture area of S*200 km where S is segment length. $M_w$ is based on Area of S*200 km and a slip of 10 meters with a rock rigidity of $3x10^{10}$ $Nm^{-2}$*

### 6.5.3 The 1797 and 1833 Events and Central Sumatra Hazard Potential

The limits of the inferred rupture areas of the 1797 and 1833 events fit with our model, with the exception of the southern limit of the 1833 event. Coral uplift data for the 1833 event are not available south of the Pagai-selatan island as no islands exist (Figure 6.5). Written records of shaking and damage and high uplift at the southern Mentawai Islands led Newcomb and McCann, (1987) to

propose that the rupture must have propagated to at least 5°S. Our model, however, places a segment boundary just south of the Mentawai Islands at 3.4°S. A recent study by Lindsay et al. (2016) calculated the theoretical rupture area based on the coral observations for the 1797 and 1833 events. From their work they show that the main slip areas of each event occur in separate patches within the purple cluster. The southern termination point of the 1833 event is moved north to 4°S with slip of only <5 m occurring south of 3.5°S. These newly updated rupture areas seem to converge towards a boundary for the two events similar to the one reported from the clustering model. Potential explanations of the differences between results include: 1) That the 1833 rupture did not extend as far south as proposed, meaning that the 1797 and 1833 events were more similar in rupture area, or 2) 1833 was a composite rupture. From our

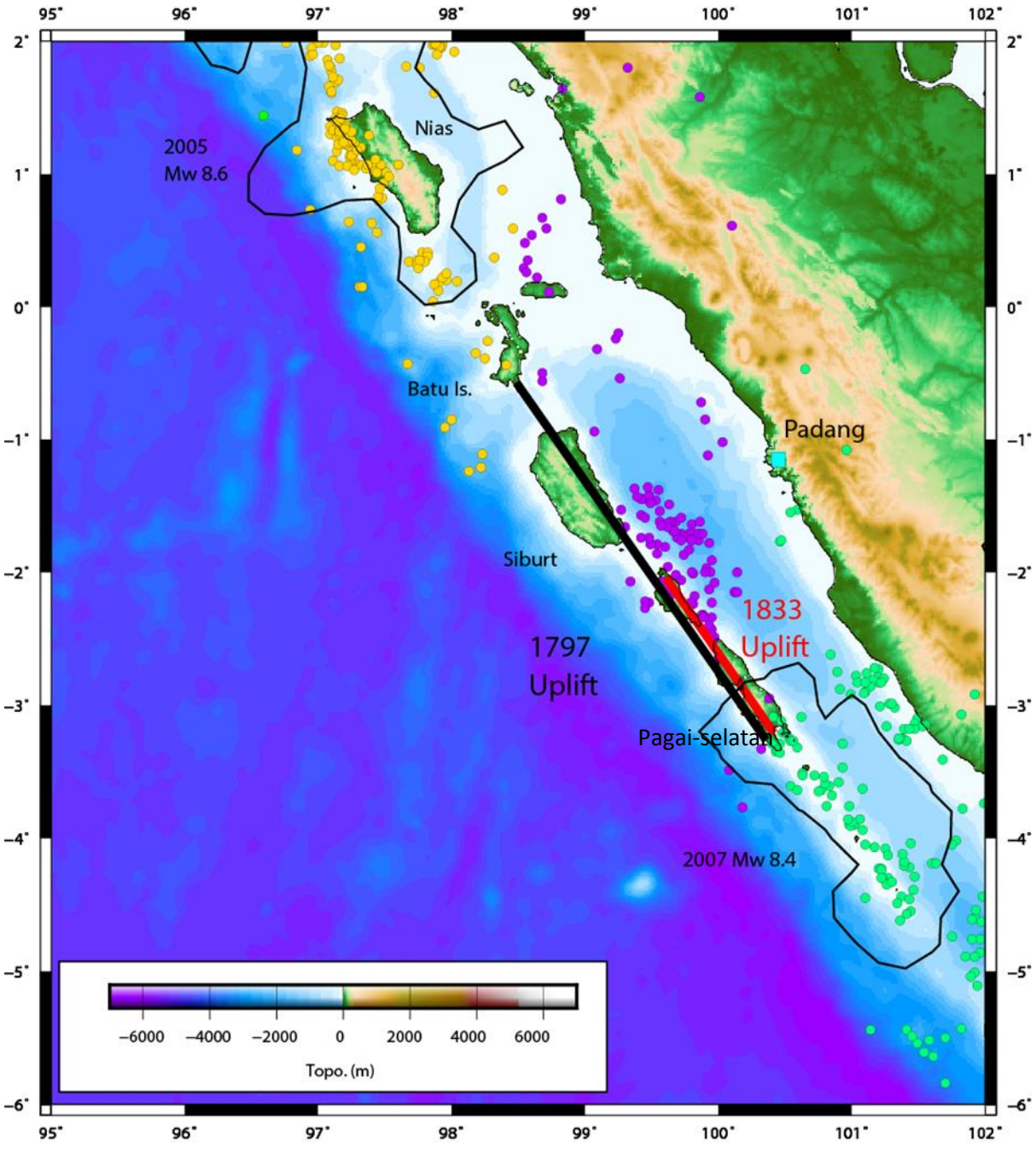

*Figure 6.5 Coral record data from Natawidjaja et al. (2006). Black line is the raw data for the 1797 event and red line is the 1833 event. Uplift was used to calculate the rupture areas for the 1833 and 1797 ruptures.*

model and present day seismicity, a future rupture area will most likely be contained within the Batu-Siberut islands cluster (purple cluster) bound by the Wharton Ridge/IFZ to the north and the 2007 8.6 event to the south. Based on this we can then infer a maximum credible magnitude for this event.

The model almost predicts the exact limits of the 1797 event calculated from coral uplift (Figure 6.5). From magnitude calculations, a 1797-type event is likely to produce a $M_w$ ~ 8.8 event. Given the significant overlap between the 1797 and 1833 events, a larger rupture is possible. We therefore also calculate a magnitude if energy from both events was released at the same time. The seismic moment from the 1797 event is ~2.2e29 and the seismic moment of the part of the 1833 event within the same cluster is ~1.1e29, giving a potential magnitude of ~$M_w$ 9.0. If both the purple and light green segments were to rupture at the same time, potential magnitude increases to $M_w$ ~9.2. Given these scenarios, a $M_w$ >9.0 is possible for the area around Siberut and the Mentawai islands.

### 6.5.4 Orientation of Cluster Boundaries

A common feature in all of the cluster models we analysed was the orientation of the cluster boundaries. Often we would observe an orientation sub-parallel to the direction of convergence. When comparing the orientation of the cluster boundaries to some of the limits of the large events within the subduction zone, we observe a strong correlation between the two. The best example of this is the southern boundary of the 2005 event which is clearly in line with the orientation of the cluster boundaries. Recent work published by Lindsay et al. (2016) derived a rupture area for the 1833 event that had north-south boundaries that were also subparallel to convergence. Other events from the zone also exhibit this ~north-south trending orientation to their rupture areas. This infers that factors controlling rupture propagation within the Sumatran zone are strongly linked to motion between the plates and linked to structure of the incoming plate (note that many of the structures of the subducting plate, such as fracture zones, are aligned ~N-S).

## 6.6 Conclusions

From our models we show that the Sumatra subduction zone is likely composed of 9 segments, defined by earthquake clusters. Boundaries between these clusters affect the rupture process but don't always inhibit large rupture propagation. We find no direct correlation between all incoming topographic highs and rupture boundaries, only certain incoming highs, including the IFZ, seem to influence in rupture. However the orientation of the cluster boundaries suggests a link to the structure of the incoming plate. From the cluster model we derive a segmentation model for the Sumatra subduction zone. Segment lengths along the Sumatra subduction zone range from 228-1370 km with associated magnitudes of $M_w$ 8.0-9.4. The Central Sumatra region has not experienced a rupture and is overdue. By linking our earthquake cluster results with historic records, we propose a potential future rupture could be as large as $M_w$ 9.0 or 9.2. The more likely scenario is the rupture of the Batu-Siberut segment which could produce a ~$M_w$ 9.0 event. A second scenario is the

complete rupture of the two segments that represent the 1797 and 1833 events and if this happens given the strain accumulation and a potential rupture length of 670 km the magnitude could be $M_w$ >9.0.

# 7 Chapter 7: Conclusions

## 7.1 Overview

In this thesis, I developed new velocity models for the Central Sumatran subduction zone down to depths of 500 km. To model the central Sumatran subduction zone we developed a new method to jointly invert for both local and teleseismic body wave arrival times to derive Vp, Vp/Vs and local hypocenter parameters using data from a local temporary deployment. To further develop the models of the central Sumatran subduction zone we conduct an inversion using data from active and local sources to further characterise the shallow crustal structure of the central Sumatran forearc.

In the last chapter we develop a segmentation model of the Sumatran seismogenic interface based on analysis of the spatial patterns of record seismicity from 14°N-6°S. From this work we propose a likely segmentation of the zone as well as discuss causes for apparent segment boundaries. From our models we propose potential future ruptures for the zone.

Below I will summarise the findings of this thesis, mainly the model developments and improvements from conducting a joint inversion. Then I will discuss the key findings of the velocity models for Sumatra and their implications to the global subduction systems. I will summarise the segmentation of the Sumatran zone and possible future work that could be developed as a result of this thesis.

## 7.2 Model Development and Improvements

We present two tomography models within this thesis, one from an inversion of teleseismic and local data and one from the inversion of active and local data. In both cases, enhancements to previous models based purely on local earthquakes were achieved.

Inclusion of teleseismic sources within the local inversion allowed us to resolve deeper parts of the model that have previously been unresolvable at length scales of 20x100 km (XZ 2D) and 40x90x40 km (XYZ 3D), which we achieve in this thesis. Local and teleseismic studies often impose slab structure in order to resolve it (e.g. Collings et al., 2012; DeShon and Schwartz, 2004; Hicks et al., 2012) however in our method the slab does not need to be imposed and we resolve slab structure down to depths of 200 km. The addition of teleseismic information did not significantly the region where local earthquake resolution was good already and the addition of teleseismic data did not improvement improve the accuracy or precisions of hypocenters. More model testing will be needed to determine if factors like weighting between rays can be used to solve this.

Overall there are no negative effects to including the teleseismic data into the local source inversion. The method is a natural progression in local inversions allowing for better insight into process beneath the subducting slab. Secondly the time it will take to sort and pick the teleseismic data set in preparation for use within the algorithm is relatively small given the similarities between picking local and teleseismic data. Therefore, I recommend incorporation of any teleseismic data from temporary arrays into inversions such as the one presented within chapter 4.

From the local and active inversion, we see improvement in the resolution in the shallow portion of the model, being able to resolve features that are 15x30x10 km in the XYZ for depths <50 km. When

comparing the two models we see differences of up to 100% in the shallow portions of the model (<5 km), and up to 30% at depths <20 km. The shallow portion of the model reflects the inability of local passive studies to resolve the shallow part of the model. It is common to blank out the top 5km in local inversion models as often the shallow portion of the model reflects the original starting model.

From the active/local inversion we see a more compelling need to use joint inversion for shallow surface structure. A direct consequence of poorly resolved crustal structure is inaccurate hypocenter locations when we compare the local/teleseismic and local/active models. When looking at hypocenters below the oceanic Moho in the local/teleseismic models, the hypocenters are between 30-50 km depth compared to 25-30 km depth within the local/active models. The depth change is likely due to better characterisation of the accretionary domain (30% lower Vp velocities are observed within the local/active model compared to the local/teleseismic model) provided by the inclusion of active shots within the Sumatran forearc. If local seismicity studies are carried out using stations located across the forearc our work shows that the carefully derivation of a local 1D velocity model is paramount as it may have large implications, such as mislocated hypocenters, then thought before.

## 7.3 Structure and Properties of the Central Sumatran subduction zone as revealed from joint tomography

The newly modified code allows for joint inversion of local hypocenter and velocity parameters with teleseismic velocity parameters. Using this modified code, we derive Vp and Vp/Vs ratio for the central Sumatran subduction system with fine scale velocity variations (20x30x20 km, XYZ) resolved down to depths of 150 km below the magmatic arc and large-scale velocity variations down to depths of 450 km (20x100 km, XZ). We relocate 1073 local events within the new model providing improved accuracy of these earthquake locations which were original located within a 1D model.

The subducting oceanic plate is approximately 35 km thick. In the shallow portions of the model (<50 km) we can differentiate between the crust and the subducting lithospheric mantle at depths <100 km. The subducting oceanic crust has P wave velocities of 7.5 km $s^{-1}$ and Vp/Vs ratios of >1.8 at depths of <50 km suggesting the crust is heavily hydrated as it subducts. A deeper, low velocity region associated with the oceanic crust is observed to depths of 70 km. This observation, seen elsewhere, is inferred to be the result of the basalt-eclogite transition (e.g. Fukao et al., 1983). The subducting lithosphere has Vp/Vs ratios of <1.7, this reduced Vp/Vs ratio likely caused by the forsterite-eclogite transition (Ji and Wang, 1999). The Vp/Vs values also give us a proxy for the base of the slab and hence the slab thickness of 35 km. Lower slab Vp/Vs ratios have been observed at the New Zealand and Japan margins (Eberhart-Phillips et al., 2015; Wang et al., 2006) and linked to the forsterite-eclogite transition.

Hypocenters within the Central Sumatra forearc are mainly located around the plate interface and dominant forearc faults such as the Mentawai Fault Zone. We also observe a cluster of seismicity seaward of the trench near the base of or below the incoming plate at a depth of 30-50 km. The seismicity is most likely caused by faults within the incoming plate extending into the sub-lithospheric mantle (Qin and Singh, 2015). The 2012 M>8 earthquakes further north also ruptured to mantle depths (Delescluse et al., 2012), confirming this is not unusual in the Indo-Australian plate.

Deep offshore faults extending into the upper mantle have been observed at Cascadia (Han et al., 2016), Nicaragua and Chile (Grevemeyer et al., 2005). Along the southern Chile margin where bend

faulting is documented, only one reflective crustal/mantle fault at 39°S has been reported (Grevemeyer et al., 2005). Studies from the Alaska (Bécel et al., 2015) and Kuril trench (Fujie et al., 2013) found no evidence for crustal/mantle faults. The 2012 >$M_w$ 8.0 Northern Sumatran (Delescluse et al., 2012) intraplate event showed that these faults have the potential to generate large events. Characterisation of these deep cutting faults and their hazard potential as they enter subduction zones is desperately needed as they could possibly be a source for > $M_w$8.0 events within a subduction zone.

The Sumatra forearc mantle wedge does not show evidence for widespread serpentinisation, with bulk velocities of the wedge being 8.0-8.2 km $s^{-1}$ and Vp/Vs ratios of approximately 1.77, suggesting unaltered mantle peridotite. Only in a very localised part of the mantle wedge corner do we observe increased Vp/Vs ratios of 1.80, but we do not see the corresponding expected drop in Vp velocities due to serpentinisation. We do observe however a thin layer of Vp/Vs ratios of greater than 1.8 just above the plate interface suggesting fluid escape from the slab and travelling back up the plate interface. Evidence for a lack of serpentinisation within the forearc was also shown when the 2004 event was shown to nucleate within the forearc mantle wedge (Dessa et al., 2009).

Forearc mantle wedges have been theorised to be either serpentinised or non-serpentinised (Hyndman and Peacock., 2003). Forearcs that show serpentinised mantle wedges are seen at the Cascadia margin (Brocher et al., 2003), Costa Rica (DeShon and Schwartz, 2004) and Nankai, Japan (Hyndman and Peacock, 2003). The cause for serpentinisation is as the plate subducts dehydration occurs and water is released from the plate into the above mantle causing the mantle peridotite to become partial serpentinised (Peacock, 1993). However observations from Central Sumatra (Collings et al., 2012; Chapter 4) show mantle wedges there are not heavily serpentinised. This suggest that either no water is being released from the subducting plate or that no water is reaching the mantle.

In the images presented in Chapter 4 we see that at the trench the oceanic crust has Vp/Vs ratios of >1.8 suggesting the crust is heavily hydrated suggesting there is plenty of water available, even though there is no apparent serpentinised mantle wedge. Seno (2005) have suggested that fluid escaping from the slab instead of entering the mantle wedge, percolates back up through fractures and faults present in the subducting crust. This likely to be happening in the Sumatran forearc mantle wedge. We know the Indo-Australian plate is heavily fractured (Qin and Singh, 2015), suggesting that fluids are possibly escaping back through fractures within the crust.

Beneath the volcanic arc we see increased Vp/Vs ratios of >1.8 extending from the plate interface to the continental Moho implying there is a degree of melting within the mantle wedge, a common observation beneath subduction volcanic arcs (e.g. Hicks et al., 2012; Hirose and Nakajima, 2008; Koulakov et al., 2009; McCaffrey et al., 2001). Observation from other subduction zones show similar anomalies beneath the volcanic arcs. Tomography studies from Costa Rica (Dinc et al., 2010) and Nicaragua (DeShon and Schwartz, 2004) all have high Vp/Vs anomalies associated with the arc.

Within the sub-slab mantle we see indirect evidence for strong trench-perpendicular fast direction anisotropy. We observe an low velocity region of Vp 7.5-8 km $s^{-1}$ between 350 and 450 km depth below the outer forearc. We interpret this anisotropic signal as due to the dominance of trench parallel rays in this area causing they observed low velocity. From our observations as well as other studies we suggest there is a high degree of mantle entrained with the subducting Sumatran slab beneath Central Sumatra. Trench-perpendicular anisotropy has been observed at serval other subduction zones such as has been attributed to a strong sense of mantle entrainment (Long and Silver, 2008; Song et al., 2012).

## 7.4 Composition of the Central Sumatran Inner Forearc

One of the more interesting findings of this research was the presence of a block of material sitting between the accretionary domain (active wedge to forearc islands) and the continental arc of

Sumatra with anomalous and distinct velocities. Velocities of >7 km $s^{-1}$ are observed at depths <9 km beneath the inner forearc and forearc basins. The edges of this block are the vertical velocity boundary with the accretionary domain to the west (boundary coinciding with the seaward forearc basin boundary and often with the forearc-parallel fault system that includes the Mentawai Fault) and the continental arc to the east (this boundary coinciding with the coastline). The continental Moho beneath the inner forearc is observed at 30 km, approximately 10 km shallower than beneath the continental arc. From our velocity observations we suggest that the inner Sumatran forearc is comprised of an uplifted ophiolitic complex which acts as a backstop for the accretionary domain. This is supported by geological field evidence from Nias island for an ophiolitic complex present within the Sumatran forearc (Karig et al., 1980; Samuel et al., 1997) . The inferred ophiolitic complex spans the entire width of the inner forearc.

Evidence for ophiolitic complexes acting as backstops can be seen in Japan (Ishiwatari et al., 1991), Newfoundland (Dewey and Casey, 2013), Alaska (Kusky and Young, 1999b) and the Great Valley California (Godfrey et al., 1997). The importance of ophiolitic complexes within each zone is unique. For example, in the Great Valley an ophiolitic complex acts as a backstop to the accretionary domain with it being accreted onto the seaward edge of the continental arc at some point in the past (Godfrey et al., 1997). Within the Great Valley the ophiolite plays an important role in the structure of the subduction zone forearc. However, in Japan ophiolitic material has been observed to be mixed in within the forearc domain, but unlike in the Great Valley the extent and size of the ophiolite is much smaller and sparse in observation, suggesting that the ophiolite was likely present at the start of subduction and has been possibly eroded over time (Ishiwatari et al., 1991). The importance here much like in the Great Valley and Sumatra, the ophiolitic material provides a possible history to the formation and/or initiation of subduction within the area.

We also sample the corner of the forearc mantle wedge and observe normal Vp values of 8.0 km $s^{-1}$ for the shallow part of the wedge. A Vp value of 8.0 km $s^{-1}$ is typical of unaltered mantle peridotite suggesting that no serpentinisation is occurring within the mantle wedge, reinforcing the results within Chapter 4.

## 7.5 Segmentation of the seismogenic interface

We use a K-means algorithm method to cluster seismicity along the Sumatran seismogenic zone. The Sumatran subduction zone is likely composed of 9 segments defined by earthquake clusters. Generally, the boundaries between these clusters affect the rupture process but do not always inhibit large rupture propagation. By examining the placement of these boundaries in relation to rupture termination for recorded events along the zone and incoming topographic features, we find that only certain topographic features are influential in defining a cluster boundary, e.g., where the projected Investigator Fracture Zone (IFZ) subducts. No earthquake rupture boundaries specifically coincide with subducting fracture zones north of the IFZ, including some discrepancies in the location of the segment boundary around Simeulue Island, the boundary of the 2004 and 2005 earthquakes.

Using empirical relationships, we estimate the maximum credible magnitude each cluster can produce, based on the maximum rupture length of that cluster. Currently parts of the Central and Southern Sumatra margin are overdue for a large rupture (e.g., 1797 historic rupture region). Using the cluster model we propose possible rupture scenarios for central Sumatra. A potential future rupture of the Mentawai islands could be as large as Mw 9.0-9.2. The more likely scenario is the rupture of the Siberut segment which is likely to produce a Mw ~9.0 event. A second scenario is the complete rupture of the two segments that represent the 1797 and 1833 events: given the present-day strain accumulation and a potential rupture length of 670 km, the magnitude would be Mw ~9.1.

Megathrust events are controlled by features on the seismogenic interface. One of the major influences of ruptures along strike is the presence of topographic highs. Global ruptures show no correlation between topographic features on the downgoing plate between different subduction zones. Several studies (e.g. Henstock et al., 2016; Sparkes et al., 2010; Bilek and Wang 2009) have shown the downgoing topographic features stop rupture as they act a places of increased strength for the plate interface by not allowing ruptures to propagate past them. Counter to this however there are several places that show that these asperities within the plate interface are the starting point for large ruptures as they allow for strain energy to accumulate over long time periods (Moreno et al., 2012). Currently for a barrier to be identified a rupture has to have occurred in close proximity to it. This presents a problem in assessing the hazard potential of a regions that have these topographically defined boundaries but their likely behaviour is unknown. This problem is in part answered by the work put forward in Chapter 6, which show no clear correlation to topographic features.

## 7.6 Future work

### 7.6.1 Sumatra

This work raises several interesting questions about Sumatra. The further quantification of the along strike extent of the anomalous velocity structure of Sumatra's inner forearc needs to be further characterised. The role faults play within the forearc and their relationship to the inner forearc and the shaping of the margin is not well understood. Globally the role of the inner forearc and how it controls the down dip limit of rupture needs to be further quantified as large events have been observed to rupture into the forearc mantle. Using Sumatra as a case study only strengthens the need to properly understand rupture dynamics at subduction zones.

### 7.6.2 Tomography

Here are 3 possible areas in which the Simul2000 algorithm can be improved: 1) Test the weighting between the local and teleseismic inversion to better quantify the effects it has on the final model as I feel including the teleseismic inversion shows great potential. 2)We have taken steps towards this in squeezing testing and assessing weighting and damping values but more has to be done. 3) Include calculation of the incidence angle of the teleseismic arrivals into the joint inversion problem such that small changes are allowed alongside hypocenter and velocity parameters is another area for improvement.

Finally an aim of the project was to include all data types within the inversion, active, local and teleseismic. Theoretically the code is in place here, yet the Simul2000 code has a maximum limit on the number of nodes currently allowed in the model. From testing the maximum number of nodes was not enough to accurately characterise both the shallow structure were the active shots are located and also the deeper part of the models was the teleseismic rays passes through. This meant that we could not invert active, local and teleseismic data at the same time as the modifications to the code would require a complete rewrite.

### 7.6.3 K-means clustering

The second part of the thesis focused on using a K-means algorithm to identify spatial patterns of seismicity. The work presented in this thesis shows great promise but due to the relatively infancy of the method there are too many possibilities to list here. I will instead suggest some of the more

interesting possibilities of this work. Currently the K-means algorithm has been used to look at mainly structures that can be represented as a 2D problem (seismic sources that do not vary with depth), fault planes and seismogenic interfaces. You can apply the algorithm to analyse seismicity at a variety of levels, for instance, applying the methodology to aftershock seismicity or the seismicity associated with volcanoes would be a logical step in assessing the capabilities of the algorithm. Expanding on this idea a global cluster model is also viable, although the coordinate system would have to be altered to account for boundary conditions that arise when using a Cartesian coordinate system. As for algorithm development, a temporal element could be introduced whereby the algorithm clusters in both space and time. In this thesis, we attempted to apply the algorithm to 3D although we found that there was not currently enough seismicity to produce robust results within limiting the dataset to a single seismic source.

# References


Abercrombie, R. E., Antolik, M., Felzer, K., & Ekström, G. (2001). The 1994 Java tsunami earthquake: Slip over a subducting seamount. *Journal of Geophysical Research: Solid Earth*, *106*(B4), 6595-6607.

Achauer, U., Evans, J. R., & Stauber, D. A. (1988). High-resolution seismic tomography of compressional wave velocity structure at Newberry Volcano, Oregon Cascade Range. *Journal of Geophysical Research: Solid Earth*, *93*(B9), 10135-10147.

Aki, K., Christoffersson, A., & Husebye, E. S. (1977). Determination of the three-dimensional seismic structure of the lithosphere. *Journal of Geophysical Research*, *82*(2), 277-296.

Aki, K., & Lee, W. H. K. (1976). ARRAY USING FIRST P ARRIVAL TIMES FROM LOCAL EARTHQUAKES. *Journal of Geophysical research*.

Amato, A., Alessandrini, B., Cimini, G., Frepoli, A., & Selvaggi, G. (1993). Active and remnant subducted slabs beneath Italy: evidence from seismic tomography. *Annali di geofisica*, *36*(2).

Ammon, C. J., Ji, C., Thio, H. K., Robinson, D., Ni, S., Hjorleifsdottir, V., Ichinose, G. (2005). Rupture process of the 2004 Sumatra-Andaman earthquake. *Science*, *308*(5725), 1133-1139.

Ansari, A., Firuzi, E., & Etemadsaeed, L. (2015). Delineation of Seismic Sources in Probabilistic Seismic-Hazard Analysis Using Fuzzy Cluster Analysis and Monte Carlo Simulation. *Bulletin of the Seismological Society of America*, *105*(4), 2174-2191.

Anderson, R. N., DeLong, S. E., & Schwarz, W. M. (1978). Thermal model for subduction with dehydration in the downgoing slab. *The Journal of Geology*, *86*(6), 731-739.

Ando, M., Nakamura, M., Matsumoto, T., Furukawa, M., Tadokoro, K., & Furumoto, M. (2009). Is the Ryukyu subduction zone in Japan coupled or decoupled?—The necessity of seafloor crustal deformation observation. *Earth, planets and space*, *61*(9), 1031-1039.

Anglin, D. K., & Fouch, M. J. (2005). Seismic anisotropy in the Izu-Bonin subduction system. *Geophysical Research Letters*, *32*(9).

Argus, D. F., & Gordon, R. G. (2001). Present tectonic motion across the Coast Ranges and San Andreas fault system in central California. *Geological Society of America Bulletin*, *113*(12), 1580-1592.

Atwater, B. F., Furukawa, R., Hemphill-Haley, E., Ikeda, Y., Kashima, K., Kawase, K., Odagiri, S. (2004). Seventeenth-century uplift in eastern Hokkaido, Japan. *The Holocene*, *14*(4), 487-501.

Baba, K., Chave, A. D., Evans, R. L., Hirth, G., & Mackie, R. L. (2006). Mantle dynamics beneath the East Pacific Rise at 17 S: Insights from the Mantle Electromagnetic and Tomography (MELT) experiment. *Journal of Geophysical Research: Solid Earth*, *111*(B2).

Bangs, N. L., Westbrook, G. K., Ladd, J. W., & Buhl, P. (1990). Seismic velocities from the Barbados Ridge complex: Indicators of high pore fluid pressures in an accretionary complex. *Journal of Geophysical Research: Solid Earth*, *95*(B6), 8767-8782.

Barber, A. J., & Crow, M. J. (2009). Structure of Sumatra and its implications for the tectonic assembly of Southeast Asia and the destruction of Paleotethys. *Island Arc*, *18*(1), 3-20.

Beaudry, D., & Moore, G. F. (1985). Seismic stratigraphy and Cenozoic evolution of West Sumatra forearc basin. *AAPG Bulletin*, *69*(5), 742-759.

Bécel, A., Shillington, D. J., Nedimović, M. R., Webb, S. C., & Kuehn, H. (2015). Origin of dipping structures in fast-spreading oceanic lower crust offshore Alaska imaged by multichannel seismic data. *Earth and Planetary Science Letters*, *424*, 26-37.

Bellier, O., & Sebrier, M. (1995). Is the slip rate variation on the Great Sumatran Fault accommodated by fore-arc stretching?. *Geophysical Research Letters*, *22*(15), 1969-1972.

Bellier, O., & Sébrier, M. (1994). Relationship between tectonism and volcanism along the Great Sumatran fault zone deduced by SPOT image analyses. *Tectonophysics*, *233*(3-4), 215-231.

Berglar, K., Gaedicke, C., Lutz, R., Franke, D., & Djajadihardja, Y. S. (2008). Neogene subsidence and stratigraphy of the Simeulue forearc basin, Northwest Sumatra. *Marine Geology*, *253*(1), 1-13.

Bilek, S. L., Schwartz, S. Y., & DeShon, H. R. (2003). Control of seafloor roughness on earthquake rupture behavior. *Geology*, *31*(5), 455-458.

Bostock, M. G., Hyndman, R. D., Rondenay, S., & Peacock, S. M. (2002). An inverted continental Moho and serpentinization of the forearc mantle. *Nature*, *417*(6888), 536-538.

Briggs, R. W., Sieh, K., Meltzner, A. J., Natawidjaja, D., Galetzka, J., Suwargadi, B., Prayudi, D. (2006). Deformation and slip along the Sunda megathrust in the great 2005 Nias-Simeulue earthquake. *Science*, *311*(5769), 1897-1901.

Brocher, T. M., Parsons, T., Tréhu, A. M., Snelson, C. M., & Fisher, M. A. (2003). Seismic evidence for widespread serpentinized forearc upper mantle along the Cascadia margin. *Geology*, *31*(3), 267-270.

Burton, P. W., & Hall, T. R. (2014). Segmentation of the Sumatran fault. *Geophysical Research Letters*, *41*(12), 4149-4158.

Byrne, D. E., Wang, W. H., & Davis, D. M. (1993). Mechanical role of backstops in the growth of forearcs. *Tectonics*, *12*(1), 123-144.

Chauhan, A. P., Singh, S. C., Hananto, N. D., Carton, H., Klingelhoefer, F., Dessa, J. X., SumatraOBS Scientific Team. (2009). Seismic imaging of forearc backthrusts at northern Sumatra subduction zone. *Geophysical Journal International*, *179*(3), 1772-1780.

Chester, F. M., Evans, J. P., & Biegel, R. L. (1993). Internal structure and weakening mechanisms of the San Andreas fault. *Journal of Geophysical Research: Solid Earth*, *98*(B1), 771-786.

Chlieh, M., Avouac, J. P., Hjorleifsdottir, V., Song, T. R. A., Ji, C., Sieh, K., Galetzka, J. (2007). Coseismic slip and afterslip of the great Mw 9.15 Sumatra–Andaman earthquake of 2004. *Bulletin of the Seismological Society of America*, *97*(1A), S152-S173.

Chlieh, M., Avouac, J. P., Sieh, K., Natawidjaja, D. H., & Galetzka, J. (2008). Heterogeneous coupling of the Sumatran megathrust constrained by geodetic and paleogeodetic measurements. *Journal of Geophysical Research: Solid Earth*, *113*(B5).

Christensen, N. I. (1978). Ophiolites, seismic velocities and oceanic crustal structure. *Tectonophysics*, *47*(1), 131-157.

Clift, P., & Vannucchi, P. (2004). Controls on tectonic accretion versus erosion in subduction zones: Implications for the origin and recycling of the continental crust. *Reviews of Geophysics*, *42*(2).

Cloos, M. (1992). Thrust-type subduction-zone earthquakes and seamount asperities: A physical model for seismic rupture. *Geology*, *20*(7), 601-604.

Collings, R., Lange, D., Rietbrock, A., Tilmann, F., Natawidjaja, D., Suwargadi, B., Saul, J. (2012). Structure and seismogenic properties of the Mentawai segment of the Sumatra subduction zone revealed by local earthquake traveltime tomography. *Journal of Geophysical Research: Solid Earth*, *117*(B1).

Collings, R., Rietbrock, A., Lange, D., Tilmann, F., Nippress, S., & Natawidjaja, D. (2013). Seismic anisotropy in the Sumatra subduction zone. *Journal of Geophysical Research: Solid Earth*, *118*(10), 5372-5390.

Contreras-Reyes, E., & Carrizo, D. (2011). Control of high oceanic features and subduction channel on earthquake ruptures along the Chile–Peru subduction zone. *Physics of the Earth and Planetary Interiors*, *186*(1), 49-58.

Cook, B. J., Henstock, T. J., McNeill, L. C., & Bull, J. M. (2014). Controls on spatial and temporal evolution of prism faulting and relationships to plate boundary slip offshore north-central Sumatra. *Journal of Geophysical Research: Solid Earth*, *119*(7), 5594-5612.

Corrigan, J., Mann, P., & INGLE, J. C. (1990). Forearc response to subduction of the Cocos ridge, Panama-Costa Rica. *Geological Society of America Bulletin*, *102*(5), 628-652.

Crosson, R. S., & Owens, T. J. (1987). Slab geometry of the Cascadia subduction zone beneath Washington from earthquake hypocenters and teleseismic converted waves. *Geophysical Research Letters*, *14*(8), 824-827.

Curray, J. R. (2005). Tectonics and history of the Andaman Sea region. *Journal of Asian Earth Sciences*, *25*(1), 187-232.

Currie, C. A., Wang, K., Hyndman, R. D., & He, J. (2004). The thermal effects of steady-state slab-driven mantle flow above a subducting plate: the Cascadia subduction zone and backarc. *Earth and Planetary Science Letters*, *223*(1), 35-48.

Das, S., & Watts, A. B. (2009). Effect of subducting seafloor topography on the rupture characteristics of great subduction zone earthquakes. In *Subduction Zone Geodynamics* (pp. 103-118). Springer Berlin Heidelberg.

Dean, S. M., McNeill, L. C., Henstock, T. J., Bull, J. M., Gulick, S. P., Austin, J. A., Permana, H. (2010). Contrasting décollement and prism properties over the Sumatra 2004–2005 earthquake rupture boundary. *Science*, *329*(5988), 207-210.

Debari, S. M., & Sleep, N. H. (1991). High-Mg, low-Al bulk composition of the Talkeetna island arc, Alaska: Implications for primary magmas and the nature of arc crust. *Geological Society of America Bulletin*, *103*(1), 37-47.

Delescluse, M., Chamot-Rooke, N., Cattin, R., Fleitout, L., Trubienko, O., & Vigny, C. (2012). April 2012 intra-oceanic seismicity off Sumatra boosted by the Banda-Aceh megathrust. *Nature*, *490*(7419), 240-244.

DeShon, H. R., Engdahl, E. R., Thurber, C. H., & Brudzinski, M. (2005). Constraining the boundary between the Sunda and Andaman subduction systems: Evidence from the 2002 Mw 7.3 Northern Sumatra earthquake and aftershock relocations of the 2004 and 2005 great earthquakes. *Geophysical research letters*, *32*(24).

DeShon, H. R., & Schwartz, S. Y. (2004). Evidence for serpentinization of the forearc mantle wedge along the Nicoya Peninsula, Costa Rica. *Geophysical research letters*, *31*(21).

Dessa, J. X., Klingelhoefer, F., Graindorge, D., André, C., Permana, H., Gutscher, M. A., SUMATRA-OBS Scientific Team. (2009). Megathrust earthquakes can nucleate in the forearc mantle: Evidence from the 2004 Sumatra event. *Geology*, *37*(7), 659-662.

Dewey, J. F., & Casey, J. F. (2013). The sole of an ophiolite: the Ordovician Bay of Islands Complex, Newfoundland. *Journal of the Geological Society*, *170*(5), 715-722.

Diament, M., Harjono, H., Karta, K., Deplus, C., Dahrin, D., Zen, M. T., Malod, J. (1992). Mentawai fault zone off Sumatra: A new key to the geodynamics of western Indonesia. *Geology*, *20*(3), 259-262.

Dinc, A. N., Koulakov, I., Thorwart, M., Rabbel, W., Flueh, E. R., Arroyo, I., Alvarado, G. (2010). Local earthquake tomography of central Costa Rica: Transition from seamount to ridge subduction. *Geophysical Journal International*, *183*(1), 286-302.

Dumitru, T. A., Wakabayashi, J., Wright, J. E., & Wooden, J. L. (2010). Early Cretaceous transition from nonaccretionary behavior to strongly accretionary behavior within the Franciscan subduction complex. *Tectonics*, *29*(5).

Eberhart-Phillips, D. (1986). Three-dimensional velocity structure in northern California Coast Ranges from inversion of local earthquake arrival times. *Bulletin of the Seismological Society of America*, *76*(4), 1025-1052.

Eberhart-Phillips, D., & Bannister, S. (2015). 3-D imaging of the northern Hikurangi subduction zone, New Zealand: variations in subducted sediment, slab fluids and slow slip. *Geophysical Journal International*, *201*(2), 838-855.

Engdahl, E. R., Van der Hilst, R. D., & Berrocal, J. (1995). Imaging of subducted lithosphere beneath South America. *Geophysical Research Letters*, *22*(16), 2317-2320.

Engdahl, E. R., Villaseñor, A., DeShon, H. R., & Thurber, C. H. (2007). Teleseismic relocation and assessment of seismicity (1918–2005) in the region of the 2004 Mw 9.0 Sumatra–Andaman and 2005 Mw 8.6 Nias Island great earthquakes. *Bulletin of the Seismological Society of America*, *97*(1A), S43-S61.

Epanomeritakis, I., Akçelik, V., Ghattas, O., & Bielak, J. (2008). A Newton-CG method for large-scale three-dimensional elastic full-waveform seismic inversion. *Inverse Problems*, *24*(3), 034015.

Fichtner, A., Kennett, B. L., Igel, H., & Bunge, H. P. (2009). Full seismic waveform tomography for upper-mantle structure in the Australasian region using adjoint methods. *Geophysical Journal International*, *179*(3), 1703-1725.

Fischer, K. M., Parmentier, E. M., Stine, A. R., & Wolf, E. R. (2000). Modeling anisotropy and plate-driven flow in the Tonga subduction zone back arc. *Journal of Geophysical Research: Solid Earth*, *105*(B7), 16181-16191.

Fisher, D., Mosher, D., Austin, J. A., Gulick, S. P., Masterlark, T., & Moran, K. (2007). Active deformation across the Sumatran forearc over the December 2004 Mw9. 2 rupture. *Geology*, *35*(2), 99-102.

Fouch, M. J., & Fischer, K. M. (1996). Mantle anisotropy beneath northwest Pacific subduction zones. *Journal of Geophysical Research: Solid Earth*, *101*(B7), 15987-16002.

Fouch, M. J., & Fischer, K. M. (1998). Shear wave anisotropy in the Mariana subduction zone. *Geophysical Research Letters*, *25*(8), 1221-1224.

Fujie, G., Kodaira, S., Yamashita, M., Sato, T., Takahashi, T., & Takahashi, N. (2013). Systematic changes in the incoming plate structure at the Kuril trench. *Geophysical Research Letters*, *40*(1), 88-93.

Fukao, Y., Hori, S., & Ukawa, M. (1983). A seismological constraint on the depth of basalt–eclogite transition in a subducting oceanic crust. *Nature*, *303*(5916), 413-415.

Geersen, J., McNeill, L., Henstock, T. J., & Gaedicke, C. (2013). The 2004 Aceh-Andaman Earthquake: Early clay dehydration controls shallow seismic rupture. *Geochemistry, Geophysics, Geosystems*, *14*(9), 3315-3323.

Genrich, J. F., Bock, Y., McCaffrey, R., Prawirodirdjo, L., Stevens, C. W., Puntodewo, S. S. O., Wdowinski, S. (2000). Distribution of slip at the northern Sumatran fault system. *Journal of Geophysical Research*, *105*(B12), 28327-28.

Godfrey, N. J., Beaudoin, B. C., Klemperer, S. L., & Mendocino Working Group. (1997). Ophiolitic basement to the Great Valley forearc basin, California, from seismic and gravity data: Implications for crustal growth at the North American continental margin. *Geological Society of America Bulletin*, *109*(12), 1536-1562.

Gorbatov, A., Widiyantoro, S., Fukao, Y., & Gordeev, E. (2000). Signature of remnant slabs in the North Pacific from P-wave tomography. *Geophysical Journal International*, *142*(1), 27-36.

Grand, S. P., van der Hilst, R. D., & Widiyantoro, S. (1997). High resolution global tomography: a snapshot of convection in the Earth. *Geological Society of America Today*, *7*(4).

Grevemeyer, I., Kaul, N., Diaz-Naveas, J. L., Villinger, H. W., Ranero, C. R., & Reichert, C. (2005). Heat flow and bending-related faulting at subduction trenches: case studies offshore of Nicaragua and Central Chile. *Earth and Planetary Science Letters*, *236*(1), 238-248.

Gubbins, D., Barnicoat, A., & Cann, J. (1994). Seismological constraints on the gabbro-eclogite transition in subducted oceanic crust. *Earth and Planetary Science Letters*, *122*(1-2), 89-101.

Gulick, S. P. S., Bangs, N. L. B., Shipley, T. H., Nakamura, Y., Moore, G., & Kuramoto, S. (2004). Three-dimensional architecture of the Nankai accretionary prism's imbricate thrust zone off Cape Muroto, Japan: Prism reconstruction via en echelon thrust propagation. *Journal of Geophysical Research: Solid Earth*, *109*(B2).

Hall, R. (1997). Cenozoic plate tectonic reconstructions of SE Asia. *Geological Society, London, Special Publications*, *126*(1), 11-23.

Hall, R. (2012). Late Jurassic–Cenozoic reconstructions of the Indonesian region and the Indian Ocean. *Tectonophysics*, *570*, 1-41.

Hall, R., & Spakman, W. (2002). Subducted slabs beneath the eastern Indonesia–Tonga region: insights from tomography. *Earth and Planetary Science Letters*, *201*(2), 321-336.

Hamilton, W. B. (1979). *Tectonics of the Indonesian region* (No. 1078). US Govt.

Hammond, William C., and Douglas R. Toomey. "Seismic velocity anisotropy and heterogeneity beneath the Mantle Electromagnetic and Tomography Experiment (MELT) region of the East Pacific Rise from analysis of P and S body waves." *Journal of Geophysical Research: Solid Earth* 108.B4 (2003).

Han, S., Carbotte, S. M., Canales, J. P., Nedimović, M. R., Carton, H., Gibson, J. C., & Horning, G. W. (2016). Seismic reflection imaging of the Juan de Fuca plate from ridge to trench: New constraints on the distribution of faulting and evolution of the crust prior to subduction. *Journal of Geophysical Research: Solid Earth*.

Hartigan, J. A., & Wong, M. A. (1979). Algorithm AS 136: A k-means clustering algorithm. *Journal of the Royal Statistical Society. Series C (Applied Statistics)*, *28*(1), 100-108.

Hayman, N. W., & Toshiya, K. (2012). Structural evolution of an inner accretionary wedge and forearc basin initiation, Nankai margin, Japan. *Earth and Planetary Science Letters*, *353*, 163-172.

Henstock, T. J., McNeill, L. C., Bull, J. M., Cook, B. J., Gulick, S. P., Austin, J. A., Djajadihardja, Y. S. (2016). Downgoing plate topography stopped rupture in the AD 2005 Sumatra earthquake. *Geology*, *44*(1), 71-74.

Henstock, T. J., McNeill, L. C., & Tappin, D. R. (2006). Seafloor morphology of the Sumatran subduction zone: Surface rupture during megathrust earthquakes?. *Geology*, *34*(6), 485-488.

Hicks, S. P., Nippress, S. E., & Rietbrock, A. (2012). Sub-slab mantle anisotropy beneath south-central Chile. *Earth and Planetary Science Letters*, *357*, 203-213.

Hicks, S. P., Rietbrock, A., Haberland, C. A., Ryder, I., Simons, M., & Tassara, A. (2012). The 2010 Mw 8.8 Maule, Chile earthquake: Nucleation and rupture propagation controlled by a subducted topographic high. *Geophysical Research Letters*, *39*(19).

Hirose, F., Nakajima, J., & Hasegawa, A. (2008). Three-dimensional seismic velocity structure and configuration of the Philippine Sea slab in southwestern Japan estimated by double-difference tomography. *Journal of Geophysical Research: Solid Earth*, *113*(B9).

Holbrook, W. S., Lizarralde, D., McGeary, S., Bangs, N., & Diebold, J. (1999). Structure and composition of the Aleutian island arc and implications for continental crustal growth. *Geology*, *27*(1), 31-34.

Huang, J., & Zhao, D. (2006). High-resolution mantle tomography of China and surrounding regions. *Journal of Geophysical Research: Solid Earth*, *111*(B9).

Husen, S., Kissling, E., & Flueh, E. R. (2000). Local earthquake tomography of shallow subduction in north Chile- A combined onshore and offshore study. *Journal of Geophysical Research*, *105*(B12), 28-183.

Husen, S., Kissling, E., & Quintero, R. (2002). Tomographic evidence for a subducted seamount beneath the Gulf of Nicoya, Costa Rica: The cause of the 1990 Mw= 7.0 Gulf of Nicoya earthquake. *Geophysical Research Letters*, *29*(8).

Hyndman, R. D., & Peacock, S. M. (2003). Serpentinization of the forearc mantle. *Earth and Planetary Science Letters*, *212*(3), 417-432.

Hyndman, R. D., Yamano, M., & Oleskevich, D. A. (1997). The seismogenic zone of subduction thrust faults. *Island Arc*, *6*(3), 244-260.

Hyndman, R. D., & Wang, K. (1993). Thermal constraints on the zone of major thrust earthquake failure: The Cascadia subduction zone. *Journal of Geophysical Research: Solid Earth*, *98*(B2), 2039-2060.

Ishii, M., Shearer, P. M., Houston, H., & Vidale, J. E. (2005). Extent, duration and speed of the 2004 Sumatra–Andaman earthquake imaged by the Hi-Net array. *Nature*, *435*(7044), 933-936.

Ishiwatari, A. (1991). Time-space distribution and petrologic diversity of Japanese ophiolites. In *Ophiolite genesis and evolution of the oceanic lithosphere* (pp. 723-743). Springer Netherlands.

Ito, K., & Kennedy, G. C. (1971). An Experimental Study of the Basalt-Garnet Granulite-Eclogite Transition. *The structure and physical properties of the Earth's crust*, 303-314.

Ito, T., Gunawan, E., Kimata, F., Tabei, T., Simons, M., Meilano, I., Sugiyanto, D. (2012). Isolating along-strike variations in the depth extent of shallow creep and fault locking on the northern Great Sumatran Fault. *Journal of Geophysical Research: Solid Earth*, *117*(B6).

Izart, A., Kemal, B. M., & Malod, J. A. (1994). Seismic stratigraphy and subsidence evolution of the northwest Sumatra fore-arc basin. *Marine Geology*, *122*(1), 109-124.

Jacob, K. H. (1970). Three-dimensional seismic ray tracing in a laterally heterogeneous spherical Earth. *Journal of Geophysical Research*, *75*(32), 6675-6689.

Ji, S., & Wang, Z. (1999). Elastic properties of forsterite–enstatite compositesup to 3.0 GPa. *Journal of Geodynamics*, *28*(2), 147-174.

Kanamori, H. (1983). Magnitude scale and quantification of earthquakes. *Tectonophysics*, *93*(3-4), 185-199.

Kanamori, H., & McNally, K. C. (1982). Variable rupture mode of the subduction zone along the Ecuador-Colombia coast. *Bulletin of the Seismological Society of America*, *72*(4), 1241-1253.

Karig, D. E., Lawrence, M. B., Moore, G. F., & Curray, J. R. (1980). Structural frame work of the fore-arc basin, NW Sumatra. *Journal of the Geological Society*, *137*(1), 77-91.

Katayama, I., Hirauchi, K. I., Michibayashi, K., & Ando, J. I. (2009). Trench-parallel anisotropy produced by serpentine deformation in the hydrated mantle wedge. *Nature*, *461*(7267), 1114-1117.

Kennett, B. L. N., Engdahl, E. R., & Buland, R. (1995). Constraints on seismic velocities in the Earth from traveltimes. *Geophysical Journal International*, *122*(1), 108-124.

Kieckhefer, R. M., Moore, G. F., Emmel, F. J., & Sugiarta, W. (1981). Crustal structure of the Sunda forearc region west of central Sumatra from gravity data. *Journal of Geophysical Research: Solid Earth*, *86*(B8), 7003-7012.

Kieckhefer, R. M., Shor, G. G., Curray, J. R., Sugiarta, W., & Hehuwat, F. (1980). Seismic refraction studies of the Sunda trench and forearc basin. *Journal of Geophysical Research: Solid Earth*, *85*(B2), 863-889.

Kieling, K., Roessler, D., & Krueger, F. (2011). Receiver function study in northern Sumatra and the Malaysian peninsula. *Journal of Seismology*, *15*(2), 235-259.

Kita, S., Hasegawa, A., Nakajima, J., Okada, T., Matsuzawa, T., & Katsumata, K. (2011, December). Precise seismic velocity structure beneath the Hokkaido corner, northern Japan: Arc-arc collision and the 1970 M 6.7 Hidaka region earthquake and the 1982 M 7.1 Urakawa-oki earthquake. In *AGU Fall Meeting Abstracts* (Vol. 1, p. 2148).

Klingelhoefer, F., Gutscher, M. A., Ladage, S., Dessa, J. X., Graindorge, D., Franke, D., Chauhan, A. (2010). Limits of the seismogenic zone in the epicentral region of the 26 December 2004 great Sumatra-Andaman earthquake: Results from seismic refraction and wide-angle reflection surveys and thermal modeling. *Journal of Geophysical Research: Solid Earth*, *115*(B1).

Kneller, E. A., & Van Keken, P. E. (2007). Trench-parallel flow and seismic anisotropy in the Mariana and Andean subduction systems. *Nature*, *450*(7173), 1222-1225.

Korenaga, J., & Sager, W. W. (2012). Seismic tomography of Shatsky Rise by adaptive importance sampling. *Journal of Geophysical Research: Solid Earth (1978–2012)*, *117*(B8).

Komatitsch, D., & Tromp, J. (1999). Introduction to the spectral element method for three-dimensional seismic wave propagation. *Geophysical journal international*, *139*(3), 806-822.

Konca, A. O., Avouac, J. P., Sladen, A., Meltzner, A. J., Sieh, K., Fang, P., Natawidjaja, D. H. (2008). Partial rupture of a locked patch of the Sumatra megathrust during the 2007 earthquake sequence. *Nature*, *456*(7222), 631-635.

Kopp, C., Fruehn, J., Flueh, E. R., Reichert, C., Kukowski, N., Bialas, J., & Klaeschen, D. (2000). Structure of the Makran subduction zone from wide-angle and reflection seismic data. *Tectonophysics*, *329*(1), 171-191.

Kopp, H., Flueh, E. R., Klaeschen, D., Bialas, J., & Reichert, C. (2001). Crustal structure of the central Sunda margin at the onset of oblique subduction. *Geophysical Journal International*, *147*(2), 449-474.

Kopp, H., Klaeschen, D., Flueh, E. R., Bialas, J., & Reichert, C. (2002). Crustal structure of the Java margin from seismic wide-angle and multichannel reflection data. *Journal of Geophysical Research: Solid Earth*, *107*(B2).

Kopp, H., & Kukowski, N. (2003). Backstop geometry and accretionary mechanics of the Sunda margin. *Tectonics*, *22*(6).

Kopp, H., Weinrebe, W., Ladage, S., Barckhausen, U., Klaeschen, D., Flueh, E. R., Papenberg, C. (2008). Lower slope morphology of the Sumatra trench system. *Basin Research*, *20*(4), 519-529.

Koulakov, I., Bohm, M., Asch, G., Lühr, B. G., Manzanares, A., Brotopuspito, K. S., Kopp, H. (2007). P and S velocity structure of the crust and the upper mantle beneath central Java from local tomography inversion. *Journal of Geophysical Research: Solid Earth*, *112*(B8).

Koulakov, I., Yudistira, T., & Luehr, B. G. (2009). P, S velocity and VP/VS ratio beneath the Toba caldera complex (Northern Sumatra) from local earthquake tomography. *Geophysical Journal International*, *177*(3), 1121-1139.

Karig, D. E., Lawrence, M. B., Moore, G. F., & Curray, J. R. (1980). Structural frame work of the fore-arc basin, NW Sumatra. *Journal of the Geological Society*, *137*(1), 77-91.

Krzanowski, W. J., & Lai, Y. T. (1988). A criterion for determining the number of groups in a data set using sum-of-squares clustering. *Biometrics*, 23-34.

Kusky, T. M., & Young, C. P. (1999). Emplacement of the Resurrection Peninsula ophiolite in the southern Alaska forearc during a ridge-trench encounter. *Journal of Geophysical Research: Solid Earth*, *104*(B12), 29025-29054.

Lopez, A. M., Stein, S., Dixon, T., Sella, G., Calais, E., Jansma, P., LaFemina, P. (2006). Is there a northern Lesser Antilles forearc block?. *Geophysical research letters*, *33*(7).

Lange, D., Rietbrock, A., Haberland, C., Bataille, K., Dahm, T., Tilmann, F., & Flüh, E. R. (2007). Seismicity and geometry of the south Chilean subduction zone (41.5 S–43.5 S): Implications for controlling parameters. *Geophysical Research Letters*, *34*(6).

Lange, D., Tilmann, F., Rietbrock, A., Collings, R., Natawidjaja, D. H., Suwargadi, B. W., Ryberg, T. (2010). The fine structure of the subducted investigator fracture zone in western Sumatra as seen by local seismicity. *Earth and Planetary Science Letters*, *298*(1), 47-56.

Lay, T., Kanamori, H., Ammon, C. J., Nettles, M., Ward, S. N., Aster, R. C., DeShon, H. R. (2005). The great Sumatra-Andaman earthquake of 26 december 2004. *Science*, *308*(5725), 1127-1133.

Lin, S. C., & Kuo, B. Y. (2013). Trench-parallel flow in the southern Ryukyu subduction system: Effects of progressive rifting of the overriding plate. *Journal of Geophysical Research: Solid Earth*, *118*(1), 302-315.

Lindsay, A., McCloskey, J., & Nic Bhloscaidh, M. (2016). Using a genetic algorithm to estimate the details of earthquake slip distributions from point surface displacements. *Journal of Geophysical Research: Solid Earth*.

Long, M. D., & Silver, P. G. (2008). The subduction zone flow field from seismic anisotropy: A global view. *science*, *319*(5861), 315-318.

Lytwyn, J., Casey, J., Gilbert, S., & Kusky, T. (1997). Arc-like mid-ocean ridge basalt formed seaward of a trench-forearc system just prior to ridge subduction: An example from subaccreted ophiolites in southern Alaska. *Journal of Geophysical Research: Solid Earth*, *102*(B5), 10225-10243.

Mackenzie, G. D., Maguire, P. K. H., Coogan, L. A., Khan, M. A., Eaton, M., & Petrides, G. (2006). Geophysical constraints on the crustal architecture of the Troodos ophiolite: results from the IANGASS project. *Geophysical Journal International*, *167*(3), 1385-1401.

Macpherson, K. A., Hidayat, D., & Goh, S. H. (2012). Receiver function structure beneath four seismic stations in the Sumatra region. *Journal of Asian Earth Sciences*, *46*, 161-176.

Magistrale, H., Day, S., Clayton, R. W., & Graves, R. (2000). The SCEC southern California reference three-dimensional seismic velocity model version 2. *Bulletin of the Seismological Society of America*, *90*(6B), S65-S76.

Martin, M., Wenzel, F., & CALIXTO Working Group. (2006). High-resolution teleseismic body wave tomography beneath SE-Romania-II. Imaging of a slab detachment scenario. *Geophysical Journal International*, *164*(3), 579-595.

Martin, M. J. R. R., Ritter, J. R. R., & CALIXTO Working Group. (2005). High-resolution teleseismic body-wave tomography beneath SE Romania—I. Implications for three-dimensional versus one-dimensional crustal correction strategies with a new crustal velocity model. *Geophysical Journal International*, *162*(2), 448-460.

Marson-Pidgeon, K., Savage, M. K., Gledhill, K., & Stuart, G. (1999). Seismic anisotropy beneath the lower half of the North Island, New Zealand. *Journal of Geophysical Research: Solid Earth*, *104*(B9), 20277-20286.

Masturyono, M. R., Wark, DA & Roecker, SW (2001). Distribution of magma beneath the Toba caldera complex, north Sumatra, Indonesia, constrained by three-dimensional P wave velocities, seismicity, and gravity data. *Geochemistry, Geophysics, Geosystems*, *2*.

Matsubara, M., Hayashi, H., Obara, K., & Kasahara, K. (2005). Low-velocity oceanic crust at the top of the Philippine Sea and Pacific plates beneath the Kanto region, central Japan, imaged by seismic tomography. *Journal of Geophysical Research: Solid Earth*, *110*(B12).

McCaffrey, R., Wark, D. A., Roecker, S. W., & Ibrahim, G. (2001). Distribution of magma beneath the Toba caldera complex, north Sumatra, Indonesia, constrained by three-dimensional P wave velocities, seismicity, and gravity data. *Geochemistry, Geophysics, Geosystems*, *2*(4).

McNeill, L. C., & Henstock, T. J. (2014). Forearc structure and morphology along the Sumatra-Andaman subduction zone. *Tectonics*, *33*(2), 112-134.

Meltzner, A. J. (2010). *Earthquake recurrence, clustering, and persistent segmentation near the southern end of the 2004 Sunda megathrust rupture* (Doctoral dissertation, California Institute of Technology).

Meltzner, A. J., Sieh, K., Chiang, H. W., Shen, C. C., Suwargadi, B. W., Natawidjaja, D. H., Briggs, R. W. (2012). Persistent termini of 2004-and 2005-like ruptures of the Sunda megathrust. *Journal of Geophysical Research: Solid Earth*, *117*(B4).

Meltzner, A. J., Sieh, K., Chiang, H. W., Wu, C. C., Tsang, L. L., Shen, C. C., Briggs, R. W. (2015). Time-varying interseismic strain rates and similar seismic ruptures on the Nias–Simeulue patch of the Sunda megathrust. *Quaternary Science Reviews*, *122*, 258-281.

Meng, L., Ampuero, J. P., Stock, J., Duputel, Z., Luo, Y., & Tsai, V. C. (2012). Earthquake in a maze: Compressional rupture branching during the 2012 Mw 8.6 Sumatra earthquake. *Science*, *337*(6095), 724-726.

Misawa, A., Hirata, K., Seeber, L., Arai, K., Nakamura, Y., Rahardiawan, R., Adachi, K. (2014). Geological structure of the offshore Sumatra forearc region estimated from high-resolution MCS reflection survey. *Earth and Planetary Science Letters*, *386*, 41-51.

Moeremans, R., Singh, S. C., Mukti, M., McArdle, J., & Johansen, K. (2014). Seismic images of structural variations along the deformation front of the Andaman–Sumatra subduction zone: implications for rupture propagation and tsunamigenesis. *Earth and Planetary Science Letters*, *386*, 75-85.

Moore, G. F., Curray, J. R., & Emmel, F. J. (1982). Sedimentation in the Sunda Trench and forearc region. *Geological Society, London, Special Publications*, *10*(1), 245-258.

Moore, G. F., Curray, J. R., Moore, D. G., & Karig, D. E. (1980). Variations in geologic structure along the Sunda fore arc, northeastern Indian Ocean. *The Tectonic and Geologic Evolution of Southeast Asian Seas and Islands*, 145-160.

Moore, G. F., & Karig, D. E. (1980). Structural geology of Nias Island, Indonesia; implications for subduction zone tectonics. *American Journal of Science*, *280*(3), 193-223.

Moreno, M., Melnick, D., Rosenau, M., Baez, J., Klotz, J., Oncken, O., Socquet, A. (2012). Toward understanding tectonic control on the M w 8.8 2010 Maule Chile earthquake. *Earth and Planetary Science Letters*, *321*, 152-165.

Mosegaard, K., & Sambridge, M. (2002). Monte Carlo analysis of inverse problems. *Inverse Problems*, *18*(3), R29.

Mosher, D. C., Austin, J. A., Fisher, D., & Gulick, S. P. S. (2008). Deformation of the northern Sumatra accretionary prism from high-resolution seismic reflection profiles and ROV observations. *Marine Geology*, *252*(3), 89-99.

Muksin, U., Bauer, K., & Haberland, C. (2013). Seismic Vp and Vp/Vs structure of the geothermal area around Tarutung (North Sumatra, Indonesia) derived from local earthquake tomography. *Journal of Volcanology and Geothermal Research*, *260*, 27-42.

Mukti, M., Singh, S. C., Deighton, I., Hananto, N. D., Moeremans, R., & Permana, H. (2012). Structural evolution of backthrusting in the Mentawai Fault Zone, offshore Sumatran forearc. *Geochemistry, Geophysics, Geosystems*, *13*(12).

Müller, R. D., Roest, W. R., Royer, J. Y., Gahagan, L. M., & Sclater, J. G. (1997). Digital isochrons of the world's ocean floor. *Journal of Geophysical Research: Solid Earth*, *102*(B2), 3211-3214.

Nakajima, J., & Hasegawa, A. (2004). Shear-wave polarization anisotropy and subduction-induced flow in the mantle wedge of northeastern Japan. *Earth and Planetary Science Letters*, *225*(3), 365-377.

Nakajima, J., Matsuzawa, T., Hasegawa, A., & Zhao, D. (2001). Three-dimensional structure of Vp, Vs, and Vp/Vs beneath northeastern Japan: Implications for arc magmatism and fluids. *Journal of Geophysical Research: Solid Earth*, *106*(B10), 21843-21857.

Natawidjaja, D. H., Sieh, K., Chlieh, M., Galetzka, J., Suwargadi, B. W., Cheng, H., Ward, S. N. (2006). Source parameters of the great Sumatran megathrust earthquakes of 1797 and 1833 inferred from coral microatolls. *Journal of Geophysical Research: Solid Earth*, *111*(B6).

Newcomb, K. R., & McCann, W. R. (1987). Seismic history and seismotectonics of the Sunda Arc. *Journal of Geophysical Research: Solid Earth*, *92*(B1), 421-439.

Nicholson, K. N., Black, P. M., & Picard, C. (2000). Geochemistry and tectonic significance of the Tangihua ophiolite complex, New Zealand. *Tectonophysics*, *321*(1), 1-15.

Ogawa, Y., & Naka, J. (1984). Emplacement of ophiolitic rocks in forearc areas: examples from central Japan and Izu-Mariana-Yap island arc system. *Geological Society, London, Special Publications*, *13*(1), 291-301.

Okada, Y. (1992). Internal deformation due to shear and tensile faults in a half-space. *Bulletin of the Seismological Society of America*, *82*(2), 1018-1040.

Oleskevich, D. A., Hyndman, R. D., & Wang, K. (1999). The updip and downdip limits to great subduction earthquakes: Thermal and structural models of Cascadia, south Alaska, SW Japan, and Chile. *Journal of Geophysical Research: Solid Earth*, *104*(B7), 14965-14991.

Parkinson, I. J., Hawkesworth, C. J., & Cohen, A. S. (1998). Ancient mantle in a modern arc: Osmium isotopes in Izu-Bonin-Mariana forearc peridotites. *Science*, *281*(5385), 2011-2013.

Pavlis, G. L., & Booker, J. R. (1980). The mixed discrete-continuous inverse problem: Application to the simultaneous determination of earthquake hypocenters and velocity structure. *Journal of Geophysical Research: Solid Earth*, *85*(B9), 4801-4810.

Peacock, S. M., & Hyndman, R. D. (1999). Hydrous minerals in the mantle wedge and the maximum depth of subduction thrust earthquakes. *Geophysical Research Letters*, *26*(16), 2517-2520.

Peacock, S. M. (1993). Large-scale hydration of the lithosphere above subducting slabs. *Chemical Geology*, *108*(1), 49-59.

Pearce, J. A., & Peate, D. W. (1995). Tectonic implications of the composition of volcanic arc magmas. *Annual Review of Earth and Planetary Sciences*, *23*(1), 251-285.

Pesicek, J. D., Thurber, C. H., Widiyantoro, S., Engdahl, E. R., & DeShon, H. R. (2008). Complex slab subduction beneath northern Sumatra. *Geophysical Research Letters*, *35*(20).

Pesicek, J. D., Thurber, C. H., Widiyantoro, S., Zhang, H., DeShon, H. R., & Engdahl, E. R. (2010). Sharpening the tomographic image of the subducting slab below Sumatra, the Andaman Islands and Burma. *Geophysical Journal International*, *182*(1), 433-453.

Pesicek, J. D., Thurber, C. H., Zhang, H., DeShon, H. R., Engdahl, E. R., & Widiyantoro, S. (2010). Teleseismic double-difference relocation of earthquakes along the Sumatra-Andaman subduction zone using a 3-D model. *Journal of Geophysical Research: Solid Earth*, *115*(B10).

Polet, J., Silver, P. G., Beck, S., Wallace, T., Zandt, G., Ruppert, S., Rudloff, A. (2000). Shear wave anisotropy beneath the Andes from the BANJO, SEDA, and PISCO experiments. *Journal of Geophysical Research: Solid Earth*, *105*(B3), 6287-6304.

Prawirodirdjo, L., Bocl, Y., McCaffrey, R., Genrich, J., Calais, E., Stevens, C., Fauzi, R. M. (1997). Geodetic observations of interseismic strain segmentation at the Sumatra subduction zone. *Geophysical research letters*, *24*(21), 2601-2604.

Qin, Y., & Singh, S. C. (2015). Seismic evidence of a two-layer lithospheric deformation in the Indian Ocean. *Nature communications*, *6*.

Raju, K. K., Ramprasad, T., Rao, P. S., Rao, B. R., & Varghese, J. (2004). New insights into the tectonic evolution of the Andaman basin, northeast Indian Ocean. *Earth and Planetary Science Letters*, *221*(1), 145-162.

Rajendran, C. P., Rajendran, K., Anu, R., Earnest, A., Machado, T., Mohan, P. M., & Freymueller, J. (2007). Crustal deformation and seismic history associated with the 2004 Indian Ocean earthquake: a perspective from the Andaman–Nicobar Islands. *Bulletin of the Seismological Society of America*, *97*(1A), S174-S191.

Rasmussen, J., & Humphreys, E. (1988). Tomographic image of the Juan de Fuca Plate beneath Washington and western Oregon using teleseismic P-wave travel times. *Geophysical Research Letters*, *15*(12), 1417-1420.

Rawlinson, N., & Urvoy, M. (2006). Simultaneous inversion of active and passive source datasets for 3-D seismic structure with application to Tasmania. *Geophysical Research Letters*, *33*(24).

Reyners, M., Eberhart-Phillips, D., Stuart, G., & Nishimura, Y. (2006). Imaging subduction from the trench to 300 km depth beneath the central North Island, New Zealand, with Vp and Vp/Vs. *Geophysical Journal International*, *165*(2), 565-583.

Ribe, N. M. (1989). Seismic anisotropy and mantle flow. *Journal of Geophysical Research: Solid Earth*, *94*(B4), 4213-4223.

Ruff, L. J., & Tichelaar, B. W. (1996). What controls the seismogenic plate interface in subduction zones?. *Subduction top to bottom*, 105-111.

Russo, R. M., & Silver, P. G. (1994). Trench-parallel flow beneath the Nazca plate from seismic anisotropy. *SCIENCE-NEW YORK THEN WASHINGTON-*, 1105-1105.

Saffer, D. M., & Tobin, H. J. (2011). Hydrogeology and mechanics of subduction zone forearcs: Fluid flow and pore pressure. *Annual Review of Earth and Planetary Sciences*, *39*, 157-186.

Saffer, D. M., & Marone, C. (2003). Comparison of smectite-and illite-rich gouge frictional properties: application to the updip limit of the seismogenic zone along subduction megathrusts. *Earth and Planetary Science Letters*, *215*(1), 219-235.

Salisbury, M. H., & Christensen, N. I. (1978). The seismic velocity structure of a traverse through the Bay of Islands ophiolite complex, Newfoundland, an exposure of oceanic crust and upper mantle. *Journal of Geophysical Research: Solid Earth*, *83*(B2), 805-817.

Salmon, M., Kennett, B. L. N., Stern, T., & Aitken, A. R. A. (2013). The Moho in Australia and New Zealand. *Tectonophysics*, *609*, 288-298.

Samuel, M. A., Harbury, N. A., Bakri, A., Banner, F. T., & Hartono, L. (1997). A new stratigraphy for the islands of the Sumatran Forearc, Indonesia. *Journal of Asian Earth Sciences*, *15*(4-5), 339347353369373-345351367371380.

Sandvol, E., & Ni, J. (1997). Deep azimuthal seismic anisotropy in the southern Kurile and Japan subduction zones. *Journal of Geophysical Research: Solid Earth*, *102*(B5), 9911-9922.

Satriano, C., Kiraly, E., Bernard, P., & Vilotte, J. P. (2012). The 2012 Mw 8.6 Sumatra earthquake: Evidence of westward sequential seismic ruptures associated to the reactivation of a N-S ocean fabric. *Geophysical Research Letters*, *39*(15).

Savage, J. C. (1983). A dislocation model of strain accumulation and release at a subduction zone. *Journal of Geophysical Research: Solid Earth*, *88*(B6), 4984-4996.

Scherwath, M., Kopp, H., Flueh, E. R., Henrys, S. A., Sutherland, R., Stagpoole, V. M., Dannowski, A. (2010). Fore-arc deformation and underplating at the northern Hikurangi margin, New Zealand. *Journal of Geophysical Research: Solid Earth*, *115*(B6).

Schlüter, H. U., Gaedicke, C., Roeser, H. A., Schreckenberger, B., Meyer, H., Reichert, C., Prexl, A. (2002). Tectonic features of the southern Sumatra-western Java forearc of Indonesia. *Tectonics*, *21*(5).

Scordilis, E. M. (2006). Empirical global relations converting M S and m b to moment magnitude. *Journal of Seismology*, *10*(2), 225-236.

Seno, T., Zhao, D., Kobayashi, Y., & Nakamura, M. (2001). Dehydration of serpentinized slab mantle: Seismic evidence from southwest Japan. *Earth, planets and space*, *53*(9), 861-871.

Seno, T. (2005). Variation of downdip limit of the seismogenic zone near the Japanese islands: Implications for the serpentinization mechanism of the forearc mantle wedge. *Earth and Planetary Science Letters*, *231*(3), 249-262.

Shiomi, K., Obara, K., & Sato, H. (2006). Moho depth variation beneath southwestern Japan revealed from the velocity structure based on receiver function inversion. *Tectonophysics*, *420*(1), 205-221.

Sieh, K., & Natawidjaja, D. (2000). Neotectonics of the Sumatran fault, Indonesia. *Journal of Geophysical Research: Solid Earth*, *105*(B12), 28295-28326.

Sieh, K., Natawidjaja, D. H., Meltzner, A. J., Shen, C. C., Cheng, H., Li, K. S., Edwards, R. L. (2008). Earthquake supercycles inferred from sea-level changes recorded in the corals of west Sumatra. *Science*, *322*(5908), 1674-1678.

Simoes, M., Avouac, J. P., Cattin, R., & Henry, P. (2004). The Sumatra subduction zone: A case for a locked fault zone extending into the mantle. *Journal of Geophysical Research: Solid Earth*, *109*(B10).

Singh, S. C., Chauhan, A. P., Calvert, A. J., Hananto, N. D., Ghosal, D., Rai, A., & Carton, H. (2012). Seismic evidence of bending and unbending of subducting oceanic crust and the presence of mantle megathrust in the 2004 Great Sumatra earthquake rupture zone. *Earth and Planetary Science Letters*, *321*, 166-176.

Singh, S. C., Hananto, N. D., & Chauhan, A. P. S. (2011). Enhanced reflectivity of backthrusts in the recent great Sumatran earthquake rupture zones. *Geophysical Research Letters*, *38*(4).

Smith, G., McNeill, L., Henstock, T. J., & Bull, J. (2012). The structure and fault activity of the Makran accretionary prism. *Journal of Geophysical Research: Solid Earth*, *117*(B7).

Smith, G. L., McNeill, L. C., Wang, K., He, J., & Henstock, T. J. (2013). Thermal structure and megathrust seismogenic potential of the Makran subduction zone. *Geophysical Research Letters*, *40*(8), 1528-1533.

Song, T. R. A., & Kawakatsu, H. (2012). Subduction of oceanic asthenosphere: evidence from sub-slab seismic anisotropy. *Geophysical Research Letters*, *39*(17).

Sparkes, R., Tilmann, F., Hovius, N., & Hillier, J. (2010). Subducted seafloor relief stops rupture in South American great earthquakes: Implications for rupture behaviour in the 2010 Maule, Chile earthquake. *Earth and Planetary Science Letters*, *298*(1), 89-94.

Spencer, C., & Gubbins, D. (1980). Travel-time inversion for simultaneous earthquake location and velocity structure determination in laterally varying media. *Geophysical Journal International*, *63*(1), 95-116.

Di Stefano, R., & Chiarabba, C. (2002). Active source tomography at Mt. Vesuvius: Constraints for the magmatic system. *Journal of Geophysical Research: Solid Earth*, *107*(B11).

Takashima, R., Kawabe, F., Nishi, H., Moriya, K., Wani, R., & Ando, H. (2004). Geology and stratigraphy of forearc basin sediments in Hokkaido, Japan: Cretaceous environmental events on the north-west Pacific margin. *Cretaceous Research*, *25*(3), 365-390.

Tang, G., Barton, P. J., McNeill, L. C., Henstock, T. J., Tilmann, F., Dean, S. M., ... & Kopp, H. (2013). 3-D active source tomography around Simeulue Island offshore Sumatra: Thick crustal zone responsible for earthquake segment boundary. *Geophysical Research Letters*, *40*(1), 48-53.

Taylor, F. W., Mann, P., Bevis, M. G., Edwards, R. L., Cheng, H., Cutler, K. B., ... & Cabioch, G. (2005). Rapid forearc uplift and subsidence caused by impinging bathymetric features: Examples from the New Hebrides and Solomon arcs. *Tectonics*, *24*(6).

Thurber, C. H. (1983). Earthquake locations and three-dimensional crustal structure in the Coyote Lake area, central California. *Journal of Geophysical Research: Solid Earth*, *88*(B10), 8226-8236.

Thurber, C. H. (1992). Hypocenter-velocity structure coupling in local earthquake tomography. *Physics of the Earth and Planetary Interiors*, *75*(1-3), 55-62.

Thurber, C. H., & Aki, K. (1987). Three-dimensional seismic imaging. *Annual Review of Earth and Planetary Sciences*, *15*(1), 115-139.

Thurber, C., & Eberhart-Phillips, D. (1999). Local earthquake tomography with flexible gridding. *Computers & Geosciences*, *25*(7), 809-818.

Thurber, C. H., & Ellsworth, W. L. (1980). Rapid solution of ray tracing problems in heterogeneous media. *Bulletin of the Seismological Society of America*, *70*(4), 1137-1148.

Tilmann, F. J., Craig, T. J., Grevemeyer, I., Suwargadi, B., Kopp, H., & Flueh, E. (2010). The updip seismic/aseismic transition of the Sumatra megathrust illuminated by aftershocks of the 2004 Aceh-Andaman and 2005 Nias events. *Geophysical Journal International*, *181*(3), 1261-1274.

Tommasi, A. (1998). Forward modeling of the development of seismic anisotropy in the upper mantle. *Earth and Planetary Science Letters*, *160*(1), 1-13.

Tromp, J., Tape, C., & Liu, Q. (2005). Seismic tomography, adjoint methods, time reversal and banana-doughnut kernels. *Geophysical Journal International*, *160*(1), 195-216.

Tsuji, Y., Nakajima, J., & Hasegawa, A. (2008). Tomographic evidence for hydrated oceanic crust of the Pacific slab beneath northeastern Japan: implications for water transportation in subduction zones. *Geophysical Research Letters*, *35*(14).

Um, J., & Thurber, C. (1987). A fast algorithm for two-point seismic ray tracing. *Bulletin of the Seismological Society of America*, *77*(3), 972-986.

Vigny, C., Socquet, A., Peyrat, S., Ruegg, J. C., Métois, M., Madariaga, R., ... & Carrizo, D. (2011). The 2010 Mw 8.8 Maule megathrust earthquake of Central Chile, monitored by GPS. *Science*, *332*(6036), 1417-1421.

Walker, K. T., Ishii, M., & Shearer, P. M. (2005). Rupture details of the 28 March 2005 Sumatra Mw 8.6 earthquake imaged with teleseismic P waves. *Geophysical Research Letters*, *32*(24).

Walther, C. H. E., Flueh, E. R., Ranero, C. R., Von Huene, R., & Strauch, W. (2000). Crustal structure across the Pacific margin of Nicaragua: Evidence for ophiolitic basement and a shallow mantle sliver. *Geophysical Journal International*, *141*(3), 759-777.

Wang, K., & Bilek, S. L. (2011). Do subducting seamounts generate or stop large earthquakes?. *Geology*, *39*(9), 819-822.

Wang, Z., & Zhao, D. (2006). Vp and Vs tomography of Kyushu, Japan: New insight into arc magmatism and forearc seismotectonics. *Physics of the Earth and Planetary Interiors*, *157*(3), 269-285.

Weatherill, G., & Burton, P. W. (2009). Delineation of shallow seismic source zones using K-means cluster analysis, with application to the Aegean region. *Geophysical Journal International*, *176*(2), 565-588.

Wells, D. L., & Coppersmith, K. J. (1994). New empirical relationships among magnitude, rupture length, rupture width, rupture area, and surface displacement. *Bulletin of the seismological Society of America*, *84*(4), 974-1002.

Wen, L., & Anderson, D. L. (1995). The fate of slabs inferred from seismic tomography and 130 million years of subduction. *Earth and Planetary Science Letters*, *133*(1-2), 185-198.

Whattam, S. A., & Stern, R. J. (2011). The 'subduction initiation rule': a key for linking ophiolites, intra-oceanic forearcs, and subduction initiation. *Contributions to Mineralogy and Petrology*, *162*(5), 1031-1045.

Wibberley, C. A., & Shimamoto, T. (2003). Internal structure and permeability of major strike-slip fault zones: the Median Tectonic Line in Mie Prefecture, Southwest Japan. *Journal of Structural Geology*, *25*(1), 59-78.

Widiyantoro, S., Kennett, B. L. N., & Van der Hilst, R. D. (1999). Seismic tomography with P and S data reveals lateral variations in the rigidity of deep slabs. *Earth and Planetary Science Letters*, *173*(1), 91-100.

Woodhouse, J. H., & Dziewonski, A. M. (1984). Mapping the upper mantle: Three-dimensional modeling of Earth structure by inversion of seismic waveforms. *Journal of Geophysical Research: Solid Earth*, *89*(B7), 5953-5986.

Xia, S., Zhao, D., & Qiu, X. (2008). Tomographic evidence for the subducting oceanic crust and forearc mantle serpentinization under Kyushu, Japan. *Tectonophysics*, *449*(1), 85-96.

Yamazaki, T., & Okamura, Y. (1989). Subducting seamounts and deformation of overriding forearc wedges around Japan. *Tectonophysics*, *160*(1-4), 207221-217229.

Yu, W. C., Song, T. R. A., & Silver, P. G. (2013). Temporal velocity changes in the crust associated with the Great Sumatra earthquakes. *Bulletin of the Seismological Society of America*, *103*(5), 2797-2809.

Yuan, H., & Dueker, K. (2005). Teleseismic P-wave tomogram of the Yellowstone plume. *Geophysical Research Letters*, *32*(7).

Zelt, C. A., Azaria, A., & Levander, A. (2006). 3D seismic refraction traveltime tomography at a groundwater contamination site. *Geophysics*, *71*(5), H67-H78.

Zhang, H., Thurber, C. H., Shelly, D., Ide, S., Beroza, G. C., & Hasegawa, A. (2004). High-resolution subducting-slab structure beneath northern Honshu, Japan, revealed by double-difference tomography. *Geology*, *32*(4), 361-364.

Zhao, D. (2004). Global tomographic images of mantle plumes and subducting slabs: insight into deep Earth dynamics. *Physics of the Earth and Planetary Interiors*, *146*(1), 3-34.

Zhao, D., Hasegawa, A., & Kanamori, H. (1994). Deep structure of Japan subduction zone as derived from local, regional, and teleseismic events. *Journal of Geophysical Research: Solid Earth*, *99*(B11), 22313-22329.

Zhao, D., Hasegawa, A., & Horiuchi, S. (1992). Tomographic imaging of P and S wave velocity structure beneath northeastern Japan. *Journal of Geophysical Research: Solid Earth*, *97*(B13), 19909-19928.

Zhao, D., Huang, Z., Umino, N., Hasegawa, A., & Yoshida, T. (2011). Seismic imaging of the Amur–Okhotsk plate boundary zone in the Japan Sea. *Physics of the Earth and Planetary Interiors*, *188*(1), 82-95.

Zhao, D., Kanamori, H., Negishi, H., & Wiens, D. (1996). Tomography of the source area of the 1995 Kobe earthquake: evidence for fluids at the hypocenter?. *Science*, *274*(5294), 1891.

Zhao, D., Wang, Z., Umino, N., & Hasegawa, A. (2007). Tomographic imaging outside a seismic network: Application to the northeast Japan arc. *Bulletin of the Seismological Society of America*, *97*(4), 1121-1132.

Zhao, D., Wang, Z., Umino, N., & Hasegawa, A. (2009). Mapping the mantle wedge and interplate thrust zone of the northeast Japan arc. *Tectonophysics*, *467*(1), 89-106.

Zhao, D., Wei, W., Nishizono, Y., & Inakura, H. (2011). Low-frequency earthquakes and tomography in western Japan: insight into fluid and magmatic activity. *Journal of Asian Earth Sciences*, *42*(6), 1381-1393.

# 8 Chapter 8: Appendix

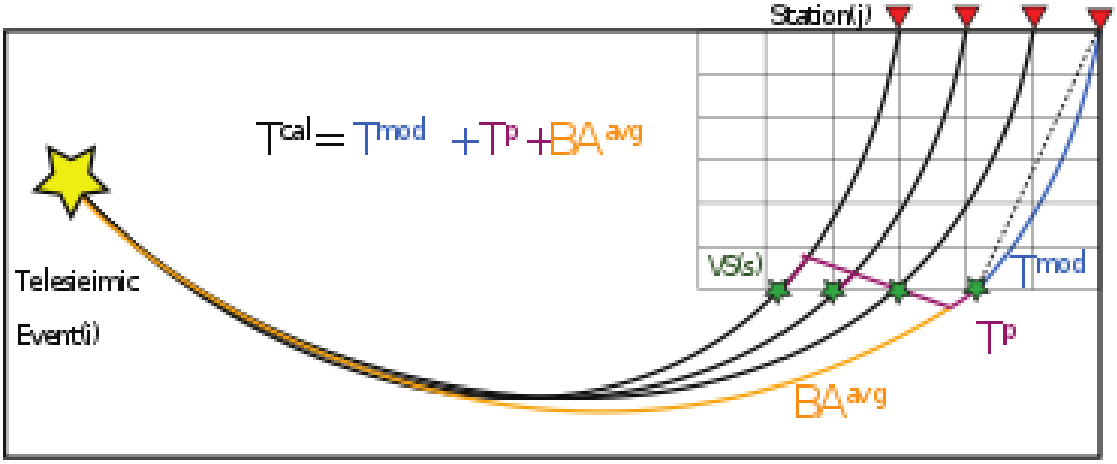


*Figure S 8.1 Schematic explain the teleseismic methodology. Were $T^{cal}$=Calculated travel time, $T^{mod}$=Travel time within the model space, $T^{p}$=plane wave correction, $BA^{avg}$ is the bulk average correction for the teleseismic event, VS(s) and station(j) are the virtual source (s) and station(j) for the in coming observation k.*

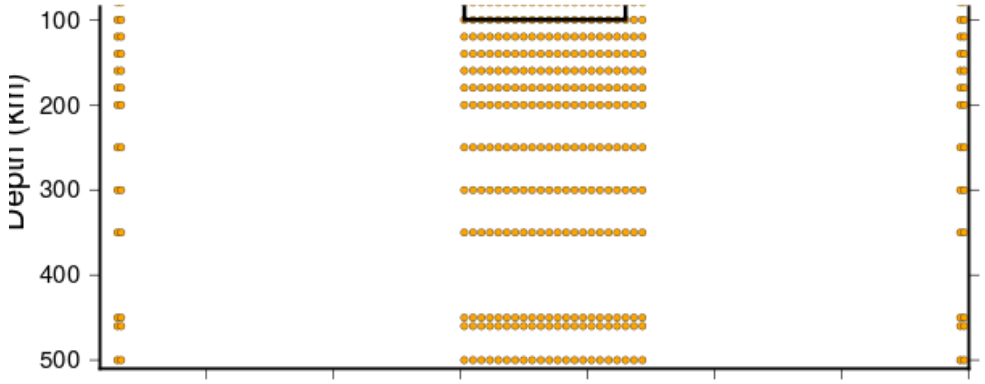


*Figure S 8.2 Full 2D node setup for the 2D and 3D X planes.*

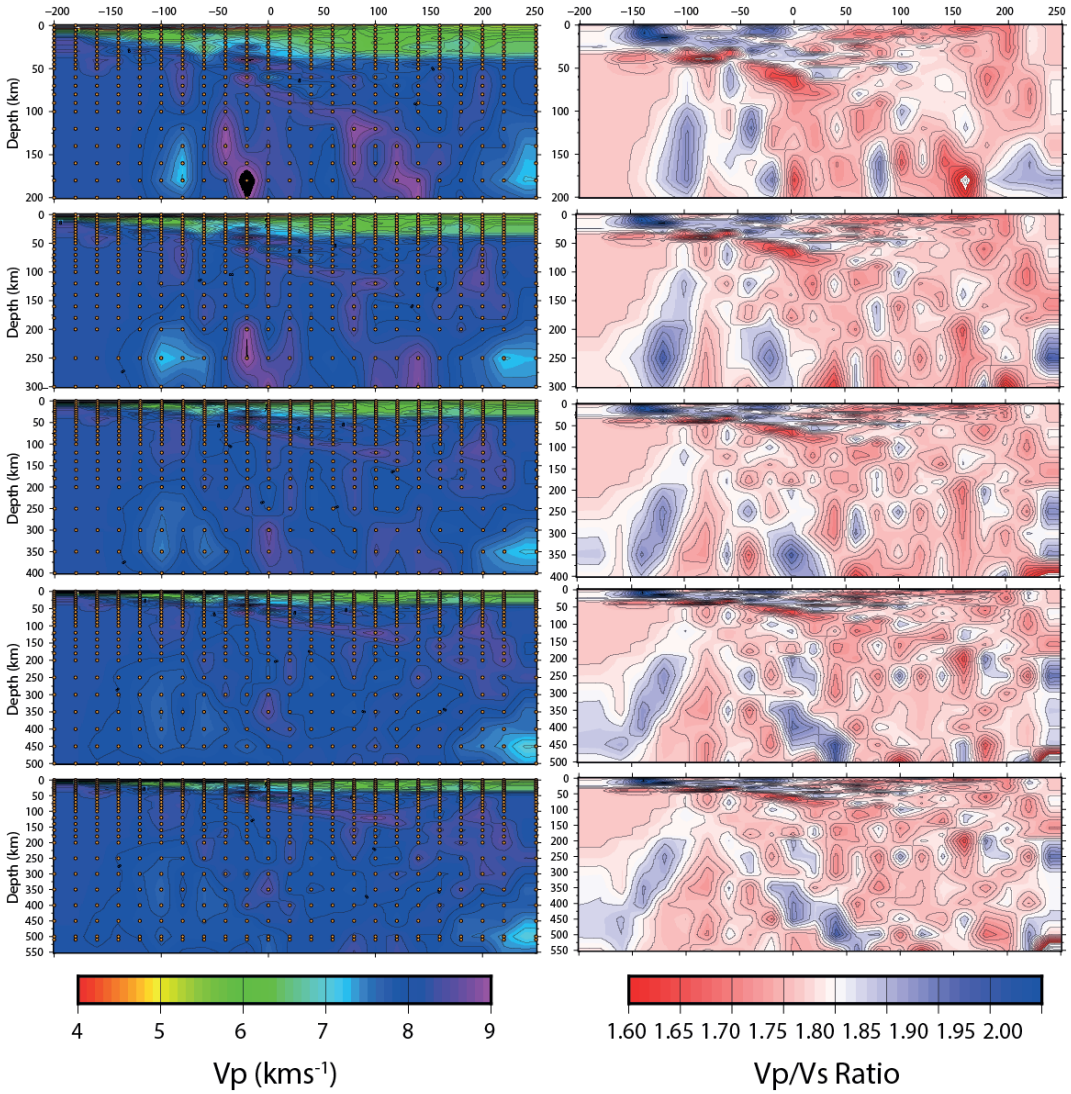


*Figure S 8.3 Squeezing tests for when the virtual source is at 200,300,400,450 and 500km depth*

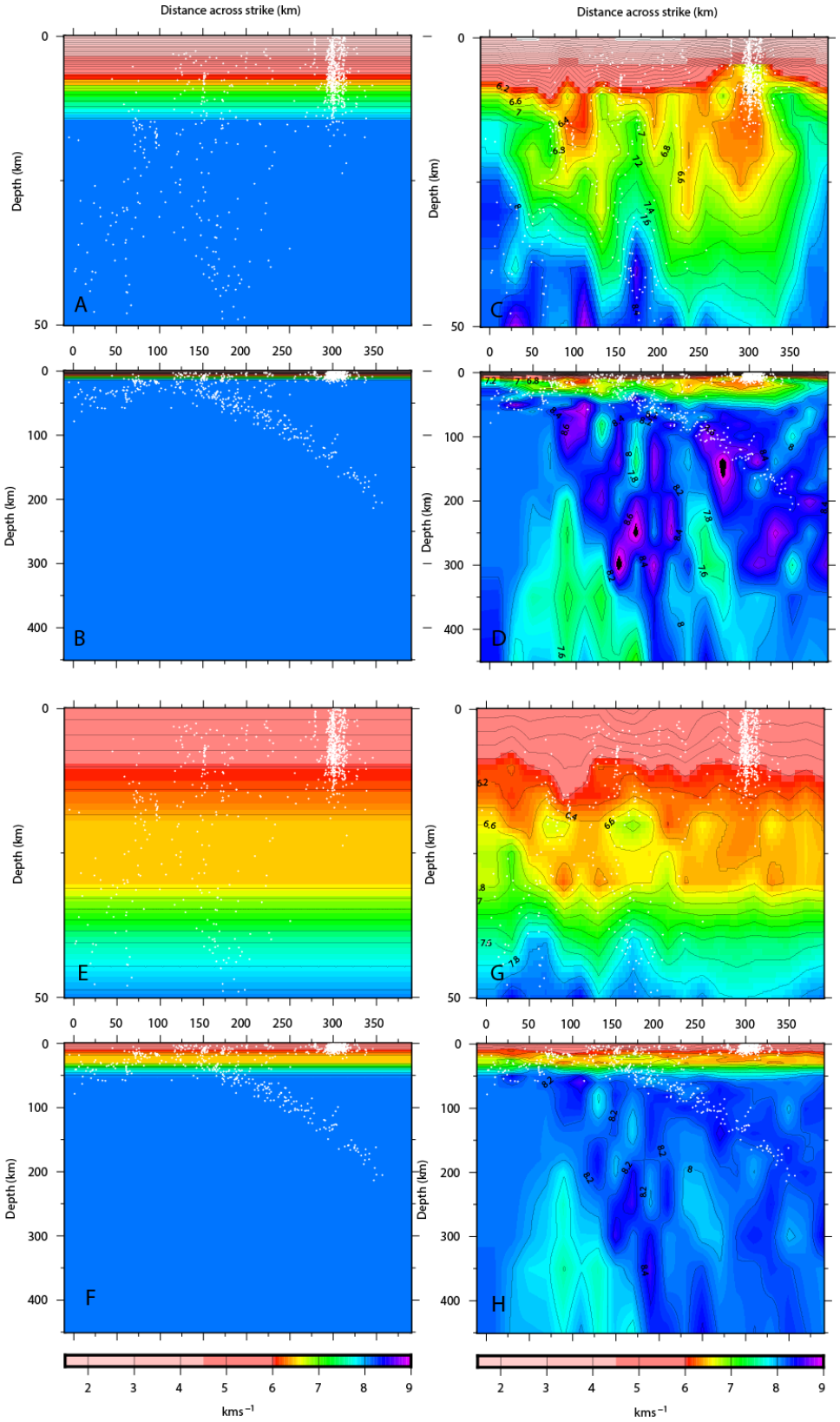


*Figure S 8.4 The resulting 2D Vp models based on different starting models. A and B are the shallow and deep oceanic 1D starting models with C and D the resulting shallow and deep Vp velocity model. E and F and G and H are the same but using a continental starting model. White dots are hypocenters.*

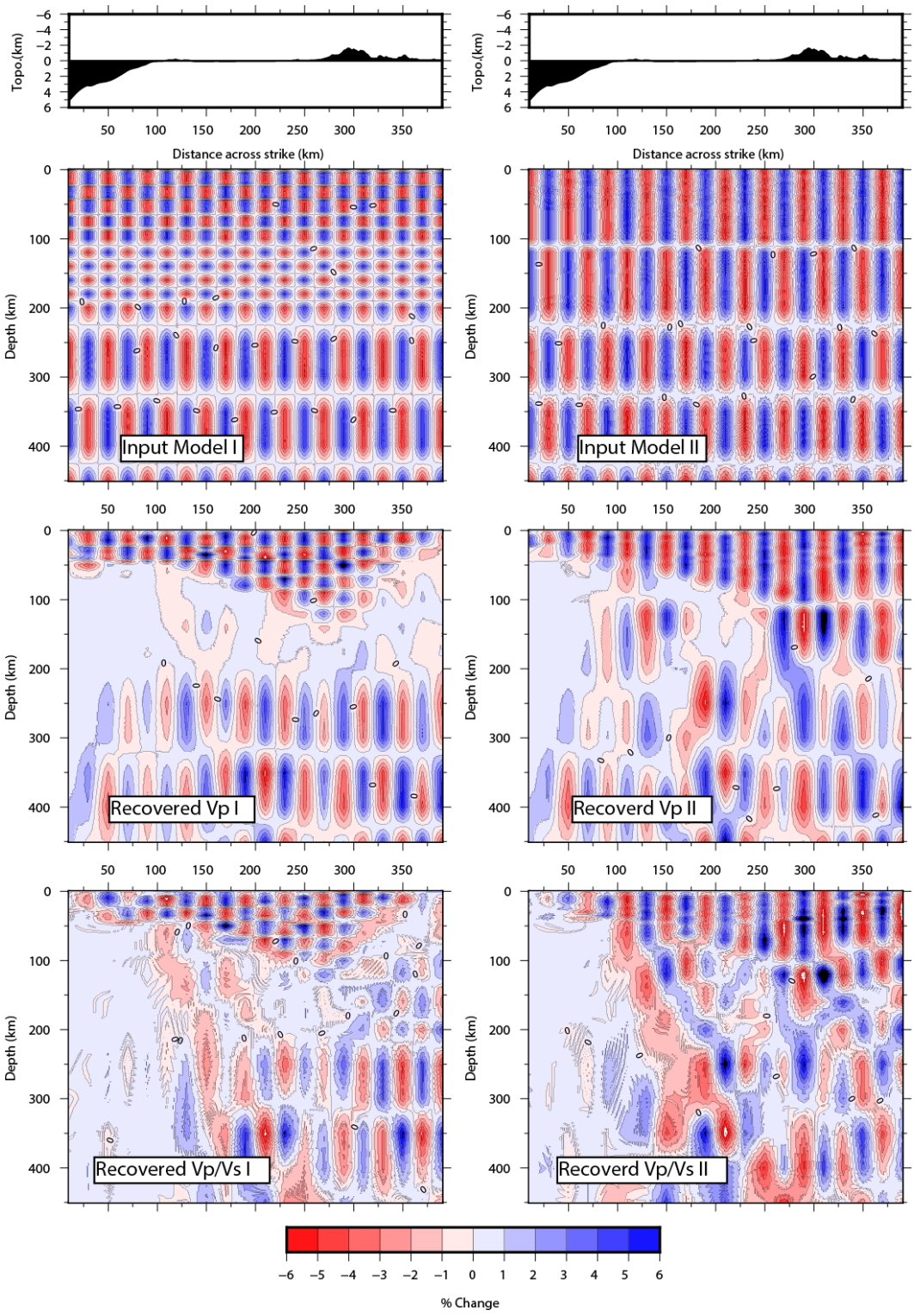


Figure S 8.5 Checkerboard test for the 2D model based on 2 different input models

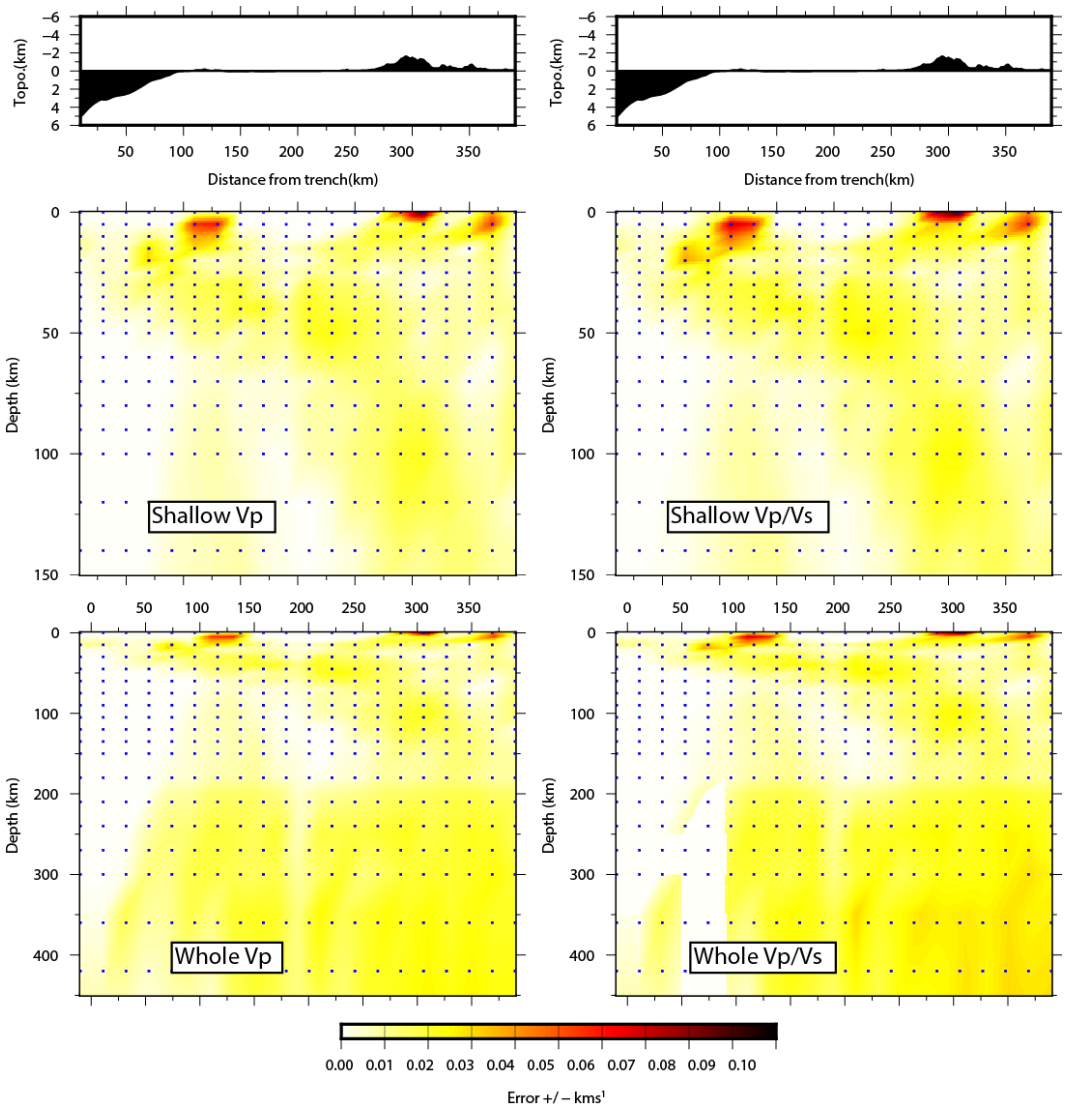


*Figure S 8.6 A slice taken from the 3D model showing errors in the Vp and Vp/Vs models. The slice was taken at 200km across strike, Perpendicular to the Batu islands.*

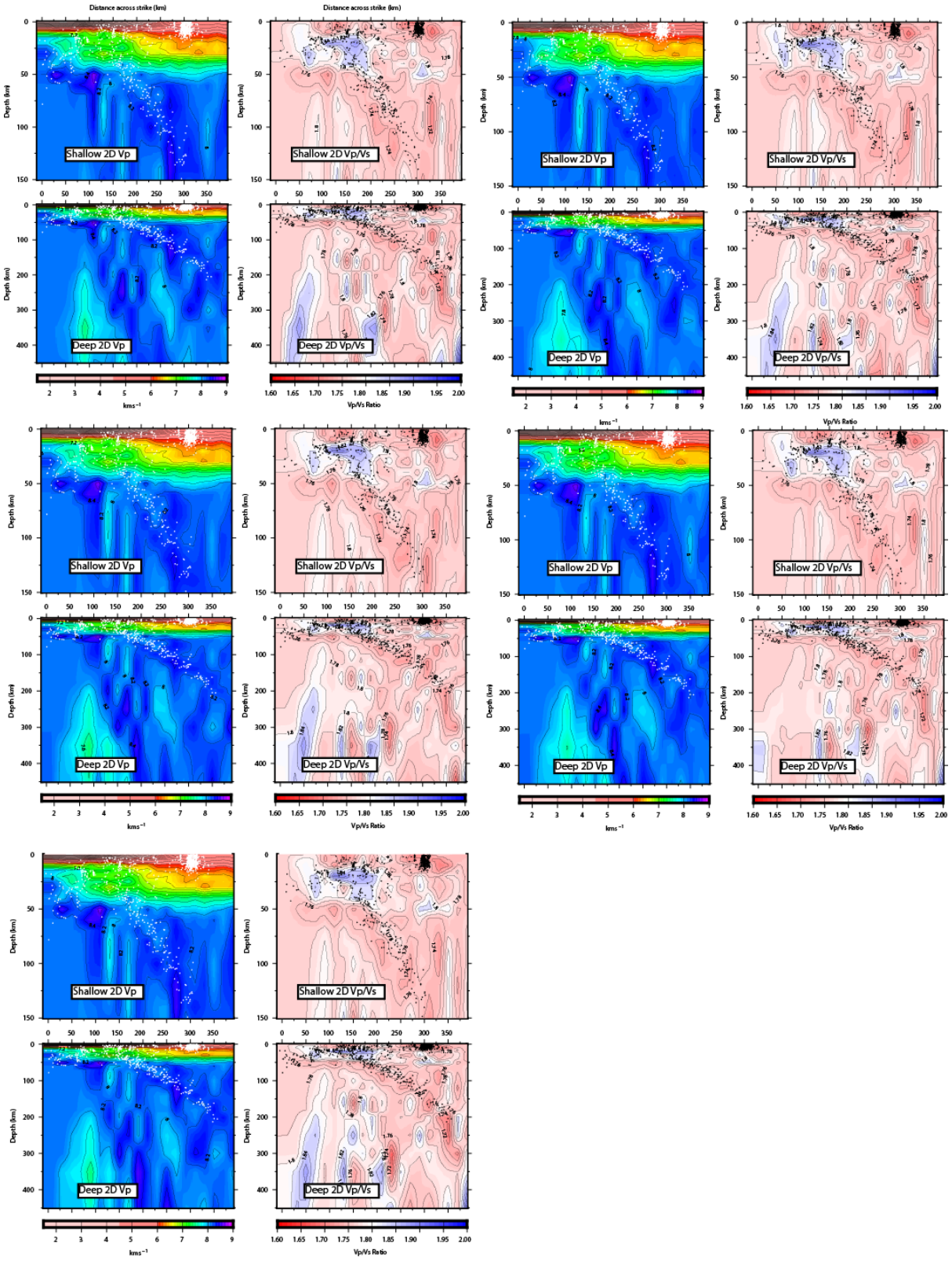


*Figure S 8.7 Bootstrapping tests conducted to test the robustness of the features in the model. Shown here are the 2D Vp and Vp/Vs results from 5 models each randomly removing 10% of the input data. All features discussed in the text are seen to be present in all the models.*

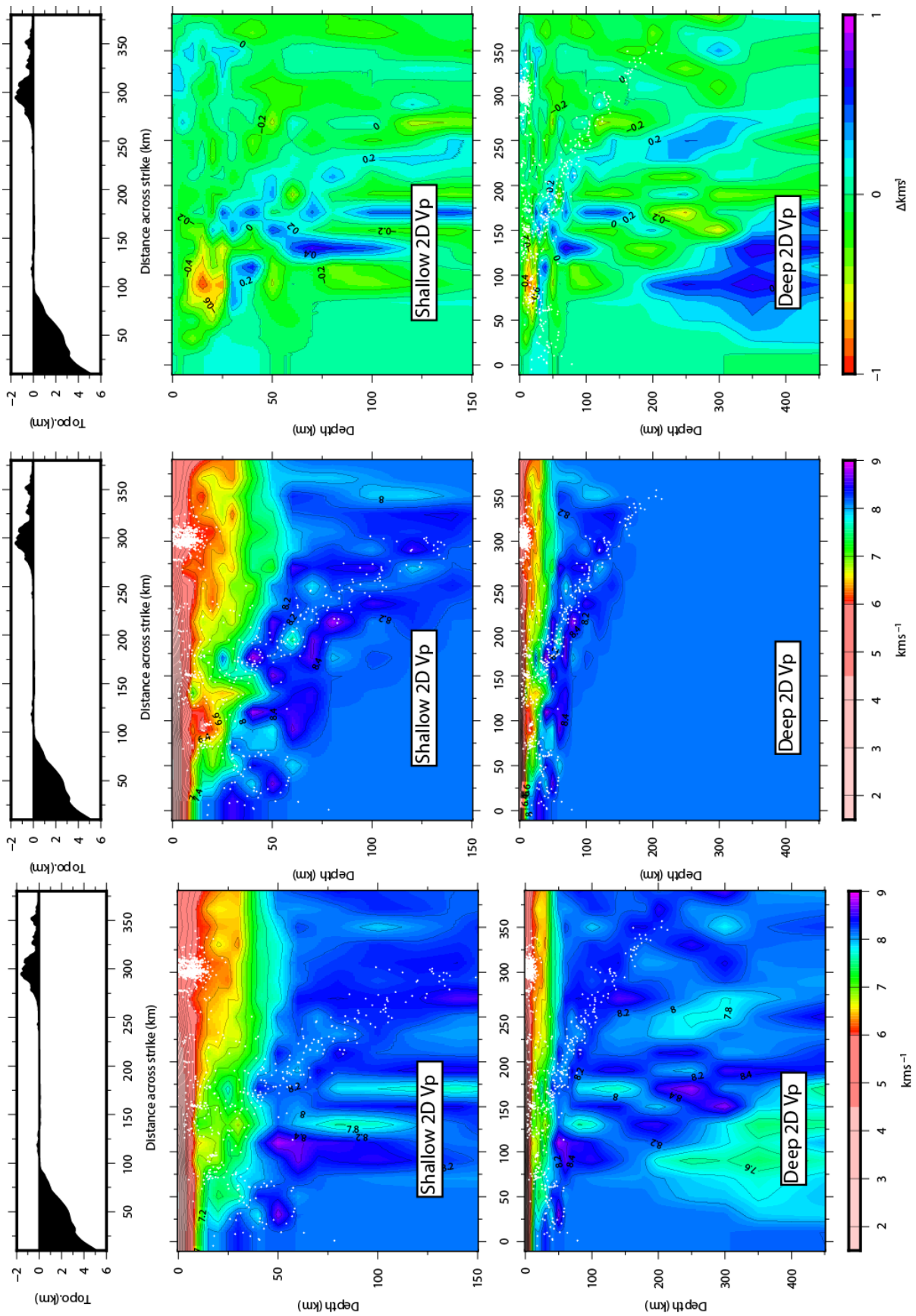


*Figure S 8.8 Comparison results for the 2D Vp Model showing the joint 2D Vp model (bottom), local data only 2D Vp model (middle) and difference between the joint and local inversions (top).*

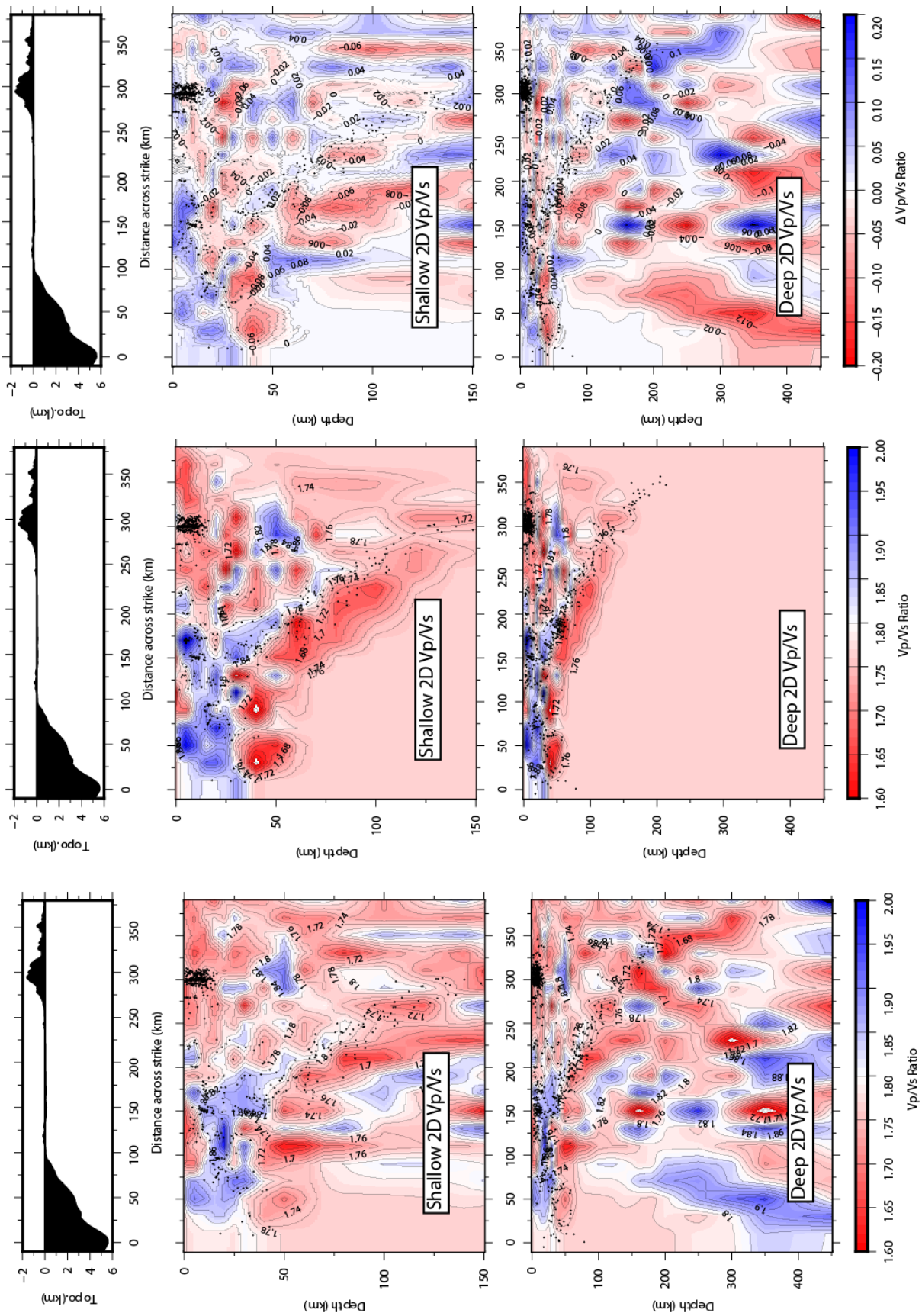


*Figure S 8.9 Comparison results for the 2D Vp/Vs model showing the joint 2D Vp/Vs model (bottom), local data only 2D Vp/Vs model (middle) and difference between the joint and local inversions (top).*

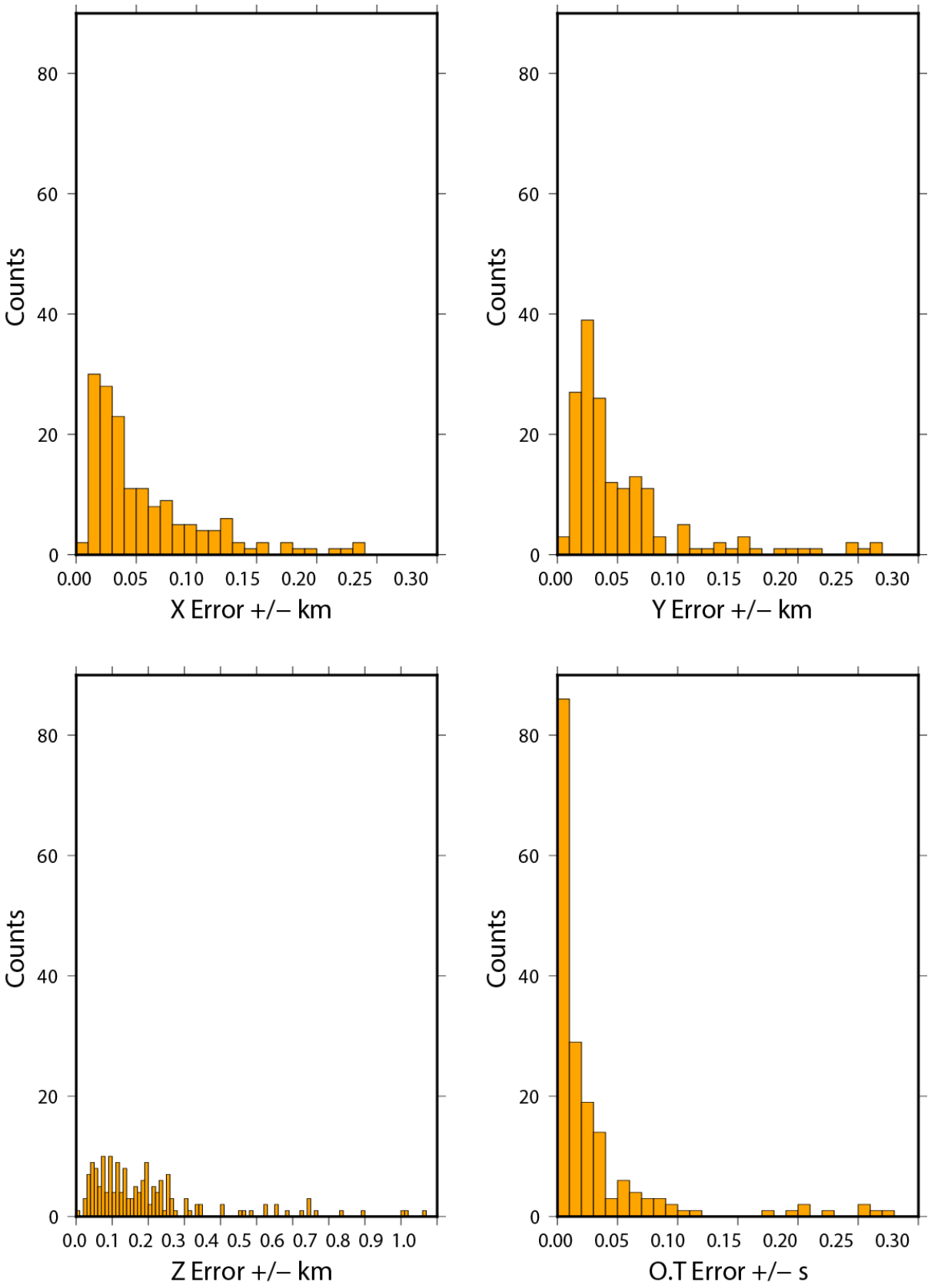


*Figure S 8.10 Errors in origin time (o.t), X,Y and Z for the relocated hypocenters from the local/active source 3D model.*

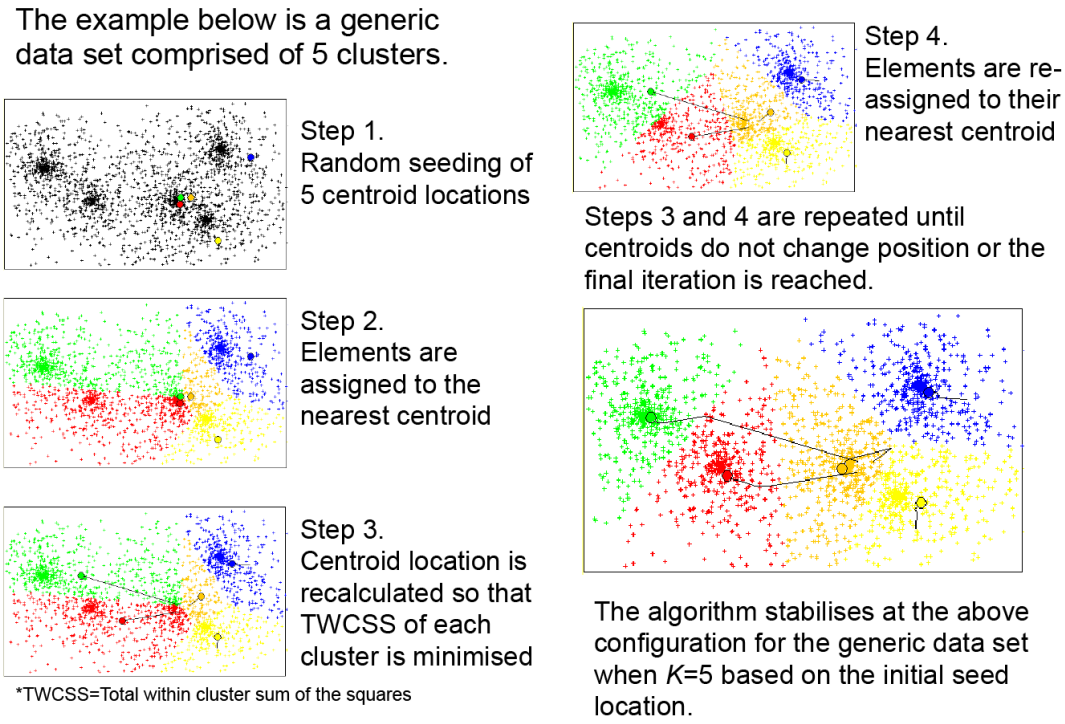


*Figure S 8.11 K-means Schematic depicting how the algorithm chooses optimum cluster location for 5 clusters*

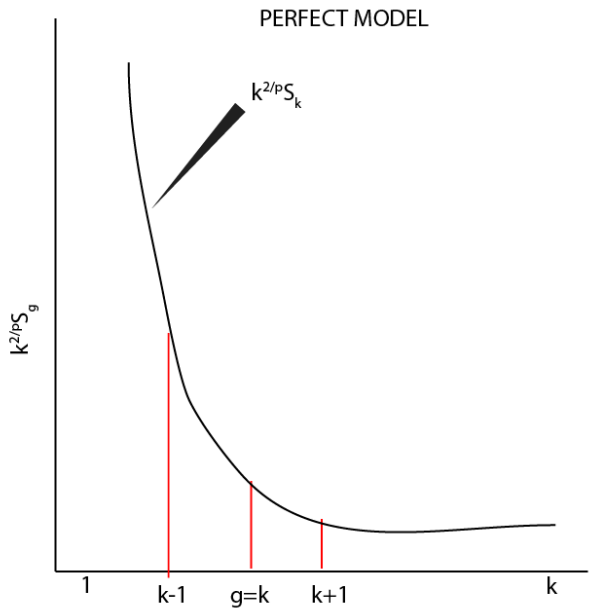


$k^{2/P}S_g$ is essensealy a function of the variaince within a model conatianing k clusters and it should remain constant for homogenous uniform data for all k clusters models.
In practicaltity it doesnt data tends to group thus $k^{2/P}S_g$ isnt constant and follows the trend seen on the graph (roughly exponetial decay).
when there is a inflection point
in the data that is defined as optium K
(on the graph the point were g=k). KL index ID's this point.

differences between k and k-1 is large postive
differences between k and k+1 is small postive
The KL index looks for this point in the data.

the KL index uses the value of $k^{2/P}S_k$ for each K

and calulates

$$KL = \frac{(K-1) - K \quad (1)}{K - K+1 \quad (2)}$$

Therefore when k<g both (1) and (2) will be large thus KL small.
When K>g both (1) and (2) will be small therefore KL small.
For K=g (1) will be large and (2) will be small therefore KL large.

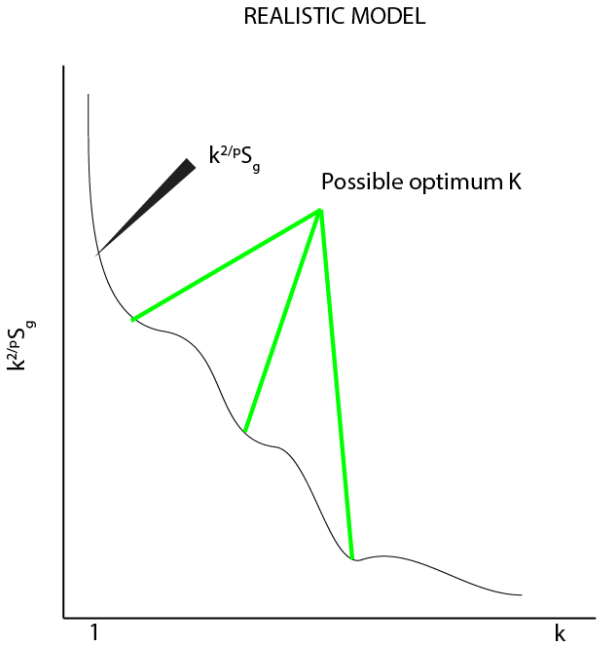


In reality serval of these so called inflections points can be defined and will all show as possible optium K values (which is what we see).
down to us to ID the opitum K using logic.

*Figure S 8.12 Explanations of how the KL index is calculated based on a K cluster model*